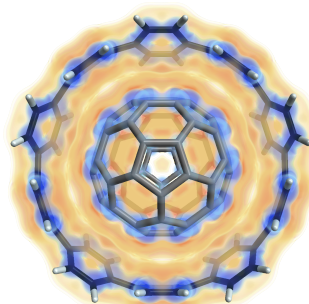


---

# **Towards unified density-functional model of van der Waals interactions**



## **Dissertation**

**zur Erlangung des akademischen Grades**

**Doctor rerum naturalium  
(Dr. rer. nat.)**

**im Fach Physik  
Spezialisierung: Theoretische Physik**

**eingereicht an der  
Mathematisch-Naturwissenschaftlichen Fakultät  
der Humboldt-Universität zu Berlin**

**von**

**Mgr. & Bc. Jan Hermann**

**geboren am 24. 4. 1989 in Český Krumlov**

**Präsidentin der Humboldt-Universität zu Berlin:  
Prof. Dr.-Ing. Dr. Sabine Kunst**

**Dekan der Mathematisch-Naturwissenschaftlichen Fakultät:  
Prof. Dr. Elmar Kulke**

---

**Gutachter/innen:**

- 1. Prof. Dr. Claudia Draxl**
- 2. Prof. Dr. Toon Verstraelen**
- 3. Dr. Denis Usvyat**

**Tag der mündlichen Prüfung:** 15. 12. 2017

I declare that I have completed the thesis independently using only the aids and tools specified. I have not applied for a doctor's degree in the doctoral subject elsewhere and do not hold a corresponding doctor's degree. I have taken due note of the Faculty of Mathematics and Natural Sciences PhD Regulations, published in the Official Gazette of Humboldt-Universität zu Berlin no. 126/2014 on 18/11/2014.

Berlin, 1 November 2017

Jan Hermann



This work is licensed under the Creative Commons Attribution-ShareAlike 4.0 International License. To view a copy of this license, visit <http://creativecommons.org/licenses/by-sa/4.0/>.

## Abstract

The ubiquitous long-range van der Waals interactions play a central role in nearly all biological and modern synthetic materials. Yet the most widely used theoretical method for calculating material properties, the density functional theory (DFT) in semilocal approximation, largely neglects these interactions, which motivated the development of many different vdW models that can be coupled with DFT calculations. Despite these efforts, existing vdW models are either limited in scope (atomic models), in efficiency by working with unoccupied one-particle states (e.g., random-phase approximation), or limited to pairwise approximation (nonlocal density functionals). The work in this thesis paves way towards a unified vdW model that combines best elements from these different classes of the vdW models.

To this end, we developed a unified theoretical framework based on the range-separated adiabatic-connection fluctuation–dissipation theorem that encompasses most existing vdW models. We show that the formulations of the theorem in terms of the density response function and the nonlocal polarizability are equivalent, introduce the concept of the semilocal effective polarizability and the corresponding effective dipole operator, and discuss the most popular vdW models in terms of these two quantities. This unified perspective suggests that a particularly effective combination should be that of the local polarizability functionals and the many-body dispersion (MBD) approach based on quantum harmonic oscillators.

We analyze the MBD correlated wave function on the prototypical case of  $\pi$ – $\pi$  interactions in supramolecular complexes and find that these interactions are largely driven by delocalized collective charge fluctuations, and that the charge density polarization resulting from these fluctuations is well described by the underlying harmonic oscillator. This demonstrates the close correspondence between the simple harmonic-oscillator model of the polarization, and the actual density response of the true electrons, further supporting the use of polarizability functionals of the density to parametrize the MBD model Hamiltonian.

To identify a balanced short-range density functional to accompany the long-range vdW model, we present a comprehensive study of the interplay between the short-range and long-range energy contributions in eight semilocal functionals and three vdW models on a wide range of systems. The binding-energy profiles of many of the DFT+vdW combinations differ both quantitatively and qualitatively, and some of the qualitative differences are independent of the choice of the vdW model, establishing them as intrinsic properties of the respective semilocal functionals. We identify the PBE functional to have the most consistent effective range across different system types.

Finally, we investigate the performance of the Vydrov–Van Voorhis polarizability functional across the periodic table, identify systematic underestimation of the polarizabilities and vdW  $C_6$  coefficients for  $s$ - and  $d$ -block elements, and develop an orbital-dependent generalization of this functional to resolve the issue. We establish the quadrupole polariz-

abilities calculated from such a polarizability functional as a natural parameter governing the range separation in a combined DFT+vdW model. Overall, our results provide the theoretical framework and key elements that are necessary for a formulation of a general and accurate vdW model.

## Zusammenfassung

Van der Waals-Wechselwirkungen (vdW) sind allgegenwärtig und spielen eine zentrale Rolle in einer großen Anzahl biologischer und moderner synthetischer Materialien. Die am weitesten verbreitete theoretische Methode zur Berechnung von Materialeigenschaften, die Dichtefunktionaltheorie (DFT) in semilokaler Näherung, vernachlässigt diese Wechselwirkungen jedoch größtenteils, was zur Entwicklung vieler verschiedener vdW-Modelle führte welche mit DFT-Rechnungen gekoppelt werden können. Ungeachtet dieser Bemühungen sind bestehende vdW-Modelle limitiert entweder in Hinblick auf ihren Anwendungsbereich (atomistische Modelle), ihre Effizienz im Umgang mit unbesetzten Einteilchen-Zuständen (z.B. Random-Phase-Approximation) oder auf Zweiteilchen-Näherungen (nichtlokale Dichtefunktionale). Die hier vorgestellte Arbeit ebnet den Weg hin zu einem vereinheitlichten vdW-Modell welches die besten Elemente dieser unterschiedlichen Klassen von vdW-Modellen vereint.

Zu diesem Zweck haben wir einen vereinheitlichten theoretischen Rahmen geschaffen, der auf dem Reichweite-separierten Adiabatischer-Zusammenhang-Fluktuations-Dissipations-Theorem aufbaut und die meisten existierenden vdW-Modelle umfasst. Wir zeigen, dass die Formulierungen des Theorems im Rahmen der Dichte-Antwortfunktion und der nichtlokalen Polarisierbarkeit äquivalent sind, führen das Konzept der semilokalen effektiven Polarisierbarkeit sowie des entsprechenden effektiven Dipoloperators ein und diskutieren die populärsten vdW-Modelle im Kontext dieser beiden Größen. Diese vereinheitlichte Perspektive legt nahe, dass eine besonders effektive Kombination durch die des Funktionalen der lokalen Polarisierbarkeit und des Ansatzes der ‘Many-Body Dispersion’ (MBD), der auf quantenmechanischen harmonischen Oszillatoren beruht, gegeben sein sollte.

Wir analysieren die MBD-korrelierte Wellenfunktion am prototypischen Beispiel von  $\pi-\pi$ -Wechselwirkungen in supramolekularen Komplexen und stellen fest, dass diese Wechselwirkungen größtenteils durch delokalisierte kollektive Ladungsfluktuationen entstehen und die aus diesen Fluktuationen resultierende Polarisation der Ladungsdichte gut im Modell des harmonischen Oszillators beschrieben werden kann. Dies verdeutlicht den engen Zusammenhang zwischen dem einfachen harmonischen Oszillator-Modell für die Polarisation und der tatsächlichen Dichteantwort der wahren Elektronen. Dies wiederum spricht für die Verwendung von Polarisierbarkeitsfunktionalen der Dichte, um den MBD-Modellhamiltonoperator zu parametrisieren.

Um zu dem langreichweiten vdW-Modell ein ausgewogenes kurzreichweites Dichtefunktional zu identifizieren, präsentieren wir eine umfassende Untersuchung zum Zusammenspiel der kurz- und langreichweiten Energiebeiträge in acht semilokalen Funktionalen und drei vdW-Modellen für eine große Spanne von Systemen. Die Bindungsenergieprofile vieler der DFT+vdW-Kombinationen unterscheiden sich sowohl quantitativ als auch qualitativ stark voneinander, wobei einige der qualitativen Unterschiede unabhängig vom vdW-Modell sind und damit intrinsische Eigenschaften des

verwendeten semilokalen Funktional darstellen. Das PBE-Funktional stellt sich als jenes mit dem konsistentesten effektiven Bereich für verschiedene Systemtypen heraus.

Schließlich untersuchen wir die Performance des Vydrov-Van Voorhis-Polarisierbarkeitsfunktional über das Periodensystem der Elemente hinweg und identifizieren eine systematische Unterschätzung der Polarisierbarkeiten und vdW- $C_6$ -Koeffizienten für  $s$ - und  $d$ -Block-Elemente. Als Lösung entwickeln wir eine orbitalabhängige Verallgemeinerung des Funktional. Die aus einem solchen Polarisierbarkeitsfunktional berechneten Quadrupol-Polarisierbarkeiten werden als natürliche Parameter etabliert, die die Bereichsseparierung in einem kombinierten DFT+vdW-Modell regeln. Insgesamt liefern unsere Ergebnisse den theoretischen Rahmen und die Schlüsselemente, die für die Formulierung eines allgemeinen und akkurate vdW-Modell nötig sind.

# Contents

Preface . . . . .	ix
<b>1 Introduction</b>	<b>1</b>
1.1 What are noncovalent interactions . . . . .	1
1.2 History and nomenclature . . . . .	2
1.3 Relation to fundamental laws of nature . . . . .	5
1.4 Routinely applied approximations . . . . .	6
<b>2 Electronic many-body problem</b>	<b>9</b>
2.1 Schrödinger equation . . . . .	9
2.2 Variational method and energy functionals . . . . .	11
2.3 Mean-field models . . . . .	12
2.4 Diffusion quantum Monte Carlo . . . . .	14
2.5 Density-functional theory . . . . .	15
2.6 Adiabatic-connection fluctuation–dissipation theorem . . . . .	17
2.7 Exchange–correlation functionals . . . . .	19
2.8 Time-dependent density-functional theory . . . . .	22
2.9 Nonlocal dipole polarizability . . . . .	23
2.10 Periodic potentials and reciprocal space . . . . .	25
2.10.1 Dielectric function from dipole polarizability . . . . .	26
2.10.2 Ewald summation of dipole interaction . . . . .	27
<b>3 Long-range electron correlation</b>	<b>29</b>
3.1 Range separation of electron correlation . . . . .	29
3.1.1 Static correlation . . . . .	31
3.2 Local effective polarizability . . . . .	33
3.2.1 Harmonic oscillator as a polarizability model . . . . .	35
3.3 Classification of vdW methods . . . . .	36
3.3.1 Coarse-graining of continuous quantities . . . . .	36
3.3.2 Truncation of many-body expansion . . . . .	39
3.3.3 Kohn–Sham response and random-phase approximation . . . . .	39
3.3.4 Nonlocal density functionals . . . . .	42

3.3.5	Pairwise interatomic models . . . . .	45
3.3.6	Many-body dispersion framework . . . . .	51
<b>4</b>	<b>Many-body dispersion method</b>	<b>55</b>
4.1	Reciprocal-space formulation . . . . .	55
4.2	Dielectric function from MBD . . . . .	57
4.3	Properties of dipole-coupled wave function . . . . .	58
4.3.1	Charge density . . . . .	58
4.3.2	First-order perturbation correction . . . . .	60
4.3.3	Anisotropic Gaussian screening . . . . .	62
4.3.4	Interaction energy decomposition . . . . .	63
4.4	Nuclear forces and self-consistency . . . . .	64
<b>5</b>	<b>Charge-oscillation nature of <math>\pi</math>-<math>\pi</math> interactions</b>	<b>67</b>
5.1	Background . . . . .	67
5.2	Benchmarking MBD binding energies with DQMC . . . . .	69
5.3	Analysis of nonlocal polarizabilities . . . . .	71
5.4	Charge polarization due to $\pi$ - $\pi$ interactions . . . . .	73
5.5	VdW interactions as collective oscillations . . . . .	74
5.6	Testing nonequilibrium geometries . . . . .	77
<b>6</b>	<b>Balancing semilocal and nonlocal correlation</b>	<b>81</b>
6.1	Ambiguity in range separation . . . . .	81
6.2	Choice of tested methods and systems . . . . .	82
6.3	Basis-set convergence of meta-GGA functionals . . . . .	85
6.4	Range-separation on benchmark datasets . . . . .	86
6.5	Three-body interactions . . . . .	91
6.6	System-size scaling . . . . .	92
6.7	SCAN reparametrizations . . . . .	93
<b>7</b>	<b>Seamless modeling of retarded vdw interactions</b>	<b>95</b>
<b>8</b>	<b>Development of a new polarizability functional</b>	<b>99</b>
8.1	Quadrupole polarizability from polarizability functional . . . . .	100
8.2	Constructing orbital-dependent polarizability functionals . . . . .	102
8.3	Volume-scaling of polarizabilities with polarizability functionals . . . . .	107
8.4	Outlook on future development . . . . .	109
<b>References</b>		<b>111</b>

# Preface

This doctoral thesis is a result of my four years at the Fritz Haber Institute in Berlin, which were directed at development of a more general and accurate model of van der Waals (vdW) interactions in molecules and materials. The presented work contributes to this goal in several ways. Chapter 1 gives a broad conceptual background that establishes what vdW forces are, the historical development of their understanding, and how they fit within the more general and fundamental physical laws of our world. Chapter 2 reviews basic concepts of quantum chemistry and solid-state physics used throughout the thesis. Chapter 3 develops a formal mathematical classification of existing methods for modeling vdW interactions, which puts them within a single framework formulated in terms of the nonlocal dipole polarizability, and makes relationships between the different models apparent. For instance, it shows that the properties of the quantum harmonic oscillator underlie many seemingly unrelated polarizability models, from continuous to coarse-grained functionals of the electron density. Chapter 4 then presents several new developments within a particular vdW model, the many-body dispersion (MBD) method, while Chapter 5 applies the newly derived results for the interacting MBD wave functions to the problem of  $\pi-\pi$  interactions. This study also demonstrates that the harmonic-oscillator model is able to capture not only the coarse-grained electronic-response properties in molecules and materials, but also the redistribution of the electron density caused by vdW interactions. This motivates the focus on the spatial distribution of the polarizability model in the last chapter. Chapter 6 is concerned with the problem of balancing semilocal and nonlocal contributions to the electron correlation energy, which is central to description of vdW-bound systems in equilibrium. This work partially rationalizes the empiricism involved in development of new vdW models stemming from the use of damping functions. Chapter 7 briefly shows that any polarizability model within the MBD framework can be used not only in standard nanoscale vdW models, which assume that the electromagnetic force acts instantly, but also to model microscale systems, where the finite speed of light must be taken into account. Finally, Chapter 8 presents a new orbital-dependent polarizability functional of the electron density, and outlines how it can be used within the MBD framework to formulate a new model of vdW interactions.

This thesis would never come to life without the support and advise of my supervisor Alexandre Tkatchenko. The countless discussions with him inspired many thoughts presented on the following pages. He also taught me many valuable lessons about scientific

writing, publishing, and general wisdom about how modern scientific research is done. I am indebted to Robert DiStasio for stimulating conversations and tireless comments about my English—he showed me the art of constructing precise sentences. My pursue of the doctoral degree would not be possible without the financial support of the Max Plack Society, which was granted by Matthias Scheffler, the director of the theory department at the Fritz Haber Institut in Berlin. Finally, I would like to express gratitude to all the members of the department, whose excitement about science gave me a great sense of motivation.

Jan Hermann  
October 2017

# Chapter 1

## Introduction

This chapter gives a conceptual introduction to the topic of van der Waals interactions, the history of the development of their theory, their relation to the current understanding of the fundamental laws of nature, and the approximations thereof that proceed the mathematical treatment of van der Waals interactions in the next chapters.

### 1.1 What are noncovalent interactions

All visible matter is made from atoms, the particles composed from very small but heavy and slow nuclei on one hand and light electrons moving at high speeds around the nuclei on the other, mutually attracted by the fundamental electromagnetic force, while nuclei are repelled from other nuclei by the same kind of force, as are electrons from other electrons. Because the electrons and their motion are very manifestly governed by the laws of quantum rather than classical mechanics, they behave more as electron liquid filling potential vessels around the nuclei, rather than as planets orbiting stars. When atoms of certain elements are arranged in certain ways, they are attracted to each other to form molecules, thin films, liquids, gels, glasses, or crystals. These effective forces between atoms, both covalent and noncovalent, are a direct result of the fundamental electromagnetic force between electrons and nuclei.

A key property of the electromagnetic force in the context of interactions in matter is that it is long-ranged, which means that although it does become weaker for larger distances between atoms, one can always find conditions under which it can not be neglected even when the atoms are far apart. Although there is only one kind of the electromagnetic force between nuclei and electrons that acts in all matter alike, the resulting bonding between atoms can be divided into several distinct categories with characteristic properties. Covalent bonds are derived from short-range interactions between localized electrons, and their formation and breaking is responsible for a majority of chemical reactions. In contrast, the arrangement of atoms in metals is such that the electrons become delocalized, interacting at short range in such a way that they avoid each other and behave as if they

did not interact in the first place, while also binding the atoms of the metal together. The motion of electrons in covalent and metallic bonds can not be explained from the electromagnetic force only, without considering the peculiar quantum-statistical behavior of electrons, which dictates that the probability amplitude of any particular configuration of electrons must be the negative of the probability amplitude of the same configuration with two electrons exchanged. This statistics does not represent any fundamental interaction between the electrons, but rather restricts their possible motion, independently of the electromagnetic force. Yet another kind of binding occurs when the mean positions of the (negatively charged) electrons are displaced relative to the (positively charged) nuclei, either by hopping to other atoms altogether or by shifting to a certain degree. The resulting effective charges then interact via the electrostatic force, either strongly at short distances (ionic bonds) or weakly over long distances. Finally, electrons always try to minimize the electric repulsion between them, such that at any given moment, when an electron is to be found on one side of some region of matter, electrons in some other region will be more likely to be found on the opposite side. This results in instantaneous effective charges that effectively interact via the electrostatic force, attracting the two regions together. Unlike the three previous bonding patterns, this attractive long-range force, named after Johannes Diderick van der Waals, can be found between all possible arrangements of atoms.

As a result of the difference in strength between the four kinds of binding, structures strongly bound by covalent, ionic, and metallic bonds often appear under common conditions as relatively stable entities, whose dynamics is governed by the weaker noncovalent interactions, which comprise the long-range electrostatic interactions and the van der Waals (vdW) forces. In this way, water molecules are bound into liquid water and ice, sheets of graphene are bound into graphite, two strands of DNA into the DNA helix, linear protein chains into complex 3D structures, molecules of drugs into their crystalline form in tablets, and when a water droplet sits on a glass surface, the water molecules are attracted to the surface by those same forces as well. In the temperature range in which life on Earth thrives, most covalent, ionic, and metallic bonds are too strong to be disrupted by the thermal motion of atoms, unless catalysts or enzymes are involved. It is often the noncovalent electrostatic and vdW interactions that govern the molecular arrangements under which the catalysts and enzymes become effective. This general mechanism directly relates material structure and function, and explains why energetically demanding chemical and biochemical reactions can be often controlled by the much weaker noncovalent interactions.

## 1.2 History and nomenclature

The first suggestion of some sort of general attractive forces between microscopic particles of matter came from the work on capillary effect and surface tension in 17<sup>th</sup> century, even before the concept of a molecule was properly established. Two centuries later, [van der](#)

Waals (1873) published a doctoral thesis in which he introduced his eponymous equation of state, which improved upon the ideal gas model by assuming a nonzero size of molecules and an unspecified attractive force between them. Thanks to its simplicity, yet great predictive power, the equation and the nature of the attractive force in particular became the focus of much research. Still before the birth of quantum mechanics, Keesom (1912) tried to explain vdW forces in gases as alignment of molecules due to electrostatic interactions between their rigid effective charges. Debye (1920) argued that such explanation predicts incorrect dependence of the attraction on temperature and molecular structure, and suggested a mechanism in which the effective charges in molecules are not rigid, but induced by other molecules in the system. But none of these two theories explained vdW attraction between the symmetric atoms of rare gases, and, as London (1937) later argued, they lacked explanation for the general “*parallelism in the different manifestations of the [van der Waals] forces*” such as their “*identity [...] in the liquid with those in the gaseous state; the phenomena of capillarity and of adsorption; the sublimation heat of molecular lattices; certain effects of broadening of spectral lines, etc.*” The needed fundamental physical laws were missing at the time, and when Jones (1924) introduced the now-famous Lennard-Jones potential between atoms at distance  $R$ , the attractive component decayed as  $1/R^5$  instead of the correct  $1/R^6$ .

When quantum mechanics was firmly established in the late 1920s, understanding of the motion of electrons in atoms and molecules was perhaps the biggest motivation for its development. One of the main results of quantum mechanics was that electrons (charges) in matter do not stop moving even in the lowest energy state, and it turned out to be precisely this movement that is the basis of the vdW attraction. The first formal quantum-mechanical derivation of long-range attraction between symmetric atoms was done by Wang (1927) for the case of two hydrogen atoms. But it was only London (1930) who generalized the result to any two molecules, and recognized this interaction as the origin of the phenomenological attractive force postulated by Van der Waals. Because the strength of the vdW interaction can be calculated from formulas that are similar to those describing optical dispersion (since the underlying electronic motions are of related kind), the attraction was called the dispersion force. Slater and Kirkwood (1931) then closed the full circle by calculating the empirical coefficient from the vdW equation from first principles for several simple gases.

While the quantum-mechanical origin of vdW forces was now clear, full understanding of all their manifestations in different materials was nowhere nearer. This was in part caused by the limitations of London’s description, which were overcome only slowly. It took 13 years for Axilrod and Teller (1943) and Mutō (1943) to independently extend London dispersion from interactions of two to interactions of three atoms or molecules. The electromagnetic force between electrons does not act instantly, but travels at the speed of light. When two oscillating electrons are further apart than is the wavelength of the light associated with those oscillations, the retarded force becomes out of phase

dispersion force

with the oscillations, which makes it weaker. Casimir and Polder (1948) realized the implications of this effect for vdW forces and derived the modified  $1/R^7$  law that is valid at large separations between interacting bodies. It was unfeasible at the time to perform full quantum-mechanical calculations of vdW forces in condensed matter, which lead Lifshitz (1956) to derive a phenomenological theory based on classical electrodynamics, which was complementary to that of London and did not derive the electronic motions from first principles, but rather postulated and parametrized them based on experimental measurements of material properties. All these theoretical developments were eventually cemented also by experiment, when Tabor and Winterton (1969) were able to directly measure the attractive vdW force between two macroscopic plates, both in the normal and the retarded regime.

Attempts at improved (more general, more accurate) theoretical description of vdW forces went through renaissance in the last two decades, mainly for two reasons: First, the known approximations to density-functional theory (DFT)—a method for calculating structure and stability of molecules and materials that became dominant in physics in the 1970s and in chemistry in the 1990s—describe to a good degree all kinds of binding described above except for the vdW force. Second, the advances in molecular biology, material design, and nanotechnology have led to studies of larger molecular structures and more heterogeneous materials, in which vdW forces play more important role compared to simpler compounds. Some of the many new approaches to vdW forces are formulated fully within DFT, other borrowed ideas from many-body perturbation theory, and yet other from molecular force fields. Many of them combine these three approaches in some way. At the time of writing this thesis, a general, yet accurate and practical model of vdW forces that works for both molecules and materials is still to be found.

As Margenau put it already in 1939, “*the term ‘van der Waals force’ is not one of very precise usage,*” and it holds to this date. Before 1930, it was a name for the unknown attractive forces responsible for the  $a/V_m^2$  term in the vdW equation of state. Then London derived the force from first principles for the case of two molecules far apart from each other (but not too far), and named it the ‘dispersion effect’. For some, this meant that vdW force *is* the dispersion effect, others understood it as the third in line after the incomplete theories of Keesom (alignment effect) and Debye (induction effect), which all together comprise vdW forces. The former use became more prevalent in physics, the latter in chemistry. Meanwhile, the term ‘noncovalent interactions’ started to be used in biochemistry in the 1960s as an umbrella term for the trio of weaker interactions between (covalently bound) molecules, and began to slowly displace the older term ‘vdW interactions’ in its broad meaning. To add to the confusion, ‘London dispersion’ has been often used to denote only the additive second-order part of the attractive force, while it became clear that although often dominant, this level of the theory is not sufficient in many circumstances. Furthermore, the retarded regime of the vdW force has been often called the ‘Casimir force’. Given this background, I use the term ‘vdW force’ or

‘vdW interaction’ (rather than dispersion) for the force caused by long-range correlation between the motions of electron. This definition covers both the regime in which finite speed of the electromagnetic interaction must be taken into account (retarded regime) as well as the special case in which the distances are short enough that the speed of light can be considered infinite (normal regime). Furthermore, it does not include the Debye and Keesom effects (electrostatic interactions), which do not depend on correlations in the electronic motion, but only on the mean positions of electrons. I use ‘noncovalent interactions’ for all intermolecular forces, which *include* the vdW force as well as the electrostatic interactions (resulting from both permanent and induced charges). I avoid the term ‘dispersion force’ and ‘dispersion interaction’.

### 1.3 Relation to fundamental laws of nature

The current working theory of the microscopic world that is not in conflict with any known experiment is the so-called Standard Model of elementary particles, which is a particular quantum field theory, the latter being a general framework for quantum theories. A subset of the Standard Model that deals with electrons and photons (particles of light) is called the quantum electrodynamics (QED). For the calculation of the dipole polarizability of a helium atom, a quantity vastly important for vdW interactions, the difference between the full Standard Model and QED is at tenth significant digit, which is below the resolution of any modern experiment (see Piela, 2014, Table 3.1). In QED, electrons and photons are constantly appearing, interacting, and disappearing excitations of electron and photon fields, which effectively leads to the Coulomb law between electrons, the foundation of description of electricity, and one of the components of Maxwell equations, the classical theory of electrodynamics. QED can in principle explain all the vdW effects discussed so far, including the retarded regime, but its equations are too complicated to be solved for anything but the smallest of atoms. Quantum field theory, and hence QED as well, arose from reconciliation of quantum mechanics with special relativity: while the macroscopic limit of ordinary quantum mechanics is nonrelativistic classical mechanics, the limit of quantum-field theories is relativistic mechanics. In ordinary quantum mechanics of electrons, which can be considered a nonrelativistic approximation to QED, electrons are considered as eternal particles that interact not by exchanging photons, but via a postulated Coulomb law. Returning back to the polarizability of the helium atom, the relativistic effects make a difference at fifth significant digit, which, while measurable in this particular case, is inconsequential for any practical vdW effects. For this reason, ordinary quantum mechanics is often considered the starting reference fundamental theory of electrons in chemistry and condensed-matter physics. (On the other hand, phenomenological models based on classical electrodynamics, which is inherently a relativistic theory, are naturally able to capture retarded vdW forces, where relativistic effects are dominant.) In quantum mechanics, a system of particles is described by a

wave function

wave function, a complex-valued function of the particle positions whose square gives the probability that the particles will be found in a given configuration. The wave function of a particular system is determined by solving the Schrödinger equation. In this framework, vdW interactions correspond to the fact that given any two electrons that are likely to be found around some nuclei, the square of the wave function will be larger when the electrons are on the far sides of the nuclei than when they are on the near sides, which is in turn caused by the mutual Coulomb repulsion between the electrons. This imbalance then leads to the nuclei being pushed by their own electrons towards each other rather than apart from each other, and this is the attractive vdW force between atoms.

## 1.4 Routinely applied approximations

The previous section established QED as the fundamental theory of electrons, and the Schrödinger equation as a good first-principles starting point, but there is a long string of approximations that need to be made to reduce the description of, say, a physical rod of metal to a solution of the Schrödinger equation for electrons. The approximations made when going from QED to ordinary quantum mechanics are fourfold: First, the mass of an electron is velocity-dependent under special relativity but not in ordinary quantum mechanics. This effect is negligible in small atoms where electrons move slowly compared to the speed of light, but it is strong in heavy nuclei, causing, for example, the yellowish color of gold. The same is true for vdW forces (the polarizability of atoms), and this type of relativistic effects cannot be neglected when treating heavy atoms from first principles. Second, electrons and nuclei have a spin, a purely quantum-mechanical property that is inherently related to magnetism, which is only postulated in ordinary quantum mechanics, while it is a theoretical necessity in QED. In ordinary quantum mechanics, all spin interactions of electrons are either neglected or treated effectively, and it is usually assumed that spin interactions and magnetism do not influence vdW interactions in a significant way. (The assumption of the existence of spin in ordinary quantum mechanics is of course central for establishing the correct quantum-statistical properties of the electrons.) Third, the Coulomb law acting instantaneously is in direct violation of special relativity. While this is negligible when the electrons are not too far apart (normal regime), it is of crucial importance for distant electrons (retarded regime). These effects cannot be easily incorporated directly into ordinary quantum mechanics, and effective theories therefore resort to its combination with the (inherently relativistic) classical electrodynamics. Fourth, in contrast to quantum mechanics vacuum is never truly empty in quantum-field theories, but rather full of virtual particles, a phenomenon called vacuum polarization. This effect, while measurable, is fortunately never quantitatively important for vdW interactions.

Even once the description of electrons is reduced to ordinary quantum mechanics, a real molecule or material consists of mutually interacting nuclei and electrons, whose

motions are fully coupled. But the nuclei are heavier than the electrons by three to four orders of magnitude, so they move much slower than the electrons. In the approximation developed by Born and Oppenheimer (1927) (BO), one considers that at any point in time the nuclei are static, and the electrons move in their static electric field. This in turn results in electronic clouds around the nuclei that act electrically on them, creating an effective mean-field nuclear force. Because of the conservation of energy in a system of nuclei and electrons, the forces on the nuclei can be alternatively obtained from the electronic energy, which, when taken as a function of the nuclear coordinates, is called the potential energy surface (PES). The BO approximation can fail either at special nuclear configurations called conical intersections, which are related to electronic excitations, or at very high temperatures that can be found in stars, neither of which is relevant for this thesis. Once the BO approximation is applied, the motion of electrons becomes a separate problem that results in a PES, which then serves as an input to another separate problem, that of the nuclei that move on the PES. The electronic problem directly determines the optical, electric, and magnetic properties of molecules and materials, as well as their photoreactivity. The shape of the PES (resulting from the electronic problem) decides about their structure and stability, as well as about most of their thermodynamic properties and chemical reactivity. VdW forces are most often manifested via their effect on the PES and the position and motion of the nuclei, but they can also influence directly the electronic properties (Ferri et al., 2015).

Born–Oppenheimer approximation



# Chapter 2

## Electronic many-body problem

This chapter briefly reviews those basic building blocks of the electronic structure theory that are necessary for the presentation of the actual new work done for this thesis. This comprises mostly the density functional theory, the adiabatic-connection fluctuation–dissipation framework, and the theory of the nonlocal dipole polarizability.

### 2.1 Schrödinger equation

The role of the second Newton law ( $d^2\mathbf{r}/dt^2 = \mathbf{F}/m$ ) in nonrelativistic quantum mechanics is played by the Schrödinger equation, which therefore underlies all material discussed in this thesis. In quantum mechanics, the state of a fixed number,  $N$ , of electrons in a molecule or a crystal is fully specified by a vector,  $|\Psi\rangle$ , from the  $N$ -electron Hilbert space. Measurable properties of the state, such as energy, are expressed as Hermitian operators, whose eigenvalues are the possibly measured values of the property, the eigenvectors form a complete orthogonal basis of the Hilbert space, and the probability of measuring an eigenvalue corresponding to a given eigenvector is given by the square of the inner product of that eigenvector and the given state. The operator for energy, called Hamiltonian,  $\hat{H}$ , has a central role in quantum mechanics because it determines time evolution of the state via the Schrödinger equation,

$$\frac{\partial|\Psi\rangle}{\partial t} = -i\hat{H}|\Psi\rangle \quad (\text{in a. u.}) \quad (2.1)$$

This equation dictates that the phases of components of a state corresponding to different energy eigenstates oscillate at different rates, and eventually appear to be random for a system in equilibrium with its environment, so that one can regard the system as an ensemble of eigenstates of the Hamiltonian. Because the probability of the  $n$ -th eigenstate ( $n = 0, 1, \dots$ ) with energy  $E_n$  at temperature  $T$  is proportional to  $\exp(-E_n/T)$ , and because the energy differences between electronic energy eigenstates typically count in at least thousands of kelvins (1 eV  $\doteq 12\,000$  K in atomic units), most matter on Earth is found in

the electronic ground state.

The nonrelativistic Hamiltonian for  $N$  electrons ( $i = 1, \dots, N$ ) in electric potential  $v_{\text{ext}}(\mathbf{r})$  consists of three terms that correspond to the kinetic energy, potential energy, and interelectronic Coulomb repulsion,

$$\hat{H} = \sum_i \frac{\hat{\mathbf{p}}_i^2}{2} - \sum_i v_{\text{ext}}(\hat{\mathbf{r}}_i) + \sum_{i < j} \frac{1}{|\hat{\mathbf{r}}_i - \hat{\mathbf{r}}_j|} \equiv \hat{T} + \hat{V}_{\text{ext}} + \hat{V}_{ee} \quad (2.2)$$

Because electrons are fermions (particles with half-integer spin), the corresponding Hilbert space is antisymmetric, meaning that when any two electrons are exchanged, the resulting state vector must be equal to the negative of the original state vector. In a free molecule or crystal, the nuclei at positions  $\mathbf{R}_A$  with charges  $q_A$  generate the external potential for the electrons,

$$v_{\text{ext}}(\mathbf{r}) = \sum_A \frac{q_A}{|\mathbf{r} - \mathbf{R}_A|} \quad (2.3)$$

In the basis of eigenstates of the position operators,  $\hat{\mathbf{r}}_i$ , and spin operators,  $\hat{s}_i$ , one can define a wave function,  $\Psi(\{\mathbf{r}_i s_i\}) = \langle \mathbf{r}_1 s_1 | \dots | \mathbf{r}_N s_N | \Psi \rangle$ , and the search for eigenvectors is then turned into a differential equation,

$$\left( -\sum_i \frac{\nabla_i^2}{2} - \sum_i \sum_A \frac{q_A}{|\mathbf{r}_i - \mathbf{R}_A|} + \sum_{i < j} \frac{1}{|\mathbf{r}_i - \mathbf{r}_j|} - E \right) \Psi(\mathbf{r}_1 s_1, \dots, \mathbf{r}_N s_N) = 0 \quad (2.4)$$

The wave function must be antisymmetric, and the solution of the equation gives possible values of the electronic energy,  $E$ , which are the eigenvalues of the Hamiltonian. This equation cannot be solved analytically already for the simplest of systems, and formulating approximate, efficient, yet accurate methods for its solution is historically the biggest problem in quantum chemistry.

The spin variables are discrete ( $s_i \in \{-\frac{1}{2}, \frac{1}{2}\}$ ), and because we operate in nonrelativistic quantum mechanics, they do not enter the Hamiltonian, but only influence the form of the spatial dependence of the wave function via the requirement of the antisymmetry (Pauncz, 1979). The spin part of the wave function can be always written in terms of the one-electron spin functions,  $\uparrow(s)$  and  $\downarrow(s)$ , whose values are either zero or one,

$$\begin{aligned} \uparrow\left(\frac{1}{2}\right) &= 1 & \downarrow\left(\frac{1}{2}\right) &= 0 \\ \uparrow\left(-\frac{1}{2}\right) &= 0 & \downarrow\left(-\frac{1}{2}\right) &= 1 \end{aligned} \quad (2.5)$$

Because of the antisymmetry, the probability of finding two electrons of the same spin at the same position is zero,  $\Psi(\mathbf{r}_s, \mathbf{r}_s, \dots) = 0$ , which is also called the Pauli exclusion principle.

## 2.2 Variational method and energy functionals

One of the oldest approaches to finding the ground state, but also a foundation of many modern methods, is based on the fact that the eigenstates of the Hamiltonian,  $|\psi_n\rangle$ , form a complete basis,

$$\begin{aligned}\langle \Psi | \hat{H} | \Psi \rangle &= \langle \Psi | \hat{H} \sum_n |\psi_n\rangle \langle \psi_n | \Psi \rangle = \sum_n E_n \langle \Psi | \psi_n \rangle \langle \psi_n | \Psi \rangle \\ &\geq E_0 \sum_n \langle \Psi | \psi_n \rangle \langle \psi_n | \Psi \rangle = E_0 \langle \Psi | \Psi \rangle = E_0\end{aligned}\quad (2.6)$$

As a result, the expectation value of the Hamiltonian is never smaller than the ground-state energy, and if the energy is understood as a functional of a wave function,  $E[\Psi]$ , the ground state can be found at its minimum,

$$|\psi_0\rangle = \arg \min_{|\Psi\rangle} E[\Psi] \quad (2.7)$$

(In fact all eigenstates can be gradually found in this fashion, by requiring that they are orthogonal to all the lower-energy eigenstates.)

Because all terms in the Hamiltonian are either one- or two-electron, do not depend on spin, and the wave function is antisymmetric, the expression for the energy functional can be simplified by partial integrations over  $\Psi$  (Parr and Yang, 1989),

$$E[\Psi] = \int d\mathbf{r} \left( -\frac{1}{2} \nabla_{\mathbf{r}}^2 \gamma(\mathbf{r}, \mathbf{r}') \right) \Big|_{\mathbf{r}'=\mathbf{r}} + \int d\mathbf{r} v_{\text{ext}}(\mathbf{r}) n(\mathbf{r}) + \frac{1}{2} \iint d\mathbf{r}_1 d\mathbf{r}_2 \frac{n_2(\mathbf{r}_1, \mathbf{r}_2)}{|\mathbf{r}_1 - \mathbf{r}_2|} \quad (2.8)$$

The energy is then expressed in terms of the first-order density matrix,  $\gamma(\mathbf{r}, \mathbf{r}')$ , the electron-pair density,  $n_2(\mathbf{r}_1, \mathbf{r}_2)$ , and the electron density,  $n(\mathbf{r}) = \gamma(\mathbf{r}, \mathbf{r})$ . In principle, the ground-state energy can be found just as well by minimizing this energy functional over all  $n$ ,  $\gamma$ , and  $n_2$  that originate from the same wave function. But this latter search constraint, called the  $N$ -representability problem, is what makes this approach unfeasible, because the sufficient conditions for  $n_2$  to be  $N$ -representable are unknown.<sup>1</sup> The electron-pair density can be written in terms of the electron density and a pair correlation (distribution) function,  $g(\mathbf{r}_1, \mathbf{r}_2)$ ,

$$n_2(\mathbf{r}_1, \mathbf{r}_2) = n(\mathbf{r}_1) n(\mathbf{r}_2) g(\mathbf{r}_1, \mathbf{r}_2) \quad (2.9)$$

If the motions of the electrons were uncorrelated, the pair correlation function would be equal to 1, but in reality the wave-function antisymmetry and the interelectronic Coulomb term cause it to deviate from 1. By using  $g = 1 - (1 - g)$ , the interelectronic energy term can be naturally split into a classical part (also called the Hartree energy), which is simply

---

<sup>1</sup> More precisely, the energy functional is a functional of the second-order density matrix,  $\gamma_2(\mathbf{r}_1 \mathbf{r}_2, \mathbf{r}'_1 \mathbf{r}'_2)$ , from which  $n_2(\mathbf{r}_1, \mathbf{r}_2) = 2\gamma_2(\mathbf{r}_1 \mathbf{r}_2, \mathbf{r}_1 \mathbf{r}_2)$  and  $\gamma_1(\mathbf{r}, \mathbf{r}') = 2 \int d\mathbf{r}_2 \gamma_2(\mathbf{r} \mathbf{r}_2, \mathbf{r}' \mathbf{r}_2)/(N-1)$ , and it is  $\gamma_2$  for which the sufficient  $N$ -representability conditions are not known.

the electrostatic energy,  $J[n]$ , of the electron charge density, and a nonclassical correction,

$$\langle \Psi | \hat{V}_{ee} | \Psi \rangle = J[n] - \frac{1}{2} \iint d\mathbf{r}_1 d\mathbf{r}_2 \frac{n(\mathbf{r}_1)n(\mathbf{r}_2)}{|\mathbf{r}_1 - \mathbf{r}_2|} (1 - g(\mathbf{r}_1, \mathbf{r}_2)) \quad (2.10)$$

The total electronic energy can then be written as a sum of four terms,

$$E[\Psi] = T[\gamma] + V_{\text{ext}}[n] + J[n] + \text{nonclassical term} \quad (2.11)$$

### 2.3 Mean-field models

Unlike the spin part of the wave function, the spatial part cannot be in general expressed in terms of one-electron functions because of the Coulomb force between electrons. For instance, the ground state of harmonium, a two-electron system described by the Hamiltonian in (2.2) with  $v_{\text{ext}}(\mathbf{r}) = r^2/8$ , has the form

$$\psi_0(\mathbf{r}_1 s_1, \mathbf{r}_2 s_2) \sim \left(1 + \frac{1}{2}|\mathbf{r}_1 - \mathbf{r}_2|\right) \exp\left(-\frac{1}{4}(r_1^2 + r_2^2)\right) (\uparrow\downarrow - \downarrow\uparrow) \quad (2.12)$$

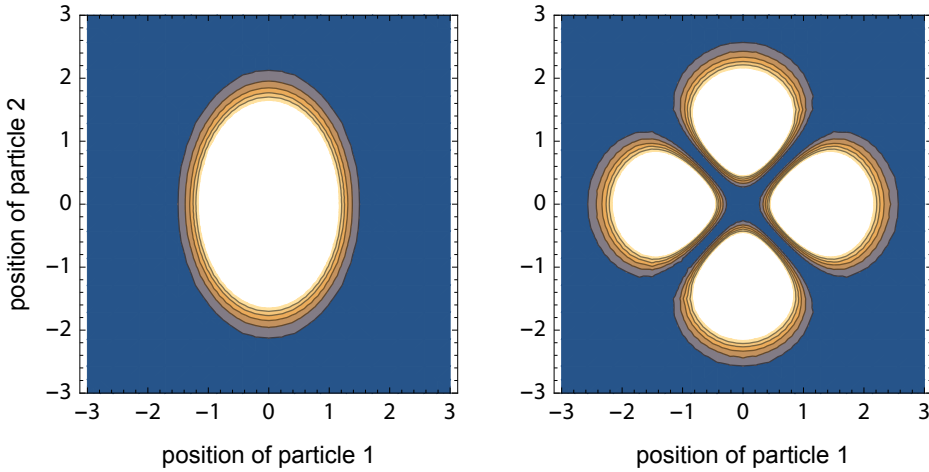
The simple prefactor  $(1 + \frac{1}{2}r_{12})$  is caused by the Coulomb term, and makes the two electrons more likely to be found far apart than close to each other. In contrast to the Pauli principle though, the Coulomb term is not strong enough to make the electrons completely avoid each other, and  $\psi_0(\mathbf{r}, \mathbf{r}) \neq 0$ . Unfortunately, harmonium is the only many-electron system with a known exact wave function in a closed form, and realistic calculations of common systems require approximate models.

Although true many-electron wave functions cannot be built from one-electron functions (also called orbitals), such constructs form the basis of almost all approximate electron models. An antisymmetrized product of spin-orbitals,  $\phi_j(\mathbf{r}_i s_i)$ , is called a Slater determinant,  $\mathcal{D}(\{\phi_j\})$ , and the approximate many-electron wave function thus formed is characterized by a simple expression for the one-electron density matrix,  $\gamma(\mathbf{r}, \mathbf{r}') = \sum_s \sum_j f_j \phi_j^*(\mathbf{r}s) \phi_j(\mathbf{r}'s)$ , in which  $f_j \in \{0, 1\}$  are the occupation numbers of the orbitals. (Generalizing from here, any  $N$ -representable density matrix can be expressed in this form by allowing any  $0 \leq f_j \leq 1$ .) Minimizing  $E[\Psi]$  with respect to this Slater-type wave function is called the Hartree–Fock (HF) approximation. The antisymmetrization of same-spin electrons works on the spatial part of the wave function (Fig. 2.1), and of opposite-spin electrons on the spin part. As a result of this, the pair correlation function for opposite-spin electrons in a Slater determinant is equal to 1, whereas that of the same-spin electrons is modified ( $n^\uparrow = n^\downarrow = n/2$  for simplicity),

$$g^{\uparrow\uparrow}(\mathbf{r}_1, \mathbf{r}_2) = g^{\downarrow\downarrow}(\mathbf{r}_1, \mathbf{r}_2) = 1 - \frac{|\gamma(\mathbf{r}_1, \mathbf{r}_2)|^2}{n(\mathbf{r}_1)n(\mathbf{r}_2)} \quad g^{\uparrow\downarrow}(\mathbf{r}_1, \mathbf{r}_2) = 1 \quad (2.13)$$

In line with the Pauli principle, the pair correlation function of same-spin electrons in the HF model starts at zero when  $\mathbf{r}_1$  equals  $\mathbf{r}_2$ , but then goes quickly to 1, around which it

**Figure 2.1 | Antisymmetrization.** Contour plots of the square of a wave function,  $|\Psi(x_1, x_2)|^2$ , of two particles in one dimension formed from two one-particle functions,  $\varphi_1(x) = \exp(-x^2)$  and  $\varphi_2(x) = \exp(-x^2/2)$ . On the left,  $\Psi$  is a simple product. On the right,  $\Psi$  is an antisymmetrized product,  $\varphi_1(x_1)\varphi_2(x_2) - \varphi_1(x_2)\varphi_2(x_1)$ . The contour levels in both plots are equal.



slowly oscillates with decreasing amplitude as  $r_{12}$  increases. (In sodium, for instance,  $g$  reaches 0.99 already at  $|\mathbf{r}_1 - \mathbf{r}_2| \approx 0.25 \text{ \AA}$ .)

The modification of  $g$  from 1 due to the antisymmetry reduces the short-range repulsion between same-spin electrons, and this part of the nonclassical term in (2.11) is called the exchange energy,

$$K[\gamma] = -\frac{1}{4} \iint d\mathbf{r}_1 d\mathbf{r}_2 \frac{|\gamma(\mathbf{r}_1, \mathbf{r}_2)|^2}{|\mathbf{r}_1 - \mathbf{r}_2|} \quad (2.14)$$

When incorporated into the exact energy functional, the remaining part of the electronic energy is called the correlation energy (despite the fact that the exchange energy also originates from a nontrivial pair correlation function),

$$E[\Psi] = T[\gamma] + V_{\text{ext}}[n] + J[n] + K[\gamma] + \text{correlation} \quad (2.15)$$

Omitting the correlation part and minimizing this functional with respect to all  $N$ -representable density matrices ( $f_j \in \{0, 1\}$  is obtained as a result) leads to the HF one-electron equations, which describe the motion of an electron in the mean field generated by all the other electrons (hence then name “mean-field” methods). In most molecules and nonconducting solids, the basic structure of the ground-state wave function is dominated by the kinetic energy, and the HF approximation works quite well in such cases, failing only quantitatively to account for the opposite-spin correlation and the small Coulomb correction to the same-spin correlation. Still, two fundamental problems exist: First, the Coulomb interaction becomes as important as the kinetic energy for the wave-function

structure<sup>2</sup> in metals, certain special materials (such as Mott insulators), and spin-unpaired (open-shell) systems, and the missing opposite-spin correlation leads to qualitatively wrong wave functions in such cases. For instance, it leads to spurious preference to “cluster” same-spin electrons together, leading to the formation of unphysical spin waves in metals in the HF approximation (Overhauser, 1962). Second, the long-range finer structure of the wave function is dominated by the Coulomb interaction, not by the antisymmetry, leading to complete neglect of vdW interactions in the HF approximation.

Approximating the correlation energy as a functional of the one-electron density matrix and minimizing that functional with respect to  $\gamma$  leads to the density-matrix functional theory (of which the HF method is a special case). Going further, the post-HF methods of quantum chemistry construct more complex wave functions on top of the Slater determinant, and approximate the correlation energy either by reapplying the variational technique or using the perturbation theory with the correlation term in the functional being the perturbation. Using linear combinations of Slater determinants instead of a single one leads to the class of multi-configurational methods.

## 2.4 Diffusion quantum Monte Carlo

The diffusion quantum Monte Carlo (DQMC) is a practical numerical method to calculate the exact electronic ground-state energy that uses the mean-field wave functions of the previous section only indirectly (Foulkes et al., 2001). Calculations performed for this thesis use it indirectly via the parametrization of effective electron models introduced below, as well as directly to calculate reference binding energies in Chapter 5.

DQMC is based on the fact that the imaginary-time evolution operator of (2.1) projects out the true ground state in the limit of the infinite time because the excited states have a higher energy and decay faster,

$$\exp(-\tau \hat{H})|\Psi\rangle = \sum_n \exp(-\tau E_n)|\psi_n\rangle \xrightarrow{\tau \rightarrow \infty} \exp(-\tau E_0)|\psi_0\rangle \quad (2.16)$$

This fact becomes numerically useful by reinterpreting the corresponding wave function as a distribution of particles and the evolution operator as describing a stochastic diffusion-and-branching process of these particles. (In fact, this process can also be interpreted as a stochastic gradient-descent minimization of the Hamiltonian expectation value, directly connecting DQMC to the standard variational techniques (Schwarz et al., 2017).) The ground-state wave function and energy can then be obtained by stochastically evolving the particles with  $\exp(-\tau(\hat{H} - E))$ , while adjusting  $E$  such that the number of the particles is kept constant, so that  $E$  eventually converges to  $E_0$ . Ending the evolution process before infinite time gives the wave function and energy with some limited, but statistically

---

<sup>2</sup> More precisely, the functional derivatives of the Coulomb energy and the kinetic energy with respect to the wave function become equally important.

known and arbitrarily good accuracy. The correspondence between the wave function and the particle distribution is only valid when the wave function is positive everywhere. This is true for the ground state of distinguishable or bosonic particles, but not for the ground state of fermions (electrons), which must be antisymmetric (for more than one particle). This makes direct application of DQMC to electrons impractical without further approximations.

The  $(3N - 1)$ -dimensional plane of points at which the wave function of  $N$  electrons is zero is called the nodal surface. In general, it is no less complicated than the full wave function, and the  $(3N - 3)$ -dimensional coincidence plane at which  $\mathbf{r}_i = \mathbf{r}_j$  and  $\Psi = 0$  by antisymmetry forms only its lower-dimensional scaffold (Ceperley, 1991). If the nodal surface of the ground-state wave function was known, the full wave function could be recovered by running a DQMC simulation independently in each nodal pocket, in which the wave function does not change sign. The fixed-node approximation then uses the nodal surface of some approximate wave function to determine these independent DQMC simulations. Because this effectively restricts the wave function to a certain form, the obtained approximate ground-state energy is variationally guaranteed to be higher than the true energy.

Modified Slater-type wave functions obtained from mean-field methods (either HF or KS-DFT, described below) are usually used to determine the nodal surface in the fixed-node approximation. The missing correlation (in the sense of a pair correlation function) in the Slater determinant,  $\mathcal{D}$ , due to the Coulomb interaction is added in an ad-hoc way via the so-called Jastrow factor,  $\mathcal{J}$ ,

$$\begin{aligned}\Psi(\{\mathbf{r}_i s_i\}) &= \exp(\mathcal{J}(\{\mathbf{r}_i s_i\})) \mathcal{D}(\{\mathbf{r}_i s_i\}) \\ \mathcal{J}(\{\mathbf{r}_i s_i\}) &= \sum_i u_1(\mathbf{r}_i s_i) + \sum_{i < j} u_2(\mathbf{r}_i s_i, \mathbf{r}_j s_j)\end{aligned}\quad (2.17)$$

The two-electron Jastrow functions,  $u_2$ , decrease the probability of two electrons coming close to each other (different for same- and opposite-spin electron pair), while the one-electron functions,  $u_1$ , restore the electron density of  $\mathcal{D}$  that would be otherwise somewhat diffused by the two-electron Jastrow functions. The particular forms of  $u_1$  and  $u_2$  are mostly a result of experimentations and can be found for instance in (Foulkes et al., 2001).

## 2.5 Density-functional theory

The theoretical framework presented in this section has led to the most widely used methods for calculating the electronic structure of molecules and materials, and it is the lack of vdW interactions in its most popular approximations that renewed the theoretical interest in vdW interactions. It provides the context, motivation, as well as essential tools for most of the work in this thesis.

One can try to go one step further from the density-matrix functional theory, and express the electronic energy in terms of the electron density only, resulting in the density-functional theory (DFT). That this is in principle possible was shown by Hohenberg and Kohn (1964) and later more rigorously by Levy (1979), who divided the minimization in (2.7) over all antisymmetric wave functions in two steps, one over wave functions with a given density, the other over all densities, thus establishing the Hohenberg–Kohn functional,  $F_{\text{HK}}$ ,

$$\begin{aligned} E_0 &= \min_{\Psi} E[\Psi] = \min_n \min_{\Psi \rightarrow n} E[\Psi] = \min_n \left( \min_{\Psi \rightarrow n} (T[\Psi] + V_{ee}[\Psi]) + V_{\text{ext}}[n] \right) \\ &\equiv \min_n (F_{\text{HK}}[n] + V_{\text{ext}}[n]) \equiv \min_n (E[n]) \end{aligned} \quad (2.18)$$

If a given input density of the Hohenberg–Kohn functional,  $F_{\text{HK}}$ , is  $\nu$ -representable, meaning that there is some external potential (other than  $V_{\text{ext}}$ ) of which ground state has that density, then the minimizing wave function,  $\Psi_{\text{HK}}$ , is the ground state for the corresponding external potential. For densities that are not  $\nu$ -representable, the HK functional is still well-defined. In either case, one can define the kinetic-energy functional,  $T[n] \equiv T[\Psi_{\text{HK}}]$ , and  $V_{ee}[n] \equiv V_{ee}[\Psi_{\text{HK}}]$ . The task of DFT is then to devise sufficiently accurate approximations to  $T[n]$  and  $V_{ee}[n]$ . (The theory can be equivalently formulated using the electron spin densities,  $n_{\uparrow}(\mathbf{r})$  and  $n_{\downarrow}(\mathbf{r})$ , which gives a more useful framework for approximations in the case of spin-polarized systems.)

Historically, the development of DFT was hampered by unsuccessful attempts at the kinetic-energy functional, whose various approximate formulations explicitly in terms of the electron density fail to reproduce any electronic shell structure in atoms. This problem was largely solved by Kohn and Sham (1965), KS, who approximated the true kinetic energy with that of an auxiliary system of noninteracting electrons ( $V_{ee} = 0$ ) having the same density as the actual system,

$$\begin{aligned} T[n] &= T[\Psi_{\text{HK}}] = T\left[\arg \min_{\Psi \rightarrow n} (T[\Psi] + V_{ee}[\Psi])\right] \\ &\approx T\left[\arg \min_{\Psi \rightarrow n} T[\Psi]\right] = \min_{\Psi \rightarrow n} T[\Psi] \equiv T_s[n] \end{aligned} \quad (2.19)$$

The wave function minimizing  $T_s$ ,  $\Psi_s$ , is always of the Slater type, and would in fact be a ground state of the noninteracting system if it was put in a particular external potential, called the KS potential,<sup>3</sup>

$$\nu_s(\mathbf{r}) = -\frac{\delta T_s[n]}{\delta n(\mathbf{r})} \quad (2.20)$$

After the KS approximation, the remaining unknown terms are collected in the so-called exchange–correlation (XC) functional (so named despite the contained kinetic-energy

---

<sup>3</sup> More precisely, it would be a ground state only if the given density is noninteracting  $\nu$ -representable, otherwise it would be an excited state.

correction),

$$\begin{aligned} E[n] &= T_s[n] + V_{\text{ext}}[n] + J[n] + (T[n] - T_s[n] + V_{ee}[n] - J[n]) \\ &\equiv T_s[n] + V_{\text{ext}}[n] + J[n] + E_{\text{xc}}[n] \end{aligned} \quad (2.21)$$

The aim of KS-DFT is then to search for approximate formulations of  $E_{\text{xc}}$  expressed explicitly in terms of the electron density.

Minimization of this functional with respect to  $N$ -representable densities leads to the KS one-electron equations (another mean-field model, but unlike the HF model, exact in principle), whose structure differs from the HF equations mathematically only in that their effective mean-field potential is local rather than nonlocal,

$$\begin{aligned} v_{\text{xc}}(\mathbf{r}) &= v_{\text{ext}}(\mathbf{r}) + \frac{\delta(J[n] + E_{\text{xc}}[n])}{\delta n(\mathbf{r})} \\ v_{\text{HF}}(\mathbf{r}, \mathbf{r}') &= \left( v_{\text{ext}}(\mathbf{r}) + \frac{\delta J[n]}{\delta n(\mathbf{r})} \right) \delta(\mathbf{r} - \mathbf{r}') + \frac{\delta K[\gamma]}{\delta \gamma(\mathbf{r}, \mathbf{r}')} \end{aligned} \quad (2.22)$$

This difference makes the KS equations somewhat less complex, and more efficient to solve numerically, which is one of the reasons for the popularity of KS-DFT over the HF method. At the minimum of  $E[n]$ , the effective-mean field potential of the KS equations,  $v_{\text{xc}}(\mathbf{r})$ , is equal to the KS potential of the auxiliary noninteracting system,  $v_s(\mathbf{r})$ .

## 2.6 Adiabatic-connection fluctuation–dissipation theorem

This section introduces the starting point for the classification of vdW methods presented in Chapter 3. The auxiliary KS system of noninteracting electrons can be adiabatically connected to the real system by slowly turning on the interelectronic Coulomb interaction,  $\lambda \hat{V}_{ee}$ , from  $\lambda = 0$  to  $\lambda = 1$ , while keeping the electron density constant by adjusting the Kohn–Sham potential.

$$\begin{aligned} F_{\text{HK}}(\lambda)[n] &= \min_{\Psi \rightarrow n}(T[\Psi] + \lambda V_{ee}[\Psi]) & v_s(\mathbf{r}; \lambda) &= -\frac{\delta F_{\text{HK}}(\lambda)[n]}{\delta n(\mathbf{r})} \\ E(\lambda)[n] &= F_{\text{HK}}(\lambda)[n] + V_s(\lambda)[n] \end{aligned} \quad (2.23)$$

The standard HK functional and KS potential are recovered for  $\lambda = 1$  and  $\lambda = 0$ , respectively, whereas the Kohn–Sham potential for the true system reduces to the external potential,  $V_s(1)[n] = V_{\text{ext}}[n]$ . The true electronic energy ( $\lambda = 1$ ) can be obtained from the noninteracting energy ( $T_s[n] + V_s[n]$ ) by integrating over  $dE/d\lambda$ ,

$$E(1)[n] = E(0)[n] + \int_0^1 d\lambda \frac{dE(\lambda)[n]}{d\lambda} \quad (2.24)$$

Because the process is adiabatic, the system is in the ground state at any point, so the HK functional is stationary with respect to the wave function of the system ( $\delta F_{\text{HK}}/\delta\Psi = 0$ ), and the expression for  $dE/d\lambda$  reduces to a simple formula (this is also called the Hellmann–Feynman theorem),

$$\begin{aligned} \frac{dE(\lambda)[n]}{d\lambda} &= \frac{\partial F_{\text{HK}}(\lambda)}{\partial\lambda}[\Psi_{\text{HK}}(\lambda)] + \frac{\delta F_{\text{HK}}(\lambda)[\Psi]}{\delta\Psi}\Bigg|_{\Psi=\Psi_{\text{HK}}(\lambda)} \frac{\partial\Psi_{\text{HK}}(\lambda)}{\partial\lambda} + \frac{dV_s(\lambda)[n]}{d\lambda} \\ &= V_{ee}[\Psi_{\text{HK}}(\lambda)] + \frac{dV_s(\lambda)[n]}{d\lambda} \end{aligned} \quad (2.25)$$

Inserting the derivative into (2.24), one gets an alternative expression for the electronic energy that provides, by comparison to (2.21), an explicit formula for the XC energy (the last term),

$$\begin{aligned} E(1)[n] &= T_s[n] + V_s(0)[n] + \int_0^1 d\lambda V_{ee}[\Psi_{\text{HK}}(\lambda)] + V_s(1)[n] - V_s(0)[n] \\ &= T_s[n] + V_{\text{ext}}[n] + J[n] - \int_0^1 d\lambda \frac{1}{2} \iint d\mathbf{r}_1 d\mathbf{r}_2 \frac{n(\mathbf{r}_1)n(\mathbf{r}_2) - n_2(\mathbf{r}_1, \mathbf{r}_2; \lambda)}{|\mathbf{r}_1 - \mathbf{r}_2|} \end{aligned} \quad (2.26)$$

The fluctuation–dissipation theorem is a deep result of (quantum) statistical physics that relates correlations in fluctuations of any physical quantity describing a system in equilibrium with the dissipative part of the nonequilibrium response of that quantity to an external perturbation of the system (Callen and Welton, 1951). The linear density response function,  $\chi$ , of an electronic system describes the change in the electron density at time  $t$  generated by a change in the external potential at time  $t' < t$ ,

$$\frac{\delta n(\mathbf{r}, t)}{\delta v_{\text{ext}}(\mathbf{r}', t')} = \chi(\mathbf{r}, \mathbf{r}', t - t') \quad (2.27)$$

It is often more convenient to Fourier-transform the time to frequency,  $u$ ,

$$\frac{\delta n(\mathbf{r}, u)}{\delta v_{\text{ext}}(\mathbf{r}', u)} = \chi(\mathbf{r}, \mathbf{r}', u) \quad (2.28)$$

A particular version of the fluctuation–dissipation theorem for the fluctuations of the electron density then enables one to express the electron-pair density,  $n_2$ , in terms of the density response. This version of the theorem, at zero temperature, is expressed in terms of the density operator,  $\hat{n}(\mathbf{r}) = \sum_i \delta(\mathbf{r} - \mathbf{r}_i)$ , (see Callen and Welton, 1951, eq. 4.8, Landau and Lifschitz, 1980, eq. 124.10, Parr and Yang, 1989, eq. 8.6.2, and Kohn et al., 1998, eq. 8),

$$\langle \Psi | (\hat{n}(\mathbf{r}_1) - n(\mathbf{r}_1)) (\hat{n}(\mathbf{r}_2) - n(\mathbf{r}_2)) | \Psi \rangle = -\frac{1}{\pi} \int_0^\infty du \text{Im} \chi(\mathbf{r}_1, \mathbf{r}_2, u) \quad (2.29)$$

The electron-pair density can be likewise expressed in terms of the density operators,

$$n_2(\mathbf{r}_1, \mathbf{r}_2) = \langle \Psi | \hat{n}(\mathbf{r}_1) \hat{n}(\mathbf{r}_2) - \hat{n}(\mathbf{r}_1) \delta(\mathbf{r}_1 - \mathbf{r}_2) | \Psi \rangle \quad (2.30)$$

With the help of following identity,

$$\langle \Psi | (\hat{n}(\mathbf{r}_1) - n(\mathbf{r}_1)) (\hat{n}(\mathbf{r}_2) - n(\mathbf{r}_2)) | \Psi \rangle = \langle \Psi | \hat{n}(\mathbf{r}_1) \hat{n}(\mathbf{r}_2) | \Psi \rangle - n(\mathbf{r}_1) n(\mathbf{r}_2) \quad (2.31)$$

one can finally relate  $n_2$  and  $\chi$ ,

$$n(\mathbf{r}_1) n(\mathbf{r}_2) - n_2(\mathbf{r}_1, \mathbf{r}_2) = \frac{1}{\pi} \int_0^\infty du \operatorname{Im} \chi(\mathbf{r}_1, \mathbf{r}_2, u) + n(\mathbf{r}_1) \delta(\mathbf{r}_1 - \mathbf{r}_2) \quad (2.32)$$

In this equation, the left-hand side is finite for  $\mathbf{r}_1 = \mathbf{r}_2$ , and the divergent second term on the right-hand side is formally canceled by the divergence of the response function at  $\mathbf{r}_1 = \mathbf{r}_2$ . Plugging this equation into (2.26), the XC energy is expressed in terms of the density response function,

$$E_{xc}[\chi] = - \int_0^1 d\lambda \frac{1}{2} \iint d\mathbf{r}_1 d\mathbf{r}_2 \frac{\frac{1}{\pi} \int_0^\infty du \operatorname{Im} \chi(\mathbf{r}_1, \mathbf{r}_2, u; \lambda) + n(\mathbf{r}_1) \delta(\mathbf{r}_1 - \mathbf{r}_2)}{|\mathbf{r}_1 - \mathbf{r}_2|} \quad (2.33)$$

A standard form of the adiabatic-connection fluctuation-dissipation (ACFD) formula is reached by introducing the Coulomb operator,  $v(R) \equiv 1/R$ , and using the Wick rotation,  $\int_0^\infty du \operatorname{Im} \chi(u) = \int_0^\infty du \chi(iu)$ , (see Landau and Lifschitz, 1980, eq. 123.20),

$$E_{xc}[\chi] = - \frac{1}{2\pi} \int_0^\infty du \iint d\mathbf{r}_1 d\mathbf{r}_2 \int_0^1 d\lambda \chi(\mathbf{r}_1, \mathbf{r}_2, iu; \lambda) v(|\mathbf{r}_1 - \mathbf{r}_2|) + Nv(0) \quad (2.34)$$

Here, the density response outside the real axis is defined via analytic continuation, and is guaranteed to be real on the imaginary axis, and decrease monotonically to zero with growing  $iu$ . The divergent second term,  $Nv(0)$ , is formally canceled by the corresponding divergence in the first term. Evaluation of the ACFD expression for the KS response function,  $\chi(\lambda = 0)$ , reduces to the HF-like expression for exchange, which can be subtracted from the total XC energy to yield the remaining correlation part,

$$E_c[\chi] = - \frac{1}{2\pi} \int_0^\infty du \iint d\mathbf{r}_1 d\mathbf{r}_2 \int_0^1 d\lambda (\chi(\mathbf{r}_1, \mathbf{r}_2, iu; \lambda) - \chi(\mathbf{r}_1, \mathbf{r}_2, iu; 0)) v(|\mathbf{r}_1 - \mathbf{r}_2|) \quad (2.35)$$

## 2.7 Exchange–correlation functionals

The search for accurate approximations of the exact XC functional,  $E_{xc}$ , has been the major goal in DFT to this date, but the first and oldest approximation, which still serves as a basis of all modern and more accurate approximations, was published in the same manuscript as the KS-DFT framework itself. The uniform electron gas (UEG) is an idealized system

of electrons on an infinite uniform background of positive charge, which is fully specified by the value of the (constant) electron density,  $n(\mathbf{r}) \equiv n$ . The exchange-energy density (exchange energy per electron),  $\varepsilon_x$ , as defined by the HF approximation, was first calculated for the UEG by Dirac (1930),

$$\varepsilon_x^{\text{UEG}}(n) = -\frac{3}{4} \left( \frac{3}{\pi} \right)^{\frac{1}{3}} n^{\frac{1}{3}} \quad (2.36)$$

The corresponding correlation-energy density,  $\varepsilon_c \equiv \varepsilon_{xc} - \varepsilon_x$ , is known to a very good degree in a closed form from many-body perturbation theory (Chachiyo, 2016),

$$\varepsilon_c^{\text{UEG}}(n) \approx \frac{\ln(2) - 1}{2\pi^2} \ln \left( 1 + 20.4563 \left( \left( \frac{4\pi}{3} \right)^{\frac{1}{3}} n^{\frac{1}{3}} + \left( \frac{4\pi}{3} \right)^{\frac{2}{3}} n^{\frac{2}{3}} \right) \right) \quad (2.37)$$

Alternatively, it can be calculated nearly exactly using DQMC (Ceperley and Alder, 1980), for which fitted analytical forms exist (Perdew and Wang, 1992). The local-density approximation (LDA) then assumes that the XC energy density of the UEG can be applied locally at each point of a nonuniform system,

$$E_{xc}^{\text{LDA}}[n] = \int d\mathbf{r} n(\mathbf{r}) \varepsilon_{xc}^{\text{UEG}}(n(\mathbf{r})) \quad (2.38)$$

The XC functionals can be also viewed as resulting from particular approximations to the so-called XC hole,  $n_{xc}$ ,

$$n_{xc}(\mathbf{r}_1, \mathbf{r}_2) = n(\mathbf{r}_1)(1 - g(\mathbf{r}_1, \mathbf{r}_2)) \quad (2.39)$$

For a fixed electron at point  $\mathbf{r}_2$ , the XC hole represents the instantaneous missing density of a single electron around  $\mathbf{r}_2$ , hence its name. The XC energy can be expressed as the Coulomb interaction of the electron density and the  $\lambda$ -averaged XC hole,

$$E_{xc} = -\frac{1}{2} \iint d\mathbf{r}_1 d\mathbf{r}_2 \frac{n(\mathbf{r}_1) \int_0^1 d\lambda n_{xc}(\mathbf{r}_1, \mathbf{r}_2; \lambda)}{|\mathbf{r}_1 - \mathbf{r}_2|} = \int d\mathbf{r} n(\mathbf{r}) \int d\mathbf{r}' \frac{-\int_0^1 d\lambda n_{xc}(\mathbf{r}, \mathbf{r}'; \lambda)}{2|\mathbf{r} - \mathbf{r}'|} \quad (2.40)$$

The LDA can then be understood as approximating the true XC hole of a system with that of the UEG of the corresponding density at each point.

The electronic motion in the UEG with the density in the range of average densities in molecules and solids consists of two major processes: the collective organized electronic fluctuations, called plasmons, and the individual motion of largely independent quasi-electrons (abstractions of electrons that behave in many regards as electrons). The true electronic motion cannot be separated exactly in this way, but it is done so under the so-called random-phase approximation (RPA) that neglects explicit interactions between the collective and single-particle motions (Bohm and Pines, 1951; Pines and Bohm, 1952;

Bohm and Pines, 1953). This separation of motion also corresponds to a range separation of the Coulomb interaction, as in (3.3). Whereas the interactions of the individual quasi-electrons are constrained to the short-range part of the potential, the plasmons interact via the long-range part. Because LDA is exact for the UEG by construction, it captures both the short-range and long-range part of the XC energy in uniform systems (that is, metals, in which the uniform regions of the electron density are formed by the conducting electrons). But these two types of electronic motion are not equally transferable to nonuniform systems. Whereas the character of short-range interactions between quasi-electrons is relatively similar in most electronic systems, the collective motion is completely determined by the particular arrangement of the atoms. For this reason, the LDA captures in general relatively well the short-range part of the XC energy in most systems, but completely misses the long-range part in nonuniform systems, which comprise all real molecules and materials except metals.

The LDA estimates the local XC energy density only from the local value of the electron density, and better approximations can be constructed using more detailed semilocal information about the electronic system. In the generalized gradient approximation (GGA), the XC energy functionals are constructed using also the magnitude of the gradient of the density,  $|\nabla n(\mathbf{r})|$ . The KS kinetic energy,  $T_s[n]$ , can be formally expressed as an integral over the local kinetic-energy density,  $\tau_s$ ,

$$T_s[n] \equiv \int d\mathbf{r} \tau_s(\mathbf{r}) \quad (2.41)$$

This constraint does not uniquely define  $\tau_s$ . Two common definitions, one directly from the kinetic-energy operator, the other expressed using only orbital gradients, are related via the Laplacian of the density,  $\nabla^2 n(\mathbf{r})$ ,

$$\begin{aligned} \tau_s^I(\mathbf{r}) &= -\frac{1}{2} \sum_j \phi_j^*(\mathbf{r}) \nabla^2 \phi_j(\mathbf{r}) & \tau_s^{II}(\mathbf{r}) &= \frac{1}{2} \sum_j |\nabla \phi_j(\mathbf{r})|^2 \\ \tau_s^I &= \tau_s^{II} - \frac{1}{4} \nabla^2 n(\mathbf{r}) \end{aligned} \quad (2.42)$$

von Weizsäcker (1935) formulated an approximate kinetic-energy density,  $\tau_W$ , as a correction to the kinetic energy of the UEG for nonuniform electron densities, which is by construction exact (on its own) for one-electron and spin-paired two-electron densities,

$$\tau_W(\mathbf{r}) = \frac{1}{8} \frac{|\nabla n(\mathbf{r})|^2}{n(\mathbf{r})} \quad (2.43)$$

The spherically averaged electron-pair density,  $\langle n_2 \rangle_\Omega(\mathbf{r}_1, r_{12}) = \int d\Omega_{12} n_2(\mathbf{r}, r_{12}\Omega_{12})$ , of the HF approximation can be to leading order in the electron-electron distance,  $r_{12}$ , expressed in terms of kinetic-energy densities (Becke and Edgecombe, 1990),

$$\langle n_2 \rangle_\Omega(\mathbf{r}, r_{12}) = \frac{1}{3} (\tau_s^{II}(\mathbf{r}) - \tau_W(\mathbf{r})) n(\mathbf{r}) r_{12}^2 + O(r_{12}^3) \quad (2.44)$$

Because the electron-pair density is a fundamental quantity for the calculation of the XC energy, this motivates the use of kinetic-energy densities and the related Laplacian in formulations of approximate XC energy functionals, which leads to the so-called meta-GGA functionals. The smaller the electron-pair density is for small  $r_{12}$ , the more localized the electrons are, which motivates the definition of a function,  $\alpha(\mathbf{r})$ , expressing the relative localization of electrons with respect to the UEG,

$$\alpha(\mathbf{r}) = \frac{\tau_s^{\text{II}}(\mathbf{r}) - \tau_w(\mathbf{r})}{\tau_s^{\text{UEG}}(n(\mathbf{r}))} \quad (2.45)$$

This electron-localization function is always positive, and tends to be small (large localization) in the intra-shell regions of atoms and in the density tails (dominated by the highest occupied orbital) and large in inter-shell and bonding regions (Sun et al., 2013). The kinetic-energy densities enter many meta-GGA functionals in the form of  $\alpha(\mathbf{r})$ .

A generalized KS approximation can be formulated by relaxing the constraint that the KS potential must be local. Such generalization then allows one to use the exchange functional of the HF method as part of an XC functional, evaluated on the one-electron orbitals of the noninteracting KS system, which are implicit functionals of the electron density (via the KS kinetic functional). These so-called hybrid functionals proved useful and in general more accurate than pure KS functionals with local KS potentials.

## 2.8 Time-dependent density-functional theory

The ACFD formula yields the exact XC energy given the exact response function of the system, and time-dependent DFT provides a formally exact prescription how to calculate the latter. Runge and Gross (1984) generalized the ground-state DFT for  $v$ -representable densities to time-dependent external potentials by proving that the map from the potentials to the densities is injective and hence invertible, establishing the time-dependent density as a fundamental quantity of the theory. Within time-dependent KS-DFT, the primary role is played not by the XC functional, which cannot be well defined, but by the time-dependent XC potential, defined such that it yields the same time-dependent density for a noninteracting system as the true external potential yields for the interacting system. The linear response of this XC potential to the changes in the density around the ground-state density is called the XC kernel,  $f_{\text{xc}}$ ,

$$f_{\text{xc}}(\mathbf{r}, \mathbf{r}', u) = \frac{\delta v_{\text{xc}}[n](\mathbf{r}, u)}{\delta n(\mathbf{r}', u)} \quad (2.46)$$

The time-independent XC potential is recovered as a restriction of the time-dependent one to static densities, which makes time-dependent KS-DFT a harder theory to approximate than ground-state DFT.

The utility of the XC kernel comes from the expression for the density response function of the  $\lambda$ -scaled interacting system in terms of the KS density response function of the noninteracting auxiliary system of electrons (Gross and Kohn, 1985),

$$\chi^{-1}(\mathbf{r}, \mathbf{r}', u; \lambda) = \chi^{-1}(\mathbf{r}, \mathbf{r}', u; 0) - \lambda v(|\mathbf{r} - \mathbf{r}'|) - f_{xc}(\mathbf{r}, \mathbf{r}', u; \lambda) \quad (2.47)$$

The KS density response is known explicitly in terms of the KS one-electron wave functions and their respective energies,  $\epsilon_i$ , (Adler, 1962; Wiser, 1963),

$$\chi(\mathbf{r}, \mathbf{r}', u; 0) = \sum_{ij} (f_i - f_j) \frac{\phi_i^*(\mathbf{r}) \phi_i(\mathbf{r}') \phi_j^*(\mathbf{r}) \phi_j(\mathbf{r}')}{\epsilon_i - \epsilon_j + iu} \quad (2.48)$$

## 2.9 Nonlocal dipole polarizability

The presentation above revolved around the density response function. This section presents a quantity that can serve as an equivalent alternative specification of the response properties of a system, but provides a better starting point for formulating approximate models of the response, as discussed in Chapter 3.

The polarization of electronic matter under the influence of an additional external electric field,  $\mathbf{E}_\Delta = -\nabla v_\Delta$ , (on top of that from the nuclei and electrons) can be expressed by the change, in the electron density,  $\Delta n$ , from the unpolarized state ( $\mathbf{E}_\Delta = 0$ ). In the linear regime, this change is related to the corresponding potential,  $v_\Delta$ , via the density response function,

$$\Delta n(\mathbf{r}, t) = \int d\mathbf{r}' \int_{-\infty}^t dt' \chi(\mathbf{r}, \mathbf{r}', t - t') v_\Delta(\mathbf{r}', t') \quad (2.49)$$

$$\Delta n(\mathbf{r}, u) = \int d\mathbf{r}' \chi(\mathbf{r}, \mathbf{r}', u) v_\Delta(\mathbf{r}', u) \quad (2.50)$$

(A time-dependent electric field implies a nonzero magnetic field, but this is neglected in the nonrelativistic treatment discussed here.) Alternatively, the polarization state can be described by the polarization density,  $\mathbf{P}$ , which can be interpreted as a dipole density, and which gives the polarized charge density via divergence,

$$-\Delta n(\mathbf{r}, u) = -\nabla \cdot \mathbf{P}(\mathbf{r}, u) \quad (2.51)$$

Each vector field, such as  $\mathbf{P}$ , can be decomposed into its longitudinal and transversal component whose rotation and divergence are zero, respectively. Unlike  $\Delta n$  (but like the vector potential in classical electrodynamics), the polarization density is not observable, and is not unique, because any other polarization density that differs only by a rotation of some vector field will yield the same  $\Delta n$ . However, its longitudinal component is unique, and equal to  $-\mathbf{E}_{\Delta\Delta}/4\pi$ , the electric field generated by the polarization density,  $\Delta n$ .

The polarization density is related to the electric field via the (nonlocal) dipole polarizability,  $\alpha$ , (Hunt, 1983),<sup>4</sup>

$$\mathbf{P}(\mathbf{r}, u) = - \int d\mathbf{r}' \alpha(\mathbf{r}, \mathbf{r}', u) \mathbf{E}_\Delta(\mathbf{r}', u) \quad (2.52)$$

In general, the response of the electron density is anisotropic,  $\mathbf{E}_\Delta$  and  $\mathbf{P}$  are not aligned, and the polarizability must be a tensor. Like  $\mathbf{P}$ , the nonlocal dipole polarizability is not uniquely defined, but its longitudinal component is. The relation between the density response function and dipole polarizability is obtained by taking the divergence of (2.52), using integration by parts,<sup>5</sup> the definitions of  $\mathbf{E}_\Delta$  and  $\mathbf{P}$ , and comparing to (2.50),

$$\begin{aligned} \chi(\mathbf{r}, \mathbf{r}', u) &= -\nabla \cdot \nabla' \cdot \alpha(\mathbf{r}, \mathbf{r}', u) \\ &= -\sum_{\iota\zeta} \frac{\partial^2}{\partial r_\iota \partial r'_\zeta} \alpha_{\iota\zeta}(\mathbf{r}, \mathbf{r}', u) \quad (\iota, \zeta = x, y, z) \end{aligned} \quad (2.53)$$

The observable density response function depends only on the (unique) longitudinal component of the dipole polarizability, and one can always fix the gauge of the polarizability to be such that its transversal component is zero.

Whereas the electron density and the density response functions are coupled via the Coulomb operator, the polarization density and dipole polarizability are coupled via the dipole operator,

$$\mathbf{T}(\mathbf{R}) = \nabla \otimes \nabla' v(|\mathbf{r} - \mathbf{r}'|) \Big|_{\substack{\mathbf{r} = \mathbf{R} \\ \mathbf{r}' = 0}} = \frac{-3\mathbf{R} \otimes \mathbf{R} + R^2 \mathbf{I}}{R^5} \quad (2.54)$$

For instance, the electrostatic Coulomb self-interaction of  $\Delta n$ , which has the corresponding  $\mathbf{P}$ , can be expressed in two equivalent ways,

$$\begin{aligned} J[\Delta n] &= \frac{1}{2} \iint d\mathbf{r}_1 d\mathbf{r}_2 \Delta n(\mathbf{r}_1) v(|\mathbf{r}_1 - \mathbf{r}_2|) \Delta n(\mathbf{r}_2) \\ &= \frac{1}{2} \iint d\mathbf{r}_1 d\mathbf{r}_2 \mathbf{P}(\mathbf{r}_1) \cdot \mathbf{T}(\mathbf{r}_1 - \mathbf{r}_2) \mathbf{P}(\mathbf{r}_2) \end{aligned} \quad (2.55)$$

<sup>4</sup> The following common notation is used for vectors from any vector space. The application of a linear map (tensor),  $M$ , to a vector,  $v$ , omits parentheses,  $M(v) \equiv Mv$ , and composition of tensors likewise,  $M(O(v)) \equiv (MO)v \equiv MOv$ . Specifically for the Euclidean space, vectors and tensors are typeset in bold, and the inner and tensor (outer) products are denoted with “.” and “ $\otimes$ ”, respectively,  $(\mathbf{u} \otimes \mathbf{v})\mathbf{w} \equiv (\mathbf{v} \cdot \mathbf{w})\mathbf{u}$ .

<sup>5</sup> For a scalar field,  $\phi(\mathbf{r})$ , and a vector field,  $\mathbf{A}(\mathbf{r})$ ,

$$\int_V d\mathbf{r} \mathbf{A}(\mathbf{r}) \cdot \nabla \phi(\mathbf{r}) = \oint_{\partial V} d\mathbf{r} \nabla \cdot (\mathbf{A}(\mathbf{r})\phi(\mathbf{r})) - \int_V d\mathbf{r} (\nabla \cdot \mathbf{A}(\mathbf{r}))\phi(\mathbf{r})$$

When  $V$  is the whole space, and  $A(\mathbf{r})\phi(\mathbf{r})$  goes to zero when  $\mathbf{r}$  goes to infinity,

$$\int d\mathbf{r} \mathbf{A}(\mathbf{r}) \cdot \nabla \phi(\mathbf{r}) = - \int d\mathbf{r} (\nabla \cdot \mathbf{A}(\mathbf{r}))\phi(\mathbf{r})$$

The total polarizability of a system,  $\alpha_{\text{tot}}$ , that relates its total induced dipole moment to a perturbing uniform field,  $\mathbf{E}(u)$ , is recovered by integrating over both arguments of the nonlocal polarizability,

$$\begin{aligned} \int d\mathbf{r} \mathbf{P}(\mathbf{r}, u) &= \left( \iint d\mathbf{r} d\mathbf{r}' \boldsymbol{\alpha}(\mathbf{r}, \mathbf{r}', u) \right) \mathbf{E}(u) \\ &= \boldsymbol{\alpha}_{\text{tot}} \mathbf{E}(u) \end{aligned} \quad (2.56)$$

## 2.10 Periodic potentials and reciprocal space

The relevant physical information in quantum mechanics is encoded in operators on the appropriate Hilbert space (Fock space if change in number of particles is considered), which can be expressed in whichever basis is the most convenient for a particular calculation. This section presents a class of bases that are best suited for systems where the external potential has a full or discrete translational symmetry. Such systems correspond to perfect crystals, but are also good models or starting point for subsequent improved treatments of imperfect crystals or nonperiodic systems after applying artificial periodic boundary condition.

As can be the time domain of response functions Fourier-transformed into the frequency domain, so can be the real space Fourier-transformed into the reciprocal space,

$$f(\mathbf{k}) = \int d\mathbf{r} f(\mathbf{r}) e^{-i\mathbf{k}\cdot\mathbf{r}} \quad (2.57)$$

While the frequency domain directly exposes the time-translational symmetry of stationary states, the reciprocal space exposes the space-translational symmetry (periodicity) in crystals. The Fourier transformation of any Bravais lattice,  $\{\mathbf{R}\}$ , is the corresponding reciprocal lattice,  $\{\mathbf{G}\}$ . The spectrum of a crystal-periodic function,  $f$ , such as the electron density, is discrete, and is conventionally defined by normalizing to the unit-cell (UC) volume,  $\Omega_{\text{UC}}$ ,

$$\begin{aligned} f(\mathbf{k}) &= (2\pi)^3 \Omega_{\text{UC}} \sum_{\mathbf{G}} \delta(\mathbf{k} - \mathbf{G}) \frac{1}{\Omega_{\text{UC}}} \int_{\text{UC}} d\mathbf{r} n(\mathbf{r}) e^{-i\mathbf{G}\cdot\mathbf{r}} \\ &\equiv (2\pi)^3 \Omega_{\text{UC}} \sum_{\mathbf{G}} \delta(\mathbf{k} - \mathbf{G}) f_{\mathbf{G}} \end{aligned} \quad (2.58)$$

For a two-point function,  $A$ , such as the response function, the sign in the exponential of the Fourier transformation is conventionally inverted for the second argument. Because a two-point function related to a crystal is periodic only in both of its arguments at the same time, its spectrum is partially discrete, partially continuous, and any two wave vectors,  $\mathbf{k}$ ,  $\mathbf{k}'$ , for which its spectrum is nonzero, can be written in terms of two reciprocal unit-cell vectors,  $\mathbf{G}$ ,  $\mathbf{G}'$ , and a single wave vector from the first Brillouin zone,  $\mathbf{q}$ ,

$$A_{\mathbf{GG}'}(\mathbf{q}) = \frac{1}{\Omega_{\text{UC}}} \int_{\text{UC}} d\mathbf{r} \int d\mathbf{r}' A(\mathbf{r}, \mathbf{r}') e^{-i\mathbf{G}\cdot\mathbf{r}} e^{i\mathbf{G}'\cdot\mathbf{r}'} e^{-i\mathbf{q}\cdot(\mathbf{r}-\mathbf{r}')} \quad (2.59)$$

The Fourier transformation reduces inner-product real-space integrals into reciprocal-space infinite sums,

$$A(\mathbf{r}, \mathbf{r}') = \int d\mathbf{r}'' B(\mathbf{r}, \mathbf{r}'') C(\mathbf{r}'', \mathbf{r}) \Leftrightarrow A_{GG'}(\mathbf{q}) = \sum_{G''} B_{GG''}(\mathbf{q}) C_{G''G'}(\mathbf{q}) \quad (2.60)$$

Because larger  $\mathbf{G}$  correspond to ever more rapid changes in real space, a reasonable approximation can be made by neglecting  $\mathbf{G}$  above some threshold, and making the  $\mathbf{q}$ -dependent matrices finite. Such a truncation of the Fourier transformation corresponds to perhaps the simplest finite one-electron basis for periodic external potentials that can be reasonably efficient when actually used to numerically solve HF or KS equations. Since the functions corresponding to a given  $\mathbf{G}$  are plane waves,  $e^{-i\mathbf{G}\cdot\mathbf{r}}$ , the computer programs that calculate the electronic structure of crystals in this way are usually referred to as plane-wave codes.

There is no reasonable cutoff when the functions being transformed are discrete, say, over atoms positions,  $\mathbf{R}_i$ ,  $A(\mathbf{r}, \mathbf{r}') = \sum_{\mathbf{R}\mathbf{R}'} \sum_{ij} \delta(\mathbf{r} - \mathbf{R} - \mathbf{R}_i) \delta(\mathbf{r}' - \mathbf{R}' - \mathbf{R}_j) A_{\mathbf{R}+\mathbf{R}_i, \mathbf{R}'+\mathbf{R}_j}$ . ( $\mathbf{R}$ ,  $\mathbf{R}'$  are lattice vectors.) In such case, it is convenient to define the Fourier transformation of the individual discrete points,

$$\begin{aligned} A_{GG'}(\mathbf{q}) &= \frac{1}{\Omega_{UC}} \sum_i \sum_{\mathbf{R}_j} A_{\mathbf{R}_i, \mathbf{R}+\mathbf{R}_j} e^{-i\mathbf{G}\cdot\mathbf{R}_i} e^{i\mathbf{G}'\cdot\mathbf{R}_j} e^{-i\mathbf{q}\cdot(\mathbf{R}_i - \mathbf{R} - \mathbf{R}_j)} \\ &= \frac{1}{\Omega_{UC}} \sum_{ij} \left( \sum_{\mathbf{R}} A_{\mathbf{R}_i, \mathbf{R}+\mathbf{R}_j} e^{-i\mathbf{q}\cdot(\mathbf{R}_i - \mathbf{R} - \mathbf{R}_j)} \right) e^{-i\mathbf{G}\cdot\mathbf{R}_i} e^{i\mathbf{G}'\cdot\mathbf{R}_j} \\ &\equiv \frac{1}{\Omega_{UC}} \sum_{ij} A_{ij}(\mathbf{q}) e^{-i\mathbf{G}\cdot\mathbf{R}_i} e^{i\mathbf{G}'\cdot\mathbf{R}_j} \end{aligned} \quad (2.61)$$

This naturally reduces reciprocal-space infinite sums into real-space finite sums,

$$A_{GG'}(\mathbf{q}) = \sum_{G''} B_{GG''}(\mathbf{q}) C_{G''G'}(\mathbf{q}) \Leftrightarrow A_{ij}(\mathbf{q}) = \sum_k B_{ik}(\mathbf{q}) C_{kj}(\mathbf{q}) \quad (2.62)$$

### 2.10.1 Dielectric function from dipole polarizability

The previous sections introduced two ways to specify the response properties of a material—the density response function and the nonlocal dipole polarizability. Both of them are useful theoretical constructs, but none of them is directly measurable in solids in a practical way. In molecules, the total polarizability can be measured and compared to theoretical predictions, but this quantity is extensive and hence not very useful for describing macroscopic material samples. This disadvantage is resolved by yet another response, the (scalar) microscopic dielectric function,  $\epsilon$ , which has a directly measurable macroscopic limit.

The dielectric function relates the change in the total electric potential (including the field from the electrons),  $\Delta\nu_{\text{tot}}$ , to that in the external potential,

$$\Delta\nu_{\text{tot}}(\mathbf{r}, u) = \int d\mathbf{r}' \epsilon^{-1}(\mathbf{r}, \mathbf{r}', u) v_{\Delta}(\mathbf{r}', u) \quad (2.63)$$

It can be expressed in terms of the density response function,

$$\begin{aligned} \epsilon^{-1}(\mathbf{r}, \mathbf{r}', u) &= \delta(|\mathbf{r} - \mathbf{r}'|) + \int d\mathbf{r}'' v(|\mathbf{r} - \mathbf{r}''|) \chi(\mathbf{r}'', \mathbf{r}', u) \\ &\Downarrow \\ \epsilon_{GG'}^{-1}(\mathbf{q}, u) &= \delta_{GG'} + \sum_{G''} v_{GG''}(\mathbf{q}) \chi_{G''G'}(\mathbf{q}, u) \\ &= \delta_{GG'} + v(|\mathbf{G} + \mathbf{q}|) \chi_{GG'}(\mathbf{q}, u) \end{aligned} \quad (2.64)$$

The (tensor) macroscopic dielectric function,  $\boldsymbol{\epsilon}_M$ , relates the macroscopic total electric field to the macroscopic external electric field,

$$\mathbf{E}(u) = \boldsymbol{\epsilon}_M^{-1}(u) \mathbf{E}_{\text{ext}}(u) \quad (2.65)$$

The macroscopic dielectric function can be obtained from the microscopic one by taking the latter's long-wavelength limit,

$$\hat{\mathbf{q}} \cdot \boldsymbol{\epsilon}_M(u) \hat{\mathbf{q}} = \lim_{\mathbf{q} \rightarrow 0} \frac{1}{\epsilon_{00}^{-1}(\mathbf{q}, u)} \quad (2.66)$$

This limit depends on the direction from which zero is approached, which is the mechanism by which a microscopic scalar quantity becomes a macroscopic tensor quantity.

### 2.10.2 Ewald summation of dipole interaction

This section presents a reciprocal-space numerical technique that will be used in Chapter 4 to speed up calculations of vdW energies. The Fourier transformations of the discrete samples of the Coulomb and dipole operators,  $v$  and  $T$ , are infinite real-space sums that converge slowly, hindering numerical evaluation,

$$\mathbf{T}_{ij}(\mathbf{q}) = \sum_{\mathbf{R}} \mathbf{T}_{\mathbf{R}_i, \mathbf{R} + \mathbf{R}_j} e^{-i\mathbf{q} \cdot (\mathbf{R}_i - \mathbf{R} - \mathbf{R}_j)} = \sum_{\mathbf{R}} \mathbf{T}(\mathbf{R}_i - \mathbf{R} - \mathbf{R}_j) e^{-i\mathbf{q} \cdot (\mathbf{R}_i - \mathbf{R} - \mathbf{R}_j)} \quad (2.67)$$

Ewald (1921) summation is a technique that splits such a sum in two parts, one of which converges quickly in the real space, and the other in the reciprocal space. The split is governed by a single parameter,  $\alpha > 0$ , which balances the rate of convergence of the two components. In the case of the dipole operator for general  $\mathbf{q}$  (Bowden and Clark, 1981), the resulting expression consists of three terms,

$$\begin{aligned} \mathbf{T}_{ij}(\mathbf{q}) &= \sum_{\mathbf{R}} \mathbf{T}_{\text{Ew,sr}}(\mathbf{R}_i - \mathbf{R} - \mathbf{R}_j; \alpha) e^{-i\mathbf{q} \cdot (\mathbf{R}_i - \mathbf{R} - \mathbf{R}_j)} \\ &\quad + \frac{1}{\Omega_{\text{UC}}} \sum_{\mathbf{G}} \mathbf{T}_{\text{Ew,lr}}(\mathbf{G} + \mathbf{q}; \alpha) e^{-i\mathbf{G} \cdot (\mathbf{R}_i - \mathbf{R}_j)} - \delta_{ij} \frac{4\alpha^3}{3\sqrt{\pi}} \mathbf{I} \end{aligned} \quad (2.68)$$

where

$$\mathbf{T}_{\text{Ew,sr}}(\mathbf{d}; \alpha) = \frac{-3\mathbf{d} \otimes \mathbf{d} B_1(\alpha d) + d^2 \mathbf{I} B_2(\alpha d)}{d^5} \quad \mathbf{T}_{\text{Ew,lr}}(\mathbf{k}; \alpha) = 4\pi \frac{\mathbf{k} \otimes \mathbf{k}}{k^2} \exp\left(-\frac{k^2}{4\alpha^2}\right) \quad (2.69)$$

$$B_1(x) = \text{erfc}(x) + \frac{2}{\pi} x \left(1 + \frac{2}{3} x^2 \exp(-x^2)\right) \quad B_2(x) = \text{erfc}(x) + \frac{2}{\pi} x \exp(-x^2) \quad (2.70)$$

The first term is a real-space sum of the short-ranged part, while the other two combined are a reciprocal-space sum of the long-ranged part.

The long-ranged part is not defined for  $\mathbf{k} = \mathbf{G} + \mathbf{q} = 0$ , and neither has an analytical limit there. This corresponds to the fact that the dipole sum is not absolutely convergent for  $\mathbf{q} = 0$ , which in turn corresponds to the physical fact that the electrostatic energy of a macroscopic sample of a dipole crystal, described by a polarization density (eq. 2.55), depends on the shape of the crystal sample. This ambiguity disappears when one studies only differences between states of such a crystal, because the shape-dependent terms cancel out. A particular choice for the limit of  $\mathbf{T}_{\text{Ew,lr}}(\mathbf{k})$  when  $\mathbf{k}$  goes to zero corresponds to a particular choice of the shape, and a common choice is a sphere,

$$\lim_{\mathbf{k} \rightarrow 0} \mathbf{T}_{\text{Ew,lr}}(\mathbf{k}; \alpha) = \frac{4\pi}{3} \mathbf{I} \quad (2.71)$$

# Chapter 3

## Long-range electron correlation

This chapter presents a review of the state of the art of microscopic models of van der Waals interactions that have been applied beyond simple toy models and have a basis in the adiabatic-connection fluctuation–dissipation (ACFD) formula for the exchange-correlation energy. While the reviewed methods are all prior works of other authors, the unified range-separation formalism based on the nonlocal polarizability, formal classification along the different approximations to the ACFD formula, and several re-derivations of existing methods are novel. Most of the original and derived results in this chapter have been published in (Hermann et al., 2017b).

### 3.1 Range separation of electron correlation

The vdW force between atomic bodies held together by covalent, ionic, or metallic binding is always caused by the long-range electron correlation, but not all effects of the long-range correlation are considered to be a vdW force. In metals, the electrons from the nonconducting bands are localized on atoms, which form nonuniform islands in the sea of approximately uniform electron density of the conducting electrons (Tao et al., 2010). Here, the long-range correlation between the conducting electrons contributes to the metallic binding. In nonmetals, however, all electrons are nonconducting, the electron density is nowhere uniform, and long-range correlation is mostly associated with vdW interactions.

The electronic structure within a single uniform subsystem differs qualitatively in many aspects from that in a nonuniform system. In a uniform system, the exchange effects, the KS density response function, and the XC kernel decay only algebraically with distance (they are long-ranged) as a result of the conducting electrons, whereas they decay exponentially (they are short-ranged) in nonuniform systems (Ge and Lu, 2015). (The true density response function decays algebraically in both cases because of electron correlation.) Correspondingly, semilocal and hybrid XC functionals capture both short-range and long-range part of the XC energy in uniform systems, but only

the short-range part in the nonuniform systems. The vdW interactions can be therefore associated with all long-range electron correlation except for that between conducting electrons within a single uniform subsystem, which is fortunately covered by semilocal and hybrid density functionals. The nonuniform situations include interactions between conducting electrons in disjoint metallic bodies, interactions of conducting electrons with localized electrons, either in the same metallic body, or in other bodies, as well as all interactions between localized electrons.

The XC energy can be formally divided into a short-range (sr) and long-range (lr) part via the ACFD formula in (2.34) by separating the double spatial integral into two parts using a range-separating function,  $f$ , which should decay at least exponentially fast,

$$\begin{aligned} \iint d\mathbf{r}_1 d\mathbf{r}_2 &= \iint d\mathbf{r}_1 d\mathbf{r}_2 (1 - f(\mathbf{r}_1, \mathbf{r}_2)) + \iint d\mathbf{r}_1 d\mathbf{r}_2 f(\mathbf{r}_1, \mathbf{r}_2) \equiv \iint_{\text{sr}} d\mathbf{r}_1 d\mathbf{r}_2 + \iint_{\text{lr}} d\mathbf{r}_1 d\mathbf{r}_2 \\ f(\mathbf{r}, \mathbf{r}) &= 0 \quad f(\mathbf{r}, \mathbf{r} + \mathbf{R}) = 1 - O(\exp(-R)) \end{aligned} \quad (3.1)$$

Considering the range-separating function to be a functional of the density,  $f \equiv f[n]$ , it can be in principle always constructed exactly for a given short-range (or long-range) part. The short-range part of the ACFD expression accounts for short-range density fluctuations interacting via the short-range part of the Coulomb operator, while the long-range part accounts for long-range fluctuations interacting via the long-range Coulomb operator. The statements above about the XC energy in uniform and nonuniform systems can then be summarized in the following way,

uniform:	$E_{\text{xc}} = \overbrace{E_{\text{x,sr}} + E_{\text{c,sr}}}^{\text{semilocal/hybrid}} + \underbrace{E_{\text{x,lr}}}_{\approx 0} + \underbrace{E_{\text{c,lr}}}_{\text{vdW}}$	(3.2)
nonuniform:	semilocal/hybrid	vdW

Of course, such a range separation is exact only in principle, because the association of a given XC functional with a particular range-separating function is unknown.

With the caveat about the uniform systems, the vdW interactions can then be associated with the long-range XC energy,

$$\begin{aligned} E_{\text{xc,lr}} &= -\frac{1}{2\pi} \int_0^\infty du \iint d\mathbf{r}_1 d\mathbf{r}_2 \int_0^1 d\lambda \chi(\mathbf{r}_1, \mathbf{r}_2, iu; \lambda) v_{\text{lr}}(\mathbf{r}_1, \mathbf{r}_2) \\ v_{\text{lr}}(\mathbf{r}, \mathbf{r}') &= f(\mathbf{r}, \mathbf{r}') v(|\mathbf{r} - \mathbf{r}'|) \end{aligned} \quad (3.3)$$

In this setup, care must be taken about the potential double counting of the long-range XC energy in uniform systems from the semilocal or hybrid functionals and from the long-range ACFD formula. This double-counting does not matter in situations when the result of a calculation is an energy difference, such as when calculating the adsorption energy of a molecule on a metal surface. But it may pose a problem in other cases, for instance when investigating a lattice expansion of a metal.

The TD-DFT Dyson-like equation for the density response function in (2.47) can be effectively range-separated by introducing some long-range effective Coulomb operator,  $\nu_{\text{eff}}$ , grouping the XC kernel (short-ranged in nonuniform systems) and the corresponding short-range Coulomb operator,  $\nu - \nu_{\text{eff}}$ , and averaging the resulting effective density response function,  $\chi_{\text{eff}}$ , over  $\lambda$ ,

$$\begin{aligned}\chi^{-1}(\mathbf{r}, \mathbf{r}', u; \lambda) &= \chi^{-1}(\mathbf{r}, \mathbf{r}', u; 0) - f_{\text{xc}}(\mathbf{r}, \mathbf{r}', u; \lambda) - \lambda(\nu(|\mathbf{r} - \mathbf{r}'|) - \nu_{\text{eff}}(\mathbf{r}, \mathbf{r}')) - \lambda\nu_{\text{eff}}(\mathbf{r}, \mathbf{r}') \\ &\approx \chi_{\text{eff}}^{-1}(\mathbf{r}, \mathbf{r}', u) - \lambda\nu_{\text{eff}}(\mathbf{r}, \mathbf{r}')\end{aligned}\quad (3.4)$$

Interpreting the response functions as tensors on the vector space of spatial functions, and using the shorthand multiplication notation for tensor composition, the full density response function can be expressed explicitly,

$$\begin{aligned}\int_0^1 d\lambda \chi(u; \lambda) &= \int_0^1 d\lambda (\chi_{\text{eff}}(u) + \chi_{\text{eff}}(u)\lambda\nu_{\text{eff}}\chi(u; \lambda)) \\ &= \int_0^1 d\lambda (\chi_{\text{eff}}(u) + \chi_{\text{eff}}(u)\lambda\nu_{\text{eff}}\chi_{\text{eff}}(u) + \chi_{\text{eff}}(u)\lambda\nu_{\text{eff}}\chi_{\text{eff}}(u)\lambda\nu_{\text{eff}}\chi(u; \lambda)) \\ &= \sum_{n=0}^{\infty} \left( \int_0^1 d\lambda \lambda^n \right) \chi_{\text{eff}}(u) (\nu_{\text{eff}}\chi_{\text{eff}}(u))^n \\ &= \sum_{n=0}^{\infty} \frac{1}{n+1} (\chi_{\text{eff}}(u)\nu_{\text{eff}})^{n+1} \nu_{\text{eff}}^{-1} \\ &= \ln(1 - \chi_{\text{eff}}(u)\nu_{\text{eff}}) \nu_{\text{eff}}^{-1}\end{aligned}\quad (3.5)$$

The effective density response function, defined in this way, is guaranteed to be short-ranged in nonuniform systems. The equivalent expressions can be written for the nonlocal dipole polarizability.

Plugging this expression to the long-range ACFD formula then gives the long-range XC energy in terms of the effective density response function and the two long-ranged Coulomb operators,  $\nu_{\text{eff}}$  and  $\nu_{\text{lr}}$ ,

$$\begin{aligned}E_{\text{xc,lr}} &= -\frac{1}{2\pi} \int_0^\infty du \iint d\mathbf{r}_1 d\mathbf{r}_2 [\ln(1 - \chi_{\text{eff}}(u)\nu_{\text{eff}}) \nu_{\text{eff}}^{-1} \nu_{\text{lr}}](\mathbf{r}_1, \mathbf{r}_2) \\ &\equiv -\frac{1}{2\pi} \int_0^\infty du \text{Tr}_{\mathbf{r}} \left( \ln(1 - \chi_{\text{eff}}(u)\nu_{\text{eff}}) \nu_{\text{eff}}^{-1} \nu_{\text{lr}} \right)\end{aligned}\quad (3.6)$$

The effective range of  $\nu_{\text{lr}}$  is governed by the complementary range of the method for the short-range XC energy (typically a semilocal XC functional), whereas the range of  $\nu_{\text{eff}}$  is controlled by the range of the model for the effective density response, discussed below.

### 3.1.1 Static correlation

In metals, strongly correlated materials, and spin-unpaired systems, the Coulomb interaction between electrons becomes at least as determining for the basic structure of the wave

function as the kinetic energy. This leads to the general failure of mean-field models such as the HF and semilocal KS-DFT approximations, except for metals and KS-DFT, in which the LDA-based XC functionals capture the electron correlation within uniform electron density effectively. In spin-unpaired (open-shell) systems, this effect is often called static or left-right correlation. Spin-unpaired systems typically result from breaking chemical bonds and separating the resulting fragments. In such cases, a mean-field method can describe well the spin-paired unbroken system, but fails for the spin-unpaired separated fragments. This might suggest that static correlation should be a part of the long-range correlation energy.

But consider the case of dissociating a hydrogen molecule in the (singlet) ground state into two hydrogen atoms. The system of two separated atoms has zero total spin, and if one electron is measured on the left atom with some spin, the other will be certainly on the right atom because of Coulomb repulsion, and it will have the opposite spin. The quantum states of the two hydrogen atoms are entangled, making them really a single quantum system, albeit noninteracting. In a mean-field method, the probabilities of finding opposite-spin electrons at some points are uncorrelated, and there is 50% chance that both electrons will be located on the same atom. This underlying issue manifests differently in the HF and KS schemes. In the HF approximation, the missing opposite-spin correlation in the wave function results in a spurious on-site repulsion. In KS-DFT, on the other hand, the lack of correlation in the KS ground state is an expected part of the theory, resulting in two hydrogen atoms with mixed spin densities. Current XC functionals then fail by giving a different XC energy for such mixed-spin hydrogen atoms than for a pure-spin hydrogen atom. This demonstrates that the problem of static correlation in DFT is in fact a local problem that can be formulated on a single isolated hydrogen atom. Alternatively, one can argue that the Coulomb operator in the ACFD formula goes to zero at large distances, whereas the static correlation persists at all distances, so it must be the short-range (on-site) structure of the (spin) density response function that determines the correct XC energy in systems with static correlation. In any case, static correlation is part of the short-range XC energy, and the long-range correlation energy is indeed responsible solely for vdW interactions (except in uniform systems).

That being said, the incorrect treatment of static correlation can have a large effect on the response properties of the electronic system, and so the long-range correlation energy as well. For instance, minimization of the total electronic energy with respect to semilocal and hybrid density functionals (which are incapable of treating static correlation) leads to electron densities that are far too diffuse and polarizable, which yields overestimated vdW interactions. This issue, however, is present already in the isolated systems, and is independent of the long-range interaction between them.

## 3.2 Local effective polarizability

This section argues that the formulation of the ACFD formula in terms of the nonlocal polarizability is a better starting point for developing approximate models than the formulation in terms of the density response function. Expressing  $\chi$  in terms of  $\alpha$ , using the same integration-by-parts technique as when deriving the relationship between  $\chi$  and  $\alpha$  in (2.53), and transferring the divergence operators on the Coulomb operator, the ACFD formula can be cast in terms of the nonlocal dipole polarizability,

$$\begin{aligned} E_{xc,lr}[\alpha] &= \frac{1}{2\pi} \int_0^\infty du \iint d\mathbf{r}_1 d\mathbf{r}_2 \int_0^1 d\lambda \alpha(\mathbf{r}_1, \mathbf{r}_2, iu; \lambda) \mathbf{T}_{lr}(\mathbf{r}_1, \mathbf{r}_2) \\ \mathbf{T}_{lr}(\mathbf{r}, \mathbf{r}') &= \nabla \otimes \nabla' v_{lr}(\mathbf{r}, \mathbf{r}') \end{aligned} \quad (3.7)$$

Following the same procedure as with the density response function, this can be recast in terms of the effective polarizability,

$$E_{xc,lr} = \frac{1}{2\pi} \int_0^\infty du \text{Tr}_r \left( \ln \left( 1 + \alpha_{\text{eff}}(u) \mathbf{T}_{\text{eff}} \right) \mathbf{T}_{\text{eff}}^{-1} \mathbf{T}_{lr} \right) \quad (3.8)$$

There are three reasons why the effective-polarizability version of the ACFD formula turns out to be a good starting point for approximate models. First, models of  $\alpha_{\text{eff}}$  can effectively capture all short-range XC effects, which modify the magnitude of the bare KS polarizability, without accounting for these effects explicitly via the Dyson equation. Second, such models do not need to represent the short-range structure of the polarizability correctly, because it interacts only via the long-range dipole operators. Third, the density response function has a complex nodal structure, as it describes depletion of the electron density at some points and its accumulation elsewhere. In contrast, the corresponding polarizability is a rotation-free smooth vector field that encodes that underlying nodal structure implicitly in terms of its local behavior via the divergence operators in (2.53). This is true even in the case of a long-ranged nonlocal density response function that is characteristic of uniform systems. Therefore, the strength of the response is translated directly into the magnitude of the polarizability, whereas it is translated only indirectly into the magnitude of the gradient of the density response function.

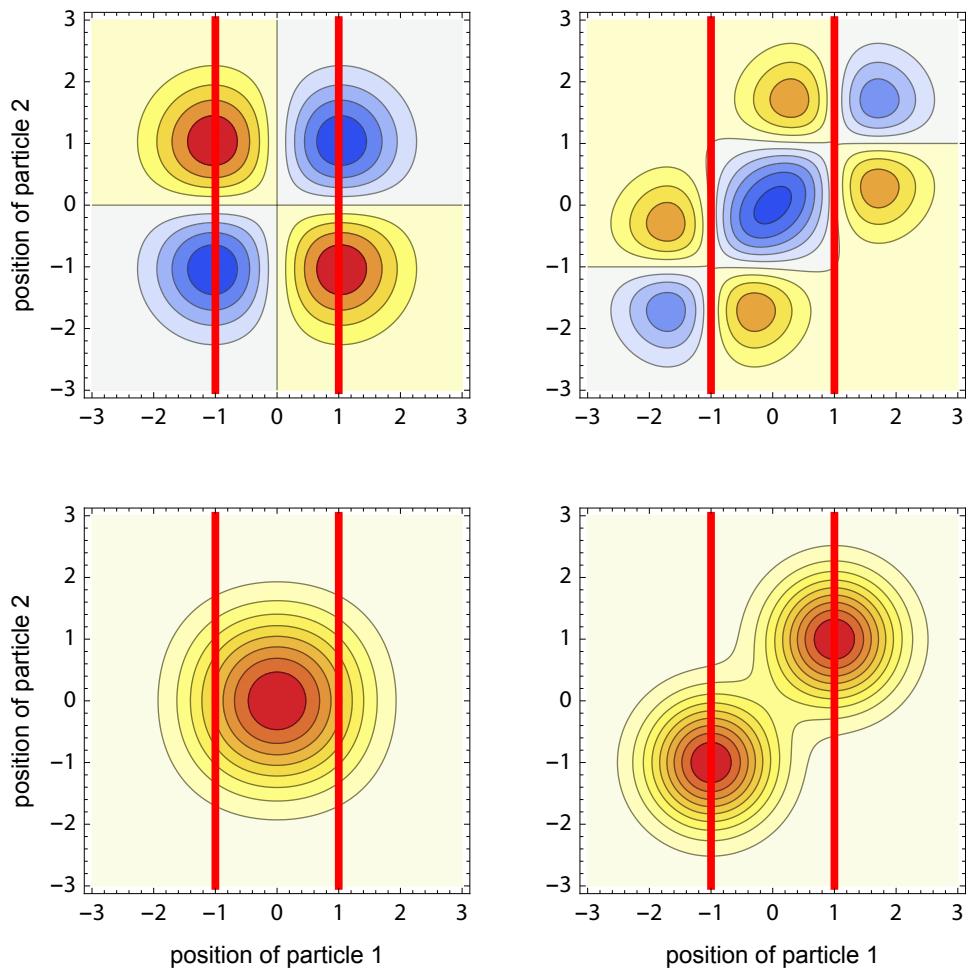
For illustration, consider two one-dimensional (1D) Gaussian charge densities located at  $\pm 1$  (crude model of atoms), and two model density response functions, one local,  $\chi_{\text{loc}}$ , the other nonlocal,  $\chi_{\text{nlc}}$ , (Figure 3.1),

$$\begin{aligned} \chi_{\text{nlc}}(x, x') &= -(e^{-(x+1)^2} - e^{-(x-1)^2})(e^{-(x'+1)^2} - e^{-(x'-1)^2}) \\ \chi_{\text{loc}}(x, x') &= -(x+1)e^{-(x+1)^2}(x'+1)e^{-(x'+1)^2} - (x-1)e^{-(x-1)^2}(x'-1)e^{-(x'-1)^2} \end{aligned} \quad (3.9)$$

In one dimension, the dipole polarizability is a scalar, and uniquely determined by integrating over the density response function,

$$\alpha^{\text{ID}}(x, x') = \int_{-\infty}^x dy \int_{-\infty}^{x'} dy' \chi^{\text{ID}}(y, y') \quad (3.10)$$

**Figure 3.1 | Density response function vs. dipole polarizability.** Contour plots of model one-dimensional nonlocal (left) and local (right) responses encoded as the density response function (top),  $\chi(x, y)$ , and the dipole polarizability (bottom),  $a(x, y)$ , defined in (3.9). The red and blue colors correspond to positive and negative values. The red lines denote the positions of the two responding Gaussian charge densities on the  $x$ -axis.



Even in these trivial models, the density response function changes sign around atoms, and has a nontrivial nodal structure, whereas the polarizability is positive everywhere. Furthermore, the nonlocal density response translates into a polarizability that is still localized, but over a larger region spanning both atoms. These observations are crucial for multipole expansions of both  $\chi$  and  $\alpha$  discussed below.

The localized nature of the dipole polarizability combined with the insensitivity of the long-range ACFD formula to the short-range structure of the effective polarizability hints at the possibility of a relatively accurate local representation of  $\alpha_{\text{eff}}$ , formally obtained by integrating over some neighborhood,  $M(\mathbf{r})$ , around each point,  $\mathbf{r}$ ,

$$\alpha_{\text{eff}}(\mathbf{r}, \mathbf{r}', u) \approx \delta(|\mathbf{r} - \mathbf{r}'|) \int_{M(\mathbf{r})} d\mathbf{r}'' \alpha_{\text{eff}}(\mathbf{r}, \mathbf{r}'', u) \equiv \delta(|\mathbf{r} - \mathbf{r}'|) \alpha_{\text{eff}}(\mathbf{r}, u) \quad (3.11)$$

Since  $\alpha_{\text{eff}}(\mathbf{r}, u)$  depends on the properties of the system only in the near neighborhood of  $\mathbf{r}$ , good semilocal approximations to it can be constructed using local quantities such as the electron density, its gradient, or the KS kinetic energy density, in a similar manner that the hierarchy of semilocal XC functionals is built. In nonuniform systems, the polarizability is localized only algebraically, the effective neighborhoods would need to be larger, and correspondingly, the range separation of the Dyson-like equation would need to be shifted towards larger separations. On the other hand, in the case of a vdW interaction between a metal and a nonmetal, the long-range nonlocal electronic fluctuations in the former do not have any long-range counterpart in the latter, preventing any correlation on such length scales, and only relatively short-range fluctuations in the metal contribute to the vdW attraction. For this reason, the local effective polarizability can effectively capture the true response even in such cases.

### 3.2.1 Harmonic oscillator as a polarizability model

The frequency dependence of the imaginary part of the density response function or dipole polarizability encodes the full optical (electromagnetic) spectrum. This is equivalent to knowing the full energy spectrum of the corresponding Hamiltonian, which is a much harder problem than calculating the ground-state energy. Accordingly, the ACFD formula contains the polarizability under the integral sign over all frequencies, and it is sufficient to model the spectrum only such that its sum-total is represented accurately. This is done conveniently by modeling directly the imaginary-axis dependence of the polarizability,  $\alpha_{\text{eff}}(\mathbf{r}, iu)$ , which is a real-valued monotonically decreasing function, and must decay quadratically in the high-frequency limit. These conditions are satisfied by a simple rational function (the simplest Padé approximant), specified by two parameters,  $\alpha(0)$  and  $\omega$ ,

$$\alpha_{\text{eff}}(\mathbf{r}, iu) \approx \frac{\alpha_{\text{eff}}(\mathbf{r}, 0)}{1 + \frac{u^2}{\omega(\mathbf{r})^2}} \quad (3.12)$$

The interpretation of this formula is provided by a charged harmonic oscillator, for which it is the exact result.

Consider a particle with a charge,  $q$ , and mass,  $m$ , in a harmonic potential,  $v_{\text{ext}}(\mathbf{r}) = m\omega^2/2$ , and under a dissipative force,  $-m\zeta d\mathbf{r}/dt$  (Lorentz oscillator). The total polarizability of such a system can be expressed in a closed form,

$$\alpha_{\text{tot}}^{\text{LO}}(u; \zeta) = \frac{q^2/m}{\omega^2 - u^2 + i\zeta u} \quad (3.13)$$

The electronic Hamiltonian without any interaction with the environment is nondissipative, and the corresponding oscillator model is recovered at the limit of  $\zeta \rightarrow 0$ ,

$$\begin{aligned} \lim_{\zeta \rightarrow 0} \alpha_{\text{tot}}^{\text{LO}}(u; \zeta) &= \frac{q^2/m}{\omega^2 - u^2} + \frac{\pi}{2} \frac{q^2}{m\omega} \delta(u - \omega) \\ \alpha_{\text{tot}}^{\text{LO}}(iu; 0) &= \frac{q^2/m\omega^2}{1 + u^2/\omega^2} \end{aligned} \quad (3.14)$$

The same result is obtained using either a classical or quantum treatment.

### 3.3 Classification of vdW methods

Most existing models of long-range correlation can be described in terms of various approximations to the range-separated effective-polarizability version of the ACFD formula in (3.8). One of them is the already discussed local representation of the effective polarizability. Two other general and common approximations are spatial coarse-graining of the system and truncation of the infinite logarithm series,  $\ln(1 - x) = \sum_{n=1} x^n/n$ . The two types of approximations are illustrated in Figure 3.2.

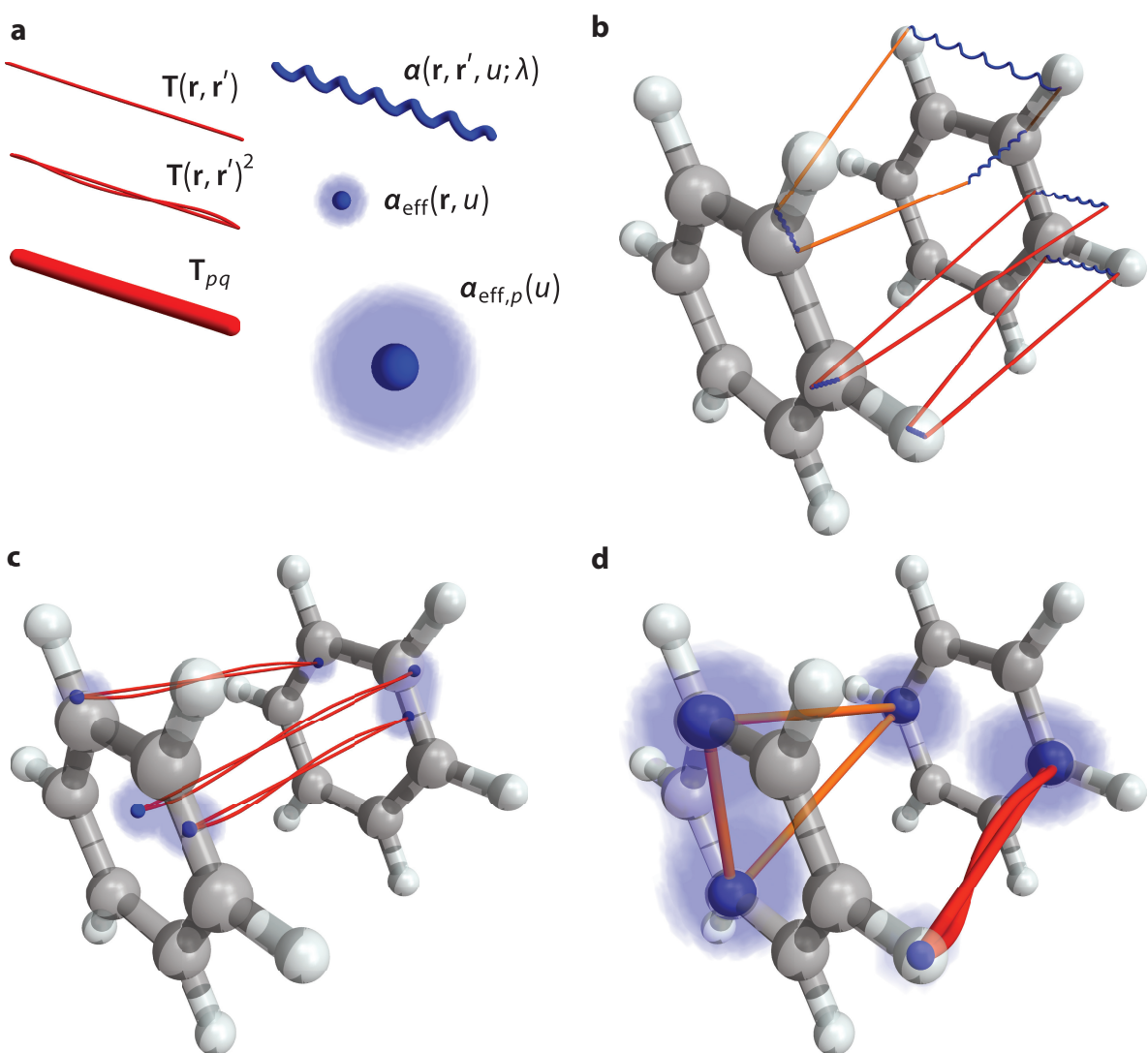
#### 3.3.1 Coarse-graining of continuous quantities

Given a set of functions,  $w_p(\mathbf{r})$ , that partition a space into fragments,  $\sum_p w_p(\mathbf{r}) \equiv 1$ , and respective centers of the fragments,  $\mathbf{R}_p$ , each spatial function or operator, such as the dipole polarizability, can be represented as a sum over the partitioned components,  $\boldsymbol{\alpha}_{pq}$ , which can be in turn expanded in the basis of solid harmonics (multipole expansion),  $\alpha_{pq, ll' mm'}$ , around the centers (Stone, 2013),

$$\boldsymbol{\alpha}(\mathbf{r}, \mathbf{r}', u) = \sum_{pq} w_p(\mathbf{r}) w_q(\mathbf{r}') \boldsymbol{\alpha}(\mathbf{r}, \mathbf{r}', u) \equiv \sum_{pq} \boldsymbol{\alpha}_{pq}(\mathbf{r}, \mathbf{r}', u) \rightarrow \alpha_{pq, ll' mm'} \quad (3.15)$$

(Here,  $l, l'$  start from 1, because the expanded quantity is a tensor. The corresponding expansion of the scalar density response function,  $\chi$ , would start from  $l = l' = 0$ .) The dipole potential is expanded correspondingly. Unlike the Fourier transformation, the

**Figure 3.2 | Coarse-graining and many-body expansion.** Different kinds of approximations to the adiabatic-connection fluctuation–dissipation formula for the long-range exchange–correlation energy are shown on the ball-and-sticks model of the benzene dimer. (a) Legend for the graphical representation of polarizabilities,  $\alpha$ , and dipole operators,  $T$ . The clouds around the effective polarizability represent its effective spatial extent. (b) The random-phase approximation is an ab-initio many-body method without coarse-graining that approximates the true coupling of the bare Kohn–Sham polarizability with a bare dipole operator. The long-range part of the XC energy is formed by terms in which at least one of the dipole operators is long-ranged. The red and orange colors denote second- and third-order terms, respectively. (c) Nonlocal density functionals are second-order effective models without coarse-graining. The polarizability is approximated locally. (d) Many-body dispersion is a coarse-grained atomic model.



multipole expansion is not invertible, but like the Fourier transformation, it introduces a correspondence between spatial integrals and infinite sums,

$$\mathbf{P}(\mathbf{r}, u) = - \int d\mathbf{r}' \boldsymbol{\alpha}(\mathbf{r}, \mathbf{r}', u) \mathbf{E}(\mathbf{r}', u) \Leftrightarrow \mathbf{P}_{p,lm}(u) = - \sum_{q,l'm'} \alpha_{pq,ll'mm'}(u) E_{q,l'm'} \quad (3.16)$$

The sums can be made implicit by arranging the multipole moments in vectors and matrices,

$$\boldsymbol{\alpha} = \begin{pmatrix} \alpha_{pp} & \alpha_{pQ} & \cdots \\ \alpha_{Qp} & \alpha_{QQ} & \cdots \\ \vdots & \vdots & \ddots \end{pmatrix}$$

$$\boldsymbol{\alpha}_{pp} = \begin{pmatrix} \alpha_{11,11xx} & \alpha_{11,11xy} & \alpha_{11,11xz} & \alpha_{12,11xx} & \cdots \\ \alpha_{11,11yx} & \alpha_{11,11yy} & \alpha_{11,11yz} & \alpha_{12,11yx} & \cdots \\ \alpha_{11,11zx} & \alpha_{11,11zy} & \alpha_{11,11zz} & \alpha_{12,11zx} & \cdots \\ \alpha_{21,11xx} & \alpha_{21,11xy} & \alpha_{21,11xz} & \alpha_{22,11xx} & \cdots \\ \vdots & \vdots & \vdots & \vdots & \ddots \end{pmatrix} \quad (3.17)$$

Under this notation, the long-range ACFD formula in (3.8) has exactly the same form, but the operators are infinite matrices instead of nonlocal functions, and the trace is not over space, but over the fragments and multipole moments,

$$E_{xc,lr} = \frac{1}{2\pi} \int_0^\infty du \text{Tr}_{p,lm} \left( \ln (1 + \boldsymbol{\alpha}_{\text{eff}}(u) \mathbf{T}_{\text{eff}}) \mathbf{T}_{\text{eff}}^{-1} \mathbf{T}_{\text{lr}} \right) \quad (3.18)$$

The motivation for this multipole reformulation is that because both  $\mathbf{T}_{\text{eff}}$  and  $\mathbf{T}_{\text{lr}}$  are long-ranged and their moments decay increasingly faster for higher  $l$ 's, all the matrix multiplications (infinite sums) converge quickly and can be approximated well by finite sums.

The feasibility of the coarse-graining and multipole expansions is dictated by the choice of the fragments and the response properties of the system. In a nonuniform system, the nonlocal effective polarizability is exponentially localized on atoms, and atom-centered fragments are a natural basis of a quickly converging multipole expansion. In a uniform system, the effective polarizability is long-ranged, diffused, and there are no natural centers for the multipole expansion, leading to large higher moments and slow convergence or even divergence of the expansion. In principle, this problem is mitigated in combination with the KS-DFT, because the long-range XC energy within the uniform systems is captured by the semilocal or hybrid functional, and the multipole convergence of the correlation energy due to interaction with a separate uniform or nonuniform system is helped by larger separations between the fragments. But such an interplay is not well understood, and none of the coarse-grained models reviewed in this chapter take advantage of this cancellation. In general, the complex interaction of the delocalized response of metals and localized response of nonmetals (insulators or

molecules) is one of the hardest problems for general approximate models of the long-range electron correlation. It has been treated in select systems by effective parametrization of the metallic response from experimental measurements of the dielectric function (Ruiz et al., 2012), but the lack of any general efficient model still hinders modeling of hybrid material interfaces.

### 3.3.2 Truncation of many-body expansion

The operator logarithm in (3.8) is defined as an infinite series, and writing it out explicitly in terms of individual orders leads to a many-body decomposition of the XC energy,

$$\begin{aligned} E_{\text{xc},\text{lr}} = & \frac{1}{2\pi} \int_0^\infty du \text{Tr}(\alpha_{\text{eff}}(u) T_{\text{lr}}) - \frac{1}{4\pi} \int_0^\infty du \text{Tr}(\alpha_{\text{eff}}(u) T_{\text{eff}} \alpha_{\text{eff}}(u) T_{\text{lr}}) \\ & + \frac{1}{6\pi} \int_0^\infty du \text{Tr}(\alpha_{\text{eff}}(u) T_{\text{eff}} \alpha_{\text{eff}}(u) T_{\text{eff}} \alpha_{\text{eff}}(u) T_{\text{lr}}) - \dots \end{aligned} \quad (3.19)$$

The name “many-body” is best motivated in the coarse-grained models where the individual terms correspond to interactions between increasing number of fragments (bodies). (The order does not necessarily correspond to the number of bodies. At fourth order, for instance, some terms are a back-and-forth interaction between two bodies.) When constructed from the bare KS polarizability, the first term would evaluate to the long-range part of the exact exchange (plus higher-order exchange screening), which is negligible in nonuniform systems but can be relevant in uniform systems (where it would be typically covered by a semilocal XC functional). With any local approximation for the effective polarizability, the first term evaluates exactly to zero. The second term is the leading term for vdW interactions and the basis of all nonlocal correlation functionals and coarse-grained pairwise methods reviewed below. The third term corresponds to the Axilrod–Teller–Muto (ATM) three-body potential (Axilrod and Teller, 1943; Mutō, 1943) when coarse-grained to atoms.

When the  $\alpha_{\text{eff}} T_{\text{eff}}$  term in the logarithm is small enough, the series converges quickly, and the logarithm can be approximated well by a truncated expansion. While this is usually not the case for the total long-range XC energy of a system,  $T_{\text{eff}}$  is often small enough between the interacting subsystems, and if one is interested only in the interaction energy, the series can be often truncated already after the second order, because the higher-order terms cancel out. However, this is not the case in general, especially in strongly polarizable systems, or in lower-dimensional systems where  $\alpha_{\text{eff}} T_{\text{eff}}$  is highly anisotropic. The degree of approximation made by truncating the infinite logarithm series is difficult to assess a priori, and Chapter 5 shows an example of a system where the higher-order terms contribute substantially to interaction energies.

### 3.3.3 Kohn–Sham response and random-phase approximation

The approximations to the ACFD formula that are full many-body and not coarse-grained can be based on the bare KS response. Because the KS density response function

can be calculated directly from the KS orbitals (eq. 2.48), these approximations are usually formulated and evaluated in the  $\chi\nu$ -representation rather than the  $\alpha\mathbf{T}$ -representation. Furthermore, because the bare response has a well-defined short-range structure, this construction allows the evaluation of the total XC energy, not only its long-range part, so the use of these methods goes far beyond long-range correlation energy. Here, however, we discuss the methods mostly from the perspective of vdW interactions.

The simplest of these methods is the RPA, which translates into zero XC kernel in the formalism of the ACFD formula and TD-DFT (Ren et al., 2012). This corresponds to setting the effective polarizability to the bare KS polarizability, and the effective dipole operator to the full dipole operator,

$$E_c^{\text{RPA}} = \frac{1}{2\pi} \int_0^\infty du \text{Tr}_\mathbf{r} \left( \ln \left( 1 + \alpha(u; \lambda = 0) \mathbf{T} \right) - \alpha(u; \lambda = 0) \right) \quad (3.20)$$

In the  $\chi\nu$ -representation, the expression can be evaluated straightforwardly using the explicit expression for  $\chi(u; \lambda = 0)$  (Furche, 2001).

The omitted XC kernel is short-ranged in nonuniform systems, but its omission influences both short-range and long-range correlation energy, because the short-range XC effects in the polarizability eventually couple via the long-range dipole operator in the ACFD formula. As a result, although RPA does not suffer from any systematic errors in the long-range correlation energies, the overall accuracy is often worse than that of the many effective models reviewed below (Olsen and Thygesen, 2013b). This is further amplified in vdW systems in equilibrium geometries, where the short-range XC energy also contributes to the total interaction energy. Attempts at improvement go both ways, replacing the short-range correlation energy with a better model than RPA, as well as improving the effective polarizability.

Kurth and Perdew (1999) suggested to correct the short-range correlation energy from RPA with that from a semilocal XC functional, in what they called the RPA+ method. Rather than explicitly range-separating the ACFD expression, RPA+ removes the RPA short-range part by subtracting correlation energy from a specially designed semilocal correlation functional,  $E_c^{\text{GGA@RPA}}$ , and reintroduces it back with standard semilocal functional,  $E_c^{\text{GGA}}$ .

$$E_c^{\text{RPA+}} = E_c^{\text{RPA}} - E_c^{\text{GGA@RPA}} + E_c^{\text{GGA}} \quad (3.21)$$

$E_c^{\text{GGA@RPA}}$  is constructed in a similar way as standard functionals, but its uniform part is parameterized to reproduce the RPA energy of the electron gas rather than the true energy. In a later version, this was refined so that also the gradient correction satisfied the short-range behavior of RPA (Yan et al., 2000). RPA+ attempts to fix the short-range correlation energy of RPA, but the long-range part is unchanged, so the vdW force remains the same, and it is only the interaction due to electron-density overlap, which occurs at equilibrium, that can be possibly improved. Furthermore, the range separation in RPA+ is unsystematic in the sense that there is no guarantee that  $E_c^{\text{GGA@RPA}}$  and  $E_c^{\text{GGA}}$  have the same effective range.

(Toulouse et al., 2004) formulated a range-separated version of the KS scheme, in which the XC functional is designed from the beginning to treat only the short-range part of the electron correlation. This leads to an alternative range separation of the ACFD formula, in which  $\alpha(\lambda)$  is not the polarizability of the wave function that minimizes  $\langle \Psi | \hat{T} + \lambda \hat{V} | \Psi \rangle$ , but rather of one that minimizes  $\langle \Psi | \hat{T} + \lambda \hat{V}_{lr} | \Psi \rangle$  (Toulouse et al., 2009). In this scheme, the RPA of the Dyson-like equation results in a model in which the effective polarizability is still equal to the bare KS polarizability, like in normal RPA, but the effective dipole operator is only the long-range part of the full operator. The underlying assumption then is that the dipole operator and the XC kernel partially cancel out at short range, giving a different estimate of the effective polarizability than normal RPA. This is supported by numerical evidence on select small systems. A similar scheme, proposed earlier by Kohn et al. (1998), also uses a range-separated version of the KS scheme, but instead of obtaining the true polarizability at the RPA level,  $\chi(\lambda)$  is obtained for each  $\lambda$  by explicitly perturbing the corresponding  $\lambda$ -scaled system with electric field.

A straightforward way to improve the RPA is to devise approximate XC kernels, which improves the short-range behavior of the polarizability, and hence both short-range and long-range correlation energies. Extending the LDA to the time domain, the adiabatic LDA (ALDA) assumes that the XC kernel has no memory, leading to a frequency-independent local XC kernel,

$$\begin{aligned} f_{xc}^{\text{ALDA}}(\mathbf{r}, \mathbf{r}', t - t') &= \delta(t - t') \frac{\delta^2 E_{\text{xc}}^{\text{LDA}}[n]}{\delta n(\mathbf{r}) \delta n(\mathbf{r}')} = \delta(t - t') \delta(\mathbf{r} - \mathbf{r}') \frac{d^2(n \varepsilon_{\text{xc}}^{\text{UEG}}(n))}{dn^2} \Big|_{n=n(\mathbf{r}')} \\ f_{xc}^{\text{ALDA}}(\mathbf{r}, \mathbf{r}', u) &= \delta(\mathbf{r} - \mathbf{r}') \frac{d^2(n \varepsilon_{\text{xc}}^{\text{UEG}}(n))}{dn^2} \Big|_{n=n(\mathbf{r}')} \end{aligned} \quad (3.22)$$

Unlike LDA, which is exact for the uniform electron gas (UEG), ALDA does not give the true XC kernel of the UEG (which is nonlocal in both time and space), and violates several known properties of the true XC kernel. Despite that, it is a useful approximation in TD-DFT calculations when one is interested only in a certain range of the frequency spectra. Still, it turns out not to be a good approximation in the ACFD formula, where it give worse results than the absent XC kernel of the RPA (Lein et al., 2000).

Olsen and Thygesen (2012) constructed a correction to ALDA by fixing its large- $\mathbf{q}$  (short-range) behavior in the UEG to better reproduce the known exact behavior. Taking this renormalized ALDA (rALDA) kernel, transforming back to real space and using the mean density in two points as the corresponding uniform density, this procedure gives a universal XC kernel,

$$f_{xc}^{\text{rALDA}}(\mathbf{r}, \mathbf{r}', u) = f_{xc}^{\text{UEG}}(|\mathbf{r} - \mathbf{r}'|; n = \frac{1}{2}(n(\mathbf{r}) + n(\mathbf{r}')) \quad (3.23)$$

This construction is computationally no more demanding than RPA, but improves upon RPA in almost every case tested (Olsen and Thygesen, 2013a, 2014). The rALDA XC kernel

gives a more realistic short-range screening of the bare KS polarizability, resulting in more accurate long-range correlation energies and better description of vdW systems.

A different path towards improving the accuracy of RPA can be taken using the many-body perturbation (MBPT) theory. This is possible because, as Gell-Mann and Brueckner (1957) showed, yet another equivalent definition of RPA is via a certain subset of Feynman diagrams, the so-called ring diagrams. Summing different subsets of the diagrams similar to those corresponding to RPA then leads to different RPA-like models and sometimes confusing terminology, when a certain modification of the XC kernel in RPA is equivalent to adding additional terms to the RPA XC energy that do not seem to be related to RPA (Scuseria et al., 2008; Jansen et al., 2010; Ángyán et al., 2011).

The second-order Møller–Plesset correlation energy (MP2) consists of the Coulomb direct and exchange terms, of which only the former is long-ranged. In this context, RPA can be understood as the sum of all MP2-like direct terms (ring diagrams) in the infinite MBPT expansion. Similarly, the MP2 exchange can be renormalized by replacing one of the Coulomb interactions with the RPA sequence of ring diagrams, leading to the second-order screen exchange (SOSEX). Furthermore, unlike in the Møller–Plesset perturbation theory, where the first order is guaranteed to be zero, single-electron excitations contribute to the XC energy in the MBPT based on KS orbitals. Combining RPA, SOSEX and RPA-renormalized single-excitation correction then results in the renormalized second-order perturbation theory (rPT2) (Ren et al., 2011, 2013). Although the MP2 exchange term is short-ranged, the renormalization in SOSEX is long-ranged, and the long-range correlation energy of rPT2 is different from that of RPA. The combined improvements of the short-range and long-range XC energy in rPT2 compared to RPA lead to improved accuracy in vdW binding energies.

### 3.3.4 Nonlocal density functionals

The models of long-range correlation energy reviewed in this section are in the class of approximations to the ACFD formula that truncate the many-body expansion at second order, but do not do any spatial coarse-graining. This leads to XC functionals that are characterized by nonlocal dependence of the XC energy density on the electron density via some nonlocal kernel,  $\Phi$ ,

$$E_{c,lr}^{\text{nl-df}} = \frac{1}{2} \int d\mathbf{r} d\mathbf{r}' n(\mathbf{r}) n(\mathbf{r}') \Phi[n](\mathbf{r}, \mathbf{r}') = \int d\mathbf{r} n(\mathbf{r}) \int d\mathbf{r}' \frac{1}{2} n(\mathbf{r}') \Phi[n](\mathbf{r}, \mathbf{r}') \quad (3.24)$$

The derivation of (3.24) from the ACFD formula for the XC energy starts with truncating the logarithm expansion at second order,

$$E_{xc,lr} \approx \frac{1}{2\pi} \int_0^\infty du \text{Tr}_{\mathbf{r}, \mathbb{R}^3} \left( \boldsymbol{\alpha}_{\text{eff}}(u) \mathbf{T}_{lr} - \frac{1}{2} \boldsymbol{\alpha}_{\text{eff}}(u) \mathbf{T}_{\text{eff}} \boldsymbol{\alpha}_{\text{eff}}(u) \mathbf{T}_{lr} \right) \quad (3.25)$$

Here,  $\text{Tr}_{\mathbb{R}^3}$  denotes the trace over the three Cartesian vector components. In the next step, the effective polarizability is approximated with a local isotropic polarizability,

$$\alpha_{\text{eff}}(\mathbf{r}, \mathbf{r}', u) \approx \mathbf{I}\alpha_{\text{eff}}(\mathbf{r}, u)\delta(\mathbf{r} - \mathbf{r}') \quad (3.26)$$

This results in the first-order term being zero, which means that such a functional cannot capture any exchange energy, which is intentional, since the nonlocal functionals are designed to capture only the long-range correlation energy. The locality of the effective polarizabilities reduces two of the four integrals in the second-order term, and the isotropy allows to take the polarizabilities out of the trace,

$$\begin{aligned} E_{c,\text{lr}} &\approx -\frac{1}{4\pi} \int_0^\infty du \iint d\mathbf{r} d\mathbf{r}' \text{Tr}_{\mathbb{R}^3} (\alpha_{\text{eff}}(\mathbf{r}, u) \mathbf{T}_{\text{eff}}(\mathbf{r}, \mathbf{r}') \alpha_{\text{eff}}(\mathbf{r}', u) \mathbf{T}_{\text{lr}}(\mathbf{r}', \mathbf{r})) \\ &= -\frac{1}{4\pi} \int_0^\infty du \iint d\mathbf{r} d\mathbf{r}' \alpha_{\text{eff}}(\mathbf{r}, u) \alpha_{\text{eff}}(\mathbf{r}', u) \text{Tr}_{\mathbb{R}^3} (-\mathbf{T}_{\text{eff}}(\mathbf{r}, \mathbf{r}') \mathbf{T}_{\text{lr}}(\mathbf{r}, \mathbf{r}')) \end{aligned} \quad (3.27)$$

Both  $\mathbf{T}_{\text{eff}}$  and  $\mathbf{T}_{\text{lr}}$  go to the bare dipole operator for large distances, and the trace can be rewritten in terms of a range-separating function,  $f$ ,

$$\text{Tr}_{\mathbb{R}^3} (-\mathbf{T}_{\text{eff}}(\mathbf{r}, \mathbf{r}') \mathbf{T}_{\text{lr}}(\mathbf{r}, \mathbf{r}')) \equiv f(\mathbf{r}, \mathbf{r}') \frac{6}{|\mathbf{r} - \mathbf{r}'|^6} \quad (3.28)$$

This is the origin of the  $1/R^6$  dependence of the pairwise vdW force.

A general form of the local effective polarizability used in many models is obtained from the polarizability of a harmonic oscillator by setting the ratio of the charge and mass to that of an electron,  $q/m = 1$ , and substituting the electron density for the charge,

$$\alpha_{\text{tot}}^{\text{HO}}(iu) = \frac{q^2/m}{\omega^2 + u^2} \rightarrow \alpha_{\text{eff}}[n](\mathbf{r}, iu) = \frac{n(\mathbf{r})}{\omega_{\text{eff}}^2[n](\mathbf{r}) + u^2} \quad (3.29)$$

Besides the obvious reason of modeling electrons, the charge-mass ratio of one is motivated by the  $f$ -sum rule for an electronic system that dictates that  $\alpha_{\text{tot}}(iu) \rightarrow N/u^2$  ( $N$  is the number of electrons), which the form above automatically satisfies. (Strictly speaking, this is not necessary, because the rule does not need to be satisfied in any local form, and furthermore, the local effective polarizability is not supposed to integrate to the total polarizability without any long-range coupling. However, the local form is a straightforward way to satisfy the global rule.) The local effective resonance frequency,  $\omega_{\text{eff}}^2$ , can be in general any functional of the electron density, but is often approximated locally.

Combining (3.29), (3.28), and (3.27), the approximated ACFD formula can be recast in the form of a nonlocal density functional, where the nonlocal kernel is a functional of the effective resonance frequency and the (unspecified) range-separating function,

$$E_{c,\text{lr}} \approx \frac{1}{2} \iint d\mathbf{r} d\mathbf{r}' n(\mathbf{r}) n(\mathbf{r}') \left( -\frac{3}{\pi} \int_0^\infty du \frac{1}{\omega^2[n](\mathbf{r}) + u^2} \frac{1}{\omega^2[n](\mathbf{r}') + u^2} \frac{f(\mathbf{r}, \mathbf{r}')}{|\mathbf{r} - \mathbf{r}'|^6} \right) \quad (3.30)$$

The asymptotic behavior of the long-range correlation energy calculated in this way is fully specified by  $\omega_{\text{eff}}$ .

The first general functional of this form, referred to simply as the vdW density functional (vdW-DF), was developed by Dion et al. (2004) as a culmination of a program set up by Andersson, Langreth, and Lundqvist (1996). The program was followed along a different branch by Hult et al. (1996, 1999), but this effort did not result in a general functional of only the electron density. Although the derivation of the vdW-DF starts from the ACFD formula, it follows quite a different direction than the framework in this chapter, and most of the approximations along the way are done in reciprocal space, until everything is transformed back to real space in the end. However, the final result can still be cast in the form of (3.30).

The effective resonance frequency in the vdW-DF is constructed from a GGA-type XC energy density,

$$\omega_{\text{vdW-DF}}^2[n](\mathbf{r}) = 4\pi^2 \varepsilon_{\text{xc}}^{\text{vdW-DF}}[n]^4 = 4\pi^2 \left( \varepsilon_{\text{xc}}^{\text{UEG}}(n) + A \left| \frac{\nabla n}{n^{7/6}} \right|^2 \right)^4 \quad (3.31)$$

The first equality is motivated by using  $\omega_{\text{eff}}^2$  to calculate the XC energy of a slowly varying electron gas via the ACFD formula. The particular choice of the semilocal approximation to the XC energy density is rather arbitrary and completely independent of the semilocal functional potentially used to complete the vdW-DF at short range. The value of the numerical parameter  $A$  can be derived in different ways using different first-principles arguments, leading to substantially different values and results for vdW binding energies (Lee et al., 2010).

A serious disadvantage of the vdW-DF in light of other long-range correlation models is that its range-separating function is fixed by the underlying theory. Because of the construction in the reciprocal space, the parameter  $A$  appears both in the effective resonance frequency and the range-separating function. Since the asymptotic behavior of any nonlocal functional depends only on  $\omega_{\text{eff}}$ , not the range-separating function, the parameter  $A$  is essentially fixed, and there is no remaining freedom in the range-separating function that could be adjusted for a particular choice of a short-range semilocal functional in a full KS-DFT calculation.

The form of the range-separating function is complex due to the reciprocal-space formulation, but there are two underlying physical motivations for it. When the two oscillators given by the resonance frequencies  $\omega_{\text{eff}}$  are close to each other such that their ground-state wave functions would overlap, the underlying model does not work anymore, the corresponding part of the XC energy must be covered by the semilocal functional, and the dipole coupling must be damped. This is effectively achieved by increasing the resonance frequency as  $k^2$  in the reciprocal space. The second damping mechanism is that the nonlocal functional must evaluate to zero for the uniform electron gas, whose long-range correlation energy is already covered by a semilocal or a hybrid functional. This

forces the range-separating function to negative values at short range, to counterbalance the attractive contribution from the long range.

The complex form of the vdW-DF was gradually simplified by Vydrov and Van Voorhis. In the vdW-DF-09 (Vydrov and Van Voorhis, 2009), the range-separating mechanism was constructed independently of the effective resonance, making the nonlocal functional adaptable to any semilocal or hybrid functional, which also resulted in improved accuracy for vdW binding energies. Furthermore, the local resonance frequency was somewhat modified,

$$\omega_{\text{vdW-DF-09}}^2[n](\mathbf{r}) = (4\pi)^2 \underbrace{\frac{4^3\pi^2}{3^6}}_{\approx 0.87} \left( \epsilon_x^{\text{UEG}}(n) + B \left| \frac{\nabla n}{n^{2/3}} \right|^2 \right)^4 \quad (3.32)$$

Further simplification was achieved in the VV09 functional, which used a substantially different form of  $\omega_{\text{eff}}$ ,

$$\omega_{\text{VV09}}^2[n](\mathbf{r}) = \frac{4\pi}{3} n(\mathbf{r}) + C \frac{|\nabla n|^4}{n^4} \quad (3.33)$$

Here,  $4\pi n$  is the resonance frequency of the macroscopic (small- $\mathbf{q}$  limit) plasmon fluctuations of the uniform electron gas. The factor of  $1/3$  comes from the Clausius–Mossotti relation between the microscopic local polarizability and the macroscopic dielectric function. The density-gradient term is a local model of a band gap obtained from considering the behavior of the electron density in the density tail of a finite system. The range-separating mechanism of VV09 is still constructed in reciprocal space.

The final attempt at a simplified formulation of the vdW-DF, named VV10, was constructed entirely in real space (Vydrov and Van Voorhis, 2010). Both the resonance frequency and range-separating function of (3.30) have a simple form in VV10. The former is the same as in VV09, and the latter is constructed using the same mechanism of reduced polarizabilities of overlapped oscillators as in the original vdW-DF, but in real space,

$$f_{\text{VV10}}(\mathbf{r}, \mathbf{r}') = \frac{\alpha_{\text{eff}}(\mathbf{r}, iu; \omega = \omega_{\text{VV09}} + D n^{1/3}/|\mathbf{r} - \mathbf{r}'|^2) \alpha_{\text{eff}}(\mathbf{r}', iu; \omega = \omega_{\text{VV09}} + D n^{1/3}/|\mathbf{r} - \mathbf{r}'|^2)}{\alpha_{\text{eff}}(\mathbf{r}', iu; \omega = \omega_{\text{VV09}}) \alpha_{\text{eff}}(\mathbf{r}', iu; \omega = \omega_{\text{VV09}})} \quad (3.34)$$

As  $1/|\mathbf{r} - \mathbf{r}'|^2$  grows at short distances, the effective resonance frequency of the local oscillators increases, reducing their polarizability. The parameter  $D$  is used to adjust the range of this mechanism.

### 3.3.5 Pairwise interatomic models

The oldest approaches to fix the missing long-range electron correlation in HF or semilocal KS-DFT calculations are of the interatomic pairwise form,

$$E_{\text{c,lr}} \approx -\frac{1}{2} \sum_{pq} C_{6,pq} \frac{f(\mathbf{R}_p, \mathbf{R}_q)}{|\mathbf{R}_p - \mathbf{R}_q|^6} \quad (3.35)$$

Here,  $f$  is some range-separating (damping) function,  $\mathbf{R}_q$  are the atom coordinates, and the so-called dispersion coefficients,  $C_{6,pq}$ , determine the asymptotic interaction between two atoms. This type of interatomic potential has origin in empirical force fields dating back to the Lennard–Jones potential, even before it was clear that the correct leading term of the vdW force is  $1/R^6$ . In the context of electronic-structure methods, it was first used by Hepburn et al. (1975) to correct interaction curves of rare-gas dimers from HF calculations. This approach was later extended to molecules and KS-DFT calculations, and the  $C_6$  coefficients were extended to a wider range of systems (Halgren, 1992; Mooij et al., 1999; Elstner et al., 2001; Wu and Yang, 2002). Grimme (2004) then presented a parametrization of  $C_6$  and  $f$ , termed DFT-D ('D' for dispersion), that could in principle be applied to any molecule or solid, in combination with any XC functional. This marked a start of routine addition of the long-range correlation energy to semilocal KS-DFT calculations.

The pairwise interatomic model of (3.35) can be obtained as a coarse-grained truncated approximation to the ACFD formula. The derivation follows the same course of second-order truncation and local approximation to the effective polarizability as nonlocal vdW XC functionals, but starting from the coarse-grained multipole-expanded ACFD formula in (3.18),

$$E_{c,lr} \approx \frac{1}{4\pi} \int_0^\infty du \text{Tr}_{p,lm} (\alpha_{\text{eff}}(iu) \mathbf{T}_{\text{eff}} \alpha_{\text{eff}}(iu) \mathbf{T}_{lr}) \quad (3.36)$$

Here, the trace is over multipole moments and fragments, which are chosen to be atoms in most cases. (In this context, the formal definition of an atom in a molecule is given by some partition function.) Approximating the local effective polarizability as isotropic,  $\alpha_{\text{eff},pll'mm'} = \delta_{ll'} \delta_{mm'} \alpha_{\text{eff},pl}$ , the formula is reduced as in the case of nonlocal vdW XC functionals,

$$\begin{aligned} E_{c,lr} &\approx \frac{1}{4\pi} \int_0^\infty du \sum_{pq} \sum_{ll'} \alpha_{\text{eff},pl}(iu) \alpha_{\text{eff},ql'}(iu) [\text{Tr}_m(\mathbf{T}_{\text{eff}} \mathbf{T}_{lr})]_{pq, ll'} \\ &= -\frac{1}{2} \sum_{pq} \sum_{ll'} \left( \frac{K_{ll'}}{2\pi} \int_0^\infty du \alpha_{\text{eff},pl}(iu) \alpha_{\text{eff},ql'}(iu) \right) \frac{f_{ll'}(\mathbf{R}_p, \mathbf{R}_q)}{|\mathbf{R}_p - \mathbf{R}_q|^{2+2l+2l'}} \end{aligned} \quad (3.37)$$

$$\begin{aligned} &\equiv -\frac{1}{2} \sum_{pq} \sum_{ll'} C_{2+2l+2l', pq} \frac{f_{ll'}(\mathbf{R}_p, \mathbf{R}_q)}{|\mathbf{R}_p - \mathbf{R}_q|^{2+2l+2l'}} \\ K_{ll'} &= \lim_{\mathbf{R} \rightarrow \infty} \frac{\sum_m T_{ll'mm}(\mathbf{R})}{|\mathbf{R}|^{2+2l+2l'}} \end{aligned} \quad (3.38)$$

The standard pairwise formula of (3.35) is recovered by keeping only the lowest dipole-dipole term ( $l = l' = 1, K_{11} = 6$ ), where the expression for the corresponding dispersion coefficient is called the Casimir–Polder integral,

$$C_{6,pq} = \frac{3}{\pi} \int_0^\infty du \alpha_{\text{eff},pl}(iu) \alpha_{\text{eff},ql}(iu) \quad (3.39)$$

Some pairwise methods are formulated directly in terms of the dispersion coefficients, not the underlying polarizabilities, in which case approximate combination rules for calculating unknown heteronuclear coefficients from known homonuclear coefficients are useful. Such rules can be derived from the Casimir–Polder integral using some model polarizability. An often used rule is obtained from the harmonic-oscillator model,

$$\begin{aligned} C_{6,pq}^{\text{HO}} &= \frac{3}{\pi} \int_0^\infty du \frac{\alpha_p(0)\omega_p^2}{\omega_p^2 + u^2} \frac{\alpha_q(0)\omega_q^2}{\omega_q^2 + u^2} = \frac{3\alpha_p(0)\alpha_q(0)\omega_p\omega_q}{2(\omega_p + \omega_q)} \\ &= \frac{2C_{6,pp}C_{6,qq}}{C_{6,pp}\frac{\alpha_q(0)}{\alpha_p(0)} + C_{6,qq}\frac{\alpha_p(0)}{\alpha_q(0)}} \end{aligned} \quad (3.40)$$

Using the single-pole polarizability of the harmonic oscillator in situations where the true spectrum is more complex, such as in the equation above, is called the [Unsöld \(1927\)](#) approximation.

The models of Grimme are different from the rest reviewed in this section in that they are formulated only in terms of the geometry of a molecule,  $\{\mathbf{R}_p\}$ , not the electron density. This makes them straightforwardly useful even for empirical short-range electronic models that do not produce any electronic density, but at the same time, it makes it much harder to achieve truly general models, because the electron density encodes much useful information about the system.

The first version of DFT-D used fixed homonuclear  $C_6$  coefficients, the combination of (3.40) with all polarizability ratios set to 1, and a range-separating function constructed from vdW radii that did not go to 1 in infinity ([Grimme, 2004](#)). The second version was a numerical reparametrization of the first one with a changed combination rule, which set the polarizability ratios equal to those of the  $C_6$  coefficients ([Grimme, 2006](#)). In the first and second version, the atomic  $C_6$  coefficients do not depend on the molecular environment, which is a crude approximation. The third version was an improvement in several regards ([Grimme et al., 2010](#)). The range separation was modified to obey the correct asymptotic behavior. An elementary dependence of the  $C_6$  coefficients on the environment was included via geometrical factors estimating the coordination number of an atom. The dipole–quadrupole term ( $l = 1, l' = 2$ ) from (3.37) was included, and a three-atom correction was suggested, which is the third-order triple-dipole term in the logarithm expansion of the coarse-grained ACFD formula. The corresponding dispersion coefficients,  $C_8$  and  $C_9$ , are obtained by combination rules similar to those for the  $C_6$  coefficient.

Soon after the first version of DFT-D and in stark contrast to it, [Becke and Johnson \(2005b\)](#) developed a method to calculate  $C_6$  coefficients from first principles, using an approximation to the polarizability based on the dipole moment of the XC hole of the HF model, the exchange-hold dipole method (XDM). Their initial derivation was rather heuristic, with a wrong prefactor, but the final result can be in fact obtained directly from

the Casimir–Polder integral using the fluctuation–dissipation theorem for the density response function of (2.32) and the Unsöld approximation:

$$\begin{aligned}
C_6 &= \frac{3}{\pi} \int_0^\infty du \alpha_{\text{tot}}(iu)^2 \approx \frac{3}{\pi} \int_0^\infty du \left( \frac{\alpha_{\text{tot}}(0)}{1+u^2/\omega^2} \right)^2 = \frac{3}{4} \alpha_{\text{tot}}(0)^2 \omega \\
&= \frac{1}{2} \alpha_{\text{tot}}(0) \frac{3}{\pi} \int_0^\infty du \frac{\alpha_{\text{tot}}(0)}{1+u^2/\omega^2} = \frac{1}{2} \alpha_{\text{tot}}(0) \frac{3}{\pi} \int_0^\infty du \alpha_{\text{tot}}(iu) \\
&= \frac{1}{2} \alpha_{\text{tot}}(0) \frac{1}{\pi} \int_0^\infty du \text{Tr}_{\mathbb{R}^3} (\alpha_{\text{tot}}(iu)) \\
&= \frac{1}{2} \alpha_{\text{tot}}(0) \frac{1}{\pi} \int_0^\infty du \iint d\mathbf{r} d\mathbf{r}' \text{Tr}_{\mathbb{R}^3} (\alpha(\mathbf{r}, \mathbf{r}', iu)) \\
&= \frac{1}{2} \alpha_{\text{tot}}(0) \iint d\mathbf{r} d\mathbf{r}' \text{Tr}_{\mathbb{R}^3} (-\mathbf{r} \otimes \mathbf{r}' \frac{1}{\pi} \int_0^\infty \chi(\mathbf{r}, \mathbf{r}', iu)) \\
&= \frac{1}{2} \alpha_{\text{tot}}(0) \iint d\mathbf{r} d\mathbf{r}' \mathbf{r} \cdot \mathbf{r}' n(\mathbf{r}) (n_{\text{xc}}(\mathbf{r}, \mathbf{r}') + \delta(\mathbf{r} - \mathbf{r}')) \\
&= \frac{1}{2} \alpha_{\text{tot}}(0) \int d\mathbf{r} \left( \mathbf{r} n(\mathbf{r}) \cdot \int d\mathbf{r}' \mathbf{r}' (n_{\text{xc}}(\mathbf{r}, \mathbf{r}') + \delta(\mathbf{r} - \mathbf{r}')) \right) \\
&\equiv \frac{1}{2} \alpha_{\text{tot}}(0) \int d\mathbf{r} \mathbf{d}_n(\mathbf{r}) \cdot \mathbf{d}_{\text{xc}}(\mathbf{r})
\end{aligned} \tag{3.41}$$

Here, the  $C_6$  coefficient is expressed in terms of the static polarizability and the correlation between the local dipole moment of the total density and of the XC hole with its reference electron. This expression provides accurate  $C_6$  coefficients when provided with accurate correlated XC holes, but fails short of good accuracy when evaluated with the approximate XC hole from the HF model (Ángyán, 2007). The XDM uses a slightly modified expression that autocorrelates the XC hole dipole moment,

$$C_6 \approx \frac{1}{2} \alpha_{\text{tot}}(0) \int d\mathbf{r} \mathbf{d}_{\text{xc}}(\mathbf{r}) \cdot \mathbf{d}_{\text{xc}}(\mathbf{r}) \tag{3.42}$$

This version works remarkably well with the HF XC hole, but the reasons for this unexpected accuracy are not well understood (Ángyán, 2007; Heßelmann, 2009; Ayers, 2009). A semilocal approximation to the XC hole by Becke and Roussel (1989) works as well as that from the HF model, and with the additional benefit of reduced computational complexity (Becke and Johnson, 2005a).

To formulate a general interatomic pairwise method, the dipole moment of the XC hole is coarse-grained using the partitioning scheme devised by Hirshfeld (1977). In this scheme, the atomic partition functions,  $w_p$ , are constructed from radially averaged electron densities of isolated atoms,  $n^{\text{free}}$ ,

$$w_p^{\text{Hirsh}}(\mathbf{r}) = \frac{n_p^{\text{free}}(|\mathbf{r} - \mathbf{R}_p|)}{\sum_q n_q^{\text{free}}(|\mathbf{r} - \mathbf{R}_q|)} \tag{3.43}$$

The corresponding static dipole polarizabilities of the atomic fragments are calculated from free-atom dipole polarizabilities, assuming that they scale linearly with the Hirshfeld measure of a volume (Hirshfeld volume),

$$\alpha_{p1}(0) = \alpha_{p1}^{\text{free}}(0) \frac{V_p^{\text{Hirsh}}[n]}{V_p^{\text{Hirsh}}[n^{\text{free}}]} \quad (3.44)$$

$$V_p^{\text{Hirsh}}[n] = \int d\mathbf{r} n(\mathbf{r}) w_p^{\text{Hirsh}}(\mathbf{r}) |\mathbf{r} - \mathbf{R}_p|^3 \quad (3.45)$$

The fragment  $C_6$  coefficients are then calculated from the fragment polarizabilities and coarse-grained XC hole dipole moment,

$$C_{6,pp}^{\text{XDM}} = \frac{1}{2} \alpha_{p1}(0) \int d\mathbf{r} w_p(\mathbf{r}) \mathbf{d}_{\text{xc}}(\mathbf{r}) \cdot \mathbf{d}_{\text{xc}}(\mathbf{r}) \quad (3.46)$$

The harmonic-oscillator combination rule is used to get the rest of the  $C_6$  coefficients. The XDM can be extended to higher-multipole dispersion coefficients by calculating higher multipole moments of the XC hole polarization around each atomic center (Becke and Johnson, 2006; Johnson and Becke, 2006).

The XDM dispersion coefficients were paired with two distinct empirical suggestions for the range-separating function, one based on the ratio of approximate short-range and long-range correlation energies, the other on the vdW radii (Becke and Johnson, 2007),

$$f_{11}^{\text{XDM1}}(\mathbf{R}_p, \mathbf{R}_q) = \left( 1 + A \left( \frac{C_{6,pq}/|\mathbf{R}_p - \mathbf{R}_q|^6}{E_{c,p}^{\text{free}} + E_{c,q}^{\text{free}}} \right) \right)^{-1} \quad (3.47)$$

$$f_{11}^{\text{XDM2}}(\mathbf{R}_p, \mathbf{R}_q) = \left( 1 + A \left( \frac{R_{\text{vdW},p} + R_{\text{vdW},q} + B}{|\mathbf{R}_p - \mathbf{R}_q|} \right)^6 \right)^{-1} \quad (3.48)$$

Here,  $E_{c,p}^{\text{free}}$  is the correlation energy of a free atom calculated with some semilocal correlation functional.

A simple yet accurate interatomic pairwise method was developed by Tkatchenko and Scheffler (2009) (TS), who extended the free-atom scaling approach to all the atomic parameters, including the  $C_6$  coefficients and the vdW radii, and thus formulating the calculation of interatomic pairwise vdW interactions into a true density functional. Assuming that the excitation energies of the atoms are independent of the volume, the Unsöld approximation and the Casimir–Polder integral dictate that the  $C_6$  coefficients scale with the second power of the Hirshfeld volume ratio,

$$C_{6,pq} = C_{6,pq}^{\text{free}} \left( \frac{V_p^{\text{Hirsh}}[n]}{V_p^{\text{Hirsh}}[n^{\text{free}}]} \right)^2 \quad (3.49)$$

The free-atom reference values may not be the most effective choice in metals and some solids, whose electron density is often substantially different from the superposition of

free-atom densities. Zhang et al. (2011) and Ruiz et al. (2012) used an adapted TS method, where the reference values are obtained from bulk macroscopic dielectric constant. The TS method uses a logistic function as a range-separating function, with the free-atom vdW radii naturally scaled by the cubic root of the Hirshfeld-volume ratio,

$$f_{II}^{\text{TS}}(\mathbf{R}_p, \mathbf{R}_q) = \left( 1 + \exp \left[ -A \left( B \frac{|\mathbf{R}_p - \mathbf{R}_q|}{R_{\text{vdw},p} + R_{\text{vdw},q}} - 1 \right) \right] \right)^{-1} \quad (3.50)$$

Sato and Nakai (2009, 2010) developed an atomic pairwise method based on the local effective polarizability functional from the vdW-DF-09 nonlocal functional. Their local response dispersion (LRD) method is an explicit realization of the coarse-graining approach outlined in Section 3.3.1. A system is described by the local effective polarizability given by the harmonic-oscillator formula with the resonance frequency from (3.32). The atomic fragments are defined using the partitioning functions from the scheme by Becke (1988), which is most often used to define atomic radial grids in KS-DFT calculations, but here it is used as an alternative to the Hirshfeld partitioning. The partitioned polarizability is used to calculate a coarse-grained representation of the system via multipole expansion and Casimir–Polder integrals up to the  $C_{10}$  coefficient. The LRD method uses yet another range-separating function, parametrized by the polarizabilities in place of the vdW radii,

$$f_{II}^{\text{LRD}}(\mathbf{R}_p, \mathbf{R}_q) = \exp \left( - \left( \frac{|\mathbf{R}_p - \mathbf{R}_q|}{A(\sqrt[3]{\alpha_{\text{eff},p}} + \sqrt[3]{\alpha_{\text{eff},q}}) + B} \right)^6 \right) \quad (3.51)$$

Silvestrelli (2008) formulated a pairwise method in which the coarse-grained fragments are not atoms, but Wannier functions (WFs) (Marzari et al., 2012). Wannier functions are any set of localized one-electron wave functions that in principle form a complete basis. In finite molecular systems, they are called Boys orbitals. The Wannier functions of conducting and nonconducting electrons are localized algebraically and exponentially, respectively. In the vdW-WF method, each WF is approximated with a single spherically symmetric exponential function that has the same width (second central moment) as the true WF. The polarizability of the approximate WF is calculated with the polarizability functional of Andersson, Langreth, and Lundqvist (1996) (ALL),

$$\alpha_{\text{eff},p}(iu) = \int_{\mathbf{r} \in \Omega_A} d\mathbf{r} \frac{n_p(\mathbf{r})}{4\pi n_p(\mathbf{r}) + u^2}, \quad \Omega_A = \{ \mathbf{r} : |\nabla n_p(\mathbf{r})| < k n_p(\mathbf{r})^{7/6} \} \quad (3.52)$$

Here,  $n_p$  is the electron density of the WF and  $k$  is a nonempirical constant. The  $C_6$  coefficients between the WFs are calculated from the Casimir–Polder integral, and the range-separating function is the same as in the TS method, with vdW radii of the WFs defined via an electron density cutoff (Silvestrelli et al., 2009). The vdW-WF scheme has two theoretical shortcomings: first, the partitioning of the total electron density

is only approximate because of the use of the approximate WFs, and second, the ALL polarizability functional was designed for the total electron density, not one-electron densities.

Coarse-grained methods in which the fragment polarizabilities and  $C_6$  coefficients are calculated directly, rather than obtained by explicit partitioning of some continuous quantity, may be sensitive to a particular choice of the partitioning scheme. This motivated a series of modified Hirshfeld partitioning schemes that should capture better the redistribution of the electron density in a molecule with respect to free atoms. Steinmann and Corminboeuf (2010, 2011) adapted the XDM to use the self-consistent Hirshfeld scheme, which gives a more consistent description of ionic systems (Bultinck et al., 2007). Bučko et al. (2013, 2014) did the same with the TS method. The self-consistent Hirshfeld partitioning uses the same stockholder formula in (3.43) as the original scheme, but the reference densities are generalized and depend recursively on the partitioning, leading to equations that need to be solved iteratively (Verstraelen et al., 2012). A common form of the generalized reference densities, used in the modified XDM and TS methods, is a linear combination of free-atom and free-ion densities that maintains the charge of the Hirshfeld-partitioned atomic density. This scheme is complicated by the instability of many isolated anions, which requires addition of auxiliary negative charges, making the partitioning somewhat arbitrary.

### 3.3.6 Many-body dispersion framework

The fourth and final class of approximations to the ACFD formula covers nontruncated coarse-grained models. A common theme of all such models is to interpret the Unsöld approximation with its single resonance frequency literally, and model a real molecular system as a collection of coupled charged oscillators. The corresponding Hamiltonian describes a system of distinguishable particles characterized by a charge,  $q_i$ , and a mass,  $m_i$ , each having its own harmonic potential defined by the resonance frequency,  $\omega_i$ , and a center,  $\mathbf{R}_i$ , interacting via the Coulomb force,

$$\hat{H}_{\text{osc}} = \sum_i \frac{\hat{\mathbf{p}}_i^2}{2} + \sum_i \frac{1}{2} m_i \omega_i^2 |\hat{\mathbf{r}}_i - \mathbf{R}_i|^2 + \sum_{i < j} q_i q_j \left( \frac{1}{|\hat{\mathbf{r}}_i - \hat{\mathbf{r}}_j|} - \frac{1}{|\hat{\mathbf{r}}_i - \mathbf{R}_j|} - \frac{1}{|\mathbf{R}_i - \hat{\mathbf{r}}_j|} + \frac{1}{|\mathbf{R}_i - \mathbf{R}_j|} \right) \quad (3.53)$$

The centers of the harmonic potentials additionally host a compensating charge of the opposite sign. If the centers are the same as those of the atoms, this Hamiltonian can be interpreted as a very crude approximation to the electronic Hamiltonian, in which all electrons of individual atoms are described by distinguishable pseudoelectrons that move in an effective potential which is the combined result of the nuclear potential and the mean field of the electrons. In particular, any exchange effects and hence charge transfer

and delocalization are scrapped. Expanding the Coulomb operator in a multipole series and keeping only the dipole term results in dipole-coupled oscillator Hamiltonian,

$$\hat{H}_{\text{dosc}} = \sum_i \frac{\hat{\mathbf{p}}_i^2}{2} + \sum_i \frac{1}{2} m_i \omega_i^2 |\hat{\mathbf{r}}_i - \mathbf{R}_i|^2 + \sum_{i < j} q_i q_j (\hat{\mathbf{r}}_i - \mathbf{R}_i) \mathbf{T} (\mathbf{R}_j - \mathbf{R}_i) (\hat{\mathbf{r}}_j - \mathbf{R}_j) \quad (3.54)$$

A useful property of this Hamiltonian is that it can be solved exactly by coordinate transformation. Introducing mass-scaled coordinates,  $\hat{\xi}_i = \sqrt{m_i} (\hat{\mathbf{r}}_i - \mathbf{R}_i)$ ,  $\hat{\boldsymbol{\xi}} = (\hat{\xi}_1 \hat{\xi}_2 \dots)$ , using the expression for the polarizability of a charged harmonic oscillator in (3.13), and the fact that the kinetic-energy operator is invariant with respect to unitary transformations, the dipole-coupled Hamiltonian can be transformed into uncoupled quasi oscillators,

$$\begin{aligned} \hat{H}_{\text{dosc}} &= \sum_i \frac{\hat{\mathbf{p}}_i^2}{2} + \sum_i \frac{1}{2} \omega_i^2 \hat{\xi}_i^2 + \frac{1}{2} \sum_{ij} \omega_i \omega_j \sqrt{\alpha_i(0) \alpha_j(0)} \hat{\xi}_i \mathbf{T}_{ij} \hat{\xi}_j \\ &\equiv \sum_i \frac{\hat{\mathbf{p}}_i^2}{2} + \frac{1}{2} \hat{\boldsymbol{\xi}} \mathbf{Q}(\boldsymbol{\alpha}(0), \boldsymbol{\omega}, \mathbf{T}) \hat{\boldsymbol{\xi}} \\ &= \sum_i \frac{\hat{\mathbf{p}}_i'^2}{2} + \frac{1}{2} \hat{\boldsymbol{\xi}}' \tilde{\boldsymbol{\omega}}^2 \hat{\boldsymbol{\xi}}' \\ &= \sum_{n=1}^{3N} \left( \frac{\hat{p}_n'^2}{2} + \frac{1}{2} \tilde{\omega}_n^2 \hat{\xi}_n'^2 \right) \end{aligned} \quad (3.55)$$

Here,  $\tilde{\omega}_n^2$  are eigenvalues of the real symmetric matrix  $\mathbf{Q}$ ,  $\mathbf{Q} = \mathbf{V} \tilde{\boldsymbol{\omega}}^2 \mathbf{V}^T$ , and  $\hat{\boldsymbol{\xi}}'$  are the coupled coordinates,  $\hat{\boldsymbol{\xi}}' = \mathbf{V}^T \hat{\boldsymbol{\xi}}$ , which describe different collective oscillations. The ground-state wave function of this system is then a simple product of the single-oscillator ground-state wave functions, and the ground-state energy is a sum of the single-oscillator ground-state energies,  $E_0 = \sum_n \tilde{\omega}_n / 2$ . Drawing analogy with the RPA, the individual oscillators model the particle-like quasi electrons in some coarse-grained way, while the coupled oscillations model the wave-like electron oscillations. This Hamiltonian has been used many times to obtain various qualitative properties of long-range electron correlation (Bade, 1957; Bade and Kirkwood, 1957; Mahan, 1965; Lucas, 1967; Renne and Nijboer, 1967; Donchev, 2006), but only recently to formulate general quantitative methods.

The relevance of the dipole-coupled oscillator model to the true electronic system can be derived directly from the coarse-grained ACFD formula in (3.18). Assuming that the effective and long-range dipole operators are equal,  $\mathbf{T}_{\text{lr}} = \mathbf{T}_{\text{eff}}$ , using the Unsöld and local approximations for the effective frequency,  $\boldsymbol{\alpha}_{\text{eff}}(iu) = \boldsymbol{\alpha}(0)/(1 + u^2/\boldsymbol{\omega}^2)$ , and truncating the multipole expansion at  $L$ -th order, the integration over frequencies can be performed analytically (Tkatchenko et al., 2013),

$$E_{\text{c,lr}} \approx \frac{1}{2\pi} \int_0^\infty du \text{Tr}_{p,\mathbb{R}^3} \left( \ln(1 + \boldsymbol{\alpha}_{\text{eff}}(iu) \mathbf{T}_{\text{lr}}) \right)$$

$$\begin{aligned}
&= \frac{1}{2\pi} \int_0^\infty du \operatorname{Tr}_{p,\mathbb{R}^3} \left( \ln \left( \frac{\boldsymbol{\omega}^2 + \boldsymbol{\alpha}_{\text{eff}}(0)^{\frac{1}{2}} \boldsymbol{\omega} \mathbf{T}_{\text{lr}} \boldsymbol{\alpha}_{\text{eff}}(0)^{\frac{1}{2}} \boldsymbol{\omega} + u^2}{\boldsymbol{\omega}^2 + u^2} \right) \right) \\
&= \frac{1}{2\pi} \int_0^\infty du \operatorname{Tr}_{p,\mathbb{R}^3} \left( \ln (\mathbf{Q}(\boldsymbol{\alpha}_{\text{eff}}(0), \boldsymbol{\omega}, \mathbf{T}_{\text{lr}}) + u^2) - \ln(\boldsymbol{\omega}^2 + u^2) \right) \\
&= \frac{1}{2\pi} \int_0^\infty du \operatorname{Tr}_{p,\mathbb{R}^3} \left( \ln(\tilde{\boldsymbol{\omega}}^2 + u^2) - \ln(\boldsymbol{\omega}^2 + u^2) \right) = \sum_{n=1}^{3N} \frac{1}{2\pi} \int_0^\infty du \ln \left( \frac{\tilde{\omega}_n^2 + u^2}{\omega_n^2 + u^2} \right) \\
&= \sum_{n=1}^{L(L+2)N} \frac{\tilde{\omega}_n}{2} - \sum_{l=1}^L \sum_{p=1}^N (2l+1) \frac{\omega_p}{2} \quad (3.56)
\end{aligned}$$

When truncated at the dipole term ( $L = 1$ ), the matrix  $\mathbf{Q}$  is identical to that in (3.55), and the approximate long-range correlation energy is equal to the difference in the ground-state energy between the dipole-coupled oscillators and noninteracting oscillators.

The exact equivalence between the dipole-coupled oscillators and the approximated ACFD formula breaks when going beyond the dipole approximation. The effective Hamiltonian that corresponds to the matrix  $\mathbf{Q}$  truncated at  $L$ -th multipole order has  $L(L+2)N$  independent coordinates,  $\xi$ , each with a corresponding resonance frequency and polarizability, and the analytic integration over frequency can be performed for any  $L$ . In contrast, the coupled-oscillator Hamiltonian has always  $3N$  coordinates, independent of the degree of the multipole expansion of the Coulomb operator, and the interaction terms above the dipole order are formed from nonlinear combinations of the coordinates, making the Hamiltonian unsolvable in closed form.

Use of the coupled-dipole approach to formulate general methods for the long-range correlation energy was initiated in the many-body dispersion (MBD) model developed by Tkatchenko et al. (2012). MBD reuses the effective dynamic polarizability as approximated in the TS pairwise method and combines it with a physically motivated effective dipole operator. Motivated by the Gaussian shape of the harmonic-oscillator ground-state wave function,  $\mathbf{T}_{\text{eff}}$  in MBD is derived from the screened Coulomb interaction between two Gaussian unit-charge densities with widths  $\sigma, \sigma'$  (Mayer, 2007),

$$\nu_{gg}(|\mathbf{R}|) = \frac{1}{(\pi\sigma\sigma')^3} \iint d\mathbf{r} d\mathbf{r}' \frac{e^{-\frac{|\mathbf{r}|^2}{\sigma^2}} e^{-\frac{|\mathbf{r}'-\mathbf{R}|^2}{\sigma'^2}}}{|\mathbf{r}-\mathbf{r}'|} = \operatorname{erf} \left( \frac{|\mathbf{R}|}{\sqrt{\sigma^2 + \sigma'^2}} \right) \frac{1}{|\mathbf{R}|} \quad (3.57)$$

$$\mathbf{T}_{gg}(\mathbf{R}) = \nabla \otimes \nabla' \nu_{gg}(|\mathbf{r}-\mathbf{r}'|) \Big|_{\substack{\mathbf{r}=\mathbf{R} \\ \mathbf{r}'=0}} \quad (3.58)$$

When used as  $\mathbf{T}_{\text{eff}}$  in MBD, the widths are derived from the corresponding dipole polarizabilities, making the effective dipole operator frequency-dependent,

$$\sigma_p(u) = \left( \frac{1}{3} \sqrt{\frac{\pi}{2}} \alpha_{\text{eff},pl}(iu) \right)^{\frac{1}{3}} \quad (3.59)$$

In general,  $\mathbf{T}_{\text{lr}} \neq \mathbf{T}_{\text{eff}}$ , and the frequency integral cannot be evaluated analytically as shown above. To circumvent this obstacle, Ambrosetti et al. (2014) separated  $\mathbf{T}_{gg}$  further

into the long-range part and the short-ranged remainder,

$$\mathbf{T}_{\text{gg}}(u) = (\mathbf{T}_{\text{gg}}(u) - \mathbf{T}_{\text{lr}}) + \mathbf{T}_{\text{lr}} \equiv \mathbf{T}_{\text{sr}}(u) + \mathbf{T}_{\text{lr}} \quad (3.60)$$

The long-range correlation energy is then calculated in two steps. First, the effective polarizability is screened by the short-range dipole operator,

$$\begin{aligned} \int_0^1 d\lambda \boldsymbol{\alpha}(u; \lambda) &= \int_0^1 d\lambda (\boldsymbol{\alpha}_{\text{eff}}^{-1}(u) + \lambda \mathbf{T}_{\text{gg}}(u)) \\ &= \int_0^1 d\lambda (\boldsymbol{\alpha}_{\text{eff}}^{-1}(u) + \lambda \mathbf{T}_{\text{sr}}(u) + \lambda \mathbf{T}_{\text{lr}}) \\ &\equiv \int_0^1 d\lambda (\boldsymbol{\alpha}_{\text{sr}}^{-1}(u; \lambda) + \lambda \mathbf{T}_{\text{lr}}) \\ &\approx \int_0^1 d\lambda (\boldsymbol{\alpha}'_{\text{eff}}^{-1}(u) + \lambda \mathbf{T}_{\text{lr}}) \\ &= \ln(1 + \boldsymbol{\alpha}'_{\text{eff}}^{-1}(u) \mathbf{T}_{\text{lr}}) \end{aligned} \quad (3.61)$$

$$\boldsymbol{\alpha}'_{\text{eff},p}(u) = \sum_q \text{Tr}_{\mathbb{R}^3} (\boldsymbol{\alpha}_{\text{sr},pq}(u; \lambda = 1)) \quad (3.62)$$

Second, the dipole-coupled Hamiltonian in (3.54) is solved with  $\boldsymbol{\alpha}(0)$  and  $\boldsymbol{\omega}$  calculated from  $\boldsymbol{\alpha}'_{\text{eff}}$ , and  $\mathbf{T}$  set to  $\mathbf{T}_{\text{lr}}$ , which is defined using the range-separating function of the TS method with a smoother switching profile.

Silvestrelli (2013) developed another method inspired by MBD in which the oscillators do not model the response of the atoms, but of Wannier functions. This Wannier-based MBD is to the pairwise vdW-WN method what the range-separated MBD is to the pairwise TS method. Unlike in vdW-WN, here the polarizabilities of the Wannier functions are not calculated using a local polarizability functional, but directly from the Hirshfeld volumes of the Wannier functions.

# Chapter 4

## Many-body dispersion method

This chapter presents new developments within the many-body dispersion (MBD) method, namely the reciprocal-space formulation, the MBD dielectric constant, several analytical results for the MBD wave function, and the analysis of the MBD nuclear forces and self-consistency. Some of these results are used in the following chapters. All the presented results have been implemented in program ‘pymbd’ (Hermann, 2017), which is a standalone Python program as well as a Fortran library included in electronic-structure programs FHI-aims and DFTB+.

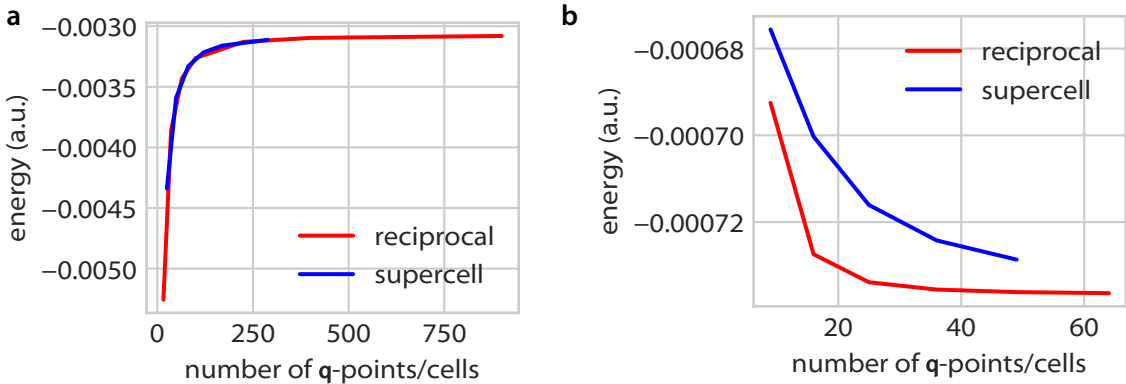
### 4.1 Reciprocal-space formulation

In a crystal, the matrices involved in the multipole expansion of the polarizability are infinite, and the normal real-space formalism becomes intractable. The most straightforward resolution is to cut a sufficiently large piece of the crystal consisting of multiple unit cells, a supercell, and apply periodic boundary conditions by summing the dipole operator over the periodic images. As shown below, this formalism, while conceptually simple, is not very efficient. The supercell approach is an unnecessary complication that introduces the issue of slow convergence with respect to the supercell size and makes the MBD calculation computationally as expensive as the corresponding KS-DFT calculation in some cases. The formalism developed in this section resolves these problems.

A more natural formulation uses the discrete version of the Fourier transformation in (2.62). The trace over the infinite number of atoms in a crystal in the MBD version of the ACFD formula in (3.56) is then transformed into a trace over atoms in a single unit cell and the reciprocal-space vectors from the first Brillouin zone,  $\mathbf{q}$ ,

$$\begin{aligned} E_{c,\text{lr}}^{\text{MBD}} &= \frac{1}{2\pi} \int_0^\infty du \text{Tr}_{\mathbf{q} \in \mathbb{R}^3} (\ln(1 + \alpha_{\text{eff}}(iu) \mathbf{T}_{\text{lr}}(\mathbf{q}))) \\ &= \frac{(2\pi)^3}{\Omega_{\text{UC}}} \int d\mathbf{q} \sum_{n=1}^{3N} \frac{\tilde{\omega}_n(\mathbf{q})}{2} - \sum_{p=1}^N 3 \frac{\omega_p}{2} \end{aligned} \quad (4.1)$$

**Figure 4.1 | Convergence of energy in the supercell and reciprocal-space approach.** Different convergence behavior for the 2D graphene layer (a) and the 3D argon crystal (b).



$$\alpha_{\text{eff},p}(\mathbf{q}, iu) = \sum_{\mathbf{R}} \alpha_{\text{eff},\mathbf{R}_p, \mathbf{R} + \mathbf{R}_p}(iu) e^{i\mathbf{q}\cdot\mathbf{R}} = \alpha_{\text{eff},p}(iu) \quad (4.2)$$

$$\mathbf{T}_{\text{lr},pq}(\mathbf{q}) = \sum_{\mathbf{R}} \mathbf{T}_{\text{lr},\mathbf{R}_p, \mathbf{R} + \mathbf{R}_q} e^{-i\mathbf{q}\cdot(\mathbf{R}_p - \mathbf{R} - \mathbf{R}_q)} \quad (4.3)$$

The diagonalization of  $\mathbf{Q}(\mathbf{q})$  that leads to  $\tilde{\omega}(\mathbf{q})$  maps again exactly on the solution of the Fourier-transformed dipole-coupled Hamiltonian, and the diagonalizing vectors,  $\mathbf{V}(\mathbf{q})$ , correspond to periodic collective electron oscillations with wavelength  $2\pi/|\mathbf{q}|$ , described by collective coupled coordinates  $\xi'(\mathbf{q})$ . Bučko et al. (2016) presented the reciprocal-space formulation of MBD without performing the analytic integration over the frequency.

The reciprocal-space formulation provides superior computational efficiency compared to the supercell approach for two reasons. The only two computationally demanding tasks in calculating the MBD energy are the formation of the dipole operator, with complexity  $O(N^2)$ ,  $N$  being the number of atoms, and the diagonalization or inversion of matrices, with complexity  $O(N^3)$ . Except for the smallest systems, the latter dominates. The reciprocal-space integration over  $\mathbf{q}$  is easily performed on an equidistant grid of  $N_q$  vectors, and the calculation of the MBD energy then involves  $N_q$  diagonalizations of the matrix  $\mathbf{Q}(\mathbf{q}_n)$ . Each diagonalization has a computational complexity  $O(N^3)$ ,  $N$  being the number of atoms in the unit cell, and the total complexity is  $O(N_q N^3)$ . In effective 1D and 2D systems (chains and layers), the rates of convergence of the energy with respect to the number of cells in the supercell,  $N_c$ , and to the number of points in the  $\mathbf{q}$ -grid are equal (Figure 4.1a), so for a given desired accuracy,  $N_c = N_q$ . But the computational cost of the supercell calculation is  $O((N_c N)^3) = O(N_c^3 N^3)$ ,  $N_c^2$  times larger than that of the reciprocal-space calculation. The second reason for the better efficiency of the reciprocal-space formulation is that because the lattice sums of the dipole operator are not absolutely convergent in 3D systems, the energy converges slower with  $N_c$  in the supercell approach than with  $N_q$  in the reciprocal-space formulation for 3D systems (Figure 4.1b),

so for a given required accuracy,  $N_q < N_c$ .

The lattice sum in the definition of  $\mathbf{T}_{lr}(\mathbf{q})$  can be efficiently computed using the Ewald summation in (2.68). The optimum balance between the computational cost of the real-space and reciprocal-space sum in the Ewald sum is reached by setting  $\alpha = 2.5/\sqrt[3]{\Omega_{UC}}$  (a.u.). Using the real-space cutoff of  $6/\alpha$  and reciprocal-space cutoff of  $10\alpha$  then leads to MBD energies that are accurate up to 10 significant digits with respect to fully converged references, while the computational cost is typically by two or more orders of magnitude smaller compared to sufficiently converged calculations of MBD energies without Ewald summation.

## 4.2 Dielectric function from MBD

All approximate vdW methods based on the range-separated ACFD formula can be tested in two independent ways. Testing against accurate reference polarizabilities gives information about  $\boldsymbol{\alpha}_{eff}$  and  $\mathbf{T}_{eff}$ , but is independent of the range-separation mechanism expressed in  $\mathbf{T}_{lr}$ , whereas comparison against benchmark interaction energies tests all these three components combined. For bulk material, there is no straightforward measurable equivalent of the total polarizability of a molecule. (The total polarizability of a finite crystal sample depends on its shape.) But an indirect measure of the bulk polarizability is provided by the macroscopic dielectric function.

Using the definitions in Section 2.10.1 and the Fourier transformation,  $\mathcal{F}$ , of the gradient operator, the dielectric function of the MBD model can be calculated straightforwardly,

$$\begin{aligned}\hat{\mathbf{q}} \cdot \boldsymbol{\epsilon}_M(u) \hat{\mathbf{q}} &= \lim_{\mathbf{q} \rightarrow 0} \frac{1}{1 + \nu(|\mathbf{q}|) \chi_{00}(\mathbf{q}, u)} \\ &= \lim_{\mathbf{q} \rightarrow 0} \frac{1}{1 + \frac{4\pi}{|\mathbf{q}|^2} \mathcal{F}[\nabla \cdot \nabla' \cdot \boldsymbol{\alpha}]_{00}(\mathbf{q}, u)} \\ &= \lim_{\mathbf{q} \rightarrow 0} \frac{1}{1 + \frac{4\pi}{|\mathbf{q}|^2} \mathbf{q} \cdot \boldsymbol{\alpha}_{00}(\mathbf{q}, u) \mathbf{q}} \quad (4.4)\end{aligned}$$

$$\begin{aligned}&= \lim_{\mathbf{q} \rightarrow 0} \frac{1}{1 + 4\pi \hat{\mathbf{q}} \cdot \boldsymbol{\alpha}_{00}(\mathbf{q}, u) \hat{\mathbf{q}}} \\ &\approx \lim_{\mathbf{q} \rightarrow 0} \frac{1}{1 + \frac{4\pi}{\Omega_{UC}} \hat{\mathbf{q}} \cdot \left( \sum_{pq} \boldsymbol{\alpha}_{pq}(\mathbf{q}, u) \right) \hat{\mathbf{q}}} \quad (4.5)\end{aligned}$$

The Unsöld approximation inherent in the MBD polarizability makes this approach of little use for the dynamic dielectric function, but the static dielectric constant should be represented as accurately as total polarizabilities of molecules. Here, the use of the Ewald summation is crucial, since the required cutoff of the full real-space summation diverges as  $\mathbf{q} \rightarrow 0$ .

In a simple cubic lattice, the bare dipole operator,  $\mathbf{T}(\mathbf{q})$ , can be written in closed form for small  $\mathbf{q}$ ,

$$\mathbf{T}(\mathbf{q}) = \frac{4\pi}{\Omega_{UC}} (\hat{\mathbf{k}} \otimes \hat{\mathbf{k}} - \frac{1}{3}\mathbf{I}) + O(|\mathbf{q}|) \quad (4.6)$$

The expression for the dielectric function above then yields the Clausius–Mossotti equation,

$$\frac{\epsilon_M(0) - 1}{\epsilon_M(0) + 2} = \frac{4\pi}{3} \frac{\alpha_{eff}(0)}{\Omega_{UC}} \quad (4.7)$$

With more complex unit cells and the effective dipole operator from MBD, the resulting dielectric function is in general anisotropic. Therefore, this approach can be interpreted as a generalization of the Clausius–Mossotti approximation.

### 4.3 Properties of dipole-coupled wave function

The diagonalization of the  $\mathbf{Q}$  matrix of the MBD Hamiltonian in (3.55) results in the coupled resonance frequencies,  $\tilde{\omega}$ , which give the MBD energy, as well as the eigenvectors,  $\mathbf{V} = (\mathbf{v}_1 \mathbf{v}_2 \dots)$ , which define the coupled coordinates,  $\tilde{\xi} = \mathbf{V}^T \xi$ , in which the MBD Hamiltonian decouples into a noninteracting Hamiltonian. The ground-state wave function is the product of harmonic-oscillator ground-state wave functions,

$$\psi_0(\{\tilde{\xi}_n\}) = \prod_n \left( \frac{\tilde{\omega}_n}{\pi} \right)^{\frac{1}{4}} \exp \left( -\frac{1}{2} \tilde{\omega}_n \tilde{\xi}_n^2 \right) \quad (4.8)$$

This section presents several new analytical results for this correlated wave function, some of which are used in Chapter 5.

#### 4.3.1 Charge density

When interpreted as an approximation to the full electronic Hamiltonian, the pseudo electrons in the MBD Hamiltonian effectively model the polarizable electrons in the valence shells of atoms. One may then ask what is the charge density of these pseudo electrons, how is it different from the noninteracting system, and whether this change captures the true electron-density redistribution caused by long-range electron correlation.

The charge density of any system of  $N$  charged particles is defined as an expectation value of the charge-density operator,

$$n(\mathbf{r}) = \langle \Psi | \sum_i q_i | \mathbf{r}_i = \mathbf{r} \rangle \langle \mathbf{r}_i = \mathbf{r} | \Psi \rangle = \int \cdots \int d\mathbf{r}_1 \cdots d\mathbf{r}_N \sum_i q_i \delta(\mathbf{r} - \mathbf{r}_i) \Psi(\{\mathbf{r}_j\})^2 \quad (4.9)$$

To evaluate this expression for (4.8), we first transform the wave function back to  $\xi$  and gather the product of the exponentials,

$$\Psi(\{\xi_i\}) = \left( \prod_i \left( \frac{\tilde{\omega}_i}{\pi} \right)^{\frac{1}{4}} \right) \exp \left( -\frac{1}{2} \sum_{jk} \underbrace{\sum_i V_{ji} \tilde{\omega}_i V_{ki}}_{\Omega_{jk}} \xi_j \xi_k \right) \quad (4.10)$$

In the following, we use  $\sum_{i \notin A}$  for a sum that skips the  $A$ -th particle and  $\sum_{i \in A}$  for a sum over the three Cartesian coordinates of the  $A$ -th particle. For a given  $A$ , we divide the sum over  $jk$  according to the order of  $\xi_{i \in A}$ ,

$$\begin{aligned} \sum_{jk} \Omega_{jk} \xi_j \xi_k &= \sum_{\substack{j \notin A \\ k \notin A}} \Omega_{jk} \xi_j \xi_k + 2 \sum_{\substack{p \in A \\ k \notin A}} \Omega_{pk} \xi_p \xi_k + 2 \sum_{\substack{p \in A \\ q \in A}} \Omega_{pq} \xi_p \xi_q \\ &\equiv \xi_A'^T \Omega_A'' \xi_A' + 2 \xi_A'^T \Omega_A' \xi_A + \xi_A^T \Omega_A \xi_A \end{aligned} \quad (4.11)$$

The linear term can be removed by completing the square with respect to  $\xi_A'$ ,

$$\sum_{jk} \Omega_{jk} \xi_j \xi_k = (\xi_A'^T - \mathbf{h}_A^T) \Omega_A'' (\xi_A' - \mathbf{h}_A) + \xi_A^T \Omega_A \xi_A - \xi_A^T \Omega_A'^T \Omega_A''^{-1} \Omega_A' \xi_A \quad (4.12)$$

Here,  $\mathbf{h}_A$  is some quantity that does not depend on  $\xi_A'$ . We can now factor out the exponential and the  $3N$ -dimensional integral,

$$n(\mathbf{r}) = \sum_A q_A \left( \int \cdots \int d\mathbf{r}_1 \cdots d\mathbf{r}_{A-1} d\mathbf{r}_{A+1} \cdots d\mathbf{r}_N \right) \int d\mathbf{r}_A \delta(\mathbf{r} - \mathbf{r}_A) \dots \quad (4.13)$$

First, we evaluate the integrals in parentheses. Because  $\mathbf{h}_A$  is just a constant coordinate shift, and the integrals are over the whole space,  $\mathbf{h}_A$  can be transformed away. Furthermore, we can rotate  $\Omega_A''$  into a new basis where it becomes diagonal, which factors the  $3(N-1)$ -dimensional integral into a product of  $3(N-1)$  1-dimensional integrals over Gaussian functions of the form  $\exp(-\bar{\omega}_{A,i} \xi_{A,i}^2)$ , where  $\bar{\omega}_{A,i}$  are the eigenvalues of  $\Omega_A''$ . (The factor of  $\frac{1}{2}$  disappears due to the square of the wave function.)

Second, the integral over  $\mathbf{r}_A$  picks the value of the following function at point  $\mathbf{r}$  via the  $\delta$ -function,

$$\exp \left( - \underbrace{\xi_A^T (\Omega_A - \Omega_A'^T \Omega_A''^{-1} \Omega_A')}_{\Omega^{(A)}} \xi_A \right) \quad (4.14)$$

Combining (4.9), (4.10), (4.12), and the previous two paragraphs, and transforming from  $\xi_A$  back to  $\mathbf{r}_A$ , we get

$$n(\mathbf{r}) = \sum_A q_A \left( \frac{m_A}{\pi} \right)^{\frac{3}{2}} \sqrt{\frac{\prod_{i=1}^{3N} \tilde{\omega}_i}{\prod_{i=1}^{3(N-1)} \bar{\omega}_{A,i}}} \exp \left( - m_A (\mathbf{r} - \mathbf{R}_A)^T \Omega^{(A)} (\mathbf{r} - \mathbf{R}_A) \right) \quad (4.15)$$

### 4.3.2 First-order perturbation correction

The dipole-coupled wave function can serve as a zeroth-order Hamiltonian in a perturbation expansion with the perturbation equal to the difference between the full Coulomb interaction and the dipole interaction,  $\hat{V}_{ee} - \hat{V}_{pp}$ . The first-order correction does not capture any correlation energy from the higher multipoles (those start at second order), but it can serve as a measure of how effective is the Gaussian-screened dipole potential of MBD at mimicking the full Coulomb interaction at short range.

The first-order perturbation energy is just the expectation value of the perturbation Hamiltonian for the ground state,

$$E_{MBD}^{(1)} = \langle \psi_0 | V_{ee} - V_{pp} | \psi_0 \rangle \quad (4.16)$$

The expectation value of the Coulomb operator is a sum of two-particle terms,

$$\langle \psi_0 | \frac{1}{2} \sum_{AB} \frac{q_A q_B}{|\mathbf{r}_A - \mathbf{r}_B|} | \psi_0 \rangle \quad (4.17)$$

In analogy to the calculation of  $n(\mathbf{r})$ , for each particle pair we rotate the  $3(N-2)$  coordinates that are not in the Coulomb term such that the corresponding integrals become integrals over Gaussian functions, and then evaluate the remaining 6-dimensional integral over  $\mathbf{r}_A$  and  $\mathbf{r}_B$ .

Introducing  $\xi_{AB} = (\xi_A \xi_B)$ , a 6-dimensional vector, and  $\Omega^{(AB)}$  which is an equivalent of  $\Omega^{(A)}$  from the previous section, we can write the necessary integral as

$$I_1 = \iint d\xi_A d\xi_B \frac{\exp(-\xi_{AB}^T \Omega^{(AB)} \xi_{AB})}{|\mathbf{r}_A - \mathbf{r}_B|} \quad (4.18)$$

We start by rewriting the Coulomb potential as an integral,

$$\frac{1}{|\mathbf{r}_A - \mathbf{r}_B|} = \frac{2}{\sqrt{\pi}} \int_0^\infty du \exp(-|\mathbf{r}_A - \mathbf{r}_B|^2 u^2) \quad (4.19)$$

Inserting into (4.18), and transforming to  $\mathbf{r}_A$ , we get a 7-dimensional integral over a Gaussian,

$$I_1 = 2\sqrt{\frac{m_A m_B}{\pi}} \iint d\mathbf{r}_A d\mathbf{r}_B \int_0^\infty du \times \exp \left[ -(\mathbf{r}_{AB} - \mathbf{R}_{AB})^T \Omega_m'^{(AB)} (\mathbf{r}_{AB} - \mathbf{R}_{AB}) - \mathbf{r}_{AB}^T \mathbf{U}_2 \mathbf{r}_{AB} \right] \quad (4.20)$$

Here,  $\Omega'^{(AB)}$  absorbed the masses and  $\mathbf{U}_2$  is defined as

$$\mathbf{U}_2 = u^2 \begin{pmatrix} 1 & 0 & 0 & -1 & 0 & 0 \\ 0 & 1 & 0 & 0 & -1 & 0 \\ 0 & 0 & 1 & 0 & 0 & -1 \\ -1 & 0 & 0 & 1 & 0 & 0 \\ 0 & -1 & 0 & 0 & 1 & 0 \\ 0 & 0 & -1 & 0 & 0 & 1 \end{pmatrix} \quad (4.21)$$

Following with the integrand only, we rearrange terms and complete the square with respect to  $\mathbf{r}_{AB}$ ,

$$\begin{aligned} & \exp \left[ -\mathbf{r}_{AB}^T (\Omega_m'^{(AB)} + \mathbf{U}_2) \mathbf{r}_{AB} + 2\mathbf{R}_{AB}^T \Omega_m'^{(AB)} \mathbf{r}_{AB} - \mathbf{R}_{AB}^T \Omega_m'^{(AB)} \mathbf{R}_{AB} \right] \\ &= \exp \left[ -(\mathbf{r}_{AB} - \mathbf{h}_{AB})^T (\Omega_m'^{(AB)} + \mathbf{U}_2) (\mathbf{r}_{AB} - \mathbf{h}_{AB}) \right] \\ &\quad \times \exp \left[ -\mathbf{R}_{AB}^T (\Omega_m'^{(AB)} - \Omega_m'^{(AB)} (\Omega_m'^{(AB)} + \mathbf{U}_2)^{-1} \Omega_m'^{(AB)}) \mathbf{R}_{AB} \right] \end{aligned} \quad (4.22)$$

As in the charge-density calculation, the first exponential can be shifted and rotated into a diagonal form, upon which the spatial integrals can be easily evaluated,

$$\iint d\mathbf{r}_A d\mathbf{r}_B \exp \left[ -\mathbf{r}_{AB}^T (\Omega_m'^{(AB)} + \mathbf{U}_2) \mathbf{r}_{AB} \right] = \frac{\pi^3}{\sqrt{\prod_{i=1}^6 \lambda_{AB,i}(u)}} \quad (4.23)$$

Here,  $\lambda_{AB,i}(u)$  are the eigenvalues of  $(\Omega_m'^{(AB)} + \mathbf{U}_2)$ . The remaining 1-dimensional integral over  $u$  from 0 to  $\infty$  has a finite integrand that decays exponentially to zero, and can be quickly evaluated numerically.

Combining all parts together, we get

$$\begin{aligned} \langle \Psi | \frac{1}{2} \sum_{AB} \frac{q_A q_B}{|\mathbf{r}_A - \mathbf{r}_B|} | \Psi \rangle &= \frac{1}{2} \sum_{AB} q_A q_B \sqrt{\frac{\prod_{i=1}^{3N} \tilde{\omega}_i}{\prod_{i=1}^{3(N-2)} \tilde{\omega}_{AB,i}}} \\ &\quad \times \int_0^\infty du \frac{\exp \left[ -\mathbf{R}_{AB}^T (\Omega_m'^{(AB)} - \Omega_m'^{(AB)} (\Omega_m'^{(AB)} + \mathbf{U}_2)^{-1} \Omega_m'^{(AB)}) \mathbf{R}_{AB} \right]}{\sqrt{\prod_{i=1}^6 \lambda_{AB,i}(u)}} \end{aligned} \quad (4.24)$$

The calculation of the dipole term,  $\langle \psi_0 | V_{pp} | \psi_0 \rangle$ , is straightforward. First, we transform the dipole potential to the coupled basis and gather the prefactors,

$$\tilde{T}_{ij} = \sum_{kl} C_{ki} C_{lj} \omega_k \omega_l \sqrt{\alpha_k(0) \alpha_{l(0)}} T_{kl} \quad (4.25)$$

Then,

$$\begin{aligned} \langle \Psi | V_{pp} | \Psi \rangle &= \langle \Psi | \frac{1}{2} \sum_{ij} \tilde{\xi}_i \tilde{\xi}_j \tilde{T}_{ij} | \Psi \rangle \\ &= \frac{1}{2} \sum_{i \neq j} \tilde{T}_{ij} \left( \frac{\tilde{\omega}_i \tilde{\omega}_j}{\pi^2} \right)^{\frac{1}{4}} \int d\tilde{\xi}_i \tilde{\xi}_i \exp \left( -\frac{1}{2} \tilde{\omega}_i \tilde{\xi}_i^2 \right) \int d\tilde{\xi}_j \tilde{\xi}_j \exp \left( -\frac{1}{2} \tilde{\omega}_j \tilde{\xi}_j^2 \right) \\ &\quad + \frac{1}{2} \sum_i \tilde{T}_{ii} \sqrt{\frac{\tilde{\omega}_i}{\pi}} \int d\tilde{\xi}_i \tilde{\xi}_i^2 \exp(-\tilde{\omega}_i \tilde{\xi}_i^2) = \sum_i \frac{\tilde{T}_{ii}}{4\tilde{\omega}_i} \end{aligned} \quad (4.26)$$

The  $i \neq j$  terms vanished because the integrands are odd functions.

### 4.3.3 Anisotropic Gaussian screening

The technique used in the previous section can be also used to generalize the Gaussian screening of the Coulomb interaction, used in MBD to derive the effective dipole interaction, to anisotropic Gaussian charge densities. This might be used to construct appropriate range separation for atomic fragments with anisotropic polarizabilities, which is investigated in Chapter 8. Integrals of the same kind are routinely evaluated in all quantum-chemistry algorithms based on Gaussian basis sets, but those are always with isotropic Gaussian functions.

The electrostatic energy of two Gaussian unit-charge densities located at  $\mathbf{R}_A$  with anisotropic widths  $\sigma_A = 1/\sqrt{\mathbf{K}_A}$  is expressed as an integral similar in form to (4.18),

$$I_2(\mathbf{K}_1, \mathbf{K}_2) = \frac{\sqrt{\det(\mathbf{K}_1 \mathbf{K}_2)}}{\pi^3} \iint d\mathbf{r}_1 d\mathbf{r}_2 \frac{e^{-(\mathbf{r}_1 - \mathbf{R}_1) \cdot \mathbf{K}_1 (\mathbf{r}_1 - \mathbf{R}_1)} e^{-(\mathbf{r}_2 - \mathbf{R}_2) \cdot \mathbf{K}_2 (\mathbf{r}_2 - \mathbf{R}_2)}}{|\mathbf{r}_1 - \mathbf{r}_2|} \quad (4.27)$$

The prefactor ensures proper normalization,

$$\lim_{a \rightarrow \infty} I_2(a\mathbf{K}_1, a\mathbf{K}_2) = \frac{1}{|\mathbf{R}_1 - \mathbf{R}_2|} \quad (4.28)$$

By identifying  $m_A = 1$  and  $\Omega^{(12)} \equiv \mathbf{K} = \mathbf{K}_1 \oplus \mathbf{K}_2$ ,  $I_2$  is mapped to  $I_1$  of the previous section, and the final result is obtained by following the same procedure,

$$I_2(\mathbf{K}_1, \mathbf{K}_2) = \frac{2}{\sqrt{\pi}} \int_0^\infty du \sqrt{\frac{\det \mathbf{K}}{\det(\mathbf{K} + \mathbf{U}_2)}} \exp \left[ -\mathbf{R}^T (\mathbf{K} - \mathbf{K}(\mathbf{K} + \mathbf{U}_2)^{-1} \mathbf{K}) \mathbf{R} \right] \quad (4.29)$$

As before, the integrand is finite everywhere and decays exponentially to zero, so the integral can be efficiently evaluated by numerical quadrature.

For the isotropic case,  $\mathbf{K}_A = \mathbf{I}/\sigma_A^2$ , this reduces to (3.58),

$$\begin{aligned} I_1(\sigma_1, \sigma_2) &= \frac{2}{\sqrt{\pi}} \int_0^\infty du \left( 1 + u^2(\sigma_1^2 + \sigma_2^2) \right)^{-\frac{3}{2}} \exp \left[ -\frac{u^2 |\mathbf{R}_1 - \mathbf{R}_2|^2}{1 + u^2(\sigma_1^2 + \sigma_2^2)} \right] \\ &= \frac{2}{\sqrt{\pi}} \int_0^{1/\sqrt{\sigma_1^2 + \sigma_2^2}} dv \exp(-v^2 |\mathbf{R}_1 - \mathbf{R}_2|^2) \\ &= \text{erf} \left( \frac{|\mathbf{R}_1 - \mathbf{R}_2|}{\sqrt{\sigma_1^2 + \sigma_2^2}} \right) \frac{1}{|\mathbf{R}_1 - \mathbf{R}_2|} \end{aligned} \quad (4.30)$$

The corresponding dipole operator is obtained by applying the tensor gradient,

$$\begin{aligned} \nabla_{\mathbf{R}_1} \otimes \nabla_{\mathbf{R}_2} I_2 &\equiv \nabla_{\mathbf{R}_1} \otimes \nabla_{\mathbf{R}_2} \int_0^\infty du i_2(u) = \int_0^\infty du \nabla_{\mathbf{R}_1} \otimes \nabla_{\mathbf{R}_2} i_2(u) \\ &= \int_0^\infty du \left( -2\mathbf{K}_{12} + 4(\mathbf{K}_{11}\mathbf{R}_1 + \mathbf{K}_{12}\mathbf{R}_2) \otimes (\mathbf{K}_{12}\mathbf{R}_1 + \mathbf{K}_{22}\mathbf{R}_2) \right) i_2(u) \end{aligned} \quad (4.31)$$

$$\begin{bmatrix} \mathbf{K}_{11} & \mathbf{K}_{12} \\ \mathbf{K}_{12} & \mathbf{K}_{22} \end{bmatrix} \equiv \mathbf{K} - \mathbf{K}(\mathbf{K} + \mathbf{U}_2)^{-1} \mathbf{K} \quad (4.32)$$

#### 4.3.4 Interaction energy decomposition

The interaction energy of two systems,  $S_1, S_2$ , is calculated with any total-energy method as the difference between the energy of the combined system and the subsystems,

$$E^{(\text{int})}(S_1, S_2) = E(S_1 S_2) - E(S_1) - E(S_2) \quad (4.33)$$

By construction, the pairwise vdW methods give a clear interpretation of the interaction energy in terms of pairs of atoms (fragments) in which the atoms are from different subsystems,

$$E_{\text{c,lr}}^{(\text{int})}(S_1, S_2) \approx - \sum_{A \in S_1, B \in S_2} C_{6,AB} \frac{f(\mathbf{R}_A, \mathbf{R}_B)}{|\mathbf{R}_A - \mathbf{R}_B|^6} \quad (4.34)$$

In the pairwise picture, the total collective oscillations in the system are decomposed into oscillations between individual pairs of atoms, and because this decomposition is identical in the total system and the individual subsystems, only the inter-system oscillations contribute to the interaction energy. But in MBD, the total long-range correlation energy has the form of a sum of energies of the individual collective oscillations, which are fully delocalized and different in the total system and the subsystems. Using the transformation between the uncoupled and coupled coordinates, however, the coupled oscillation energies of the subsystems can be projected into the coupled basis of the system and vice versa, which leads to a decomposition of the MBD interaction energy into the individual collective oscillations of the system. This provides a clear physical picture of the binding that is utilized in Chapter 5.

The MBD interaction energy between two subsystems is expressed in terms of the coupled oscillation frequencies of the system,  $\tilde{\omega}$ , and of the subsystems,  $\tilde{\omega}_1, \tilde{\omega}_2$ , and the uncoupled oscillation frequencies in the system,  $\omega$ , and in the subsystems,  $\omega_1, \omega_2$ ,

$$E_{\text{MBD}}^{(\text{int})} = \sum_{n=1}^{3N} \frac{(\tilde{\omega})_n}{2} - \sum_{n'=1}^{3N} \frac{(\tilde{\omega}_1 \oplus \tilde{\omega}_2)_{n'}}{2} - \sum_{n''=1}^{3N} \frac{(\omega - \omega_1 \oplus \omega_2)_{n''}}{2} \quad (4.35)$$

Here,  $n$  runs over the coupled coordinates of the system,  $n'$  over coupled coordinates of the subsystems, and  $n''$  over the uncoupled coordinates, and we wish to project the frequencies in such a way that the whole expression is a single sum either over  $n$  or over  $n'$ . In general, the effective noninteracting frequency of a given oscillator in the subsystem and in the total system are not equal in MBD,  $\omega \neq \omega_1 \oplus \omega_2$ , due to the slightly different Hirshfeld partitioning and short-range polarizability screening between the system and the subsystems.

Using the eigenvectors,  $\mathbf{V}_1 = (\mathbf{v}_1 \mathbf{v}_2 \dots)$ ,  $\mathbf{V}_2$ , of the subsystem MBD matrices,  $\mathbf{Q}_1, \mathbf{Q}_2$ , and the eigenvectors,  $\mathbf{V}$ , of the total-system MBD matrix,  $\mathbf{Q}$ , we can construct a projector from the basis of the coupled subsystem coordinates,  $\tilde{\xi}_1 \oplus \tilde{\xi}_2$ , to the basis of the coupled system coordinates,  $\tilde{\xi}$ ,

$$\mathbf{P} = \mathbf{V}^T (\mathbf{V}_1 \oplus \mathbf{V}_2) \quad (4.36)$$

This projector is orthonormal and retains the norm of a vector, but the total MBD energy is a 1-norm of the vector of oscillation energies,  $E_{\text{MBD}} = |\boldsymbol{\omega}/2|_1$ , which is retained by an elementwise (Hadamard) square of the projector,

$$(\mathbf{P}^{\circ 2})_{ij} = (\mathbf{P})_{ij}^2 \quad (4.37)$$

Likewise,  $(\mathbf{V}^{\circ 2})^T$  and  $(\mathbf{V}_1^{\circ 2} \oplus \mathbf{V}_2^{\circ 2})^T$  are projectors from the uncoupled basis of noninteracting oscillators to the coupled basis of the total system and the subsystems, respectively. With these projectors at hand, (4.35) can be expressed as a single sum over the coupled coordinates of the system or the subsystems,

$$E_{\text{MBD}}^{(\text{int})} = \sum_{n=1}^{3N} \frac{1}{2} \left( \tilde{\boldsymbol{\omega}} - \mathbf{P}^{\circ 2}(\tilde{\boldsymbol{\omega}}_1 \oplus \tilde{\boldsymbol{\omega}}_2) - (\mathbf{V}^{\circ 2})^T(\boldsymbol{\omega} - \boldsymbol{\omega}_1 \oplus \boldsymbol{\omega}_2) \right)_n \quad (4.38)$$

$$E_{\text{MBD}}^{(\text{int})} = \sum_{n'=1}^{3N} \frac{1}{2} \left( (\mathbf{P}^{\circ 2})^T \tilde{\boldsymbol{\omega}} - \tilde{\boldsymbol{\omega}}_1 \oplus \tilde{\boldsymbol{\omega}}_2 - (\mathbf{V}_1^{\circ 2} + \mathbf{V}_2^{\circ 2})^T(\boldsymbol{\omega} - \boldsymbol{\omega}_1 \oplus \boldsymbol{\omega}_2) \right)_{n'} \quad (4.39)$$

The vectors under the summation signs can now be interpreted as different decompositions of the MBD interaction energy into the coupled oscillations.

## 4.4 Nuclear forces and self-consistency

In this section, we analyze the problem of nuclear forces in a combined KS-DFT+MBD calculation. Nuclear forces are the (negative of) total derivatives of the energy with respect to the positions of the nuclei, and are the necessary quantity for structure optimization, calculations of vibration spectra, and derived quantities. As such, they are one of the cornerstones of computational chemistry and computational material physics.

In the following, we assume that the KS calculation is done in a finite one-electron basis,  $\{|\mu\rangle\}$ , which leads to the description of any particular KS state,  $|\Psi\rangle$ , in terms of the matrix elements,  $P_{\mu\nu}$ , of the density-matrix operator,  $|\Psi\rangle\langle\Psi|$ . This enables expressing any measurable quantity, such as energy or the electron density,  $n$ , in terms of the density matrix,

$$\begin{aligned} n(\mathbf{r}) &= \langle \Psi | \hat{n}(\mathbf{r}) | \Psi \rangle = \langle \Psi | \sum_{\mu} |\mu\rangle \langle \mu | \hat{n}(\mathbf{r}) \sum_{\nu} | \nu \rangle \langle \nu | \Psi \rangle \\ &= \sum_{\mu\nu} \langle \mu | \Psi \rangle \langle \Psi | \nu \rangle \langle \mu | \hat{n}(\mathbf{r}) | \nu \rangle = \sum_{\mu\nu} P_{\mu\nu} \varphi_{\mu}(\mathbf{r}) \varphi_{\nu}(\mathbf{r}) \end{aligned} \quad (4.40)$$

The total KS energy,  $E_{\text{KS}}$ , is a system-dependent (via the external potential) functional of the electron density, and hence of the density matrix and the one-electron basis. In a standard KS calculation, the nuclear coordinates and the one-electron basis are fixed, and the KS ground state is found by minimizing the total energy (via the HK theorem) with respect to the density matrix, so that the partial derivatives are zero,  $\partial E_{\text{KS}} / \partial P_{\mu\nu} = 0$ . The

total derivative of the KS energy consists of three terms via the chain rule ( $\alpha = x, y, z$ ),

$$\frac{dE_{KS}(\{R_{A\alpha}\}, \{\varphi_\mu\}, \mathbf{P})}{dR_{B\beta}} = \underbrace{\frac{\partial E_{KS}}{\partial R_{B\beta}}}_{\text{Feynman forces}} + \underbrace{\sum_{\mu\nu} \frac{\partial E_{KS}}{\partial P_{\mu\nu}} \frac{\partial P_{\mu\nu}}{\partial R_{B\beta}}}_{=0} + \underbrace{\sum_\mu \int d\mathbf{r} \frac{\delta E_{KS}}{\delta \varphi_\mu(\mathbf{r})} \frac{\partial \varphi_\mu(\mathbf{r})}{\partial R_{B\beta}}}_{\text{Pulay forces}} \quad (4.41)$$

The first term is the explicit derivative, which is equal to the electrostatic force from the electron density on the nucleus  $B$  (Feynman, 1939), the second term is zero because of the energy minimization, and the third term is nonzero only when the one-electron basis depends on the nuclear coordinates.

The MBD energy,  $E_{MBD}$ , is a function of the nuclear coordinates and of the Hirshfeld volumes (eq. 3.45),  $V_A = \int d\mathbf{r} n(\mathbf{r}) v_A(\mathbf{r})$ , which in turn are functionals of the electron density, and hence of the density matrix and the one-electron basis. The total derivative is obtained via chain rules,

$$\begin{aligned} \frac{dE_{MBD}(\{R_{A\alpha}\}, \{V_A\})}{dR_{B\beta}} &= \frac{\partial E_{MBD}}{\partial R_{B\beta}} + \sum_A \frac{\partial E_{MBD}}{\partial V_A} \frac{dV_A}{dR_{B\beta}} \\ &= \frac{\partial E_{MBD}}{\partial R_{B\beta}} + \sum_A \frac{\partial E_{MBD}}{\partial V_A} \left( \frac{\partial V_A}{\partial R_{B\beta}} + \int d\mathbf{r} \frac{\delta V_A}{\delta n(\mathbf{r})} \frac{dn(\mathbf{r})}{dR_{B\beta}} \right) \\ &= \frac{\partial E_{MBD}}{\partial R_{B\beta}} + \sum_A \frac{\partial E_{MBD}}{\partial V_A} \left( \int d\mathbf{r} \frac{\partial v_A(\mathbf{r})}{\partial R_{B\beta}} n(\mathbf{r}) + \int d\mathbf{r} v_A(\mathbf{r}) \left( \sum_{\mu\nu} \frac{\partial n(\mathbf{r})}{\partial P_{\mu\nu}} \frac{\partial P_{\mu\nu}}{\partial R_{B\beta}} + \sum_\mu \frac{\partial n(\mathbf{r})}{\partial \varphi_\mu(\mathbf{r})} \frac{\partial \varphi_\mu(\mathbf{r})}{\partial R_{B\beta}} \right) \right) \\ &= \frac{\partial E_{MBD}}{\partial R_{B\beta}} + \sum_A \frac{\partial E_{MBD}}{\partial V_A} \left( \int d\mathbf{r} \frac{\partial v_A(\mathbf{r})}{\partial R_{B\beta}} n(\mathbf{r}) - 2 \int d\mathbf{r} v_A(\mathbf{r}) \sum_{\mu\in B, v} P_{\mu v} \varphi_v(\mathbf{r}) \nabla_\beta \varphi_\mu(\mathbf{r}) \right) \\ &\quad + \underbrace{\sum_{\mu\nu} \left( \sum_A \frac{\partial E_{MBD}}{\partial V_A} \int d\mathbf{r} v_A(\mathbf{r}) \varphi_\mu(\mathbf{r}) \varphi_v(\mathbf{r}) \right) \frac{\partial P_{\mu\nu}}{\partial R_{B\beta}}}_{\partial E_{MBD}/\partial P_{\mu\nu}} \quad (4.42) \end{aligned}$$

Combining the KS and MBD forces together, the final expression consists of seven terms,

$$\begin{aligned} \frac{d(E_{KS} + E_{MBD})}{dR_{B\beta}} &= (\text{KS Feynman forces}) + (\text{KS Pulay forces}) + \underbrace{\frac{\partial E_{MBD}}{\partial R_{B\beta}}}_I \\ &\quad + \underbrace{\sum_A \frac{\partial E_{MBD}}{\partial V_A} \left( \int d\mathbf{r} \frac{\partial v_A(\mathbf{r})}{\partial R_{B\beta}} n(\mathbf{r}) - 2 \int d\mathbf{r} v_A(\mathbf{r}) \sum_{\mu\in B, v} P_{\mu v} \varphi_v(\mathbf{r}) \nabla_\beta \varphi_\mu(\mathbf{r}) \right)}_{\text{IIa}} \quad \underbrace{\text{IIb}}_{\text{IIb}} \end{aligned}$$

$$+ \sum_{\mu\nu} \left( \underbrace{\frac{\partial E_{\text{KS}}}{\partial P_{\mu\nu}}}_{\text{IIIa}} + \underbrace{\frac{\partial E_{\text{MBD}}}{\partial P_{\mu\nu}}}_{\text{IIIb}} \right) \frac{\partial P_{\mu\nu}}{\partial R_{B\beta}} \quad (4.43)$$

Term I is the direct force, computed with the Hirshfeld volumes fixed, and was given independently by Blood-Forsythe et al. (2016) and Bučko et al. (2016) as analytic expressions. This is by far the dominant part of the MBD forces. Calculation of terms IIa and IIb requires  $\partial E_{\text{MBD}}/\partial V_A$ , also given by Blood-Forsythe et al. (2016). Term IIa is the force due to the dependence of the Hirshfeld-volume weight on the nuclear coordinates, and can be calculated straightforwardly from derivatives of the radial free-atom densities. Using a plane-wave basis set, Blood-Forsythe et al. (2016) found that the contribution of this term to the total forces is non-negligible in a test set of peptides. Term IIb would be equal to zero in basis sets that do not depend on the nuclear coordinates (such as plane waves), and is the equivalent of the Pulay forces for the KS energy.

Terms IIIa and IIIb arise from the dependence of the density matrix on the nuclear positions. When the MBD calculation is performed only after the KS-DFT calculation is converged (a posteriori), then IIIa is zero, and IIIb is nonzero. On the other hand, when the MBD KS potential,  $\delta E_{\text{MBD}}[n]/\delta n(\mathbf{r})$ , is calculated and included self-consistently in the KS calculation, then the total DFT+MBD energy is minimized with respect to the density matrix, and IIIa and IIIb together are zero. The effect of self-consistency of the pairwise TS method on the resulting electron densities was investigated by Ferri et al. (2015). The MBD KS potential can be calculated directly from the knowledge of  $\partial E_{\text{MBD}}/\partial V_A$ ,

$$\nu_{\text{KS,MBD}}(\mathbf{r}) = \frac{\delta E_{\text{MBD}}}{\delta n(\mathbf{r})} = \sum_A \frac{\partial E_{\text{MBD}}}{\partial V_A} \frac{\delta V_A}{\delta n(\mathbf{r})} = \sum_A \frac{\partial E_{\text{MBD}}}{\partial V_A} \nu_A(\mathbf{r}) \quad (4.44)$$

We have implemented the evaluation of terms IIa, IIb, and of the MBD KS potential in the FHI-aims code (Blum et al., 2009), which uses an atom-centered basis set, to test the relative importance of the terms in (4.43). For testing purposes, we used 10 dimers from the S22 benchmark set of small organic dimers at equilibrium geometries, and the black allotrope of phosphorus as an instance of a layered material with strong inter-layer vdW interactions. As a benchmark, we used 5-point finite differencing to calculate the true forces. In all cases, we found that the difference between the forces in a self-consistent and a posteriori MBD calculation, which can serve as an estimate of the magnitude of term IIIb, is below the inherent accuracy of the KS calculation. The terms IIa and IIb were individually non-negligible, in line with the previous results, but surprisingly, the combined term fell again below the baseline accuracy in all cases. This explains and solidifies the empirical observation that the derivatives of Hirshfeld volumes are non-negligible in a plane-wave basis, but can be neglected altogether in atom-centered basis sets in most circumstances.

# Chapter 5

## Charge-oscillation nature of $\pi$ - $\pi$ interactions

This chapter uses the decomposition of the coupled-oscillator wave function and the expression for the coupled-oscillator density from Chapter 4 to give a clear physical picture of binding in  $\pi$ - $\pi$  stacked systems. This study illustrates the benefits of formulating a method (MBD in this case) via a model Hamiltonian, which gives automatically access not only to the energy but also to the wave function. The results show that the  $\pi$ - $\pi$  stacking is associated with vdW interactions originating from collective nonlocal oscillations, which explains the difficulties of pairwise vdW methods to describe these systems accurately. It is demonstrated that besides interaction energies, the harmonic oscillators can yield also a good prediction of the vdW-associated redistribution of the electron density, which then partially motivates the focus on the spatial distribution of the local polarizability in Chapter 8. Most of the results in this chapter have been published in (Hermann et al., 2017a). The diffusion quantum Monte-Carlo calculations were done by prof. Dario Alfè from University College London.

### 5.1 Background

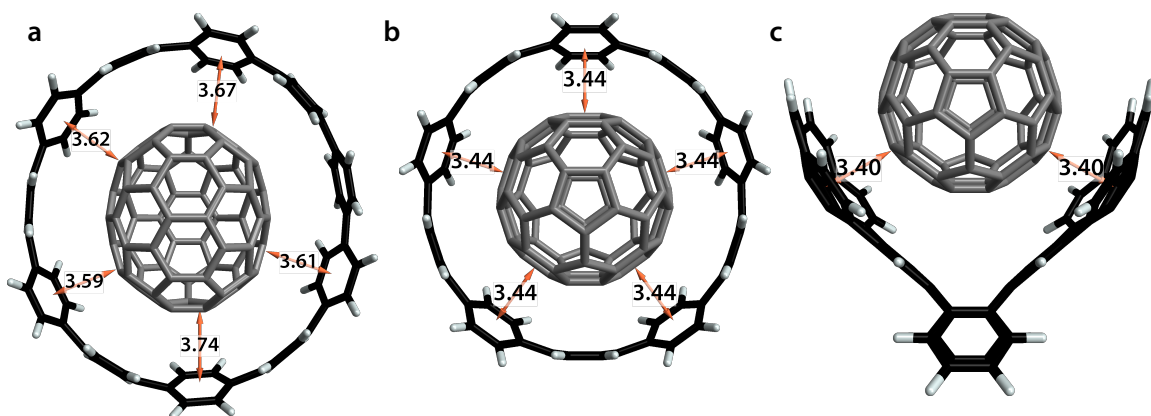
Noncovalent  $\pi$ - $\pi$  interactions is the name given by chemists to the common stacking pattern of planar or locally planar molecular systems that are characterized by  $\pi$  orbitals—the aromatic systems. The binding pattern having its own name is supported by its importance in chemistry and biology.  $\pi$ - $\pi$  interactions play a key role in the formation of the double-helix structure of RNA and DNA by stabilizing the stacked nucleobases (Hunter, 1993). In general, they contribute to most chemical and biological self-assembly mechanisms, including protein folding (Ariga et al., 2008; Zhang, 2003). Biochemical recognition, inherent in drug design, is often driven by stacking of aromatic compounds (Meyer et al., 2003). The recently established field of vdW heterostructures studies layered materials with functional properties designed by precise ordering of layers (Geim and Grigorieva, 2013). The stability of such structures is largely driven by aromatic stacking interactions.

Despite their distinct nature,  $\pi$ - $\pi$  interactions are just a result of the fundamental long-range electron interactions, and as such can be calculated with excellent precision using high-level methods of quantum chemistry, when the systems are small enough that such calculations are feasible. Benzene dimer, a prototypical aromatic stacked system, has been investigated by many authors using methods such as the coupled-cluster theory and symmetry-adapted perturbation theory (SAPT) (Hobza et al., 1996; Kim et al., 2000; Sinnokrot et al., 2002; Sinnokrot and Sherrill, 2006; DiStasio et al., 2007; Podeszwa et al., 2006), and these studies determined its binding energy of  $\sim 2.7$  kcal/mol to within 2% accuracy. But due to their complex formulations, these methods cannot provide any understanding of the binding energy, and hence the stacking pattern, in terms of the underlying electronic motions. The SAPT provides decomposition of the total binding energy in terms of exchange, electrostatic, induction, and dispersion components, but these decompositions are not in any way qualitatively specific to  $\pi$ - $\pi$  interactions. Earlier, Hunter and Sanders (1990) tried to give a qualitative picture of  $\pi$ - $\pi$  interactions in terms of the characteristic arrangement of permanent quadrupole moments in aromatic systems, but this model is not supported by the high-level calculations. This led some to suggest that there is indeed nothing electronically special about  $\pi$ - $\pi$  stacking and that the use of the term  $\pi$ - $\pi$  “interactions” cannot be justified.

On the other hand, long-range plasmon oscillations in low-dimensional zero-gap materials, including the aromatic graphene, lead to characteristic power laws in the dependence of the binding energy on distance (Dobson et al., 2006; Bordag et al., 2006). The zero electronic gap in graphene is directly related to the system of conjugated  $\pi$  bonds, and so at least in this particular case,  $\pi$ - $\pi$  interactions are supported by a particular collective electronic motion. This view was further supported by Misquitta et al. (2010), who showed that the smallness of the gap is inversely proportional to the length scale of the plasmon oscillations and hence the electronic response. In contrast to the high-level methods of quantum chemistry, these plasmon-based models give a good qualitative understanding of the interactions, but cannot provide quantitative description of the binding. This is caused by the analytic formulation of the models, which enables deriving the qualitative results, but cannot be easily extended to the microscopic atomic description.

The MBD method, combined with semilocal KS-DFT calculations, reaches close to the quantitative accuracy of high-level electronic-structure methods, while giving the qualitative insight of simple response models. Furthermore, it is easily applicable to large systems, which are inaccessible to the methods of quantum chemistry. The ability to provide insight stems from the formulation of the MBD method as a simple Hamiltonian model. This gives access to not only the energy, but also the underlying wave function. Using the tools presented in Chapter 4, this wave function can be analyzed, and this analysis can provide answers to the question whether the  $\pi$ - $\pi$  stacking is characterized by some specific electronic phenomenon.

**Figure 5.1 | Equilibrium structures of supramolecular complexes of fullerene C<sub>70</sub>.** The arrows denote the distances from centers of 6-member aromatic rings to the nearest point on the fullerene. The three host molecules are [11]-cycloparaphenylenes (**a**), [10]-cycloparaphenylenes (**b**), and the “buckycatcher” C<sub>60</sub>H<sub>24</sub> (**c**) (Sygula et al., 2007).

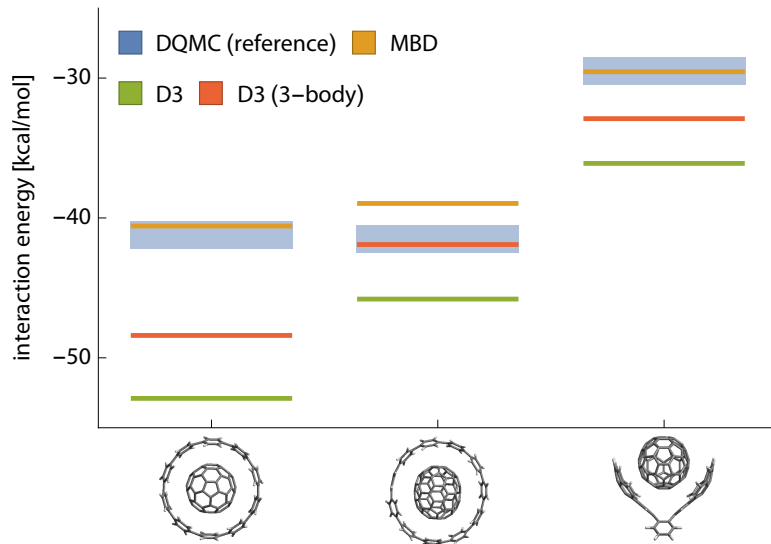


## 5.2 Benchmarking MBD binding energies with DQMC

In general, any interpretations of the results by any DFT+vdW approach are complicated by the ambiguity in the range separation between the short-range DFT part and long-range vdW part. To avoid this issue, we studied  $\pi-\pi$  stacking pattern in supramolecular complexes, where the binding energy is dominated by the long-range part, and all qualitative answers are therefore delegated to the analysis of the MBD method. Furthermore, supramolecular chemistry is a relatively new field with much focus on the design of novel complexes with targeted properties (Kawase, 2012). As such, a good intuitive understanding of the involved interactions is especially important.

We chose three supramolecular complexes (Figure 5.1) as representative examples of  $\pi-\pi$  interactions, which will be denoted C<sub>1</sub>, C<sub>2</sub>, and C<sub>3</sub> in the order introduced below. All three are already synthesized host–guest systems, in which the guest molecule is the C<sub>70</sub> fullerene with D<sub>5h</sub> symmetry, sometimes also called “rugbyballene” for its elongated shape. Two host molecules are [11]- and [10]-cycloparaphenylenes (CPP) (Jasti et al., 2008), which are the simplest precursors of (11, 11) and (10, 10) armchair nanotubes, and the whole complexes with the fullerene molecule are therefore precursors of “nanotube pea pods” (Okada et al., 2001; Monthioux, 2002). The third host is the C<sub>60</sub>H<sub>24</sub> tweezers-like molecule that was specifically designed as a host for the C<sub>60</sub> fullerene (Sygula et al., 2007), hence the name “buckycatcher”. The buckycatcher–fullerene complex is a typical example of convex–concave systems, which are investigated as potential ball-and-socket joint interfaces (Kawase and Kurata, 2006; Kawase, 2012). All three complexes were previously investigated theoretically using the DFT+D3 approach (Grimme, 2012; Risthaus and Grimme, 2013; Antony et al., 2015).

**Figure 5.2 | Binding energies of supramolecular complexes with different methods.** The blue box for the DQMC method has a height of 2 kcal/mol and denotes the statistical uncertainty (70%) of the result.



Before analyzing the binding mechanism within the MBD model, we first want to verify that it describes correctly the binding energetics. In principle, the experimental Gibbs energies of formation could serve as reference data against which the calculated binding energies could be compared. They were measured for all three complexes in a solution, and the obtained values are 7, 7 and 5 kcal/mol (Iwamoto et al., 2013) and (Mück-Lichtenfeld et al., 2010) for  $C_1$  to  $C_3$ , respectively. But calculation of Gibbs energies of formation in a solution from binding energies in vacuum requires further calculations of the temperature and solvation effects. Whereas the temperature effects can be estimated relatively accurately from molecular vibrations using harmonic approximation, the quantitative uncertainty of available solvation models is substantially worse than the accuracy of state-of-the-art DFT+vdW models (Yang et al., 2013).

To avoid these issues, we compare the DFT+MBD binding energies against a higher-level theoretical reference. The size of the complexes prevents the use of the standard reference method of quantum chemistry, the coupled-cluster method with single, double and perturbative triple excitations (CCSD(T)). As a feasible alternative, we chose the DQMC method (Section 2.4), which scales much better with system size and is easily parallelizable, so that calculations on the present systems are feasible. The only potential systematic error in the DQMC method, caused by the fixed-node approximation, has been shown to be negligible for binding energies of vdW complexes (Dubecký et al., 2013), yielding results within 0.1 kcal/mol of the CCSD(T) method.

The binding energies of the three complexes calculated with the DQMC, DFT+MBD and DFT+D3 methods are compared in Figure 4.1. The energies of the complexes were calculated with respect to the energies of the relaxed components. The equilibrium geometries as well as the DFT+D3 results were taken from refs. (Risthaus and Grimme, 2013) ands (Antony et al., 2015). We used the GGA functional of Perdew, Burke, and Ernzerhof (1996a) (PBE) as the short-range complement of the MBD method. In Chapter 6, we show that this functional is particularly consistent in the degree of short-range XC energy that it captures. Being a stochastic method, the DQMC energies are always calculated with a certain statistical uncertainty that can be chosen freely by the amount of computational time invested in the calculation. Here, we chose the uncertainty of  $\pm 1$  kcal/mol, which is enough to judge the accuracy of the DFT+vdW methods. Interestingly, the ratios of the binding energies correspond quite accurately to the ratios of the Gibbs energies of formation. This suggests that temperature and solvation effects do not differ significantly between the three complexes.

The results demonstrate that the PBE+MBD method is able to capture both absolute and relative energetics of the complexes. The largest deviation of PBE+MBD is 2.5 kcal/mol in the case of complex  $C_2$ , while the energies of the other two complexes are estimated withing the statistical error of the DQMC method. The near-degenerate complexes  $C_1$  and  $C_2$  are estimated to be only 1.5 kcal/mol apart. In contrast, the DFT-D3 method systematically overestimates the binding energies by 7–12 kcal/mol, and the  $C_1$  and  $C_2$  complexes differ by 7 kcal/mol. Adding the 3-body correction in D3 improves the systematic overbinding, but the relative energetics of  $C_1$  and  $C_2$  is not improved. In solution at room temperature, the difference of 7 kcal/mol between the two complexes would result in a near nonexistence of  $C_2$ .

### 5.3 Analysis of nonlocal polarizabilities

The failure of the DFT-D3 method is much larger on the relative scale than could be anticipated from its accuracy on smaller complexes, including  $\pi-\pi$  complexes such as benzene dimer. This discrepancy serves as a further motivation for understanding the specific nature of the vdW interactions in  $\pi-\pi$  stacked systems. The two main differences between the D3 and MBD methods are in the models for the atomic dynamic polarizabilities ( $C_6$  coefficients) and in the truncation of the many-body expansion of the ACFD formula (D3 is truncated at second order, third with 3-body correction, MBD is not truncated). In both methods, the polarizability models are mostly local (geometric in D3, density-based in MBD), and any deficiency of the D3 model in this regard would manifest equally in smaller systems, which is not the case, leaving the many-body effects as potential explanation for the overbinding and missing degeneracy in the D3 description.

By evaluating the MBD screening equation in (3.61) for the whole complex, and the host and guest molecules independently, the many-body effects can be formally divided

into intra- and intermolecular. Writing the dipole operator in a block form, where the blocks correspond to the host (h) and guest (g) molecules,

$$\mathbf{T} = \begin{pmatrix} \mathbf{T}_{hh} & \mathbf{T}_{hg} \\ \mathbf{T}_{hg} & \mathbf{T}_{gg} \end{pmatrix} \quad (5.1)$$

the fully coupled nonlocal dipole–dipole polarizability of the complex has an approximately block-diagonal form,

$$\boldsymbol{\alpha} = \boldsymbol{\alpha}_h \oplus \boldsymbol{\alpha}_g + \begin{pmatrix} O(\mathbf{T}_{hg}^2) & O(\mathbf{T}_{hg}) \\ O(\mathbf{T}_{hg}) & O(\mathbf{T}_{hg}^2) \end{pmatrix} \quad (5.2)$$

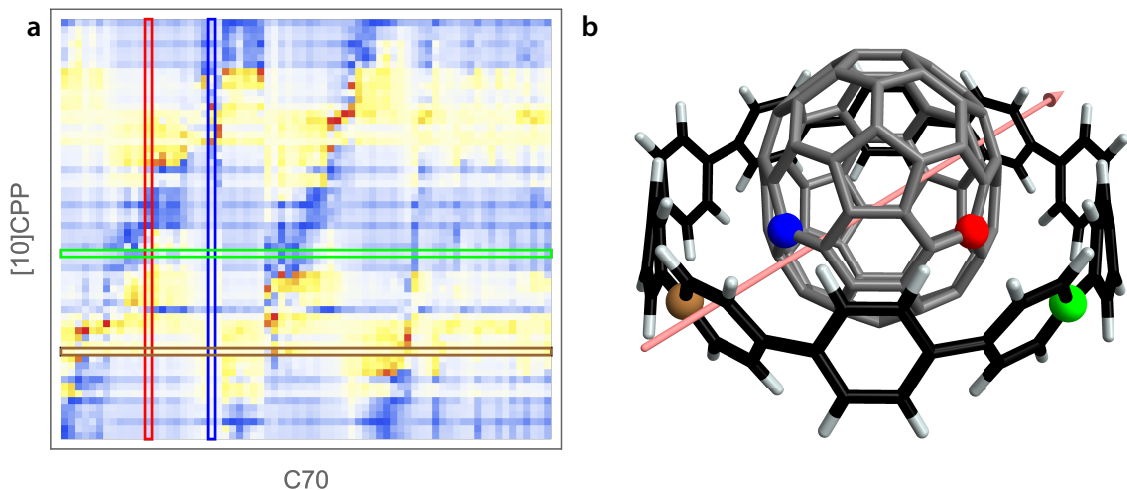
Here, the nonlocal polarizabilities of the isolated host and guest molecules,  $\boldsymbol{\alpha}_h$  and  $\boldsymbol{\alpha}_g$ , capture the intramolecular many-body effects, which are manifested in nontrivial dependence of the total polarizability on system size (Gobre and Tkatchenko, 2013; Ruzsinszky et al., 2012). Whereas the short-range screening usually depolarizes the system under the effect of a field, the long-range intramolecular correlation enhances the polarization. As a result, the total polarizability can be both smaller or greater than the sum of atomic polarizabilities, based on the geometry, size and overall dimensionality of the system. For instance, the bulky geometry of most fullerenes leads to smaller total polarizabilities with respect to the polarizability of  $sp^2$  carbon atoms (Tkatchenko et al., 2012). In contrast, linear and planar geometries often lead to larger polarizabilities, as demonstrated for example by the increased stabilization of linear acene dimers (Grimme, 2008; Ehrlich et al., 2013). In the CPP–C<sub>70</sub> complexes studied here, the electrodynamic screening decreases the total polarizability of the fullerenes by 25% with respect to the sum of the Hirshfeld-scaled free-atom polarizabilities, whereas the polarizability of [10]- and [11]CPP is increased by 31% and 34%, respectively. This small difference cannot explain the inability of the D3 method, in which the intramolecular screening is neglected, to predict the degeneracy between the two complexes.

The off-diagonal blocks,  $\boldsymbol{\alpha}_{hg}$ , in the nonlocal polarizability encode the majority of the intermolecular many-body effects, and are directly related to the binding energy,

$$E_{\text{int,MBD}} = \frac{1}{4\pi} \int_0^\infty du \text{Tr}_{p,\mathbb{R}^3} (\boldsymbol{\alpha}_{hg}(iu)\mathbf{T}_{hg}) + O(\mathbf{T}_{hg}^3) \quad (5.3)$$

(This expression is second-order in the intermolecular coupling, but infinite-order in the intramolecular coupling, so it contains, for instance, all three-atom Axilrod–Teller terms, which are second-order in intermolecular coupling and first-order in intramolecular coupling.) Figure 5.3 shows the off-diagonal part of the polarizability in [10]CPP–C<sub>70</sub>. In the Hamiltonian formulation of the MBD method, the off-diagonal polarizability translates into the difference in the coupled oscillations between the full complex and the isolated host and guest, analyzed in the next section.

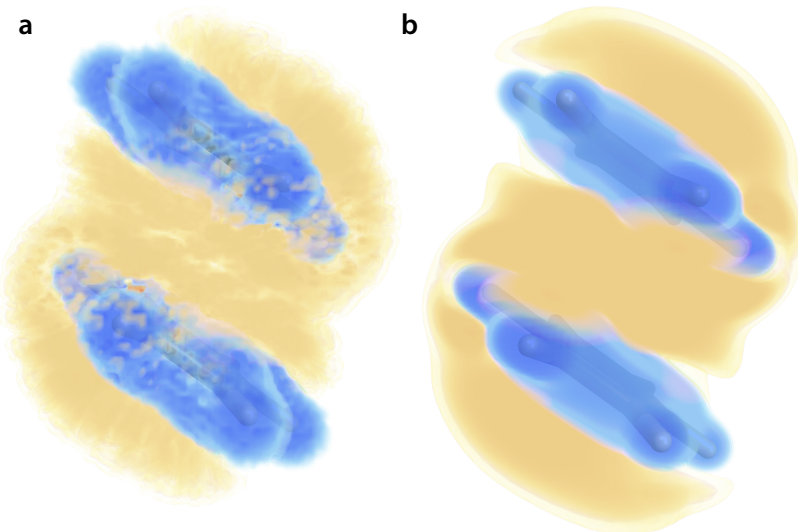
**Figure 5.3 | Intermolecular part of the static nonlocal polarizability in [10]CPP–C<sub>70</sub>.** The heat map (a) shows the carbon–carbon xx elements of the polarizability, with yellow/red and blue colors corresponding to the positive and negative values. The colored stripes denote the atoms depicted with the corresponding color in the molecular structure (b). The pink arrow shows the x axis.



## 5.4 Charge polarization due to $\pi$ - $\pi$ interactions

This section gives some evidence that the MBD Hamiltonian is capable of modeling more aspects of the full electronic system than just its long-range correlation energy. VdW interactions usually induce only a small change in the electronic density (Thonhauser et al., 2007; Vydrov et al., 2008), but can also lead to substantial polarization with measurable effects (Ferri et al., 2015). In the many-body perturbation picture, the long-range intermolecular Coulomb force induces virtual excitations to higher-energy one-particle states, which are always more diffused than the occupied states. As a result, the electron density shifts to the outer regions of the atoms. In DFT, the local KS potential becomes slightly slower decaying with increasing distance from the atoms, which again results in the electron density shifting somewhat outwards. An example of this phenomenon in the case of benzene dimer is shown in Figure 5.4a, calculated with the PBE+TS XC functional (Ferri et al., 2015). In MBD, the interaction between the molecules induces new collective nonlocal oscillations that have on average lower energies than in the isolated fragments, and since oscillators with lower ground-state energy have more diffused wave functions, this leads to a more diffuse total charge density of the oscillators calculated with (4.15). (This approach is different from doing DFT+MBD calculations self-consistently, where the total density would be of the real electrons, only slightly modified by  $\delta E_{\text{MBD}}[n]/\delta n(\mathbf{r})$ .) Comparison on the benzene dimer of the KS-DFT charge polarization due to vdw interactions and of the MBD oscillator polarization (Figure 5.4) shows a remarkable match between

**Figure 5.4 | Charge polarization due to vdW interactions.** Electron density difference (charge polarization) induced by vdW interactions between the benzene dimer and isolated monomers calculated with the PBE+TS XC functional (a) and the MBD Hamiltonian (b). Yellow and blue color represent accumulation and depletion of the charge density, respectively. The magnitude of the polarization is mapped to color saturation, with 50% corresponding to  $2 \times 10^{-5}$  (a.u.).



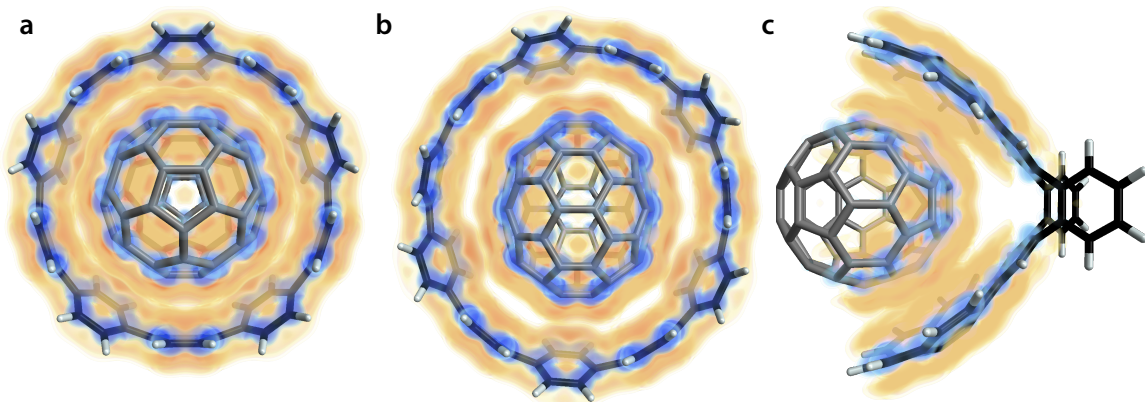
the two approaches. This suggests that although the oscillators in the MBD Hamiltonian cannot in a reasonable way model the total electron density, they can model changes in the electron density induced by long-range electron correlation. The agreement between the KS-DFT and MBD charge polarizations is even quantitative, with 0.0101 and 0.0097 displaced electrons (integral of  $\max(0, \Delta n)$ ), respectively.

Turning back to the supramolecular complexes, their charge polarization due to vdW interactions as calculated from the MBD density is shown in 5.5. The charge polarization gives an indirect measure of which spatial parts of the monomers contribute most to the binding. Comparison of the complexes indicates that the charge fluctuations on the fragments are relatively well separated in the [11]CPP complex, but not in the [10]CPP complex, resulting in stronger many-body effects beyond the second-order (pairwise) expansion of the long-range correlation energy in [10]CPP–C<sub>70</sub>. This explains the stronger overbinding of the [10]CPP complex by the D3 method.

## 5.5 VdW interactions as collective oscillations

The polarization of the MBD charge densities due to intermolecular interactions is a combined effect of all the coupled oscillation modes. This section analyzes the individual modes and their relation to the total binding energy. Solving the MBD Hamiltonian for

**Figure 5.5 | Charge polarization due to vdw interactions.** The same visualization as in Figure 5.4 for the three supramolecular complexes in Figure 5.1.



the complex and the isolated fragments leads to different modes with different energies. Figure 5.6 shows that the distribution of the energies is broadened in the complex with respect to the fragments, so the binding mechanism is not a simple general shift of all the energies. Rather, to first order in  $T_{hg}$ , the energy spectrum is symmetrically broadened, with no change to the total energy, and only in second order in  $T_{hg}$  is the whole spectrum shifted to lower energies, leading to binding. This is in contrast to orbital hybridization in molecules, where the energy splitting can be considered symmetric and the covalent binding arises from partial occupancy. In the MBD ground state, none of the coupled modes are occupied, the total energy is the energy of the zero-point fluctuations, and the binding arises from an asymmetric split of the subsystem energy levels.

Using the decomposition technique from Section 4.3.4, we can identify oscillation modes that contribute most to the binding energy. The decomposition in (4.38) in terms of the coupled modes of the whole complex turns out not to be very useful, because the most organized and collective modes contribute both positively and negatively. In contrast, decomposing the binding energy along the coupled modes of the individual subsystems as in (4.39) leads to mostly binding contributions. To transform back to the full system, we multiply this decomposition by  $P^{\circ 2}$ . The most contributing coupled modes (Figure 5.7) have clear interpretation as global dipole and quadrupole oscillations. These results suggest that an alternative to the pairwise picture of vdw interactions as correlation between dipoles and quadrupoles on pairs of atoms is a collective picture where the whole electronic system oscillates in a wave-like fashion. These molecular oscillations, also called molecular plasmons in other contexts (Lauchner et al., 2015), are of the same nature as plasmons in metals or electronic dipole waves in nanomaterials (Ambrosetti et al., 2016).

So far, we showed that the binding in supramolecular  $\pi-\pi$  complexes can be understood in terms of collective wave-like electronic fluctuations. Next, we demonstrate that this is quite characteristic of these systems, and the oscillations in other types of complexes

**Figure 5.6 | MBD densities of states.** Distributions of the coupled-oscillator energies smoothed with Gaussian broadening of 0.06 eV.

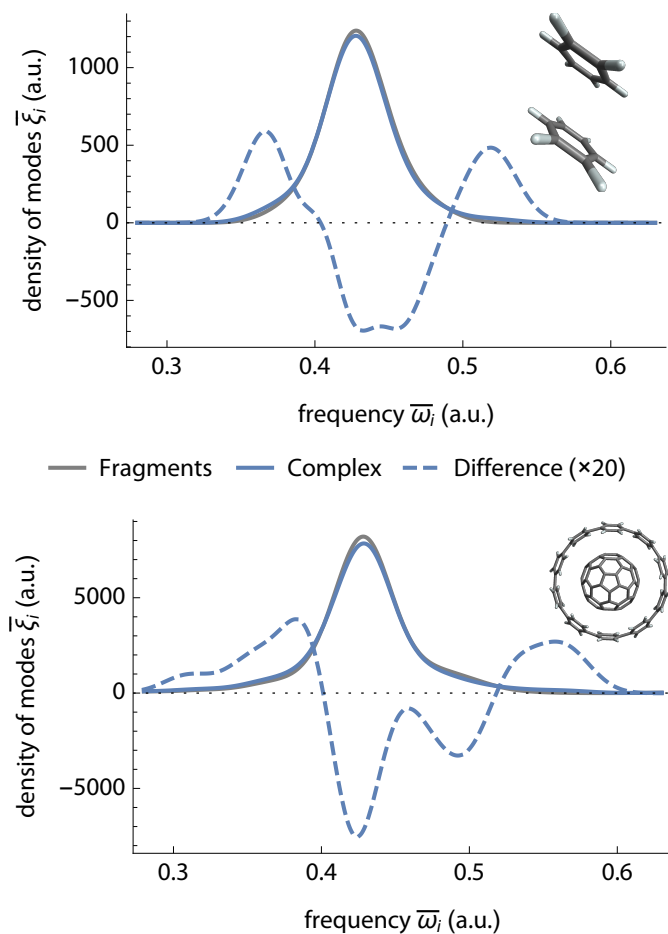
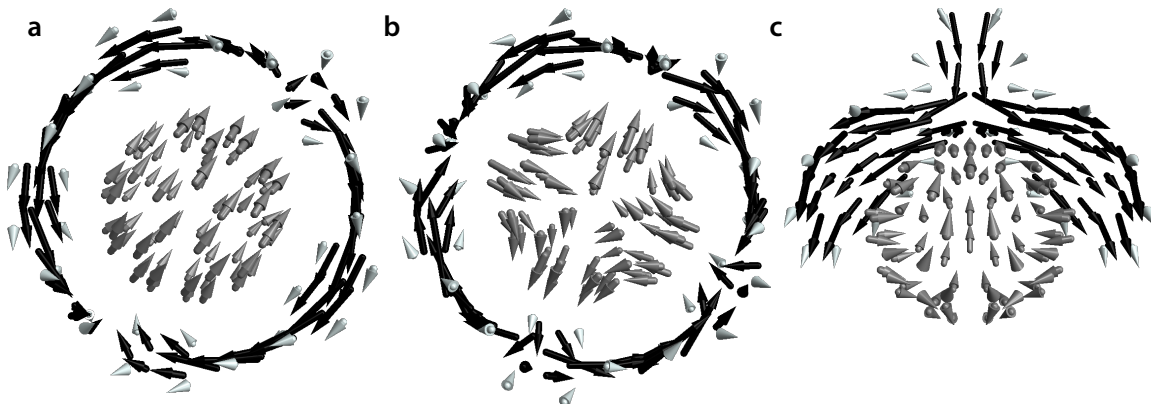


**Figure 5.7 | Most binding oscillation modes.** The doubly degenerate most binding (a) and second most binding (b) oscillation mode of [10]CPP–C<sub>70</sub>, and the most binding mode of buckycatcher–C<sub>70</sub>. The arrow on each atom denotes an in-phase dipole oscillation.

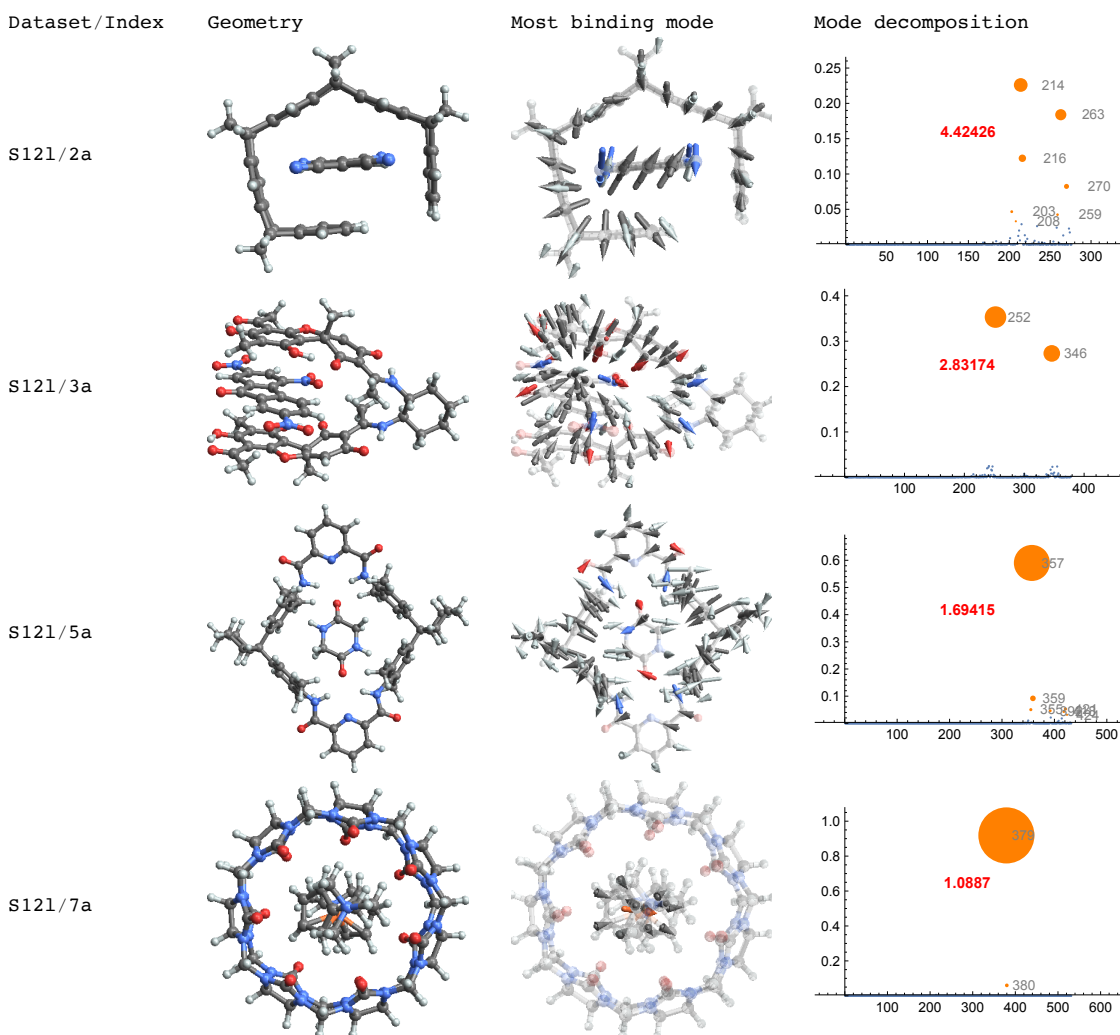


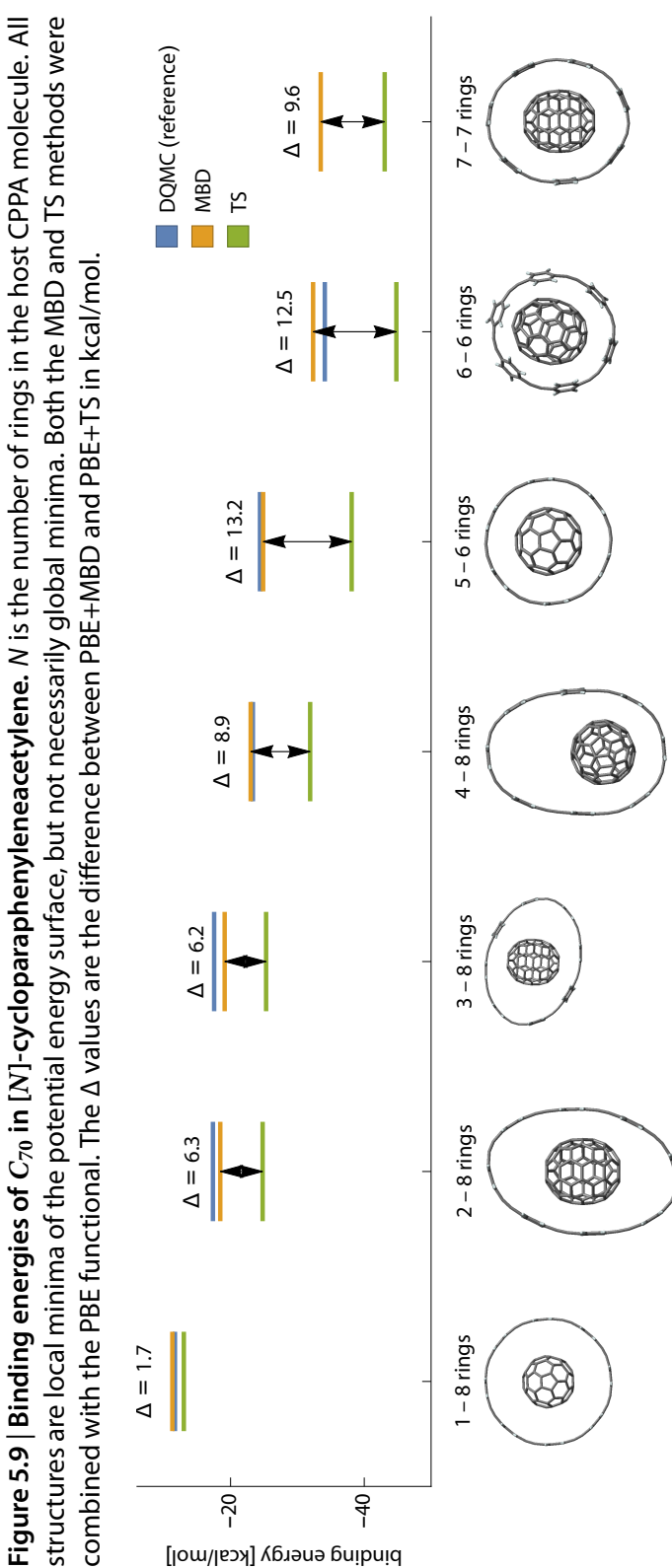
are either localized or disorganized. Figure 5.8 shows the most binding oscillation modes of two  $\pi$ - $\pi$  complexes (2a and 3a) and two complexes which are bound by unspecific vdW and electrostatic interactions (5a and 7a). As in the three fullerene complexes, the most binding mode in the  $\pi$ - $\pi$  complexes is uniformly delocalized over the whole complex. Furthermore, the decomposition of these modes into the subsystem modes shows that they are not dominated by a single subsystem mode, but are a combination of several subsystem modes, indicating their strong coupling. In contrast, the most binding modes of the non- $\pi$ - $\pi$  complexes are rather disorganized, and even if delocalized, the motion has no collective nature. Accordingly, these modes are dominated by a single subsystem mode, so instead of strong coupling as in the stacked complexes, here a single subsystem mode induces only weak oscillations on the other subsystem. This suggests that the long-range electronic oscillations in these systems could be effectively decomposed into pairwise contributions, and indeed, the pairwise approaches are much more accurate for these types of complexes than for the  $\pi$ - $\pi$  complexes.

## 5.6 Testing nonequilibrium geometries

All structures investigated in the previous sections were equilibrium structures. This section presents an extension of the DQMC benchmark of the MBD model to nonequilibrium structures. The higher-order many-body effects are sensitive to the symmetry of the system, and it is imaginable that some hidden error-canceling mechanism in equilibrium structures could lead to the high accuracy of MBD for the three C<sub>70</sub> complexes. However, Figure 5.9 shows that the excellent agreement between PBE+MBD and DQMC is achieved even for several nonequilibrium geometries, with the largest deviation of 1.7 kcal/mol (5%).

**Figure 5.8 | Most binding oscillation modes in different types of binding.** Each row in the table corresponds to a complex from the S12L benchmark dataset (Risthaus and Grimme, 2013). The right-most column shows squares of the coefficients of the decomposition of the most binding mode of the complex into the modes of the monomers. The number in red is the inverse of the largest coefficients. The oscillation arrows are put only on atoms where the magnitude of the dipole is larger than 10% of the maximum magnitude.





In contrast, the pairwise PBE+TS method overbinds the complexes by 2 to 13 kcal/mol. The nonuniform difference between TS and MBD shows that higher-order many-body effects are more sensitive to the geometry than the baseline pairwise vdW energy. In general, the relative difference between TS and MBD is larger in more tightly stacked geometries, which is in line with the larger error of D3 on the [10]CPP–C<sub>70</sub> complex.

# Chapter 6

## Balancing semilocal and nonlocal correlation

This chapter presents a numerical analysis of the general range-separation approach between KS-DFT and vdW methods that served as a basis for Chapter 3. It shows that even though the effective range of semilocal XC functionals is not known explicitly, meaningful information about it can be obtained from the dependence of the DFT+vdW energies on the range-separating parameters of the vdW methods. This approach rationalizes the choice of the underlying XC functional in a DFT+vdW method, which enables unbiased development of new vdW models—the topic of Chapter 8. The analysis stands on a large number of DFT and vdW calculations performed with different programs that are documented in detail in a public git repository ([Hermann and Tkatchenko](#)).

### 6.1 Ambiguity in range separation

As discussed in Section 3.1, the DFT+vdW approach is based on the range separation of the XC energy, where a semilocal or hybrid KS-DFT and a vdW method cover the short- and long-range parts of the XC energy, respectively. In nonmetals, the exchange energy is short-ranged and the long-range XC energy consists only of the correlation energy. The rest of Chapter 3 then reviewed different methods for the long-range correlation energy, in most of which the range-separation is explicitly built-in via some distance-dependent function. But as is clear from the brief exposition in Section 2.7, the range-separation is not explicit in semilocal (hybrid) XC functionals (there is no sense of interelectronic distance in them), but is an implicit and relatively uncontrolled result of their construction and of the general shape of atomic and molecular densities. As a result, the range-separating functions of the vdW methods cannot be guided theoretically by the behavior of the semilocal functionals, but become essentially empirical “damping” functions, whose parameters are fitted to reproduce accurate binding energies or other derived properties when combined with a particular semilocal functional.

In equilibrium, the contribution to the interaction energy of both the KS-DFT and

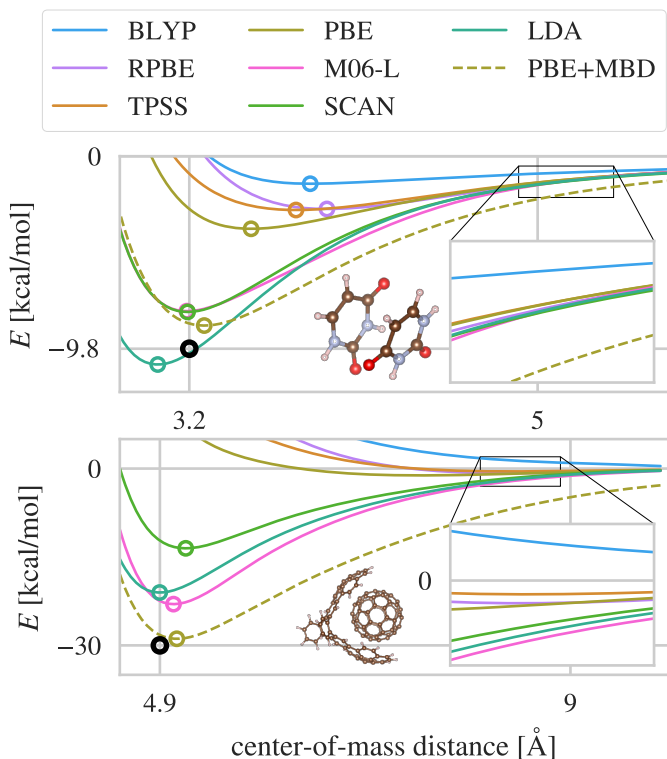
the vdW parts are substantial in most systems, and the empirical approach to the range separation results in a state where it is not clear if a particular success (or failure) of a particular DFT+vdW combination is a result of the semilocal functional, the vdW method, or the system-dependent compatibility between the effective ranges of the two. In an attempt to shed light on this problem, this chapter presents a detailed numerical study of the interplay between the short-range and long-range contributions to the XC energy on a large spectrum of systems. The central part of the analysis is concerned with the dependence of the errors in binding energies of different DFT+vdW combinations on the respective range-separation parameters of the vdW models.

## 6.2 Choice of tested methods and systems

To get as much insight as possible from a numerical analysis, we selected a broad range of semilocal (hybrid) functionals, vdW methods and vdW-bound systems. The XC functionals studied in this work span first four rungs of the “Jacob’s ladder of density functionals” (Perdew and Schmidt, 2001). The first rung is occupied by a single functional, the LDA. Although binding curves calculated with the LDA have incorrect asymptotic behavior and decay too fast, as expected from a local functional, equilibrium binding energies of vdW systems are usually strongly overestimated by LDA. This spurious binding is not caused by the correlation part of LDA, but by the exchange part. This feature is then shared in smaller degree by the next three rungs of the Jacob’s ladder as well. Whereas the HF exchange energy is always a repulsive contribution to the noncovalent interaction energy, many semilocal XC functionals bind noncovalent systems to a certain, usually insufficient degree via their exchange part. This is caused by the implicit cancellation of errors between exchange and correlation in KS-DFT, and is reflected in the fact that most of the literature on the topic of vdW interactions and XC functionals is concerned with exchange, not correlation functionals (Zhang et al., 1997; Peng et al., 2016).

The second rung covers the GGA functionals. It has been in this class of functionals, where most of the search for semilocal functionals with an “appropriate” XC range has been done, and mostly within the context of the vdW-DF nonlocal functional, because of the difficulties with the adaptation of its effective range. Several special-purpose functionals designed to combine well with long-range correlation models were developed, ranging from completely new constructions (Pernal et al., 2009; Wellendorff et al., 2012), to recombinations of older forms (Cooper, 2010; Hamada, 2014; Berland and Hyldgaard, 2014), to simple reparameterizations of standard functionals (Zhang and Yang, 1998; Klimeš et al., 2010, 2011). (An “ideal” exchange functional in this regard would be different from the exact exchange, because it would still contain a part of the short-range post-HF correlation that is not covered by GGA correlation functionals.) All of these functionals perform well for vdW-bound systems (when combined with a vdW model), but not much is known about their accuracy for other systems, preventing them from becoming general

**Figure 6.1 | Range of functionals.** Binding energy curves of a stacked uracil dimer (top) and a C<sub>60</sub>-buckycatcher complex (bottom) with different XC functionals. The circles denote minima, the black circle corresponds to a reference value (see text). PBE+MBD is shown as an example of a method with the correct (algebraic) asymptotic behavior.



methods. Here, we test the most popular general-purpose GGA functional, PBE.

In the context of vdW interactions, considerably less attention has been paid to the to the third rung, the meta-GGA functionals, from which we include two functionals in our study. The meta-GGA of Tao, Perdew, Staroverov, and Scuseria (2003) (TPSS) shares many aspects in its construction with the PBE functional, and also behaves similarly in description of noncovalent systems. In contrast, the “strongly constrained and appropriately normed” (SCAN) functional of Sun et al. (2015) is a substantial departure from PBE. It is a recent development, which is intended to replace PBE for all purposes, with promising results across a broad range of systems in chemistry and physics, in many cases reaching the accuracy of hybrid functionals at a fraction of their computational cost (Sun et al., 2016). SCAN is still only a semilocal functional, however, and does not describe long-range electron correlation, resulting in a lack of long-range vdW interactions, as illustrated in Figure 6.1.

The fourth rung of functionals contains GGAs and meta-GGAs with partial admixture

of exact exchange. As in the HF method, exact exchange does not contribute to the vdW attraction at any distance, but substantially improves accuracy of (meta-)GGAs for many chemical problems. Here, we study the hybrid GGAs PBE0 (Perdew et al., 1996b; Adamo and Barone, 1999) and B3LYP (Becke, 1993). We also analyze SCAN0 (Hui and Chai, 2016), a PBE0-like version of SCAN with 25% of exact exchange. We do not include the fifth-rung functionals, such as the random-phase approximation or double-hybrid functionals, because they already contain long-range electron correlation by construction, at the price of much increased computational cost.

We chose three vdW methods to pair with the semilocal functionals, motivated by the following idea. The semilocal functionals do not have an effective built-in range, but if a particular DFT+vdW is accurate and general, it can be said that the range of the XC functional must be complementary to that of the particular parametrization of the vdW model. Hence, the vdW models, for which the effective range is known explicitly through their range-separation functions, can serve as a probe of the range of the XC functionals. However, since the range separation in these effective models (both semilocal XC and vdW) is certainly not isotropic and is system dependent, judging the effective range from a single vdW method could lead to a bias. To avoid this potential issue, we chose three vdW models with sufficiently different damping mechanisms.

In MBD (Section 3.3.6), the range-separation is controlled by a single sigmoid-shape damping function in (3.50), whose range is controlled via a single parameter,  $B \equiv \beta^{\text{MBD}}$ ,  $A = 6$ , that determines at which fraction of a distance that is a sum of vdW radii of two atoms is the dipole potential damped to 50%. In the VV10 nonlocal functional (Section 3.3.4), the parameter  $D = 3^{\frac{2}{3}} \pi^{\frac{5}{6}} b^{\text{VV10}} / 2$  in (3.34) controls the rate at which the effective resonance frequency of the local dipole response at two points increases (and hence polarizability decreases) as the points get closer to each other. Both MBD and VV10 are functionals of the electron density, and likewise, the damping mechanism is density-dependent. In contrast, the D3 method (Section 3.3.5) depends only on the local geometry of the atomic structure around each atom, and unlike in MBD the atomic vdW radii are fixed and do not depend on the electron density. The particular form of damping in D3 received some attention (Grimme et al., 2011; Schröder et al., 2015; Smith et al., 2016; Witte et al., 2017), and of the two main variants (both based on atomic vdW radii), the original one is similar to that used in MBD, whereas the other, originally from Johnson and Becke (2006) (BJ), has a different limiting behavior at short range. Since our goal here is to cover a broad range of vdW models, we use the BJ damping for its distinction from the damping used in MBD. The BJ-damped D3 method uses three parameters that control its short-range behavior:  $s_8^{\text{D}3}$  controls global mixing of the dipole–quadrupole term (which is inherently short-ranged due to its faster algebraic decay compared to the dipole–dipole term), and the closely related  $a_1^{\text{D}3}$  and  $a_2^{\text{D}3}$  control the onset of the dipole–dipole term ( $a_1^{\text{D}3}$  scales vdW radii,  $a_2^{\text{D}3}$  offsets them).

Whereas the vdW models have an explicit correlation range, the range of semilocal

density functionals is only implicit, and the combined DFT+vdW models are therefore constructed by optimizing the range separation in vdW models against some benchmark properties, usually binding or lattice energies. Several benchmark sets of vdW-bound systems have been established, of which we use predominantly three: the S66 set of 66 smaller organic dimers (Řezáč et al., 2011), the X23 set of 23 molecular crystals (Otero-de-la-Roza and Johnson, 2012; Reilly and Tkatchenko, 2013), and the S12L set of 12 large supramolecular complexes (Grimme, 2012). The S66 set is especially useful here, because each of the 66 dimers is given at 8 intermolecular distances distributed around the equilibrium distance, enabling at least partial separation of the short- and long-range behavior of a method.

Here, we shortly discuss only the expected accuracy of the reference values in the benchmark sets, and refer the reader to the cited works for additional details. The S66 set was benchmarked with the coupled-cluster method with single, double, and perturbative triple excitations at the complete basis-set limit (CCSD(T)/CBS), a method that has been itself benchmarked to give at least an order-of-magnitude more accurate binding energies than any of the DFT+vdW methods investigated here (Řezáč and Hobza, 2013). The X23 benchmark lattice energies were obtained from experimental sublimation enthalpies by subtracting the zero-point vibration energy, with the estimated uncertainty of 1 kcal/mol. This was recently confirmed by CCSD(T) calculations of the benzene crystal (13.4 kcal/mol compared to the benchmark value of 12.4 kcal/mol) (Yang et al., 2014). The S12L reference binding energies were obtained by subtracting calculated solvation and zero-point energies from experimental free energies of association. Such a procedure has inherent uncertainty of several kcal/mol, which is supported by recent accurate diffusion quantum Monte Carlo calculations of the C<sub>70</sub>-buckycatcher complex (30 ± 1 kcal/mol compared to the benchmark value of 27.5 kcal/mol) (Zen et al., 2016).

### 6.3 Basis-set convergence of meta-GGA functionals

Before delving in the analysis, we shortly discuss the issue of converging the KS-DFT binding energies with respect to basis-set size. Table 6.1 shows the binding energy of stacked uracil dimer (Figure 6.1) calculated with the PBE and SCAN functionals, with and without counterpoise correction, and with several different basis sets. With the correlation-consistent basis sets of Dunning (1989), the rate of convergence of both the PBE and SCAN functionals is similar. With counterpoise correction, anything better than cc-pVDZ has acceptable accuracy (~0.2 kcal/mol), and without counterpoise correction, only aug-cc-pVQZ gives such level of accuracy. On the other hand, the numerical basis sets of FHI-aims give sufficient accuracy for PBE without counterpoise correction already on the “tight” level, which is an order of magnitude smaller than aug-cc-pvQZ. Yet for SCAN, the “tight” level without counterpoise correction is insufficient, and only addition of the diffuse functions from the tier-4 group leads to converged binding energies. The

**Table 6.1 | Dependence of PBE and SCAN binding energies (kcal/mol) of parallel-stacked uracil dimer on the basis-set size.**

basis set <sup>a</sup>	PBE		SCAN	
	$\Delta_{\text{CP}}$ <sup>b</sup>	$E_{\text{int}}^{(\text{CP})}$ <sup>c</sup>	$\Delta_{\text{CP}}$	$E_{\text{int}}^{(\text{CP})}$
cc-pVDZ	3.54	-2.07	2.88	-7.07
cc-pVTZ	1.42	-2.63	1.12	-7.82
cc-pVQZ	0.62	-2.72	0.43	-7.93
aug-cc-pVDZ	0.96	-2.70	1.02	-7.97
aug-cc-pVTZ	0.51	-2.75	0.54	-7.97
aug-cc-pVQZ	0.07	-2.76	0.00	-7.98
tight	0.18	-2.69	1.19	-7.92
really_tight	0.19	-2.68	0.90	-7.92
tight+tier-4	-0.29	-2.77	-0.17	-7.99

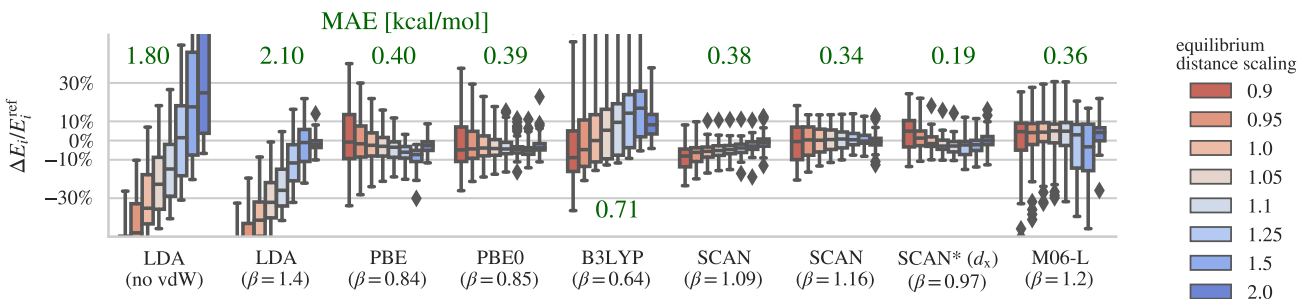
<sup>a</sup>"(aug)-cc-pVXZ" are the correlation-consistent X-zeta basis sets of Dunning (1989), the "tight" basis sets are the default sets of the FHI-aims program (Blum et al., 2009), "+tier-4" denotes the addition of all available basis functions. <sup>b</sup>Difference between the counterpoise corrected and uncorrected binding energies. <sup>c</sup>Counterpoise corrected binding energy.

use of the "tight" basis set leads to systematic overbinding of all vdW bound systems. This behavior is shared by the M06 family of meta-GGA functionals, but not by the TPSS functional. Taking into account the results presented below, the slow convergence of the binding energy can be associated with meta-GGA functionals that take advantage of the abnormal behavior of the density in density-tail overlaps (small density, small reduced gradient, large electron delocalization function) to bind vdW systems more strongly in equilibrium.

## 6.4 Range-separation on benchmark datasets

The performance of approximate DFT+vdW methods on a given benchmark dataset is evaluated by comparing calculated binding energies,  $E_i$ , to the reference values,  $E_i^{\text{ref}}$ , yielding a distribution of errors,  $\Delta E_i = E_i - E_i^{\text{ref}}$ . Since the interaction energies in vdW systems span orders of magnitude, we use relative errors,  $\Delta_r E_i = \Delta E_i / (-E_i^{\text{ref}})$  (assuming  $E_i$  are negative). The comparison of error distributions between different methods and systems is aided by introducing various statistical measures. Two popular measures are the mean absolute error (MAE),  $\sum_i |\Delta E_i| / N$ , and mean absolute relative error (MARE),  $\sum_i |\Delta_r E_i| / N$ , which both individually serve well as a single numerical indicator of performance, but do not provide much insight into the actual error distributions. Instead, we use the mean

**Figure 6.2 | Distributions of relative errors in binding energies on the S66 set of several DFT+MBD combinations.** The distributions are displayed as box-and-whisker plots: a box shows the quartiles and whiskers represent the rest of the distribution, except for outliers that are more than 2.5-fold the interquartile distance from the box, which are shown individually. The x-axis labels denote the functional and the value of the MBD range-separation parameter,  $\beta^{\text{MBD}}$ . The blue-red spectrum encodes the scaling,  $q$ , of the respective equilibrium distances of individual complexes. The green numbers indicate the mean absolute error (kcal/mol) for  $q = 1$ . The values of  $\beta^{\text{MBD}}$  were selected as follows:  $\beta$ -values shown for PBE, PBE0, B3LYP, SCAN\* (see text), and M06-L optimize MARE around  $q = 1$ ;  $\beta = 1.4$  for LDA optimizes MARE for  $q = 2$ ; and for SCAN and all  $q$ ,  $\beta = 1.09$  optimizes SDRE, and  $\beta = 1.16$  optimizes MRE.



relative error (MRE),  $\sum_i \Delta_r E_i / N$ , and the standard deviation of the relative errors (SDRE),

$$\text{SDRE} = \frac{1}{N} \sqrt{\sum_i (\Delta_r E_i - \text{MRE})^2}$$

This enables us to study both the systematic error of a method (overall underbinding or overbinding), represented by MRE, as well as the “statistical” error (how consistent a method is in terms of the range of errors), represented by SDRE.

To study the range of the density functionals LDA, PBE, TPSS, SCAN, PBE0, B3LYP, SCAN0, and M06-L, we evaluated their combinations with the vdW methods MBD, VV10, and D3 at a range of their respective range-separation parameters, on the benchmark sets S66, X23, S12L, and other sets not discussed in this text. We present a subset of these results below in Figures 6.2 and 6.4, while the full data, obtained with FHI-aims (Blum et al., 2009) and Quantum Espresso (Giannozzi et al., 2009; Hamann, 2013), as well as computational details and other resources, are shared via a Git repository (Hermann and Tkatchenko).

The case of the S66 set and different DFT+MBD combinations (Figure 6.2) shows that summarizing the error distributions into a single number such as the mean absolute error reduces the method comparison to a one-dimensional classification, whereas comparing the full distributions in fact reveals distinct patterns specific to individual functionals. Of the tested functionals, LDA is the only one that systematically overbinds S66 at equilibrium

even without any long-range correction. At the same time, when the equilibrium distances are scaled by 2, LDA predicts essentially no binding. In this regard, although LDA binds vdW systems in equilibrium (too) strongly, it is very short-ranged. The tail behavior can be fixed accurately by MBD with  $\beta^{\text{MBD}} = 1.4$ , but the short-range overbinding cannot be compensated by a vdW energy term. The increased overestimation of the XC energy with decreased distance then leads to the well-known underestimation of binding distances by LDA. Already LDA thus illustrates that the degree to which a (semi-)local functional binds vdW systems is in general not a good measure for how well-suited it is for a generally applicable DFT+vdW method.

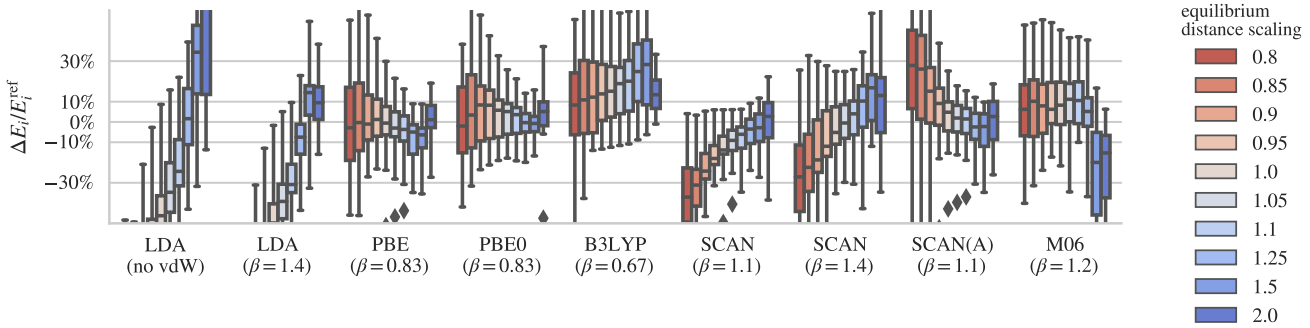
In contrast, both PBE and PBE0 are strongly underbinding S66 at all intermolecular separations, but with MBD and appropriate range separation ( $\beta^{\text{MBD}} \approx 0.83$ ), the resulting PBE+MBD and PBE0+MBD methods are well balanced, with symmetric error distributions, MAE independent of distance, and SDRE monotonously increasing at shorter distances. The admixture of exact exchange decreases SDRE from 10.2% with PBE to 8.7% with PBE0 at equilibrium, but in general has only a small effect. Another hybrid GGA, B3LYP, behaves as a true opposite of LDA, being at the same time very repulsive, yet quite long-ranged. Even with a fairly short-range correlation covered by MBD ( $\beta^{\text{MBD}} \approx 0.7$ ), B3LYP+MBD still underbinds at equilibrium, and perhaps more surprisingly at longer distances. In contrast to PBE/PBE0, the distributions are highly asymmetric, with underbound outliers being mostly the hydrogen-bonded complexes.

With SCAN, optimizing for MRE and SDRE leads to somewhat different values of  $\beta^{\text{MBD}}$ , 1.09 and 1.16, respectively, and correspondingly different error distribution profiles. Both of these  $\beta$  values are substantially larger than that for PBE, demonstrating the potentially longer range of SCAN. When SDRE is optimized, SCAN+MBD has consistently narrower error distributions compared to PBE+MBD across all distances, with a slight systematic overbinding that grows with decreasing distances. When MRE is optimized, the profile of SCAN+MBD is similar to that of PBE+MBD, with smaller outliers. Adding exact exchange in SCAN0 (not shown) has even smaller effect than in PBE0, making the SCAN and SCAN0 error distributions almost indistinguishable.

Finally, M06-L requires only slightly larger amount of long-range correlation than SCAN, and most of the complexes from the S66 set are described well around equilibrium. But several outliers are strongly overbound, and all complexes are overbound at longer distances, which is in line with previous studies (Goerigk, 2015). Both issues may stem from the fact that the heavily fitted M06-L is parametrized also on the S22 set, a smaller version of S66, but S66 contains additional complexes and out-of-equilibrium complexes for which M06-L was not “trained”.

To test the universality of the observations on the S66 set, we have repeated the same analysis for the X40 set of dimers of small halogenated hydrocarbons (Figure 6.3). The overall errors are larger, because of the difficulty of modeling the polarizability of atoms with large partial charge, however, the general trends are similar to those found on the

**Figure 6.3 | Distributions of relative errors in binding energies on the X40 set of several DFT+MBD combinations.**



See Figure 6.2 for caption.

**Table 6.2 | Overall performance of DFT+MBD methods.**

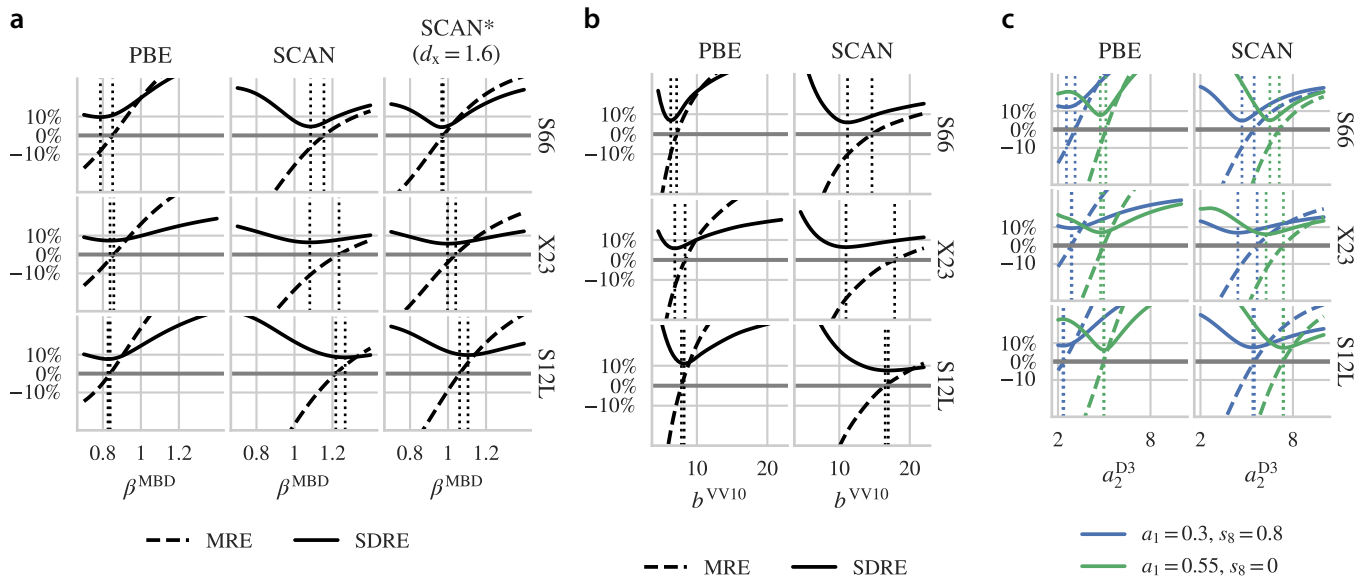
functional	MARE <sup>a</sup>			MRE <sup>b</sup>			$\beta^{\text{MBD,c}}$
	S66	X23	S12L	S66	X23	S12L	
LDA	32%	21%	12%	-31%	-17%	0.1%	$\infty$
B3LYP	15%	8.0%	12%	5.2%	-2.4%	2.5%	0.64
PBE	8.4%	6.1%	5.3%	-2.1%	-2.6%	-0.4%	0.84
PBE0	7.6%	5.4%	6.5%	-1.1%	-1.7%	-4.4%	0.85
SCAN	4.8%	8.4%	11%	-3.0%	-7.7%	-10%	1.12
M06-L	9.2%	16%	29%	2.4%	-16%	-28%	1.20

<sup>a</sup>Mean absolute relative error. <sup>b</sup>Mean relative error. <sup>c</sup>Range-separation parameter of MBD minimizing MARE.

S66 set.

Of the tested functionals, PBE and SCAN (or their hybrid versions) show a potential to work as general balanced DFT+vdW methods. To rule out the possibility that this conclusion about the two functionals is specific to MBD, we studied how MRE and SDRE of their combinations with MBD, VV10, and D3 depend on the respective range-separation parameters (Figure 6.4). Comparing the results for the S66 set shows that all three vdW models have similar behavior, including the increased ambiguity in optimizing either for SDRE or MRE on the X23 set in the case of SCAN. It is the case even for D3, which is potentially more flexible when adapting to a functional thanks to its three parameters. Furthermore, Figure 6.4 shows that whereas the optimal range separation of the vdW models is shared across different system types for the PBE functional, this is not the case for SCAN, for which the XC range seems to grow with the system size. All these observations are true for all three vdW models. Summarized results for other functionals

**Figure 6.4 | Dependence of means (MRE) and standard deviations (SDRE) of relative errors in binding energies on range-separation parameters.** Three long-range correlation models with their respective parameters are shown: (a) MBD with  $\beta^{\text{MBD}}$ , (b) VV10 with  $b^{\text{VV10}}$ , and (c) D3 with  $a_2^{\text{D3}}$ . Density functionals correspond to columns, and benchmark sets to rows within each subplot. Only the equilibrium-distance configurations of the S66 set are used. SCAN\* denotes two reparameterizations of the SCAN functional discussed in the text. The vertical dotted lines show where MRE equals to zero or SDRE reaches minimum. For DFT+D3, two choices are shown of the two other range-separation parameters in D3:  $a_1^{\text{D3}}$  and  $s_8^{\text{D3}}$ .

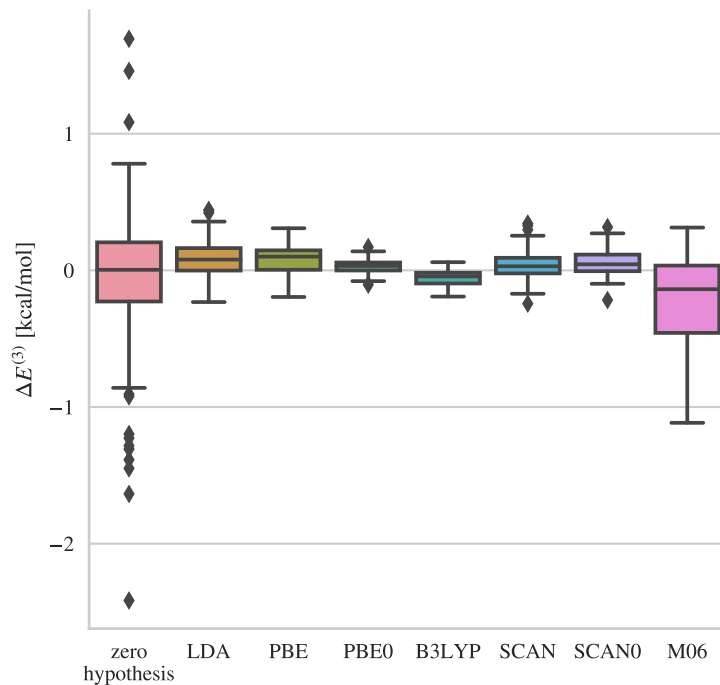


are presented in Table 6.2.

SCAN has been previously combined with VV10 by Peng et al. (2016) and with D3 and VV10 by Brandenburg et al. (2016). The obtained optimal values of  $b^{\text{VV10}}$  were 15.7 and 14.0, respectively, and optimal parametrization of D3 was found to be  $s_8^{\text{D3}} = 0$ ,  $a_1^{\text{D3}} = 0.54$  and  $a_2^{\text{D3}} = 5.4$ . From the results in Figure 6.4, this corresponds to an optimal MRE on S66 for SCAN+VV10 (but systematic overbinding on X23 and S12L), and to optimal statistical error (SDRE) for SCAN+D3, leading again to some degree of systematic overbinding. Brandenburg et al. (2016) associated this tendency mainly with hydrogen-bonded systems, which is in line with the observed overbinding of various ice structures by SCAN (without any vdW correction) (Chen et al., 2016).

Peng et al. (2016) argued that shifting the range separation between a semilocal functional and a vdW model towards the latter is beneficial. Such a shift could also avoid some of the problems that long-range correlation models need to deal with at short range, such as the quadrupole interaction. Our results confirm that such a shift is indeed possible in principle, but with the caveat that the description of the intermediate range by the density

**Figure 6.5 | Distributions of relative errors in 3-body interaction energies on the 3B-69 set.** The box-and-whisker plot is of the same kind as Figure 1 in the main text. The “zero hypothesis” corresponds to a method which always gives zero 3-body interaction energy.



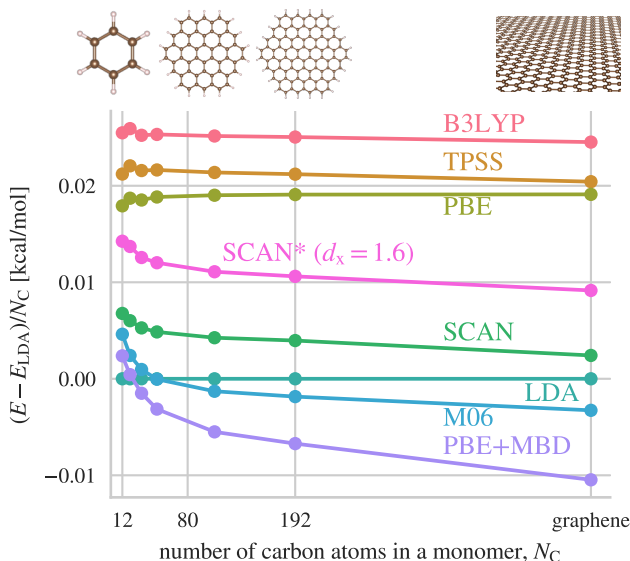
functional must be balanced and independent of system size.

## 6.5 Three-body interactions

The total lattice energy of a molecular crystal can be decomposed into pairwise interactions between molecules, interactions between triples of molecules, etc. Going up to four-body terms, Yang et al. (2014) was able to calculate the lattice energy of the benzene crystal within the accuracy of 0.8 kcal/mol. Previously, Tkatchenko and von Lilienfeld (2008) found that many popular semilocal functionals overestimate the 3-body interaction energies in rare-gas dimers and crystals.

In the context of our present study, the 3B-69 dataset of 3-body interaction energies consists of three trimer structures from each molecular crystal from the X23 dataset (Řezáč et al., 2015). In principle, this set could provide yet another independent (and more sensitive) measure of the range separation. Interestingly, it turns out that the 3-body interaction energies are by far dominated by the short-range contribution from the semilocal functionals rather than the long-range 3-body terms, both with the many-body dispersion method as well as the 3-body correction of the D3 method. Figure 6.5 presents errors in

**Figure 6.6 | Binding energies of graphene-flake dimers.** The individual data points correspond to (increasing in size) benzene, naphthalene, pyrene, coronene, two larger circular hexagonal flakes (shown), and graphene. All dimers are in a parallel-displaced configuration, as cut out from a graphite crystal without any geometry relaxations. The plotted quantity is binding energy with respect to the LDA binding energy, per carbon atom. The (infinite) number of atoms in graphene is set arbitrarily to 500.



the 3-body interaction energies of the 3B-69 set calculated with the semilocal functionals studied above. Compared to a hypothetical method with zero 3-body interaction energies, most functionals give substantially better estimates, the only exception being M06. However, the performance on the 3-body interactions does not seem to correlate with the performance for the total binding energies. The LDA, PBE, and SCAN functionals perform comparably, whereas the B3LYP functional, which is relatively bad on the total binding energies gives very accurate 3-body interaction energies.

## 6.6 System-size scaling

To gain further insight into the range of the functionals beyond statistical analysis, we calculated the binding energies of a series of graphene-flake dimers ranging from a benzene dimer to a graphene bilayer using DFT without any long-range correction (Figure 6.6). We consider LDA as a reference short-range functional, accounting for any potential edge effects, and PBE+MBD as a reference full-range method. The functionals B3LYP, PBE, and TPSS have a similar behavior to LDA, with the binding energies being offset only by a constant. In contrast, the SCAN and M06 show a much stronger dependence on

the system size, both at the small and large ends of the spectrum. The difference in the offset to LDA between benzene dimer and graphene is 60% for M06 and 35% for SCAN with respect to PBE+MBD. The ability to capture at least partially this system-size effect could be seen as advantageous, but it is unfortunate for developing DFT+vdW methods, because it breaks the core assumption that the functionals behave as short-range models of the electron correlation. After all, these functionals are semilocal by construction and the fact that they are sensitive to this strongly nonlocal environment is contradicting this semilocality. Furthermore, there are no known nontrivial exact constraints on the XC energy of overlapping density tails, and so the behavior of current semilocal functionals for such systems is essentially an uncontrolled result of the overall functional design, which complicates any development of “farsighted” density functionals.

Both SCAN and M06 are meta-GGAs, but so is TPSS, which does not show this sensitivity. We speculate that in the case of SCAN, this sensitivity is caused by the particular parametrization of its dependence on the dimensionless electron localization parameter,  $\alpha$ . SCAN uses the density parameter  $\alpha$  in (2.45) directly by interpolating and extrapolating forms constructed for  $\alpha = 0$  and  $\alpha = 1$ , using the following function:

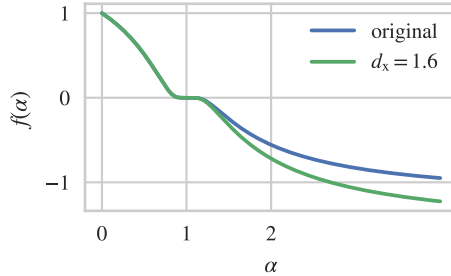
$$f(\alpha) = \exp(-c_{1x}\alpha/(1-\alpha))\theta(1-\alpha) - d_x \exp(c_{2x}/(1-\alpha))\theta(\alpha-1) \quad (6.1)$$

where  $\theta$  is the Heaviside step function, and  $c_{1x} = 0.667$ ,  $c_{2x} = 0.8$ , and  $d_x = 1.24$  are three of the total seven parameters in SCAN which are determined by fitting to properties (norms) of several model systems. The values of  $\alpha$  typically count in single figures within the electronic valence shells and decay slowly to zero with distance from the electronic system, while crossing  $\alpha = 1$  at some point (Sun et al., 2013; Becke and Edgecombe, 1990). Among meta-GGA functionals, SCAN has a relatively wide plateau around  $\alpha = 1$  (due to Eq. 6.1) (Loos, 2017), where the enhancement factor,  $F_x$ , is equal to 1, the value for the uniform electron gas. This results in spatial regions in the electron density tails (dominated by HOMO, the highest-occupied molecular orbital) that are described with a uniform-like functional instead of the more appropriate single-orbital form of  $\alpha \approx 0$ . This can lead to sudden spikes in the exchange-correlation potential fairly outside the spatial regions where covalent bonding occurs (Brandenburg).

## 6.7 SCAN reparametrizations

In the series of graphene-flake dimers, the electronic gap (calculated with SCAN) decreases from 4.7 eV for benzene dimer to 0.9 eV for graphene bilayer, which makes the density tail decay slower with increasing system size. Because the  $\alpha = 1$  behavior of SCAN makes it quite sensitive in the density tails, whose overlap also encodes the vdW bonding on the electron-density level, it only makes sense that SCAN is able to extract the nonlocal information about the system size via the decreasing electronic gap. This mechanism

**Figure 6.7 | Interpolation and extrapolation used in the SCAN exchange functional.** The fixed points that are inter- and extrapolated are  $\alpha = 0$  and  $\alpha = 1$ . The shape of the function is controlled with three parameters,  $c_{1x} = 0.667$ ,  $c_{2x} = 0.8$ , and  $d_x = 1.24$  (original values).



could be also partially responsible for the discrepancies in optimal range separation for SCAN observed on the S66, X23, and S12L sets (Figure 6.4).

To check this hypothesis, we constructed several reparameterizations of SCAN and tested them on these benchmark sets. We focused on the three parameters in Eq. 6.1 because their values are determined weakly, having been fitted only to system-specific rather than universal norms. We found that the overall XC range of SCAN can be changed substantially by modifying either of these parameters, without any regression in the overall performance of the SCAN+vdW methods. However, the systems-size dependence of the optimal range separation for SCAN is not affected by either of them. For illustration, Figures 6.2, 6.4, and 6.6 show results for a SCAN reparametrization with  $d_x$  changed from 1.24 to 1.6, which minimizes the overall error on S66 and reduces the XC range of SCAN (optimal  $\beta^{\text{MBD}}$  of 0.97). Figure 6.6 clearly shows that the reparameterization does not change the sensitivity of SCAN in the density tails, as it only shifts the binding energy in graphene flakes by a constant.

Our toy reparameterization of the SCAN functional illustrates that the XC range of even a very sophisticated functional can be changed by a single parameter, whose value is not fixed by any physical constraint. At the same time, it shows that a more subtle behavior of the XC range such as the system-size dependence is likely a result of the inherent functional form rather than a specific value of a numerical parameter. Furthermore, we did not evaluate any other properties besides vdW binding, and it is quite possible that the new parameter values would introduce regressions for other systems. To give a true alternative parametrization, the original fitting procedure would need to be performed with an additional constraint on vdW binding, perhaps expressed via a single simple system, which is beyond the scope of this work.

## Chapter 7

# Seamless modeling of retarded vdW interactions

This chapter briefly discusses the extension of the MBD method to distances at which the finite speed of light cannot be neglected, resulting in the so-called retarded vdW (Casimir) interactions. Previously, microscopic models of vdW interactions such as MBD were restricted to the non-retarded regime, whereas the macroscopic continuous models used for description of Casimir interactions could not be used at short distances and must have been parametrized from experimental data. Here, we show that these two descriptions can be unified within a single framework, which then enables seamless calculation of vdW energies both at the non-retarded and retarded (Casimir) regimes. This unification also extends the applicability of the new developments in Chapter 8, because any improvements in a model of material response can be directly used in the study of Casimir physics. The results discussed in this chapter have been published in (Venkataram, Hermann, Tkatchenko, and Rodriguez, 2017). The Maxwell-equation scattering calculations were done by Prashanth Venkataram, the DFT and polarizability screening calculations by myself, and the unified theoretical framework is a result of joint work.

The ACFD formula and hence the MBD correlation energy in (3.56) originate from the nonrelativistic quantum mechanics, which assumes that the electromagnetic forces in the form of the Coulomb law acts instantly over any distance. This limits the applicability of MBD to systems that are separated by less than hundreds of angstroms, at which point the time it takes for light to travel between the interacting objects becomes comparable to the frequency of the electronic oscillations that drive the vdW interactions. (The speed of light,  $c$ , in atomic units is approximately 137, the inverse of the fine-structure constant.) The well-known effect of this retardation of the electromagnetic force is the asymptotic  $1/R^7$  attraction that replaces the nonrelativistic  $1/R^6$  power law.

The extension of MBD to account for this retardation consists of two steps. First, the instantaneous dipole operator (eq. 2.54) is replaced with its frequency-dependent retarded

version, which is proportional to the Green's function,  $\mathbf{G}_0$ , of the electric field,

$$\tilde{\mathbf{T}}(\mathbf{R}, u) = \frac{4\pi u^2}{c^2} \mathbf{G}_0 = (\nabla \otimes \nabla' - \frac{u^2}{c^2} \mathbf{I}) e^{-|\mathbf{r}-\mathbf{r}'|u/c} \nu(|\mathbf{r}-\mathbf{r}'|) \Big|_{\substack{\mathbf{r}=\mathbf{R} \\ \mathbf{r}'=0}} \quad (7.1)$$

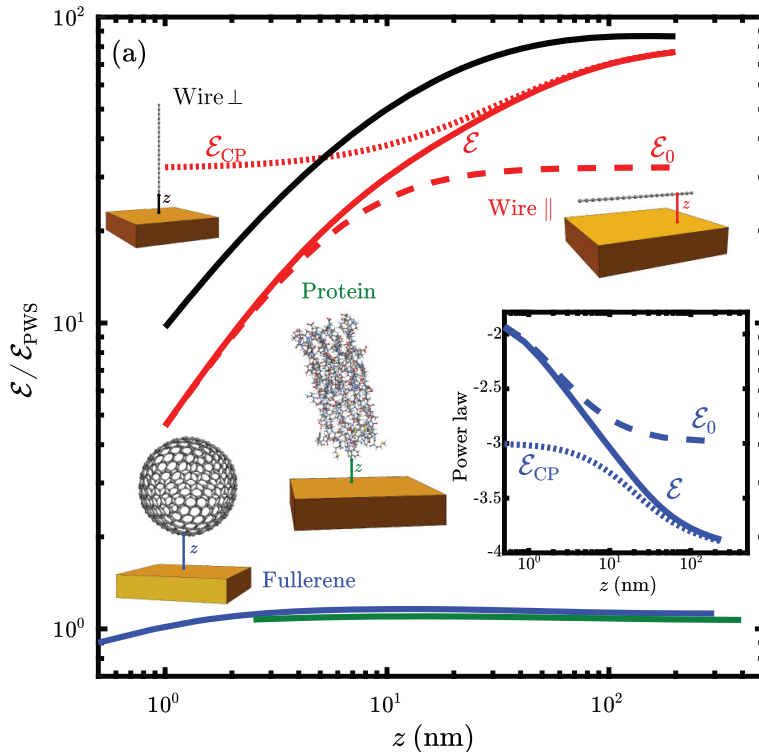
This substitution prevents one to perform the analytic integration over frequencies analytically (see eq. 3.56), but otherwise it is a straightforward modification of the MBD method.

The second step is necessary only because of the kind of systems that we want to study. The prototypical systems studied in the context of Casimir interactions consist of small microscopic bodies such as molecules, and macroscopic objects with nontrivial shapes or surface gratings (Rodriguez et al., 2011; Woods et al., 2016). The latter are typically large enough that microscopic description of individual atoms in them is unnecessary and, furthermore, such large atomic calculations would be unfeasible. As an alternative, efficient approaches solve directly the continuous Maxwell equations either with scattering or finite-differencing methods (Rodriguez et al., 2007; Rahi et al., 2009). This raises the issue of connecting the continuous and microscopic descriptions. It turns out that such a connection is naturally enabled by the form of the MBD expression for the interaction energy. Consider the MBD interaction energy of two bodies,  $A$  and  $B$ ,

$$\begin{aligned} E_{\text{int}} &= E_{AB} - E_A - E_B \\ &= \frac{1}{2\pi} \int_0^\infty du \text{Tr} \left( \ln(1 + (\boldsymbol{\alpha}_A + \boldsymbol{\alpha}_B)\tilde{\mathbf{T}}) - \ln(1 + \boldsymbol{\alpha}_A\tilde{\mathbf{T}}) - \ln(1 + \boldsymbol{\alpha}_B\tilde{\mathbf{T}}) \right) \\ &= \frac{1}{2\pi} \int_0^\infty du \text{Tr} \left( \ln((1 + \boldsymbol{\alpha}_A\tilde{\mathbf{T}} + \boldsymbol{\alpha}_B\tilde{\mathbf{T}})(1 + \boldsymbol{\alpha}_A\tilde{\mathbf{T}})^{-1}(1 + \boldsymbol{\alpha}_B\tilde{\mathbf{T}})^{-1}) \right) \\ &= \frac{1}{2\pi} \int_0^\infty du \text{Tr} \left( \ln((1 + \boldsymbol{\alpha}_B\tilde{\mathbf{T}}(1 + \boldsymbol{\alpha}_A\tilde{\mathbf{T}})^{-1})(1 + \boldsymbol{\alpha}_B\tilde{\mathbf{T}})^{-1}) \right) \\ &\equiv \frac{1}{2\pi} \int_0^\infty du \text{Tr} \left( \ln((1 + \boldsymbol{\alpha}_B\tilde{\mathbf{T}}_A)(1 + \boldsymbol{\alpha}_B\tilde{\mathbf{T}})^{-1}) \right) \\ &= \frac{1}{2\pi} \int_0^\infty du \text{Tr} \left( \ln(1 + \boldsymbol{\alpha}_B\tilde{\mathbf{T}}_A) - \ln(1 + \boldsymbol{\alpha}_B\tilde{\mathbf{T}}) \right) \\ &= E_B(\tilde{\mathbf{T}}_A) - E_B(\tilde{\mathbf{T}}) \end{aligned} \quad (7.2)$$

Here, we defined  $\tilde{\mathbf{T}}_A = \tilde{\mathbf{T}}(1 + \boldsymbol{\alpha}_A\tilde{\mathbf{T}})^{-1}$ , which is the retarded dipole operator screened by the electromagnetic response of the body  $A$ , and the interaction energy between  $A$  and  $B$  was recast as the difference in the total energy of  $B$  calculated with the bare and screened dipole operators. The definition of  $\tilde{\mathbf{T}}_A$  has the form of a Dyson-like equation analogous to that for the interacting nonlocal polarizability, which points to two equivalent points of view on the ground-state system of bodies of matter interacting via the electromagnetic force—one as fluctuating polarizations of the electronic density propagated (in the Green's function sense) by the electromagnetic field, the other as fluctuations in the electromagnetic field propagated by the electronic response of the matter.

**Figure 7.1 | Retardation effects in vdW interactions.** Interaction energies of a perpendicular (black) and parallel (red) carbyne wire, fullerene C<sub>500</sub>, and a protein with a golden surface calculated with different models are plotted relative to the prediction of a pairwise approximation as a function of the vertical distance,  $z$ .  $\mathcal{E}$  is the full retarded MBD method (eq. 7.2),  $\mathcal{E}_0$  is the nonrelativistic approximation ( $c \rightarrow \infty$  in (7.1)), and  $\mathcal{E}_{CP}$  is the so-called “Casimir–Polder approximation” which approximates the whole microscopic object with a single point. The inset shows the local power-law asymptote for the plate–fullerene system.



Using the formulation in (7.2), the MBD interaction energy of a macroscopic body (which can be also a collection of macroscopic bodies) and a set of microscopic objects can be calculated in the following way. First, one obtains the Green’s function of the electric field in the presence of the macroscopic body by an efficient continuous macroscopic method. Second, the screened retarded dipole operator is calculated from the Green’s function using (7.1). Third, the vdW interaction energy is calculated using the regular MBD method with the screened and bare dipole operators according to (7.2). Figure 7.1 illustrates the effects of the retardation on the interactions of several prototypical systems with a golden plate. The full retarded MBD interaction energy calculated with 7.2 transitions between the nonrelativistic approximation (the regular MBD), which becomes exact at short distances, and the relativistic Casimir–Polder approximation, which models the microscopic objects as point objects, and becomes exact at large separations. In this regard,

this unified framework represents a new seamless approach to multi-scale modeling that enables accurate description of intermolecular interactions at a range spanning several orders of magnitude.

## Chapter 8

# Development of a new polarizability functional

The work presented in the last chapter is motivated by a development of a unified and more general vdW method based on the MBD framework (Section 3.3.6). As shown in Chapter 5 and elsewhere (Hermann et al., 2017b), many-body effects can play a profound role in vdW interactions, and the MBD approach is thus an appropriate starting point for a general and accurate vdW model. But the parametrization of the harmonic oscillators based on the free-atom reference values and Hirshfeld-volume scaling used in the MBD method has several disadvantages compared to the local polarizability models of nonlocal density functionals (Section 3.3.4). First, the Hirshfeld-volume model is based on the assumption that the electron density of atoms in molecules and materials is not qualitatively different from isolated atoms, but only contracted to a certain degree by the environment. This is largely the case in systems without strong charge transfer between atoms, but fails considerably in ions, where the added or removed electrons change the electron density significantly, as well as in metals, where the electrons in the conducting bands are completely delocalized from atoms. Second, the Hirshfeld-volume parametrization provides only two of the three parameters that specify a harmonic oscillator (for instance  $(m, q, \omega)$  or  $(\alpha(0), C_6, m)$ ). Whereas these two parameters,  $\alpha(0)$  and  $\omega$  (or equivalently  $C_6$ ), fix the asymptotic long-range interaction, they do not give sufficient information to fix the width of the oscillators. This limitation is avoided either by using the (ambiguous) atomic vdW radii to range-separate the MBD Hamiltonian, or with a semi-classical expression for the oscillator width in terms of the dipole polarizability, which is used in the dipole-screening equation. Besides introducing empirical elements into the model, neither of these approaches can be easily generalized to describe anisotropy in the range separation. Third, the Hirshfeld-volume scheme is inherently tied to atomic partitioning. If, say, one wanted to place additional harmonic oscillators on the centers of covalent bonds, the Hirshfeld partitioning could not support such a model. None of these issues are shared by local polarizability functionals. They have no inherent bias towards neutral atoms, the third oscillator parameter can be obtained from the spatial distribution of the polarizability as quadrupole polarizability (Section 8.1), and any partitioning of space can be directly used

to partition the polarizability and formulate a MBD-like fragment-based method. This chapter investigates the use of polarizability functionals in formulation of a MBD-based vdW method.

In the next section, we analyze how the local polarizability functional yields quadrupole polarizabilities of the interacting fragments, and how these can be used to naturally define the range separation in the MBD approach. The following section then investigates the accuracy of existing polarizability functionals across the periodic table, analyzes the failures, and presents a new functional that is more accurate. The third section deals with the connection between the polarizability functionals and the volume-scaling approach, by comparing the scaling power laws predicted by the functionals to reference benchmark values. Finally, we present an outlook on how to incorporate a local polarizability functional into a complete MBD-based vdW method.

## 8.1 Quadrupole polarizability from polarizability functional

The quadrupole–quadrupole polarizability of an object (isolated atom, any fragment of a molecule, a molecule) is an operator that relates the electric field on the object generated by a distant electric quadrupole to the induced quadrupole moment on the object. Equivalently, it can also be defined as a quadrupole response of the object to a gradient of the electric field. For spherically symmetric objects, such as isolated atoms, the quadrupole–quadrupole polarizability is the lowest nonzero multipole moment of the polarizability after the lowest dipole–dipole moment. Here, we derive the quadrupole–quadrupole polarizability of an object defined by a spatial distribution of the dipole polarizability, which is the model represented by any local polarizability functional.

Consider an object with a local polarizability density,  $\alpha(\mathbf{r})$ , under an influence of an external electric field of the form  $\mathbf{E}(\mathbf{r}) = \mathbf{E}'\mathbf{r}$ ,  $\mathbf{E}'$  being the (constant) spatial derivative of the field,  $\nabla_i E_j(\mathbf{r}) = E'_{ji}$ . The field will induce dipole polarization,  $\mathbf{P} = \alpha\mathbf{E}'\mathbf{r}$ , and the resulting induced quadrupole moment,  $\mathbf{Q}$ , can then be calculated as

$$\begin{aligned} Q_{ij} &= \int d\mathbf{r} \Delta n(\mathbf{r}) \frac{1}{2} (3r_i r_j - r^2 \delta_{ij}) \\ &= \int d\mathbf{r} \nabla \cdot \mathbf{P}(\mathbf{r}) \frac{1}{2} (3r_i r_j - r^2 \delta_{ij}) \quad (\text{p.p.}) \\ &= \int d\mathbf{r} \frac{1}{2} [3(r_i P_j(\mathbf{r}) + r_j P_i(\mathbf{r})) - 2 \sum_m r_m P_m(\mathbf{r}) \delta_{ij}] \\ &= \sum_{kl} \int d\mathbf{r} \frac{1}{2} [3(r_i r_l \alpha_{jk}(\mathbf{r}) + r_j r_l \alpha_{ik}(\mathbf{r})) - 2 \sum_m r_m r_l \alpha_{mk}(\mathbf{r}) \delta_{ij}] E'_{kl} \\ &= \sum_{kl} C_{ijkl} \delta_{ij} E'_{kl} \end{aligned} \quad (8.1)$$

Here,  $C_{ijkl}$  is the quadrupole–quadrupole polarizability of the object in Cartesian coordinates.

All existing polarizability functionals as well as the new ones introduced in this chapter are isotropic,  $\alpha_{ij}(\mathbf{r}) = \alpha(\mathbf{r})\delta_{ij}$ , so that

$$C_{ijkl} = \int d\mathbf{r} \frac{1}{2} [3(r_i r_l \delta_{jk} + r_j r_l \delta_{ik}) - 2 \sum_m r_m r_l \delta_{mk} \delta_{ij}] \alpha(\mathbf{r}) \quad (8.2)$$

As a result, the quadrupole–quadrupole polarizability can be anisotropic even with an isotropic polarizability functional, as long as the density of the object is anisotropic. This is in contrast to the coarse-grained dipole–dipole polarizabilities, which are always isotropic when calculated from an isotropic polarizability functional, regardless of the spatial distribution of the polarizability.

For isotropic objects (such as isolated atoms), however, both dipole–dipole and quadrupole–quadrupole polarizabilities are isotropic. This result can be obtained by setting  $r_i r_j = \delta_{ij} r^2 / 3$  in the expression above, which is valid if the integral is over the whole space and the integrand is radially symmetric,

$$C_{ijkl} = \frac{1}{2} (\delta_{il} \delta_{jk} + \delta_{jl} \delta_{ik} - \frac{2}{3} \delta_{kl} \delta_{ij}) \int d\mathbf{r} \alpha(\mathbf{r}) r^2 \quad (8.3)$$

Here,  $\mathbf{C}$  is an isotropic traceless 4th-order tensor as expected. In the solid-harmonic basis (Section 3.3.1), the corresponding quadrupole polarizability is expressed as

$$\alpha_{22,mm'} = \delta_{mm'} \alpha_2 = \delta_{mm'} \int d\mathbf{r} \alpha(\mathbf{r}) r^2 \quad (8.4)$$

The formula above provides a particularly simple interpretation of the quadrupole polarizability as a second radial moment of the local polarizability distribution. In this regard, it encodes information about the spatial distribution of the polarizability density, and hence can naturally define the width of the oscillators in the MBD model. In particular, the Gaussian width,  $\sigma^2$ , (see eq. 3.58) of the particle density of a quantum harmonic oscillator in ground state is equal to  $1/m\omega = 3\alpha_2(0)/4\alpha(0)$ . By substituting (8.4), we get

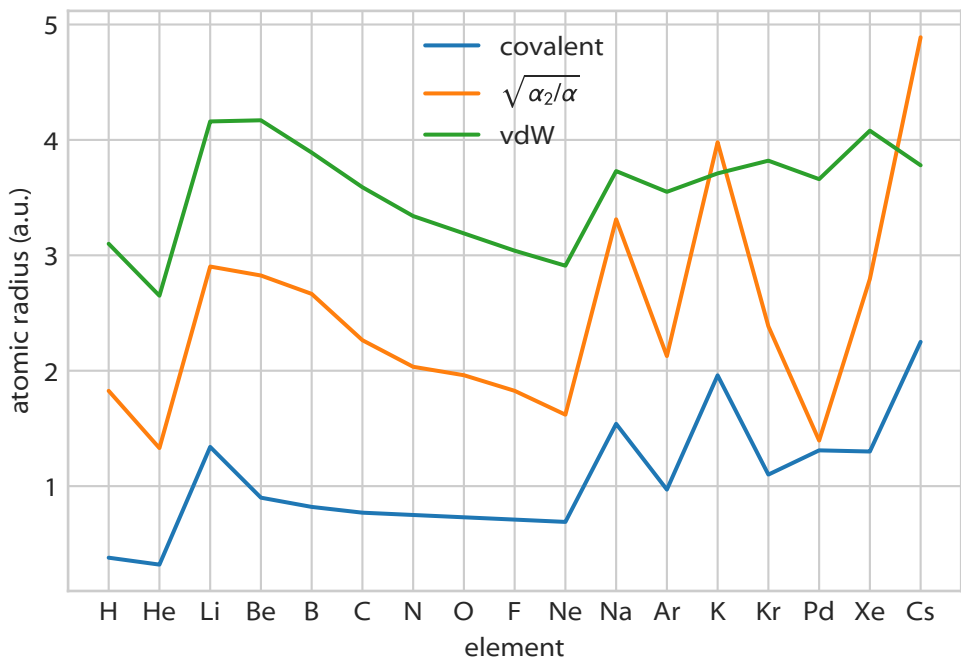
$$\sigma^2 = \frac{3}{4} \frac{\int d\mathbf{r} r^2 \alpha(\mathbf{r}, u=0)}{\int d\mathbf{r} \alpha(\mathbf{r}, u=0)} \quad (8.5)$$

Interestingly, this interpretation of the quadrupole polarizability also yields a new possible definition of atomic radii based on polarizabilities. Assume a model of an atom as a thin spherical shell (representing the valence electrons), where all the polarization response is concentrated at distance  $R_{\text{pol}}$ . It then follows that this radius must satisfy

$$R_{\text{pol}} = \sqrt{\frac{\alpha_2(0)}{\alpha(0)}} \quad (8.6)$$

The magnitude of this “polarizability radius” is between covalent and vdW radii for most atoms (Figure 8.1). Like vdW radii and unlike covalent radii, the polarizability

**Figure 8.1 | Comparison of different definitions of atomic radii.** Covalent radii are taken from (Cordero et al., 2008), vdW radii from (Tkatchenko and Scheffler, 2009; Bondi, 1964). The atomic radius defined from the ratio of the quadrupole and dipole polarizability (yellow) is derived in (8.6).



radii decrease within the second row. Like covalent radii and unlike vdW radii, the polarizability radii of alkali atoms are substantially larger than those of the noble-gas atoms in the same period, and they grow with increasing atomic number. For palladium, the only transition-metal element in the set, the polarizability radius is almost equal to the covalent radius.

## 8.2 Constructing orbital-dependent polarizability functionals

In this section, we generalize the VV polarizability functional (eq. 3.33) to achieve a more balanced performance across the periodic table. This is a first necessary step if the Hirshfeld-scaling is to be replaced with a local polarizability functional without deteriorating accuracy, because the former is exact for isolated atoms by construction. The general form of the VV functional is

$$\alpha_{VV}[n](iu) = \frac{n}{An + B|\nabla n/n|^4 + u^2} \quad (8.7)$$

In the VV functional,  $A = \frac{1}{3} \times 4\pi \doteq 4.2$  is set such that the asymptotic interaction of two spheres of uniform electron gas is reproduced exactly. This value of  $A$  can be also derived from the Clausius–Mossotti equation by taking the dielectric function of the uniform electron gas. But both these arguments have shortcomings. The local polarizability functional is supposed to take into account only exchange and local correlation effects, not the fully nonlocal electron correlation. If it was used in a many-body vdW model to describe the two uniform-gas spheres, the long-range screening would be described explicitly by the model, and should not be accounted for in the polarizability functional. Furthermore, the asymptotic interaction between the spheres was calculated semi-classically (Lucas et al., 1975) without considering any edge effects on the boundary of the sphere where true electron density would decay continuously outside the spherical positively-charged compensating background. The Clausius–Mossotti relation between microscopic polarizability and macroscopic dielectric function is valid only for dielectric materials, which the uniform gas is not, and furthermore, the used Lindhard formula for the dielectric function is only approximate and for the macroscopic response equal to the classical Drude model. In this regard, we consider the particular choice of the value of the parameter  $A$  rather arbitrary.

The value of the parameter  $B \doteq 0.0089$  was fitted to reproduce reference  $C_6$  coefficients in the VV functional. But the following simple reformulation of the VV form gives a clear interpretation of this numerical value. The local resonance frequency,  $\omega^2 = An + B|\nabla n/n|^4$ , is a measure of the electron delocalization—delocalized electrons are more polarizable. Another measure of delocalization is the kinetic energy, which can be seen for example from the local expansion of the electron pair correlation function in (2.44). Correspondingly, the VV functional can be rewritten in terms of the von Weizsäcker kinetic energy functional,

$$\alpha_{VV}[n](iu) = \frac{n}{An + (B'\tau_W/n)^2 + u^2} \quad (8.8)$$

Here,  $B' = 8\sqrt{B} \doteq 0.75$ . The ratio  $\tau_W/n$  in the density tail of any finite electronic system is equal to the ionization potential, while  $\omega$  measures the local effective electronic gap. The value of 0.75 corresponds for instance to the  $1s \rightarrow 2p$  transition in the hydrogen atom, which is the lowest-energy transition that contributes to the dipole polarizability. In this sense, the term  $An$  can be considered as an effective damping that captures the contributions of the higher-energy transitions to the polarizability.

To evaluate the performance of the VV polarizability functional for atoms across the periodic table, we have calculated the dipole and quadrupole polarizabilities and  $C_6$  coefficients for all atoms up to barium (Figure 8.2). We used KS-DFT with the PBE functional and a radial atomic solver to calculate the electronic structure. In general, the VV functional gives reasonable static polarizabilities and  $C_6$  coefficients for  $p$ -block elements, but underestimates them both for  $d$ -block metals and even more for  $s$ -block metals. Surprisingly, static quadrupole polarizabilities are predicted quite accurately even

**Figure 8.2 | VdW parameters across periodic table predicted with polarizability functionals.** From top to bottom, the plots are of the dipole polarizability with respect to the Hirshfeld volume ( $\langle r^5 \rangle$ ), the quadrupole polarizability with respect to  $\langle r^5 \rangle$ , and the homonuclear  $C_6$  coefficient with respect to the square of the Hirshfeld volume.  $Z$  is the atomic number. Plotted are the reference values (black) for the dipole polarizabilities,  $C_6$  coefficients (Gould and Bučko, 2016), and quadrupole polarizabilities (Abdalmoneam and Beck, 2014; Schmidt et al., 1979; Sternheimer, 1970; Reinsch and Meyer, 1978; Sahoo, 2007; Komasa, 2001), as well as the values obtained from the VV10 polarizability functional and the functionals developed in Section 8.2.

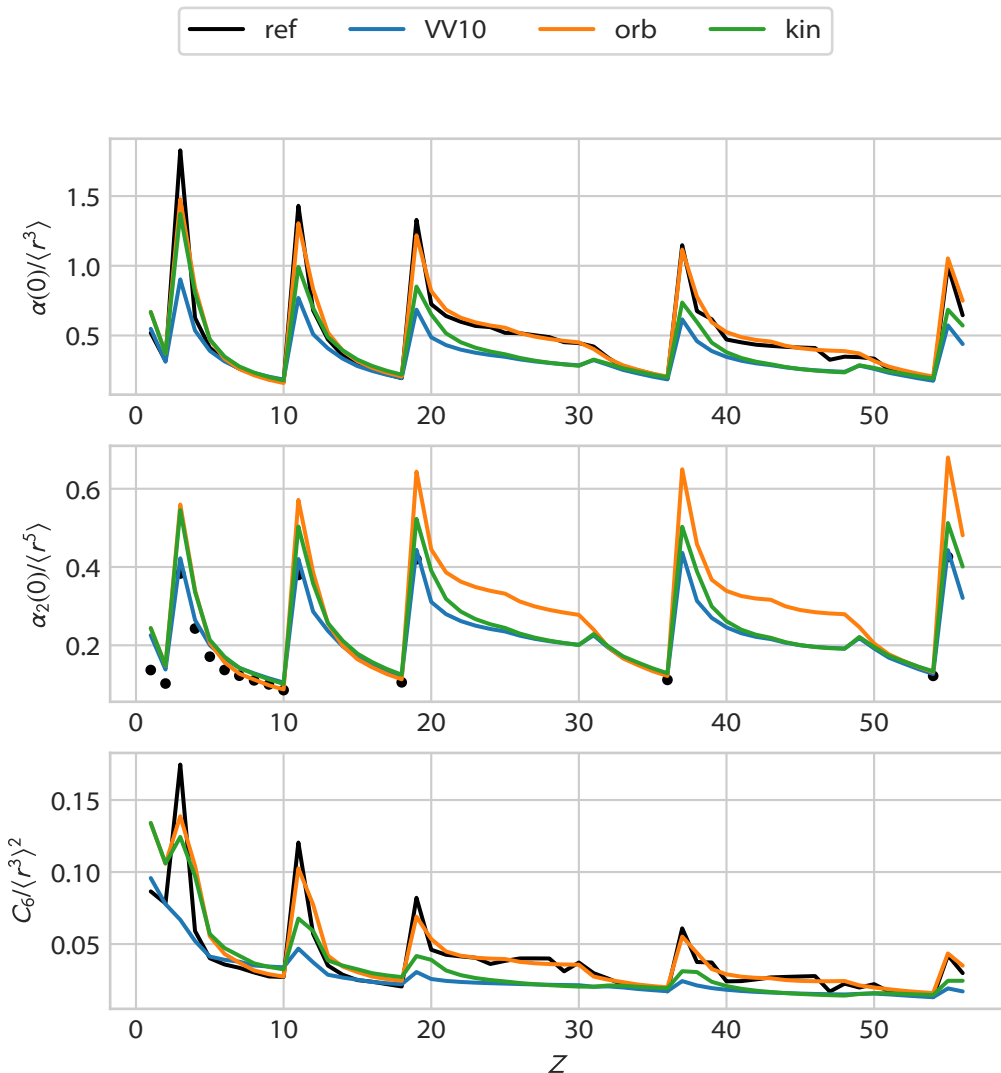
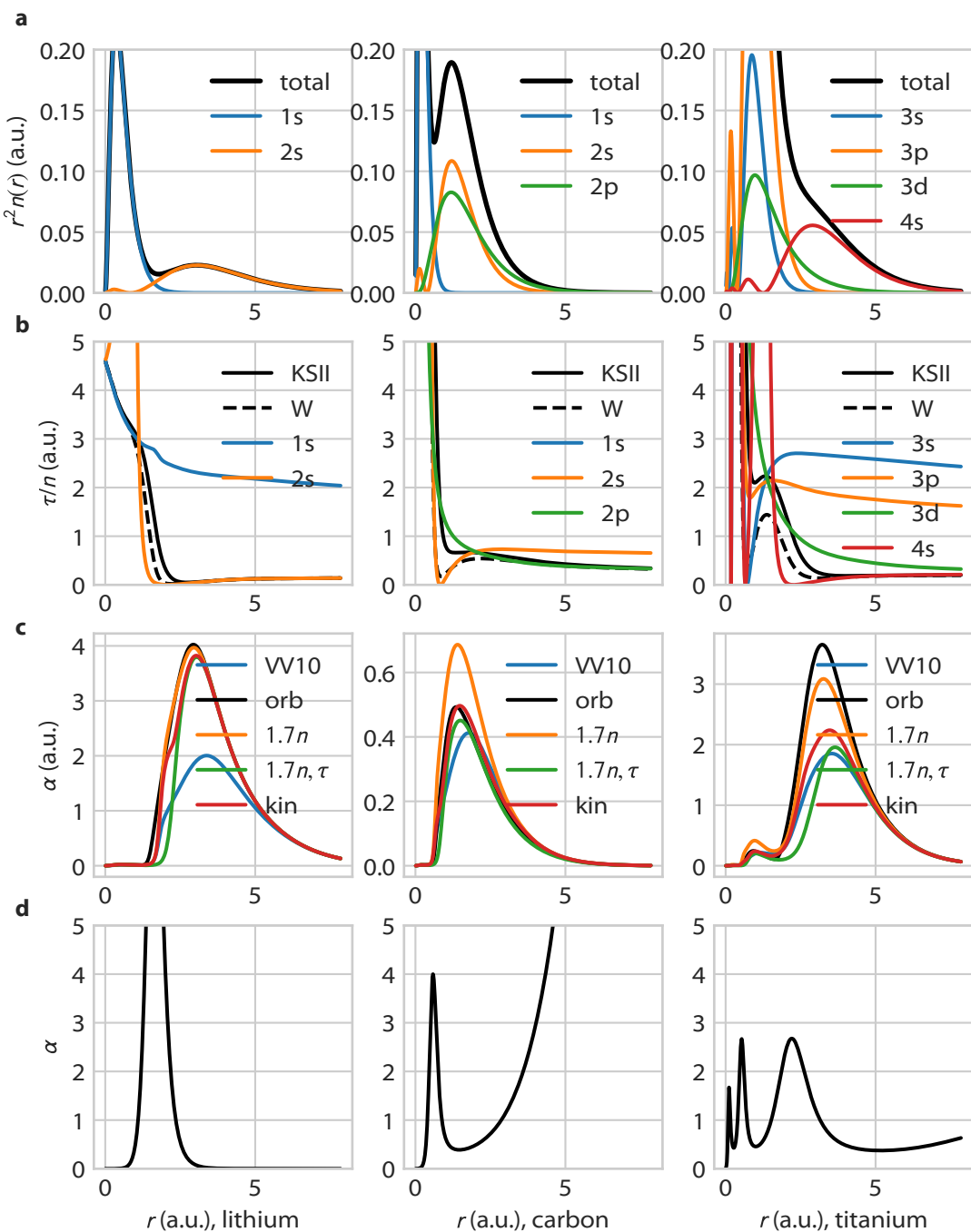


**Figure 8.3 | Polarizability functionals and isolated atoms.** The plots show several density-based quantities in radially symmetric isolated atoms of lithium ( $[\text{He}] 2s^1$ ), carbon ( $[\text{He}] 2s^2 2p^2$ ), and titanium ( $[\text{Ar}] 3d^2 4s^2$ ) in columns from left to right. (a) Radial plots of the total electron density (black),  $r^2 n(r)$ , and its decomposition into individual electron orbitals. (b) The KS kinetic-energy density of the second kind (black, eq. 2.42), its decomposition into electron orbitals, and the von Weizsäcker kinetic-energy functional (black, dashed, eq. 2.43). (c) Local polarizability density from the VV functional as well as new functionals developed in Section 8.2. (d) The electron-localization parameter  $\alpha$  (eq. 2.45).



for *s*-block metals. In terms of a local polarizability model, this can be interpreted such that the response is estimated correctly in the density tails, which dominate the radial contribution to the quadrupole polarizability (due to the  $r^2$  factor in (8.4)), but severely underestimated closer to the nucleus for the *s*- and *d*-metals. To better understand this failure, we have analyzed the individual orbital contributions to the electron density and the different models of the local kinetic energy density (Figure 8.3). Comparison of the lithium (*s*), carbon (*p*), and titanium (*d*) atoms suggests that the differences in the performance between the three blocks of the periodic table may stem from the fact that although the valence electrons are responsible for most of the electronic response (unlike the XC energy, which is dominated by the inner shells), the electron density of the inner electronic shells shields the valence density. A functional that only “sees” the total density cannot recognize between the inner and valence shells, which then leads to the underestimation of the polarizability. This explanation is also in line with the accurate prediction of the quadrupole polarizabilities, which are mostly determined by the regions of the electron density beyond the overlap of the valence and inner shells.

To test this hypothesis, we formulate a generalization of the VV functional that applies a VV-like form to the individual KS orbitals,

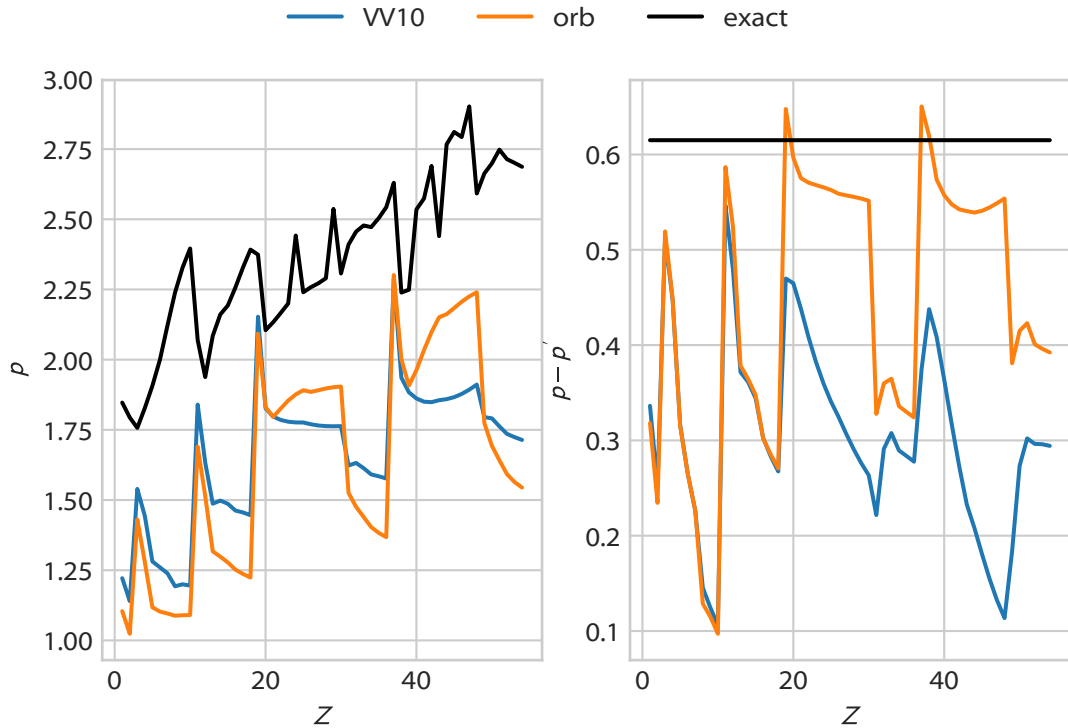
$$\alpha_{\text{orb}}(\mathbf{r}, iu) = \sum_i \frac{f_i |\phi_i(\mathbf{r})|^2}{An(\mathbf{r}) + (B' |\nabla \phi_i(\mathbf{r})|^2 / 2 |\phi_i(\mathbf{r})|^2)^2 + u^2} \quad (8.9)$$

Here,  $f_i$  is the occupation number of the  $i$ -th orbital,  $|\phi_i(\mathbf{r})|^2$  is its normalized electron density, and  $|\nabla \phi_i(\mathbf{r})|^2 / 2$  its contribution to the KS kinetic energy density of the second kind,  $\tau_{\text{II}}$  (eq. 2.42). To retain the good performance of the VV functional for quadrupole polarizabilities, we keep the parameter  $B'$  fixed at the VV value, and optimize  $A = 1.7$  by minimizing the mean absolute relative error in the polarizabilities. Figure 8.2 shows that the new functional, denoted “orb”, improves upon the VV functional for the *s*- and *d*-block elements, while having the same accuracy for the *p*-block species, both in terms of the dipole polarizabilities and  $C_6$  coefficients. Compared to the VV functional, the quadrupole polarizabilities are somewhat overestimated for the *s*-block elements, and there are no available reference data for the *d*-block elements.

The improved performance of the orbital-dependent formulation is promising, but has a theoretical drawback—namely, it is not invariant with respect to orbital rotation. This introduces certain arbitrariness in the model, and makes it computationally more demanding for evaluation in atom-centered basis sets, because the functional cannot be formulated in terms of the density matrix. Figure 8.3d shows that the inter-shell regions are well distinguished by the density parameter  $\alpha$  (eq. (2.45)). As a result, the orbital dependence can be simulated by interpolating between the KS kinetic energy density and the von Weizsäcker functional, which is accurate in the intra-shell regions,

$$\alpha_{\text{kin}}[n](iu) = \frac{n}{An + f(\alpha[n])(B' \tau_W/n)^2 + (1 - f(\alpha[n]))(B' \tau_{\text{KS}}^{\text{II}}/n)^2 + u^2} \quad (8.10)$$

**Figure 8.4 | Scaling of atomic polarizabilities and  $C_6$  coefficients with Hirshfeld volumes.**  $Z$  is the atomic number. The power-law scaling is defined as  $\alpha(0)/\alpha_{\text{free}}(0) = (V/V_{\text{free}})^p$  and  $C_6/C_{6,\text{free}} = (V/V_{\text{free}})^{p'}$ , with the contracted atoms defined by confining with an external potential of the form  $r^2/r_c^3$ . The reference values for  $p$  and  $p'$  are taken from (Gould, 2016). The reference constant difference  $p - p' \approx 0.615$  is accurate to within 0.1 for most elements.

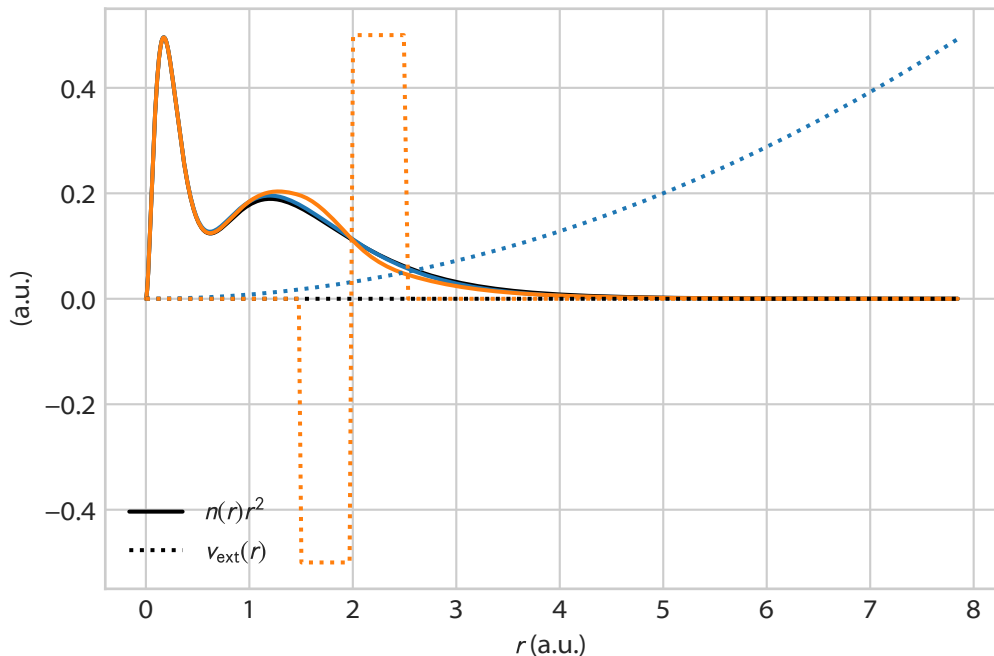


We choose an arbitrary sigmoid function for the interpolation,  $f(\alpha) = (1 + (\alpha - 1)/\sqrt{1 + (\alpha - 1)^2})/2$ , with the switching point at  $\alpha = 1$ , the value that  $\alpha$  has in the uniform electron gas. Figure 8.2 shows that this formulation is a promising improvement over the VV functional for the lighter elements, but the difference between the two functionals becomes small with growing  $Z$ .

### 8.3 Volume-scaling of polarizabilities with polarizability functionals

The polarizability functional should serve as a replacement for the TS volume-scaling approach in the unified MBD model. The TS model assumes (Section 3.3.5) that the polarizability of an atom scales linearly with its Hirshfeld volume ( $p = 1$ ), and the  $C_6$  coefficient with the square of the volume ( $p' = 2$ ). On the other hand, Gould (2016)

**Figure 8.5 | The effect of different confinement potentials on the carbon atom.** The radial quadratic potential (blue) and the radial localized potential at distance corresponding to the C–H distance in methane (yellow) yield the same change in the Hirshfeld volume.



calculated accurate polarizabilities and  $C_6$  coefficients of confined atoms with TD-DFT and found that  $p$  and  $p'$  depend substantially on the atomic number, and range from 1.75 to 2.75 and from 1.15 to 2.1, respectively. We have calculated the scaling coefficients  $p$  and  $p'$  as predicted by the polarizability functionals VV and “orb” by evaluating them on the electron densities of the confined atoms (Figure 8.4). In contrast to the polarizabilities and  $C_6$  coefficients, the volume-scaling behavior is represented rather poorly by the polarizability functionals both qualitatively and quantitatively. The scaling coefficients are underestimated, and the trends within each period of the periodic table are reversed. No significant difference is observed between the VV and “orb” functionals.

To understand better this failure, we investigated the dependence of the scaling behavior on the confining potential. Gould tested polynomial potentials of the form  $r^n/r_c^{n+1}$ , with  $n = 2, 3, 4$ , and found only negligible dependence on  $n$ . But these three potentials are qualitatively similar, and quite different from the confinement that acts on atoms in molecules. Figure 8.5 compares the effect on the carbon atom of the quadratic confining potential ( $n = 2$ ) and a localized step potential at a distance corresponding to the C–H distance in methane. Although the effect on the Hirshfeld volume is the same in both cases (reduction by 20%, c.f. 30% in methane), the latter has a much stronger effect. This is caused by the strong sensitivity of the Hirshfeld volume on the density-tail behavior due

to the  $r^3$  factor. Likewise, the two potentials differ in their effect on the polarizability as predicted by the polarizability functionals. Whereas the quadratic potential yields  $p' = 1.0$  (reference value of  $p' = 1.4$ ), the localized potential yields  $p' = 1.4$  (no reference available). The same values are obtained both with the VV and “orb” polarizability functional. Given the lack of available reference volume-scaling data for other than the polynomial confining potentials, these results have two potential interpretations. Either the true volume-scaling behavior is indeed independent of the confining potential shape, and the difference in the scaling coefficients predicted by the polarizability functionals is artificial. This would mean that the functionals perform better for more realistic confinements. The other interpretation would be that the volume-scaling behavior depends significantly on the potential shape, in which case the reference results from the polynomial potentials do not bear much relevance to the confinement of atoms in molecules. In either case, the large deviations of the polarizability functionals from the reference values in Figure 8.4 do not necessarily have implications for the accuracy of the functionals in realistic molecules and materials.

## 8.4 Outlook on future development

In this final section, we outline the path towards a complete MBD-based vdW model that uses the polarizability functional developed above. The goal of such a method is to unify the accuracy of MBD with the electronic-structure universality of nonlocal vdW functionals (such as VV10).

**Partitioning** The first step in formulating a coarse-grained model is the choice of partitioning of the space into fragments. In the approach based on scaling free-atom values with Hirshfeld-volume ratios (the TS model), the total polarizability (even before any screening) depends on the choice of the partitioning, which makes the choice particularly important. This is the reason why the TS method based on iterative Hirshfeld partitioning gives significantly better results for ionic system than regular Hirshfeld partitioning. In contrast, the total polarizability of a system described by a local polarizability functional is simply an integral over the whole space, and is independent of a particular partitioning. The choice should therefore play a less important role, and any atomic partitioning should be sufficient.

**Free-atom reference data** One of the core advantages of the TS method that makes it accurate is the use of reference data for free atoms. The orbital-dependent formulation of the VV functional developed above improves its performance across the periodic table, but still is not exact. A straightforward correction that makes the model exact for free atoms is to scale the coarse-grained polarizabilities of atoms in

a molecule with the ratio of the exact and approximate polarizability of free atoms,

$$\alpha_i(iu) = \frac{\alpha_{i,\text{free,ref}}(0)}{\alpha_{i,\text{free},\alpha[n]}(0)} \int d\mathbf{r} w_i(\mathbf{r}) \alpha[n](\mathbf{r}, iu) \quad (8.11)$$

**Polarizability screening** The use of the density gradient in GGA functionals and of the kinetic-energy density in meta-GGA functionals makes them in general longer-ranged than the LDA, which uses only the density (Chapter 6), because the density derivatives encode more detailed information about the electronic structure. Along the same lines, the local polarizability functionals, which use semilocal density information, can be expected to capture larger portion of the effect of neighboring atoms on the polarizability than the Hirshfeld-volume scaling that uses only the electron density. We expect that this may render the short-range polarizability screening unnecessary.

**Range separation** As discussed in Section 8.1, the quadrupole polarizabilities that can be calculated from a local polarizability functional provide a natural measure of the width of the fragments represented by harmonic oscillators. This enables replacing the range-separation based on vdW radii with a scheme that is independent of explicit free-atom reference, which has two advantages. First, it enables the potential use of finer partitioning that is only partially based on atoms. For instance, one could consider placing a fragment on each covalent bond in the system. This would make the coarse-graining finer and would limit the errors associated with neglecting higher multipole moments. Second, the quadrupole polarizabilities calculated even from an isotropic polarizability functional are in general anisotropic, and thus naturally lead to anisotropic range separation. This should prove especially useful for hybrid interfaces, where the electron density on a metallic surface is strongly delocalized in the directions parallel to the surface, but localized in the perpendicular direction.

## References

- M. H. Abdalmoneam and D. R. Beck. Dipole and quadrupole polarizabilities of Ni II and parameters of an effective potential for Ni I Rydberg states. *J. Phys. B: At. Mol. Opt. Phys.*, 47(8):085003, 2014. doi:[10.1088/0953-4075/47/8/085003](https://doi.org/10.1088/0953-4075/47/8/085003).
- C. Adamo and V. Barone. Toward reliable density functional methods without adjustable parameters: The PBE0 model. *J. Chem. Phys.*, 110(13):6158–6170, Mar. 1999. doi:[10.1063/1.478522](https://doi.org/10.1063/1.478522).
- S. L. Adler. Quantum theory of the dielectric constant in real solids. *Phys. Rev.*, 126(2):413–420, Apr. 1962. doi:[10.1103/PhysRev.126.413](https://doi.org/10.1103/PhysRev.126.413).
- A. Ambrosetti, A. M. Reilly, R. A. DiStasio, Jr., and A. Tkatchenko. Long-range correlation energy calculated from coupled atomic response functions. *J. Chem. Phys.*, 140(18):18A508, May 2014. doi:[10.1063/1.4865104](https://doi.org/10.1063/1.4865104).
- A. Ambrosetti, N. Ferri, R. A. DiStasio, Jr., and A. Tkatchenko. Wavelike charge density fluctuations and van der Waals interactions at the nanoscale. *Science*, 351(6278):1171–1176, Mar. 2016. doi:[10.1126/science.aae0509](https://doi.org/10.1126/science.aae0509).
- Y. Andersson, D. C. Langreth, and B. I. Lundqvist. Van der Waals interactions in density-functional theory. *Phys. Rev. Lett.*, 76(1):102–105, Jan. 1996. doi:[10.1103/PhysRevLett.76.102](https://doi.org/10.1103/PhysRevLett.76.102).
- J. G. Ángyán. On the exchange-hole model of London dispersion forces. *J. Chem. Phys.*, 127(2):024108, July 2007. doi:[10.1063/1.2749512](https://doi.org/10.1063/1.2749512).
- J. G. Ángyán, R.-F. Liu, J. Toulouse, and G. Jansen. Correlation Energy Expressions from the Adiabatic-Connection Fluctuation–Dissipation Theorem Approach. *J. Chem. Theory Comput.*, 7(10):3116–3130, 2011. doi:[10.1021/ct200501r](https://doi.org/10.1021/ct200501r).
- J. Antony, R. Sure, and S. Grimme. Using dispersion-corrected density functional theory to understand supramolecular binding thermodynamics. *Chem. Commun.*, 51(10):1764–1774, Jan. 2015. doi:[10.1039/C4CC06722C](https://doi.org/10.1039/C4CC06722C).
- K. Ariga, J. P. Hill, M. V. Lee, A. Vinu, R. Charvet, and S. Acharya. Challenges and breakthroughs in recent research on self-assembly. *Sci. Technol. Adv. Mater.*, 9(1):014109, Jan. 2008. doi:[10.1088/1468-6996/9/1/014109](https://doi.org/10.1088/1468-6996/9/1/014109).
- B. M. Axilrod and E. Teller. Interaction of the van der Waals type between three atoms. *J. Chem. Phys.*, 11(6):299–300, June 1943. doi:[10.1063/1.1723844](https://doi.org/10.1063/1.1723844).
- P. W. Ayers. A perspective on the link between the exchange(-correlation) hole and dispersion forces. *J. Math. Chem.*, 46(1):86–96, 2009. doi:[10.1007/s10910-008-9451-y](https://doi.org/10.1007/s10910-008-9451-y).
- W. L. Bade. Drude-Model Calculation of Dispersion Forces. I. General Theory. *J. Chem. Phys.*, 27(6):1280–1284, Dec. 1957. doi:[10.1063/1.1743991](https://doi.org/10.1063/1.1743991).
- W. L. Bade and J. G. Kirkwood. Drude-Model Calculation of Dispersion Forces. II. The Linear Lattice. *J. Chem. Phys.*, 27(6):1284–1288, Dec. 1957. doi:[10.1063/1.1743992](https://doi.org/10.1063/1.1743992).
- A. D. Becke. A multicenter numerical integration scheme for polyatomic molecules. *J. Chem. Phys.*, 88(4):2547–2553, Feb. 1988. doi:[10.1063/1.454033](https://doi.org/10.1063/1.454033).
- A. D. Becke. Density-functional thermochemistry. III. The role of exact exchange. *J. Chem. Phys.*, 98(7):5648–5652, Apr. 1993. doi:[10.1063/1.464913](https://doi.org/10.1063/1.464913).

- A. D. Becke and K. E. Edgecombe. A simple measure of electron localization in atomic and molecular systems. *J. Chem. Phys.*, 92(9):5397–5403, May 1990. doi:[10.1063/1.458517](https://doi.org/10.1063/1.458517).
- A. D. Becke and E. R. Johnson. A density-functional model of the dispersion interaction. *J. Chem. Phys.*, 123(15):154101, Oct. 2005a. doi:[10.1063/1.2065267](https://doi.org/10.1063/1.2065267).
- A. D. Becke and E. R. Johnson. Exchange-hole dipole moment and the dispersion interaction. *J. Chem. Phys.*, 122(15):154104, Apr. 2005b. doi:[10.1063/1.1884601](https://doi.org/10.1063/1.1884601).
- A. D. Becke and E. R. Johnson. Exchange-hole dipole moment and the dispersion interaction: High-order dispersion coefficients. *J. Chem. Phys.*, 124(1):014104, Jan. 2006. doi:[10.1063/1.2139668](https://doi.org/10.1063/1.2139668).
- A. D. Becke and E. R. Johnson. Exchange-hole dipole moment and the dispersion interaction revisited. *J. Chem. Phys.*, 127(15):154108, Oct. 2007. doi:[10.1063/1.2795701](https://doi.org/10.1063/1.2795701).
- A. D. Becke and M. R. Roussel. Exchange holes in inhomogeneous systems: A coordinate-space model. *Phys. Rev. A*, 39(8):3761–3767, Apr. 1989. doi:[10.1103/PhysRevA.39.3761](https://doi.org/10.1103/PhysRevA.39.3761).
- K. Berland and P. Hyldgaard. Exchange functional that tests the robustness of the plasmon description of the van der Waals density functional. *Phys. Rev. B*, 89(3):035412, Jan. 2014. doi:[10.1103/PhysRevB.89.035412](https://doi.org/10.1103/PhysRevB.89.035412).
- M. A. Blood-Forsythe, T. Markovich, R. A. DiStasio, Jr., R. Car, and A. Aspuru-Guzik. Analytical nuclear gradients for the range-separated many-body dispersion model of noncovalent interactions. *Chem. Sci.*, 7(3):1712–1728, Feb. 2016. doi:[10.1039/C5SC03234B](https://doi.org/10.1039/C5SC03234B).
- V. Blum, R. Gehrke, F. Hanke, P. Havu, V. Havu, X. Ren, K. Reuter, and M. Scheffler. Ab initio molecular simulations with numeric atom-centered orbitals. *Comput. Phys. Commun.*, 180(11):2175–2196, Nov. 2009. doi:[10.1016/j.cpc.2009.06.022](https://doi.org/10.1016/j.cpc.2009.06.022).
- D. Bohm and D. Pines. A Collective Description of Electron Interactions. I. Magnetic Interactions. *Phys. Rev.*, 82(5):625–634, June 1951. doi:[10.1103/PhysRev.82.625](https://doi.org/10.1103/PhysRev.82.625).
- D. Bohm and D. Pines. A Collective Description of Electron Interactions: III. Coulomb Interactions in a Degenerate Electron Gas. *Phys. Rev.*, 92(3):609–625, Nov. 1953. doi:[10.1103/PhysRev.92.609](https://doi.org/10.1103/PhysRev.92.609).
- A. Bondi. Van der Waals Volumes and Radii. *J. Phys. Chem.*, 68(3):441–451, Mar. 1964. doi:[10.1021/j100785a001](https://doi.org/10.1021/j100785a001).
- M. Bordag, B. Geyer, G. L. Klimchitskaya, and V. M. Mostepanenko. Lifshitz-type formulas for graphene and single-wall carbon nanotubes: Van der Waals and Casimir interactions. *Phys. Rev. B*, 74(20):205431, Nov. 2006. doi:[10.1103/PhysRevB.74.205431](https://doi.org/10.1103/PhysRevB.74.205431).
- M. Born and R. Oppenheimer. Zur Quantentheorie der Moleküle [On quantum theory of molecules]. *Ann. Phys.*, 389(20):457–484, Jan. 1927. doi:[10.1002/andp.19273892002](https://doi.org/10.1002/andp.19273892002).
- G. J. Bowden and R. G. Clark. Fourier transforms of dipole-dipole interactions using Ewald's method. *J. Phys. C Solid State Phys.*, 14(27):L827, 1981. doi:[10.1088/0022-3719/14/27/005](https://doi.org/10.1088/0022-3719/14/27/005).
- J. G. Brandenburg. (private communication, 2017).
- J. G. Brandenburg, J. E. Bates, J. Sun, and J. P. Perdew. Benchmark tests of a strongly constrained semilocal functional with a long-range dispersion correction. *Phys. Rev. B*, 94(11):115144, Sept. 2016. doi:[10.1103/PhysRevB.94.115144](https://doi.org/10.1103/PhysRevB.94.115144).
- T. Bučko, S. Lebègue, J. Hafner, and J. G. Ángyán. Improved Density Dependent Correction for the Description of London Dispersion Forces. *J. Chem. Theory Comput.*, 9(10):4293–4299, Oct. 2013. doi:[10.1021/ct400694h](https://doi.org/10.1021/ct400694h).
- T. Bučko, S. Lebègue, J. G. Ángyán, and J. Hafner. Extending the applicability of the Tkatchenko-Scheffler dispersion correction via iterative Hirshfeld partitioning. *J. Chem. Phys.*, 141(3):034114, July 2014. doi:[10.1063/1.4890003](https://doi.org/10.1063/1.4890003).
- T. Bučko, S. Lebègue, T. Gould, and J. G. Ángyán. Many-body dispersion corrections for periodic systems: An efficient reciprocal space implementation. *J. Phys.: Condens. Matter*, 28(4):045201, 2016. doi:[10.1088/0953-8984/28/4/045201](https://doi.org/10.1088/0953-8984/28/4/045201).
- P. Bultinck, C. V. Alsenoy, P. W. Ayers, and R. Carbó-Dorca. Critical analysis and extension of the Hirshfeld atoms in molecules. *J. Chem. Phys.*, 126(14):144111, Apr. 2007. doi:[10.1063/1.2715563](https://doi.org/10.1063/1.2715563).

- H. B. Callen and T. A. Welton. Irreversibility and generalized noise. *Phys. Rev.*, 83(1):34–40, July 1951. doi:[10.1103/PhysRev.83.34](https://doi.org/10.1103/PhysRev.83.34).
- H. B. G. Casimir and D. Polder. The influence of retardation on the London–van der Waals forces. *Phys. Rev.*, 73(4):360–372, Feb. 1948. doi:[10.1103/PhysRev.73.360](https://doi.org/10.1103/PhysRev.73.360).
- D. M. Ceperley. Fermion nodes. *J Stat Phys*, 63(5–6):1237–1267, June 1991. doi:[10.1007/BF01030009](https://doi.org/10.1007/BF01030009).
- D. M. Ceperley and B. J. Alder. Ground State of the Electron Gas by a Stochastic Method. *Phys. Rev. Lett.*, 45(7):566–569, Aug. 1980. doi:[10.1103/PhysRevLett.45.566](https://doi.org/10.1103/PhysRevLett.45.566).
- T. Chachiyo. Communication: Simple and accurate uniform electron gas correlation energy for the full range of densities. *J. Chem. Phys.*, 145(2):021101, July 2016. doi:[10.1063/1.4958669](https://doi.org/10.1063/1.4958669).
- J. Chen, A. Zen, J. G. Brandenburg, D. Alfè, and A. Michaelides. Evidence for stable square ice from quantum Monte Carlo. *Phys. Rev. B*, 94(22):220102, Dec. 2016. doi:[10.1103/PhysRevB.94.220102](https://doi.org/10.1103/PhysRevB.94.220102).
- V. R. Cooper. Van der Waals density functional: An appropriate exchange functional. *Phys. Rev. B*, 81(16):161104, Apr. 2010. doi:[10.1103/PhysRevB.81.161104](https://doi.org/10.1103/PhysRevB.81.161104).
- B. Cordero, V. Gómez, A. E. Platero-Prats, M. Revés, J. Echeverría, E. Cremades, F. Barragán, and S. Alvarez. Covalent radii revisited. *Dalton Trans.*, 0(21):2832–2838, May 2008. doi:[10.1039/B801115J](https://doi.org/10.1039/B801115J).
- P. J. W. Debye. Die van der Waalsschen Kohäsionskräfte [Van der Waals cohesion forces]. *Phys. Z.*, 21:178–187, 1920. URL <https://babel.hathitrust.org/cgi/pt?id=mdp.39015086723080;view=1up;seq=210>.
- M. Dion, H. Rydberg, E. Schröder, D. C. Langreth, and B. I. Lundqvist. Van der Waals density functional for general geometries. *Phys. Rev. Lett.*, 92(24):246401, June 2004. doi:[10.1103/PhysRevLett.92.246401](https://doi.org/10.1103/PhysRevLett.92.246401).
- P. A. M. Dirac. Note on Exchange Phenomena in the Thomas Atom. *Math. Proc. Camb. Philos. Soc.*, 26(3):376–385, July 1930. doi:[10.1017/S0305004100016108](https://doi.org/10.1017/S0305004100016108).
- R. A. DiStasio, Jr., G. von Helden, R. P. Steele, and M. Head-Gordon. On the T-shaped structures of the benzene dimer. *Chem. Phys. Lett.*, 437(4–6):277–283, Apr. 2007. doi:[10.1016/j.cplett.2007.02.034](https://doi.org/10.1016/j.cplett.2007.02.034).
- J. F. Dobson, A. White, and A. Rubio. Asymptotics of the Dispersion Interaction: Analytic Benchmarks for van der Waals Energy Functionals. *Phys. Rev. Lett.*, 96(7):073201, Feb. 2006. doi:[10.1103/PhysRevLett.96.073201](https://doi.org/10.1103/PhysRevLett.96.073201).
- A. G. Donchev. Many-body effects of dispersion interaction. *J. Chem. Phys.*, 125(7):074713, Aug. 2006. doi:[10.1063/1.2337283](https://doi.org/10.1063/1.2337283).
- M. Dubecký, P. Jurečka, R. Derian, P. Hobza, M. Otyepka, and L. Mitas. Quantum Monte Carlo Methods Describe Noncovalent Interactions with Subchemical Accuracy. *J. Chem. Theory Comput.*, 9(10):4287–4292, Oct. 2013. doi:[10.1021/ct4006739](https://doi.org/10.1021/ct4006739).
- T. H. Dunning, Jr. Gaussian basis sets for use in correlated molecular calculations. I. The atoms boron through neon and hydrogen. *J. Chem. Phys.*, 90(2):1007, 1989. doi:[10.1063/1.456153](https://doi.org/10.1063/1.456153).
- S. Ehrlich, J. Moellmann, and S. Grimme. Dispersion-Corrected Density Functional Theory for Aromatic Interactions in Complex Systems. *Acc. Chem. Res.*, 46(4):916–926, Apr. 2013. doi:[10.1021/ar3000844](https://doi.org/10.1021/ar3000844).
- M. Elstner, P. Hobza, T. Frauenheim, S. Suhai, and E. Kaxiras. Hydrogen bonding and stacking interactions of nucleic acid base pairs: A density-functional-theory based treatment. *J. Chem. Phys.*, 114(12):5149–5155, Mar. 2001. doi:[10.1063/1.1329889](https://doi.org/10.1063/1.1329889).
- P. P. Ewald. Die Berechnung optischer und elektrostatischer Gitterpotentiale [Calculation of optical and electrostatic lattice potentials]. *Ann. Phys.*, 369(3):253–287, Jan. 1921. doi:[10.1002/andp.19213690304](https://doi.org/10.1002/andp.19213690304).
- N. Ferri, R. A. DiStasio, Jr., A. Ambrosetti, R. Car, and A. Tkatchenko. Electronic Properties of Molecules and Surfaces with a Self-Consistent Interatomic van der Waals Density Functional. *Phys. Rev. Lett.*, 114(17):176802, Apr. 2015. doi:[10.1103/PhysRevLett.114.176802](https://doi.org/10.1103/PhysRevLett.114.176802).
- R. P. Feynman. Forces in Molecules. *Phys. Rev.*, 56(4):340–343, Aug. 1939. doi:[10.1103/PhysRev.56.340](https://doi.org/10.1103/PhysRev.56.340).
- W. M. C. Foulkes, L. Mitas, R. J. Needs, and G. Rajagopal. Quantum Monte Carlo simulations of solids. *Rev. Mod. Phys.*, 73(1):33–83, Jan. 2001. doi:[10.1103/RevModPhys.73.33](https://doi.org/10.1103/RevModPhys.73.33).
- F. Furche. Molecular tests of the random phase approximation to the exchange-correlation energy functional. *Phys. Rev. B*, 64(19):195120, Oct. 2001. doi:[10.1103/PhysRevB.64.195120](https://doi.org/10.1103/PhysRevB.64.195120).

- X. Ge and D. Lu. Local representation of the electronic dielectric response function. *Phys. Rev. B*, 92(24):241107, Dec. 2015. doi:[10.1103/PhysRevB.92.241107](https://doi.org/10.1103/PhysRevB.92.241107).
- A. K. Geim and I. V. Grigorieva. Van der Waals heterostructures. *Nature*, 499(7459):419–425, July 2013. doi:[10.1038/nature12385](https://doi.org/10.1038/nature12385).
- M. Gell-Mann and K. A. Brueckner. Correlation Energy of an Electron Gas at High Density. *Phys. Rev.*, 106(2):364–368, Apr. 1957. doi:[10.1103/PhysRev.106.364](https://doi.org/10.1103/PhysRev.106.364).
- P. Giannozzi, S. Baroni, N. Bonini, M. Calandra, R. Car, C. Cavazzoni, D. Ceresoli, G. L. Chiarotti, M. Cococcioni, I. Dabo, A. D. Corso, S. de Gironcoli, S. Fabris, G. Fratesi, R. Gebauer, U. Gerstmann, C. Gougoussis, A. Kokalj, M. Lazzeri, L. Martin-Samos, N. Marzari, F. Mauri, R. Mazzarello, S. Paolini, A. Pasquarello, L. Paulatto, C. Sbraccia, S. Scandolo, G. Sclauzero, A. P. Seitsonen, A. Smogunov, P. Umari, and R. M. Wentzcovitch. QUANTUM ESPRESSO: A Modular and Open-Source Software Project for Quantum Simulations of Materials. *J. Phys. Condens. Matter*, 21(39):395502, 2009. doi:[10.1088/0953-8984/21/39/395502](https://doi.org/10.1088/0953-8984/21/39/395502).
- V. V. Gobre and A. Tkatchenko. Scaling laws for van der Waals interactions in nanostructured materials. *Nat. Commun.*, 4:2341, Aug. 2013. doi:[10.1038/ncomms3341](https://doi.org/10.1038/ncomms3341).
- L. Goerigk. Treating London-Dispersion Effects with the Latest Minnesota Density Functionals: Problems and Possible Solutions. *J. Phys. Chem. Lett.*, 6(19):3891–3896, Oct. 2015. doi:[10.1021/acs.jpclett.5b01591](https://doi.org/10.1021/acs.jpclett.5b01591).
- T. Gould. How polarizabilities and C6 coefficients actually vary with atomic volume. *J. Chem. Phys.*, 145(8):084308, Aug. 2016. doi:[10.1063/1.4961643](https://doi.org/10.1063/1.4961643).
- T. Gould and T. Bučko. C6 Coefficients and Dipole Polarizabilities for All Atoms and Many Ions in Rows 1–6 of the Periodic Table. *J. Chem. Theory Comput.*, 12(8):3603–3613, Aug. 2016. doi:[10.1021/acs.jctc.6b00361](https://doi.org/10.1021/acs.jctc.6b00361).
- S. Grimme. Accurate description of van der Waals complexes by density functional theory including empirical corrections. *J. Comput. Chem.*, 25(12):1463–1473, Sept. 2004. doi:[10.1002/jcc.20078](https://doi.org/10.1002/jcc.20078).
- S. Grimme. Semiempirical GGA-type density functional constructed with a long-range dispersion correction. *J. Comput. Chem.*, 27(15):1787–1799, Nov. 2006. doi:[10.1002/jcc.20495](https://doi.org/10.1002/jcc.20495).
- S. Grimme. Do Special Noncovalent  $\pi$ – $\pi$  Stacking Interactions Really Exist? *Angew. Chem. Int. Ed.*, 47(18):3430–3434, Apr. 2008. doi:[10.1002/anie.200705157](https://doi.org/10.1002/anie.200705157).
- S. Grimme. Supramolecular Binding Thermodynamics by Dispersion-Corrected Density Functional Theory. *Chem. Eur. J.*, 18(32):9955–9964, Aug. 2012. doi:[10.1002/chem.201200497](https://doi.org/10.1002/chem.201200497).
- S. Grimme, J. Antony, S. Ehrlich, and H. Krieg. A consistent and accurate ab initio parametrization of density functional dispersion correction (DFT-D) for the 94 elements H–Pu. *J. Chem. Phys.*, 132(15):154104, Apr. 2010. doi:[10.1063/1.3382344](https://doi.org/10.1063/1.3382344).
- S. Grimme, S. Ehrlich, and L. Goerigk. Effect of the damping function in dispersion corrected density functional theory. *J. Comput. Chem.*, 32(7):1456–1465, May 2011. doi:[10.1002/jcc.21759](https://doi.org/10.1002/jcc.21759).
- E. K. U. Gross and W. Kohn. Local density-functional theory of frequency-dependent linear response. *Phys. Rev. Lett.*, 55(26):2850–2852, Dec. 1985. doi:[10.1103/PhysRevLett.55.2850](https://doi.org/10.1103/PhysRevLett.55.2850).
- T. A. Halgren. The representation of van der Waals (vdW) interactions in molecular mechanics force fields: Potential form, combination rules, and vdW parameters. *J. Am. Chem. Soc.*, 114(20):7827–7843, Sept. 1992. doi:[10.1021/ja00046a032](https://doi.org/10.1021/ja00046a032).
- I. Hamada. Van der Waals density functional made accurate. *Phys. Rev. B*, 89(12):121103, Mar. 2014. doi:[10.1103/PhysRevB.89.121103](https://doi.org/10.1103/PhysRevB.89.121103).
- D. R. Hamann. Optimized norm-conserving Vanderbilt pseudopotentials. *Phys. Rev. B*, 88(8):085117, Aug. 2013. doi:[10.1103/PhysRevB.88.085117](https://doi.org/10.1103/PhysRevB.88.085117).
- J. Hepburn, G. Scoles, and R. Penco. A simple but reliable method for the prediction of intermolecular potentials. *Chem. Phys. Lett.*, 36(4):451–456, Dec. 1975. doi:[10.1016/0009-2614\(75\)80278-8](https://doi.org/10.1016/0009-2614(75)80278-8).
- J. Hermann. Source code of program 'pymbd'. *Zenodo*, Oct. 2017. doi:[10.5281/zenodo.1008823](https://doi.org/10.5281/zenodo.1008823).
- J. Hermann and A. Tkatchenko. doi:[10.6084/m9.figshare.5117254](https://doi.org/10.6084/m9.figshare.5117254). URL <https://github.com/azag0/dft-vdw-range>. (git repository).

- J. Hermann, D. Alfè, and A. Tkatchenko. Nanoscale  $\pi$ - $\pi$  stacked molecules are bound by collective charge fluctuations. *Nat. Commun.*, 8:14052, Feb. 2017a. doi:10.1038/ncomms14052.
- J. Hermann, R. A. DiStasio, Jr., and A. Tkatchenko. First-principles models for van der Waals interactions in molecules and materials: Concepts, theory, and applications. *Chem. Rev.*, 117(6):4714–4758, Mar. 2017b. doi:10.1021/acs.chemrev.6b00446.
- A. Heßelmann. Derivation of the dispersion energy as an explicit density- and exchange-hole functional. *J. Chem. Phys.*, 130(8):084104, Feb. 2009. doi:10.1063/1.3077939.
- F. L. Hirshfeld. Bonded-atom fragments for describing molecular charge densities. *Theoret. Chim. Acta*, 44(2):129–138, June 1977. doi:10.1007/BF00549096.
- P. Hobza, H. L. Selzle, and E. W. Schlag. Potential Energy Surface for the Benzene Dimer. Results of ab Initio CCSD(T) Calculations Show Two Nearly Isoenergetic Structures: T-Shaped and Parallel-Displaced. *J. Phys. Chem.*, 100(48):18790–18794, Jan. 1996. doi:10.1021/jp961239y.
- P. Hohenberg and W. Kohn. Inhomogeneous electron gas. *Phys. Rev.*, 136(3B):B864–B871, Nov. 1964. doi:10.1103/PhysRev.136.B864.
- K. Hui and J.-D. Chai. SCAN-based hybrid and double-hybrid density functionals from models without fitted parameters. *J. Chem. Phys.*, 144(4):044114, Jan. 2016. doi:10.1063/1.4940734.
- E. Hult, Y. Andersson, B. I. Lundqvist, and D. C. Langreth. Density functional for van der Waals forces at surfaces. *Phys. Rev. Lett.*, 77(10):2029–2032, Sept. 1996. doi:10.1103/PhysRevLett.77.2029.
- E. Hult, H. Rydberg, B. Lundqvist, and D. Langreth. Unified treatment of asymptotic van der Waals forces. *Phys. Rev. B*, 59(7):4708–4713, Feb. 1999. doi:10.1103/PhysRevB.59.4708.
- K. L. C. Hunt. Nonlocal polarizability densities and van der Waals interactions. *J. Chem. Phys.*, 78(10):6149–6155, May 1983. doi:10.1063/1.444577.
- C. A. Hunter. Sequence-dependent DNA Structure: The Role of Base Stacking Interactions. *J. Mol. Biol.*, 230(3):1025–1054, Apr. 1993. doi:10.1006/jmbi.1993.1217.
- C. A. Hunter and J. K. M. Sanders. The nature of  $\pi$ - $\pi$  interactions. *J. Am. Chem. Soc.*, 112(14):5525–5534, July 1990. doi:10.1021/ja00170a016.
- T. Iwamoto, Y. Watanabe, H. Takaya, T. Haino, N. Yasuda, and S. Yamago. Size- and Orientation-Selective Encapsulation of  $C_{70}$  by Cycloparaphenylenes. *Chem. Eur. J.*, 19(42):14061–14068, Oct. 2013. doi:10.1002/chem.201302694.
- G. Jansen, R.-F. Liu, and J. G. Ángyán. On the equivalence of ring-coupled cluster and adiabatic connection fluctuation-dissipation theorem random phase approximation correlation energy expressions. *J. Chem. Phys.*, 133(15):154106, Oct. 2010. doi:10.1063/1.3481575.
- R. Jasti, J. Bhattacharjee, J. B. Neaton, and C. R. Bertozzi. Synthesis, Characterization, and Theory of [9]-, [12]-, and [18]Cycloparaphenylenes: Carbon Nanohoop Structures. *J. Am. Chem. Soc.*, 130(52):17646–17647, Dec. 2008. doi:10.1021/ja807126u.
- E. R. Johnson and A. D. Becke. A post-Hartree-Fock model of intermolecular interactions: Inclusion of higher-order corrections. *J. Chem. Phys.*, 124(17):174104, May 2006. doi:10.1063/1.2190220.
- J. E. Jones. On the determination of molecular fields. II. From the equation of state of a gas. *Proc. R. Soc. Lond. A*, 106(738):463–477, Oct. 1924. doi:10.1098/rspa.1924.0082.
- T. Kawase. Receptors for Pristine Fullerenes Based on Concave–Convex  $\pi$ - $\pi$ Interactions. In Nazariortín and J.-F. Nierengarten, editors, *Supramolecular Chemistry of Fullerenes and Carbon Nanotubes*, pages 55–78. Wiley-VCH Verlag GmbH & Co. KGaA, 2012. ISBN 978-3-527-65012-5. doi:10.1002/9783527650125.ch3. URL <http://onlinelibrary.wiley.com/doi/10.1002/9783527650125.ch3/summary>.
- T. Kawase and H. Kurata. Ball-, Bowl-, and Belt-Shaped Conjugated Systems and Their Complexing Abilities: Exploration of the Concave–Convex  $\pi$ - $\pi$  Interaction. *Chem. Rev.*, 106(12):5250–5273, Dec. 2006. doi:10.1021/cr0509657.
- W. H. Keesom. On the second virial coefficient for monatomic gases, and for hydrogen below the Boyle-point. *Proc. KNAW*, 15:643–649, 1912. URL <http://>

- //www.dwc.knaw.nl/toegangen/digital-library-knaw/?pagetype=publDetail&pId=PU00013008.
- K. S. Kim, P. Tarakeshwar, and J. Y. Lee. Molecular Clusters of  $\pi$ -Systems: Theoretical Studies of Structures, Spectra, and Origin of Interaction Energies. *Chem. Rev.*, 100(11):4145–4186, Nov. 2000. doi:10.1021/cr990051i.
- J. Klimeš, D. R. Bowler, and A. Michaelides. Chemical accuracy for the van der Waals density functional. *J. Phys.: Condens. Matter*, 22(2):022201, 2010. doi:10.1088/0953-8984/22/2/022201.
- J. Klimeš, D. R. Bowler, and A. Michaelides. Van der Waals density functionals applied to solids. *Phys. Rev. B*, 83(19):195131, May 2011. doi:10.1103/PhysRevB.83.195131.
- W. Kohn and L. J. Sham. Self-Consistent Equations Including Exchange and Correlation Effects. *Phys. Rev.*, 140(4A):A1133–A1138, Nov. 1965. doi:10.1103/PhysRev.140.A1133.
- W. Kohn, Y. Meir, and D. E. Makarov. Van der Waals energies in density functional theory. *Phys. Rev. Lett.*, 80(19):4153–4156, May 1998. doi:10.1103/PhysRevLett.80.4153.
- J. Komasa. Dipole and quadrupole polarizabilities and shielding factors of beryllium from exponentially correlated Gaussian functions. *Phys. Rev. A*, 65(1):012506, Dec. 2001. doi:10.1103/PhysRevA.65.012506.
- S. Kurth and J. P. Perdew. Density-functional correction of random-phase-approximation correlation with results for jellium surface energies. *Phys. Rev. B*, 59(16):10461–10468, Apr. 1999. doi:10.1103/PhysRevB.59.10461.
- L. D. Landau and E. M. Lifschitz. *Statistical Physics*, volume 5. Pergamon Press, Oxford, 3rd edition, Jan. 1980. ISBN 978-0-7506-3372-7.
- A. Lauchner, A. E. Schlather, A. Manjavacas, Y. Cui, M. J. McClain, G. J. Stec, F. J. García de Abajo, P. Nordlander, and N. J. Halas. Molecular Plasmonics. *Nano Lett.*, 15(9):6208–6214, Sept. 2015. doi:10.1021/acs.nanolett.5b02549.
- K. Lee, É. D. Murray, L. Kong, B. I. Lundqvist, and D. C. Langreth. Higher-accuracy van der Waals density functional. *Phys. Rev. B*, 82(8):081101, Aug. 2010. doi:10.1103/PhysRevB.82.081101.
- M. Lein, E. K. U. Gross, and J. P. Perdew. Electron correlation energies from scaled exchange-correlation kernels: Importance of spatial versus temporal nonlocality. *Phys. Rev. B*, 61(20):13431–13437, May 2000. doi:10.1103/PhysRevB.61.13431.
- M. Levy. Universal variational functionals of electron densities, first-order density matrices, and natural spin-orbitals and solution of the  $v$ -representability problem. *Proc. Natl. Acad. Sci.*, 76(12):6062–6065, Jan. 1979. URL <http://www.pnas.org/content/76/12/6062>.
- E. M. Lifshitz. The theory of molecular attractive forces between solids (M. Hamermesh, transl.). *Sov. Phys. JETP*, 2(1):73–83, 1956. URL <http://www.jetp.ac.ru/cgi-bin/e/index/e/2/1/p73?a=list>.
- F. London. Zur Theorie und Systematik der Molekularkräfte [On theory and classification of molecular forces]. *Z. Physik*, 63(3-4):245–279, Mar. 1930. doi:10.1007/BF01421741.
- F. London. The general theory of molecular forces. *Trans. Faraday Soc.*, 33(0):8–26, Jan. 1937. doi:10.1039/TF937330008B.
- P.-F. Loos. Exchange functionals based on finite uniform electron gases. *J. Chem. Phys.*, 146(11):114108, Mar. 2017. doi:10.1063/1.4978409.
- A. Lucas. Collective contributions to the long-range dipolar interaction in rare-gas crystals. *Physica*, 35(3): 353–368, 1967. doi:10.1016/0031-8914(67)90184-X.
- A. A. Lucas, A. Ronveaux, M. Schmeits, and F. Delanaye. Van der Waals energy between voids in dielectrics. *Phys. Rev. B*, 12(12):5372–5380, Dec. 1975. doi:10.1103/PhysRevB.12.5372.
- G. D. Mahan. Van der Waals Forces in Solids. *J. Chem. Phys.*, 43(5):1569–1574, Sept. 1965. doi:10.1063/1.1696973.
- H. Margenau. Van der Waals forces. *Rev. Mod. Phys.*, 11(1):1–35, Jan. 1939. doi:10.1103/RevModPhys.11.1.
- N. Marzari, A. A. Mostofi, J. R. Yates, I. Souza, and D. Vanderbilt. Maximally localized Wannier functions: Theory and applications. *Rev. Mod. Phys.*, 84(4):1419–1475, Oct. 2012. doi:10.1103/RevModPhys.84.1419.
- A. Mayer. Formulation in terms of normalized propagators of a charge-dipole model enabling the calculation of the polarization properties of fullerenes and carbon nanotubes. *Phys. Rev. B*, 75(4):045407,

- Jan. 2007. doi:[10.1103/PhysRevB.75.045407](https://doi.org/10.1103/PhysRevB.75.045407).
- E. A. Meyer, R. K. Castellano, and F. Diederich. Interactions with Aromatic Rings in Chemical and Biological Recognition. *Angew. Chem. Int. Ed.*, 42(11):1210–1250, Mar. 2003. doi:[10.1002/anie.200390319](https://doi.org/10.1002/anie.200390319).
- A. J. Misquitta, J. Spencer, A. J. Stone, and A. Alavi. Dispersion interactions between semiconducting wires. *Phys. Rev. B*, 82(7):075312, Aug. 2010. doi:[10.1103/PhysRevB.82.075312](https://doi.org/10.1103/PhysRevB.82.075312).
- M. Monthioux. Filling single-wall carbon nanotubes. *Carbon*, 40(10):1809–1823, Aug. 2002. doi:[10.1016/S0008-6223\(02\)00102-1](https://doi.org/10.1016/S0008-6223(02)00102-1).
- W. T. M. Mooij, F. B. van Duijneveldt, J. G. C. M. van Duijneveldt-van de Rijdt, and B. P. van Eijck. Transferable ab initio intermolecular potentials. I. Derivation from methanol dimer and trimer calculations. *J. Phys. Chem. A*, 103(48):9872–9882, Dec. 1999. doi:[10.1021/jp991641n](https://doi.org/10.1021/jp991641n).
- C. Mück-Lichtenfeld, S. Grimme, L. Kobryn, and A. Sygula. Inclusion complexes of buckycatcher with  $C_{60}$  and  $C_{70}$ . *Phys. Chem. Chem. Phys.*, 12(26):7091–7097, June 2010. doi:[10.1039/B925849C](https://doi.org/10.1039/B925849C).
- Y. Mutō. Hikyokusei bunshi no aida ni sayō suru chikara ni tsuite [On forces acting between nonpolar molecules]. *Nippon Sugaku-Buturigakkwaishi*, 17:629–631, Oct. 1943. doi:[10.11429/subutsukaishii927.17.10-11-12\\_629](https://doi.org/10.11429/subutsukaishii927.17.10-11-12_629).
- S. Okada, S. Saito, and A. Oshiyama. Energetics and Electronic Structures of Encapsulated  $C_{60}$  in a Carbon Nanotube. *Phys. Rev. Lett.*, 86(17):3835–3838, Apr. 2001. doi:[10.1103/PhysRevLett.86.3835](https://doi.org/10.1103/PhysRevLett.86.3835).
- T. Olsen and K. S. Thygesen. Extending the random-phase approximation for electronic correlation energies: The renormalized adiabatic local density approximation. *Phys. Rev. B*, 86(8):081103, Aug. 2012. doi:[10.1103/PhysRevB.86.081103](https://doi.org/10.1103/PhysRevB.86.081103).
- T. Olsen and K. S. Thygesen. Beyond the random phase approximation: Improved description of short-range correlation by a renormalized adiabatic local density approximation. *Phys. Rev. B*, 88(11):115131, Sept. 2013a. doi:[10.1103/PhysRevB.88.115131](https://doi.org/10.1103/PhysRevB.88.115131).
- T. Olsen and K. S. Thygesen. Random phase approximation applied to solids, molecules, and graphene-metal interfaces: From van der Waals to covalent bonding. *Phys. Rev. B*, 87(7):075111, Feb. 2013b. doi:[10.1103/PhysRevB.87.075111](https://doi.org/10.1103/PhysRevB.87.075111).
- T. Olsen and K. S. Thygesen. Accurate Ground-State Energies of Solids and Molecules from Time-Dependent Density-Functional Theory. *Phys. Rev. Lett.*, 112(20):203001, May 2014. doi:[10.1103/PhysRevLett.112.203001](https://doi.org/10.1103/PhysRevLett.112.203001).
- A. Otero-de-la-Roza and E. R. Johnson. A benchmark for non-covalent interactions in solids. *J. Chem. Phys.*, 137(5):054103, Aug. 2012. doi:[10.1063/1.4738961](https://doi.org/10.1063/1.4738961).
- A. W. Overhauser. Spin density waves in an electron gas. *Phys. Rev.*, 128(3):1437–1452, Nov. 1962. doi:[10.1103/PhysRev.128.1437](https://doi.org/10.1103/PhysRev.128.1437).
- R. G. Parr and W. Yang. *Density-Functional Theory of Atoms and Molecules*. Number 16 in The international series of monographs on chemistry. Oxford University Press, 1989. ISBN 978-0-19-509276-9. URL <https://global.oup.com/academic/product/density-functional-theory-of-atoms-and-molecules-9780195092769>.
- R. Pauncz. *Spin Eigenfunctions*. Plenum Press, New York, 1979. ISBN 978-1-4684-8526-4. URL <http://www.springer.com/us/book/9781468485288>.
- H. Peng, Z.-H. Yang, J. P. Perdew, and J. Sun. Versatile van der Waals Density Functional Based on a Meta-Generalized Gradient Approximation. *Phys. Rev. X*, 6(4):041005, Oct. 2016. doi:[10.1103/PhysRevX.6.041005](https://doi.org/10.1103/PhysRevX.6.041005).
- J. P. Perdew and K. Schmidt. Jacob's ladder of density functional approximations for the exchange-correlation energy. *AIP Conf. Proc.*, 577(1):1–20, July 2001. doi:[10.1063/1.1390175](https://doi.org/10.1063/1.1390175).
- J. P. Perdew and Y. Wang. Accurate and simple analytic representation of the electron-gas correlation energy. *Phys. Rev. B*, 45(23):13244–13249, June 1992. doi:[10.1103/PhysRevB.45.13244](https://doi.org/10.1103/PhysRevB.45.13244).
- J. P. Perdew, K. Burke, and M. Ernzerhof. Generalized Gradient Approximation Made Simple. *Phys. Rev. Lett.*, 77(18):3865–3868, Oct. 1996a. doi:[10.1103/PhysRevLett.77.3865](https://doi.org/10.1103/PhysRevLett.77.3865).
- J. P. Perdew, M. Ernzerhof, and K. Burke. Rationale for mixing exact exchange with density functional

- approximations. *J. Chem. Phys.*, 105(22):9982–9985, Dec. 1996b. doi:10.1063/1.472933.
- K. Pernal, R. Podeszwa, K. Patkowski, and K. Szalewicz. Dispersionless Density Functional Theory. *Phys. Rev. Lett.*, 103(26):263201, Dec. 2009. doi:10.1103/PhysRevLett.103.263201.
- L. Piela. *Ideas of Quantum Chemistry*. Elsevier, 2nd edition, 2014. ISBN 978-0-444-52227-6. URL <http://www.sciencedirect.com/science/book/9780444522276>.
- D. Pines and D. Bohm. A Collective Description of Electron Interactions: II. Collective vs Individual Particle Aspects of the Interactions. *Phys. Rev.*, 85(2):338–353, Jan. 1952. doi:10.1103/PhysRev.85.338.
- R. Podeszwa, R. Bukowski, and K. Szalewicz. Potential Energy Surface for the Benzene Dimer and Perturbational Analysis of  $\pi$ - $\pi$  Interactions. *J. Phys. Chem. A*, 110(34):10345–10354, Aug. 2006. doi:10.1021/jp064095o.
- S. J. Rahi, T. Emig, N. Graham, R. L. Jaffe, and M. Kardar. Scattering theory approach to electrodynamic Casimir forces. *Phys. Rev. D*, 80(8):085021, Oct. 2009. doi:10.1103/PhysRevD.80.085021.
- A. M. Reilly and A. Tkatchenko. Understanding the role of vibrations, exact exchange, and many-body van der Waals interactions in the cohesive properties of molecular crystals. *J. Chem. Phys.*, 139(2):024705, July 2013. doi:10.1063/1.4812819.
- E.-A. Reinsch and W. Meyer. Finite-perturbation calculation of static quadrupole and mixed dipole-octupole polarizabilities for the ground states of the first-row atoms. *Phys. Rev. A*, 18(5):1793–1796, Nov. 1978. doi:10.1103/PhysRevA.18.1793.
- X. Ren, A. Tkatchenko, P. Rinke, and M. Scheffler. Beyond the Random-Phase Approximation for the Electron Correlation Energy: The Importance of Single Excitations. *Phys. Rev. Lett.*, 106(15):153003, Apr. 2011. doi:10.1103/PhysRevLett.106.153003.
- X. Ren, P. Rinke, C. Joas, and M. Scheffler. Random-phase approximation and its applications in computational chemistry and materials science. *J. Mater. Sci.*, 47(21):7447–7471, June 2012. doi:10.1007/s10853-012-6570-4.
- X. Ren, P. Rinke, G. E. Scuseria, and M. Scheffler. Renormalized second-order perturbation theory for the electron correlation energy: Concept, implementation, and benchmarks. *Phys. Rev. B*, 88(3):035120, July 2013. doi:10.1103/PhysRevB.88.035120.
- M. J. Renne and B. R. A. Nijboer. Microscopic derivation of macroscopic Van der Waals forces. *Chem. Phys. Lett.*, 1(8):317–320, Oct. 1967. doi:10.1016/0009-2614(67)80004-6.
- J. Řezáč and P. Hobza. Describing Noncovalent Interactions beyond the Common Approximations: How Accurate Is the “Gold Standard,” CCSD(T) at the Complete Basis Set Limit? *J. Chem. Theory Comput.*, 9(5):2151–2155, May 2013. doi:10.1021/ct400057w.
- J. Řezáč, K. E. Riley, and P. Hobza. S66: A Well-balanced Database of Benchmark Interaction Energies Relevant to Biomolecular Structures. *J. Chem. Theory Comput.*, 7(8):2427–2438, Aug. 2011. doi:10.1021/ct2002946.
- J. Řezáč, Y. Huang, P. Hobza, and G. J. O. Beran. Benchmark Calculations of Three-Body Intermolecular Interactions and the Performance of Low-Cost Electronic Structure Methods. *J. Chem. Theory Comput.*, 11(7):3065–3079, July 2015. doi:10.1021/acs.jctc.5b00281.
- T. Risthaus and S. Grimme. Benchmarking of London Dispersion-Accounting Density Functional Theory Methods on Very Large Molecular Complexes. *J. Chem. Theory Comput.*, 9(3):1580–1591, Mar. 2013. doi:10.1021/ct301081n.
- A. Rodriguez, M. Ibanescu, D. Iannuzzi, J. D. Joannopoulos, and S. G. Johnson. Virtual photons in imaginary time: Computing exact Casimir forces via standard numerical electromagnetism techniques. *Phys. Rev. A*, 76(3):032106, Sept. 2007. doi:10.1103/PhysRevA.76.032106.
- A. W. Rodriguez, F. Capasso, and S. G. Johnson. The Casimir effect in microstructured geometries. *Nat. Photonics*, 5(4):211–221, Apr. 2011. doi:10.1038/nphoton.2011.39.
- V. G. Ruiz, W. Liu, E. Zojer, M. Scheffler, and A. Tkatchenko. Density-Functional Theory with Screened van der Waals Interactions for the Modeling of Hybrid Inorganic–Organic Systems. *Phys. Rev. Lett.*, 108(14):146103, Apr. 2012. doi:10.1103/PhysRevLett.108.146103.

- E. Runge and E. K. U. Gross. Density-Functional Theory for Time-Dependent Systems. *Phys. Rev. Lett.*, 52(12):997–1000, Mar. 1984. doi:[10.1103/PhysRevLett.52.997](https://doi.org/10.1103/PhysRevLett.52.997).
- A. Ruzsinszky, J. P. Perdew, J. Tao, G. I. Csonka, and J. M. Pitarke. Van der Waals Coefficients for Nanostructures: Fullerenes Defy Conventional Wisdom. *Phys. Rev. Lett.*, 109(23):233203, Dec. 2012. doi:[10.1103/PhysRevLett.109.233203](https://doi.org/10.1103/PhysRevLett.109.233203).
- B. K. Sahoo. An ab initio relativistic coupled-cluster theory of dipole and quadrupole polarizabilities: Applications to a few alkali atoms and alkaline earth ions. *Chemical Physics Letters*, 448(1–3):144–149, Nov. 2007. doi:[10.1016/j.cplett.2007.09.079](https://doi.org/10.1016/j.cplett.2007.09.079).
- T. Sato and H. Nakai. Density functional method including weak interactions: Dispersion coefficients based on the local response approximation. *J. Chem. Phys.*, 131(22):224104, Dec. 2009. doi:[10.1063/1.3269802](https://doi.org/10.1063/1.3269802).
- T. Sato and H. Nakai. Local response dispersion method. II. Generalized multicenter interactions. *J. Chem. Phys.*, 133(19):194101, Nov. 2010. doi:[10.1063/1.3503040](https://doi.org/10.1063/1.3503040).
- P. C. Schmidt, A. Weiss, and T. P. Das. Effect of crystal fields and self-consistency on dipole and quadrupole polarizabilities of closed-shell ions. *Phys. Rev. B*, 19(11):5525–5534, June 1979. doi:[10.1103/PhysRevB.19.5525](https://doi.org/10.1103/PhysRevB.19.5525).
- H. Schröder, A. Creon, and T. Schwabe. Reformulation of the D3(Becke–Johnson) Dispersion Correction without Resorting to Higher than C6 Dispersion Coefficients. *J. Chem. Theory Comput.*, 11(7):3163–3170, July 2015. doi:[10.1021/acs.jctc.5b00400](https://doi.org/10.1021/acs.jctc.5b00400).
- L. R. Schwarz, A. Alavi, and G. H. Booth. Projector Quantum Monte Carlo Method for Nonlinear Wave Functions. *Phys. Rev. Lett.*, 118(17):176403, Apr. 2017. doi:[10.1103/PhysRevLett.118.176403](https://doi.org/10.1103/PhysRevLett.118.176403).
- G. E. Scuseria, T. M. Henderson, and D. C. Sorensen. The ground state correlation energy of the random phase approximation from a ring coupled cluster doubles approach. *J. Chem. Phys.*, 129(23):231101, Dec. 2008. doi:[10.1063/1.3043729](https://doi.org/10.1063/1.3043729).
- P. L. Silvestrelli. Van der Waals Interactions in DFT Made Easy by Wannier Functions. *Phys. Rev. Lett.*, 100(5):053002, Feb. 2008. doi:[10.1103/PhysRevLett.100.053002](https://doi.org/10.1103/PhysRevLett.100.053002).
- P. L. Silvestrelli. Van der Waals interactions in density functional theory by combining the quantum harmonic oscillator-model with localized Wannier functions. *J. Chem. Phys.*, 139(5):054106, Aug. 2013. doi:[10.1063/1.4816964](https://doi.org/10.1063/1.4816964).
- P. L. Silvestrelli, K. Benyahia, S. Grubisic, F. Ancilotto, and F. Toigo. Van der Waals interactions at surfaces by density functional theory using Wannier functions. *J. Chem. Phys.*, 130(7):074702, Feb. 2009. doi:[10.1063/1.3077288](https://doi.org/10.1063/1.3077288).
- M. O. Sinnokrot and C. D. Sherrill. High-Accuracy Quantum Mechanical Studies of  $\pi$ – $\pi$  Interactions in Benzene Dimers. *J. Phys. Chem. A*, 110(37):10656–10668, Sept. 2006. doi:[10.1021/jp0610416](https://doi.org/10.1021/jp0610416).
- M. O. Sinnokrot, E. F. Valeev, and C. D. Sherrill. Estimates of the Ab Initio Limit for  $\pi$ – $\pi$  Interactions: The Benzene Dimer. *J. Am. Chem. Soc.*, 124(36):10887–10893, Sept. 2002. doi:[10.1021/ja025896h](https://doi.org/10.1021/ja025896h).
- J. C. Slater and J. G. Kirkwood. The van der Waals forces in gases. *Phys. Rev.*, 37(6):682–697, Mar. 1931. doi:[10.1103/PhysRev.37.682](https://doi.org/10.1103/PhysRev.37.682).
- D. G. A. Smith, L. A. Burns, K. Patkowski, and C. D. Sherrill. Revised Damping Parameters for the D3 Dispersion Correction to Density Functional Theory. *J. Phys. Chem. Lett.*, 7(12):2197–2203, June 2016. doi:[10.1021/acs.jpclett.6b00780](https://doi.org/10.1021/acs.jpclett.6b00780).
- S. N. Steinmann and C. Corminboeuf. A System-Dependent Density-Based Dispersion Correction. *J. Chem. Theory Comput.*, 6(7):1990–2001, July 2010. doi:[10.1021/ct1001494](https://doi.org/10.1021/ct1001494).
- S. N. Steinmann and C. Corminboeuf. Comprehensive Benchmarking of a Density-Dependent Dispersion Correction. *J. Chem. Theory Comput.*, 7(11):3567–3577, Nov. 2011. doi:[10.1021/ct200602x](https://doi.org/10.1021/ct200602x).
- R. M. Sternheimer. Quadrupole Polarizabilities of Various Ions and the Alkali Atoms. *Phys. Rev. A*, 1(2):321–327, Feb. 1970. doi:[10.1103/PhysRevA.1.321](https://doi.org/10.1103/PhysRevA.1.321).
- A. J. Stone. *The Theory of Intermolecular Forces*. Oxford University Press, 2nd edition, Jan. 2013. ISBN 978-0-19-967239-4. URL <http://www.oxfordscholarship.com/view/10.1093/acprof:oso/9780199672394.001.0001/acprof-9780199672394>.

- J. Sun, B. Xiao, Y. Fang, R. Haunschmid, P. Hao, A. Ruzsinszky, G. I. Csonka, G. E. Scuseria, and J. P. Perdew. Density Functionals that Recognize Covalent, Metallic, and Weak Bonds. *Phys. Rev. Lett.*, 111(10):106401, Sept. 2013. doi:[10.1103/PhysRevLett.111.106401](https://doi.org/10.1103/PhysRevLett.111.106401).
- J. Sun, A. Ruzsinszky, and J. P. Perdew. Strongly Constrained and Appropriately Normed Semilocal Density Functional. *Phys. Rev. Lett.*, 115(3):036402, July 2015. doi:[10.1103/PhysRevLett.115.036402](https://doi.org/10.1103/PhysRevLett.115.036402).
- J. Sun, R. C. Remsing, Y. Zhang, Z. Sun, A. Ruzsinszky, H. Peng, Z. Yang, A. Paul, U. Waghmare, X. Wu, M. L. Klein, and J. P. Perdew. Accurate first-principles structures and energies of diversely bonded systems from an efficient density functional. *Nat. Chem.*, 8(9):831–836, Sept. 2016. doi:[10.1038/nchem.2535](https://doi.org/10.1038/nchem.2535).
- A. Sygula, F. R. Fronczek, R. Sygula, P. W. Rabideau, and M. M. Olmstead. A Double Concave Hydrocarbon Buckycatcher. *J. Am. Chem. Soc.*, 129(13):3842–3843, Apr. 2007. doi:[10.1021/ja070616p](https://doi.org/10.1021/ja070616p).
- D. Tabor and R. H. S. Winterton. The direct measurement of normal and retarded van der Waals forces. *Proc. R. Soc. Lond. A*, 312(1511):435–450, Sept. 1969. doi:[10.1098/rspa.1969.0169](https://doi.org/10.1098/rspa.1969.0169).
- J. Tao, J. P. Perdew, V. N. Staroverov, and G. E. Scuseria. Climbing the Density Functional Ladder: Nonempirical Meta-Generalized Gradient Approximation Designed for Molecules and Solids. *Phys. Rev. Lett.*, 91(14):146401, Sept. 2003. doi:[10.1103/PhysRevLett.91.146401](https://doi.org/10.1103/PhysRevLett.91.146401).
- J. Tao, J. P. Perdew, and A. Ruzsinszky. Long-range van der Waals attraction and alkali-metal lattice constants. *Phys. Rev. B*, 81(23):233102, June 2010. doi:[10.1103/PhysRevB.81.233102](https://doi.org/10.1103/PhysRevB.81.233102).
- T. Thonhauser, V. R. Cooper, S. Li, A. Puzder, P. Hyldgaard, and D. C. Langreth. Van der Waals density functional: Self-consistent potential and the nature of the van der Waals bond. *Phys. Rev. B*, 76(12):125112, Sept. 2007. doi:[10.1103/PhysRevB.76.125112](https://doi.org/10.1103/PhysRevB.76.125112).
- A. Tkatchenko and M. Scheffler. Accurate Molecular Van Der Waals Interactions from Ground-State Electron Density and Free-Atom Reference Data. *Phys. Rev. Lett.*, 102(7):073005, Feb. 2009. doi:[10.1103/PhysRevLett.102.073005](https://doi.org/10.1103/PhysRevLett.102.073005).
- A. Tkatchenko and O. A. von Lilienfeld. Popular Kohn-Sham density functionals strongly overestimate many-body interactions in van der Waals systems. *Phys. Rev. B*, 78(4):045116, July 2008. doi:[10.1103/PhysRevB.78.045116](https://doi.org/10.1103/PhysRevB.78.045116).
- A. Tkatchenko, R. A. DiStasio, Jr., R. Car, and M. Scheffler. Accurate and Efficient Method for Many-Body van der Waals Interactions. *Phys. Rev. Lett.*, 108(23):236402, June 2012. doi:[10.1103/PhysRevLett.108.236402](https://doi.org/10.1103/PhysRevLett.108.236402).
- A. Tkatchenko, A. Ambrosetti, and R. A. DiStasio, Jr. Interatomic methods for the dispersion energy derived from the adiabatic connection fluctuation-dissipation theorem. *J. Chem. Phys.*, 138(7):74106, Feb. 2013. doi:[10.1063/1.4789814](https://doi.org/10.1063/1.4789814).
- J. Toulouse, F. Colonna, and A. Savin. Long-range–short-range separation of the electron-electron interaction in density-functional theory. *Phys. Rev. A*, 70(6):062505, Dec. 2004. doi:[10.1103/PhysRevA.70.062505](https://doi.org/10.1103/PhysRevA.70.062505).
- J. Toulouse, I. C. Gerber, G. Jansen, A. Savin, and J. G. Ángyán. Adiabatic-Connection Fluctuation-Dissipation Density-Functional Theory Based on Range Separation. *Phys. Rev. Lett.*, 102(9):096404, Mar. 2009. doi:[10.1103/PhysRevLett.102.096404](https://doi.org/10.1103/PhysRevLett.102.096404).
- A. Unsöld. Quantentheorie des Wasserstoffmolekülions und der Born-Landéschen Abstoßungskräfte. *Z. Physik*, 43(8):563–574, Aug. 1927. doi:[10.1007/BF01397633](https://doi.org/10.1007/BF01397633).
- J. D. van der Waals. *Over de Continuiteit van den Gas- en Vloeistoftoestand [On the continuity of the gas and liquid state]*. PhD thesis, Leiden, 1873. URL <https://www.lorentz.leidenuniv.nl/history/proefschriften/>.
- P. S. Venkataram, J. Hermann, A. Tkatchenko, and A. W. Rodriguez. Unifying microscopic and continuum treatments of van der Waals and Casimir interactions. *Phys. Rev. Lett.*, 118(26):266802, June 2017. doi:[10.1103/PhysRevLett.118.266802](https://doi.org/10.1103/PhysRevLett.118.266802).
- T. Verstraelen, E. Pauwels, F. De Proft, V. Van Speybroeck, P. Geerlings, and M. Waroquier. Assessment of Atomic Charge Models for Gas-Phase Computations on Polypeptides. *J. Chem. Theory Comput.*, 8(2):

- 661–676, Feb. 2012. doi:[10.1021/ct200512e](https://doi.org/10.1021/ct200512e).
- C. F. von Weizsäcker. Zur Theorie der Kernmassen [On theory of atomic masses]. *Z. Für Phys.*, 96(7-8): 431–458, July 1935. doi:[10.1007/BF01337700](https://doi.org/10.1007/BF01337700).
- O. A. Vydrov and T. Van Voorhis. Improving the accuracy of the nonlocal van der Waals density functional with minimal empiricism. *J. Chem. Phys.*, 130(10):104105, Mar. 2009. doi:[10.1063/1.3079684](https://doi.org/10.1063/1.3079684).
- O. A. Vydrov and T. Van Voorhis. Nonlocal van der Waals density functional: The simpler the better. *J. Chem. Phys.*, 133(24):244103, Dec. 2010. doi:[10.1063/1.3521275](https://doi.org/10.1063/1.3521275).
- O. A. Vydrov, Q. Wu, and T. Van Voorhis. Self-consistent implementation of a nonlocal van der Waals density functional with a Gaussian basis set. *J. Chem. Phys.*, 129(1):014106, July 2008. doi:[10.1063/1.2948400](https://doi.org/10.1063/1.2948400).
- S. C. Wang. Die gegenseitige Einwirkung zweier Wasserstoffatome [Mutual influence of two hydrogen atoms]. *Phys. Z.*, 28:663–666, 1927.
- J. Wellendorff, K. T. Lundgaard, A. Møgelhøj, V. Petzold, D. D. Landis, J. K. Nørskov, T. Bligaard, and K. W. Jacobsen. Density functionals for surface science: Exchange-correlation model development with Bayesian error estimation. *Phys. Rev. B*, 85(23):235149, June 2012. doi:[10.1103/PhysRevB.85.235149](https://doi.org/10.1103/PhysRevB.85.235149).
- N. Wiser. Dielectric constant with local field effects included. *Phys. Rev.*, 129(1):62–69, Jan. 1963. doi:[10.1103/PhysRev.129.62](https://doi.org/10.1103/PhysRev.129.62).
- J. Witte, N. Mardirossian, J. B. Neaton, and M. Head-Gordon. Assessing DFT-D3 Damping Functions Across Widely Used Density Functionals: Can We Do Better? *J. Chem. Theory Comput.*, 13(5): 2043–2052, May 2017. doi:[10.1021/acs.jctc.7b00176](https://doi.org/10.1021/acs.jctc.7b00176).
- L. M. Woods, D. A. R. Dalvit, A. Tkatchenko, P. Rodriguez-Lopez, A. W. Rodriguez, and R. Podgornik. Materials perspective on Casimir and van der Waals interactions. *Rev. Mod. Phys.*, 88(4):045003, Nov. 2016. doi:[10.1103/RevModPhys.88.045003](https://doi.org/10.1103/RevModPhys.88.045003).
- Q. Wu and W. Yang. Empirical correction to density functional theory for van der Waals interactions. *J. Chem. Phys.*, 116(2):515–524, Jan. 2002. doi:[10.1063/1.1424928](https://doi.org/10.1063/1.1424928).
- Z. Yan, J. P. Perdew, and S. Kurth. Density functional for short-range correlation: Accuracy of the random-phase approximation for isoelectronic energy changes. *Phys. Rev. B*, 61(24):16430–16439, June 2000. doi:[10.1103/PhysRevB.61.16430](https://doi.org/10.1103/PhysRevB.61.16430).
- J. Yang, W. Hu, D. Usvyat, D. Matthews, M. Schütz, and G. K.-L. Chan. Ab initio determination of the crystalline benzene lattice energy to sub-kilojoule/mole accuracy. *Science*, 345(6197):640–643, Aug. 2014. doi:[10.1126/science.1254419](https://doi.org/10.1126/science.1254419).
- L. Yang, C. Adam, G. S. Nichol, and S. L. Cockroft. How much do van der Waals dispersion forces contribute to molecular recognition in solution? *Nat. Chem.*, 5(12):1006–1010, Dec. 2013. doi:[10.1038/nchem.1779](https://doi.org/10.1038/nchem.1779).
- A. Zen, S. Sorella, M. J. Gillan, A. Michaelides, and D. Alfè. Boosting the accuracy and speed of quantum Monte Carlo: Size consistency and time step. *Phys. Rev. B*, 93(24):241118, June 2016. doi:[10.1103/PhysRevB.93.241118](https://doi.org/10.1103/PhysRevB.93.241118).
- G.-X. Zhang, A. Tkatchenko, J. Paier, H. Appel, and M. Scheffler. Van der Waals Interactions in Ionic and Semiconductor Solids. *Phys. Rev. Lett.*, 107(24):245501, Dec. 2011. doi:[10.1103/PhysRevLett.107.245501](https://doi.org/10.1103/PhysRevLett.107.245501).
- S. Zhang. Fabrication of novel biomaterials through molecular self-assembly. *Nat. Biotechnol.*, 21(10): 1171–1178, Oct. 2003. doi:[10.1038/nbt874](https://doi.org/10.1038/nbt874).
- Y. Zhang and W. Yang. Comment on “Generalized Gradient Approximation Made Simple”. *Phys. Rev. Lett.*, 80(4):890–890, Jan. 1998. doi:[10.1103/PhysRevLett.80.890](https://doi.org/10.1103/PhysRevLett.80.890).
- Y. Zhang, W. Pan, and W. Yang. Describing van der Waals interaction in diatomic molecules with generalized gradient approximations: The role of the exchange functional. *J. Chem. Phys.*, 107(19): 7921–7925, Nov. 1997. doi:[10.1063/1.475105](https://doi.org/10.1063/1.475105).